The Internal Combustion Engine Modelling

Modelling, Estimation and Control Issues

Vigild, Christian Winge

Publication date:
2002

Document Version
Publisher's PDF, also known as Version of record

The Internal Combustion Engine

Modelling, Estimation and Control Issues

Christian Winge Vigild

SUBMITTED IN PARTIAL FULFILLMENT OF THE
REQUIREMENTS FOR THE DEGREE OF
DOCTOR OF PHILOSOPHY
AT
TECHNICAL UNIVERSITY OF DENMARK
LYNGBY, DENMARK
DECEMBER 2001

ØRSTED·DTU, Automation
DTU, Bld. 326
DK-2800 Kgs. Lyngby
Denmark
Phone +45 4525 3550

Printed in Denmark at DTU, Kgs. Lyngby
01-A-918
ISBN 87-87950-90-1

TECHNICAL UNIVERSITY OF DENMARK
INSTITUTE OF AUTOMATION

The following persons, signing here, hereby certify that they have read and recommend to the Konsistorium the acceptance of a dissertation entitled "**The Internal Combustion Engine – Modelling, Estimation and Control Issues**" by **Christian Winge Vigild** in partial fulfillment of the requirements for the degree of **Doctor of Philosophy**.

Dated: December 2001

External Examiner: _____
Lars Eriksson

Research Supervisors: _____
Elbert L. Hendricks

_____
Spencer C. Sorenson

Examining Committee: _____

TECHNICAL UNIVERSITY OF DENMARK

December, 2001

Author: **Christian Winge Vigild**
Title: **The Internal Combustion Engine – Modelling, Estimation and Control Issues**
Department: **Department of Automation**
Degree: **Ph.D.** Convocation: **-** Year: **2002**

Signature of Author

To my grandparents:

Tove & Herluf Vigild
and
Else & Kaj Nielsen

Contents

List of Figures

List of Tables

List of Articles Included

Abstract

Alternative power-trains have become buzz words in the automotive industry in the recent past. New technologies like Lithium-Ion batteries or fuel cells combined with high efficient electrical motors show promising results. However both technologies are extremely expensive and important questions like ”How are we going to supply fuel-cells with hydrogen in an environmentally friendly way?”, ”How are we going to improve the range - and recharging speed - of electrical vehicles?” and ”How will our existing infrastructure cope with such changes?” are still left unanswered. Hence, the internal combustion engine with all its shortcomings is to stay with us for the next many years. What the future will really bring in this area is uncertain, but one thing can be said for sure; the time of the pipe in – pipe out engine concept is over.

Modern engines, Diesel or gasoline, have in the recent past been provided with many new technologies to improve both performance and handling and to cope with the tightening emission legislations. However, as new devices are included, the number of control inputs is also gradually increased. Hence, the control matrix dimension has grown to a considerably size, and the typical table and regression based engine calibration procedures currently in use today contain both challenging and time-consuming tasks. One way to improve understanding of engines and provide a more comprehensive picture of the control problem is by use of simplified physical modelling – one of the main thrusts of this dissertation.

The application of simplified physical modelling as a foundation for engine estimation and control design is first motivated by two control applications. The control problem concerns Air/Fuel ratio control of Spark Ignition engines. Two different ways of control are presented; one based on a model based Extended Kalman Filter updated predictor, and one based on robust $\mathcal{H}_\infty$ techniques. Both controllers are validated on an engine dynamometer and engine data traces are presented. The successful application of the model based controllers is then the motivation behind the research in simplified engine modelling to be presented in this dissertation.

One of the objectives of this dissertation is to propose a framework for simplified modelling of internal combustion engines and selected subcomponents. This has lead to the development of a new modelling concept for Variable Geometry turbochargers, and a simplified Exhaust Gas Recirculation (EGR) model which can predict the temperature distribution along the exhaust gas recirculation system with

unsteady flows. Furthermore, since engine combustion modelling often is carried out on a phenomenological level due to its complex nature, a new regression tool is developed which eases this modelling task.

In the chapter concerning estimation, one of the most important findings is that EGR cannot be robustly controlled despite measurement of the air to fuel ratio in exhaust gas.

The work closes with a presentation of a new estimation methodology which may supply a control strategy with an estimate of the actual control direction. The estimator is utilized in a control strategy which balances the intake mass flow of a twin-turbocharged V-engine. Since there exists a point of sign reversal in the VGT position–air mass flow characteristic, whose exact location is unknown, the control problem is posed with serious stability issues. These problems have been solved with the new non-linear estimation methodology developed – a sign-reversal estimator.

Dansk resumé

Forbrændingsmotoren
–
Modellering, estimering og regulerings-problematik

Alternative køretøjer er p.t. meget omdiskuteret i medierne. Nye teknologier som Lithium-Ion batterier eller brændstofceller kombineret med høj effektive elektriske motorer har vist lovende resultater. Disse teknologier er dog begge ekstremt dyre og vigtige spørgsmål som: „Hvordan vil vi forsyne brændstofceller med hydrogen på en miljøvenlig måde?“, „Hvordan vil vi forbedre elektriske køretøjers rækkevide og opladningstid?“, og „Hvordan vil vores eksisterende infrastruktur reagerer på sådane forandringer?“ er stadig ubesvarede. Forbrændingsmotoren vil derfor, skønt alle dens ulemper, være det fortrukne fremdriftsmiddel i den næste årrække. Hvad fremtiden vil bringe indenfor automobil udvikling er dog usikker, men en ting kan blive sagt med sikkerhed; den simple rør ind–rør ud forbrændingsmotors dage er talte.

Moderne Diesel- og benzin-motorer er i de seneste år blevet udstyret med en række nye teknologier for at forbedre performance og køreegenskaber, og for at imødekomme de til stadighed hårdere emissionskrav. Men, lige så hurtigt som de nye teknologier blive monteret stiger antallet af reguleringsmuligheder. Derfor er kontrolproblemets dimension i dag vokset til en formidabel størrelse , og den typiske regressionsbaserede motorkalibreringsprocedure er blevet en vanskelig og tidskrævende opgave. En måde at forbedre motor- og kontrolproblem forståelsen på er ved at benytte simplificerede fysiske modeller – dette er et af hovedområderene i denne afhandling.

Anvendelse af simplificerede fysisk baserede modeller som grundlag for estimations- og kontrol-design er konsolideret af to kontroleksempler. Reguleringsproblemet er i begge tilfælde luft/brændstof-forhold kontrol af benzinmotorer. To vidt forskellige metoder bliver præsenteret: en baseret på et robust $\mathcal{H}_\infty$ kontroldesign, mens den anden metode er baseret på en Extended Kalman Filter opdateret prediktor. Begge regulatorer er blevet afprøvet på en motor-prøvestand med gode resultater til følge. Et udpluk af måleresultaterne er præsenteret i dette arbejde. Denne successfulde anvendelse af fysisk modelbaserede regulatorer er motivationen bag det arbejdet som vil blive præsenteret i denne afhandling.

Et af formålene er udarbejdelsen af en standardiseret metode til simpel modellering af forbrændingsmotore og udvalgte motorkomponenter. Dette arbejde har ledt til udvikling af et Variable Geometry turbo modelleringskoncept, og en simplificeret Exhaust Gas Recirculation (EGR) model, som kan predikterer temperaturdistribution trends under varierende strømningsforhold. Da selve forbrændingsprocessen i motoren er så kompliceret er modelleringsarbejdet ofte udført ud fra fænomensbetragtninger. For at lette dette modelleringsarbejde er der i dette arbejde udviklet et simpelt regressionsbaseret værktøj til at kortlægge visse motoregenskaber.

I estimationskapitlet er en alarmerende iagttagelse gjort; Ekstern udstødningsrecirkulering (EGR) kan kun kontrolleres i åbensløjfe selvom om udstødningsgasforholdene er kendt!

Afhandlingen afslutter med en præsentation af balanceringskontrol af indsugningsluftmassestrømningerne på en bi-turbo monteret V motor. Dette kontrolproblem er umådelig vanskeligt, idet der eksisterer et punkt i VGT position–kompressormassestrømnings-karakteristikken, hvis nøjagtige placering er ukendt, hvor fortegnet skifter. Dette kan naturligvis lede til alvorlige stabilitetsproblemer. Problemet er løst med en nyudviklet estimationsmetode – sign-reversal estimatoren.

Acknowledgements

During a work of this length one is inevitable bound to meet people who are able to inspire through their passion and knowledge of engine and control technologies in general.... and this work is no exception.

I joined the Engine Control Group at the Technical University of Denmark lead by Professor Elbert Hendricks and Professor Spencer C. Sorenson together with my fellow student Michael Struwe in an early period of our Master study – and from this group we also graduated as Masters. Here we found the man who many internally in the group refer to as the old dude, Professor Elbert Hendricks. Elbert's very unorthodox way of interacting with his students was at first very surprising and scaring, but after some time I came to appreciate this – we were not his students but rather his boys. Thank you...

Furthermore, I would like to thank my supervisors Elbert Hendricks and Spencer C. Sorenson for giving me the opportunity to carry out this project.

This project probably would not have been finished if had not been for two persons in particular. First, I wish to thank Dipl. Ing. Thomas Nitsche who is a dear colleague of mine here in the Diesel combustion research group at Ford Forschungszentrum, Aachen. Thomas was an invaluable sparring partner during the modelling work presented in this dissertation. His great experience with jet propulsion systems gathered through his years at Roll's Royce helped greatly in the quest of what is and what is not important in turbocharger modelling. Furthermore, in addition to just being a good friend Thomas sacrificed many hours in proof reading the manuscript and on moral support.
Thomas – thank you.

Secondly, I wish to thank Ph.D. Evangelos Karvounis, my team leader at Ford Forschungszentrum, Aachen. Evangelos is at best comparable with an astronomically phenomenon – the black hole. Everything that is worth knowing about engines regardless of gasoline or diesel, simulation and modelling is sucked in and embodied in him, hence he was and is an invaluable source of information. Evangelos was always available if a problem came up and despite being on vacation he took the time needed to resolve troubling matters. And... and ... and.
Evangelos – thank you.

Dr. Urs Christen and Ph.D.-student M.Sc. Jim Benjamin Luther are gratefully acknowledged for always being available for technical discussions and for helping out with the English language.

Ford Forschungszentrum Aachen GmbH and its people are gratefully acknowledged for all the support during the project.

On the private side I would like to thank my wife Andrea for all her support and patience during miserable times. Hopefully, we now get the time to do more together.

Last but not least I would like to thank my family for all the support they have provided from the time my vocabulary was limited to ”øf” until Andrea found my first grey hairs.

Christian Winge Vigild

Aachen, Germany
December, 2001

Introduction

Motivation

The internal combustion engine is still the main choice for personal transportation due to its relatively low production cost, proven durability and compactness. Recently new promising technologies like fuel cells or lithium–ion batteries combined with permanent magnet electrical motors have been introduced as possible successors to the internal combustion engine. However, they are still much too expensive to be considered real competitors. Hence, the internal combustion engine will remain the main means of transportation for the next many years. The continued use of the internal combustion engine, however, has in the last couple of decades become more and more an environmentally important issue - and thereby has awakened serious political interest. Figure 1 illustrates an estimated distribution of five different pollution categories between four sources. The heavy environmentally burden coming from road transportation is clear.

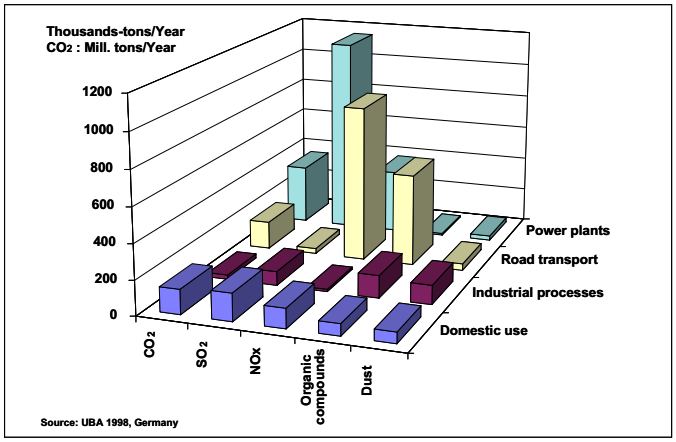

Figure 1: Estimated environmentally pollution load in 1998, [18]

In order to reduce road transportation related pollution, the government has taken various initiatives to motivate the automotive industry to invest in environmentally friendly vehicles research, for more than two decades now. One of the biggest legislation initiated improvements is probably the general use of catalytic

converters. The first family of catalysts introduced in series production was of the oxidation type, which were able to lower CO (Carbon Oxide) pollution by approximately 80%. Shortly after followed the TWC (Three Way Catalyst) (1981) and toxic exhaust gas components CO, HC (Hydrocarbon) and NO_X could now simultaneously be converted into environmentally harmless emissions. However, the TWC could only be used with gasoline engines and furthermore called for a very precise control of the AFR (Air/Fuel Ratio) around the stoichiometric level during both transient and steady state engine operation. Even small excursions outside the window of $\pm 1\%$ around the stoichiometric level lowers the TWCs efficiency drastically. A typical picture of the TWC's efficiency level is graphically illustrated in figure 2.

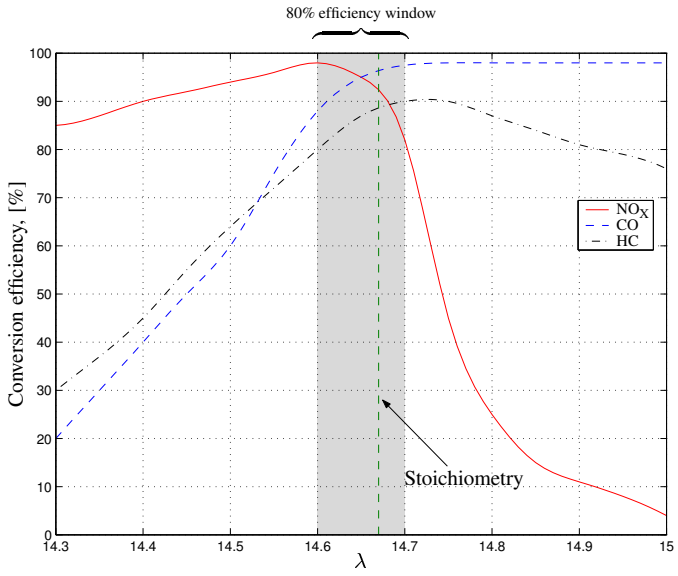

Figure 2: Typical efficiency of a Three Way Catalyst [54].

The development of environmentally friendly gasoline engines has continued, and since the application of catalytic converters, several new technologies like e.g. EGR and GDI (Gasoline Direct Injection), have been introduced to reduce toxic exhaust products. However, augmenting the basic engine design with new technologies often leads to additional degrees of control freedom, and hence *control handles* that need to be adjusted simultaneously; the control task has thus experienced an almost exponential growth.

In the later years global warming has become an environmentally issue too and has received a lot of public attention, and hence initiated political interest. The general accepted opinion is that CO_2 (Carbon Dioxide), which formerly has been recognized as a harmless combustion bi-product, promotes global warming. Hence, the outlet of CO_2 has to be controlled. Since road transportation related CO_2 constitutes a large fraction of the total global humanly generated CO_2 pro-

duction, public focus will in the future probably increase in this area. However, since CO_2 is a natural bi-product when burning a fossil fuel, the only really logical way to reduce the CO_2 outlet is to improve transport vehicle fuel economy. Another reason to improve mileage is of course the increasing fuel prices. Here, the modern Diesel engine has proven itself as a worthy competitor to the gasoline engine both in terms of drivability, performance and of course its better fuel efficiency. What used to be recognized as a smelly, heavy, and everything else than sporty engine has developed into a high torque–high performance engine without sacrificing exhaust emissions. This is due to technological improvements in areas like air boosting systems, fuel injection systems, exhaust gas recirculation systems and combustion chamber design improvements. However, just like the case with the gasoline engine this has also increased the order of the state space that needs to be controlled.

The actual handling of the the additional degrees of control freedom is often in the automotive industry encompassed by augmenting existing engine control strategies by new sub-level strategies. The sub-level strategies are, however, most often basic table look-up strategies simply imposed on an existing control structure without changing the main control structures. Hence, conventional control strategies have now evolved into control structures with often more than ten thousand calibration coefficients (see e.g. [10]), and the corresponding calibration task normally proves to be both a challenging and time consuming assignment. The work load is actually so intense that it has spawned a new kind of work force in the automotive industry – the calibrators.

Dynamic physical modelling and simulation have in the later years proven to aid tremendously in the engine design phase due to the often much more comprehensive picture provided by such models and the engine controller design is no exception. With the introduction of the electronically embedded MVEM (Mean Value Engine Model) to estimate essential engine states, several look-up tables could be eliminated. Hence, research in such models and physically based control designs are important key elements if the ever increasing engine control task is to be mastered.

Objectives and contributions

The title of the Ph.D. study was „*Robust Control of Nonlinear Systems*“. However, due to the vast variety of different control issues covered by such a title, since what control objects are not included by the nonlinear definition? and who does not want a robust control design?, this dissertation is devoted to investigation, modelling, estimation and control of the internal combustion engine; Hence, the title „*The Internal Combustion Engine – Modelling, Estimation and Control Issues*“. This is merely a specialization of the original project.

To motivate the research in the MVEM (Mean Value Engine Model) framework for estimation and control design the first chapter presents two AFR controllers

designed by utilizing the MVEM framework.

In the first application the AFR of an SI (Spark Ignition) engine is controlled around stoichiometry by a time based $\mathcal{H}_\infty$ designed controller without using predictive measures to overcome time delay limitations. Since the controller is time based, the engine time delay will vary with engine speed. However, the restrictions imposed by this dynamic variation are included in the control design, making a subsequent system inspection by μ analysis possible. Furthermore, the volumetric engine efficiency variation is thrown into the control design, making volumetric efficiency table implementation for AFR control purposes obsolete.

The next controller is based on a zero dimensional model of the intake manifold system together with an empirical model of the engine pumping fluctuation dynamics as a model background for an SI AFR event based predictor design. The model based predictor uses an EKF (Extended Kalman Filter) to initialize its states. Due to the predictive nature of the AFR control, and by postponing the intake throttle command a fixed number of event based samples, the AFR control performance may be boosted considerably compared to conventional control algorithms.

Although both controllers utilize a completely different control strategy they have both been successfully tested on an engine test bed at DTU (Technical University of Denmark). Thus, the good modelling framework of the MVEM is confirmed initiating a further research in extensions to the MVEM framework and applications; the topic set for the rest of the dissertation.

As already mentioned in the beginning of this dissertation the internal combustion engine has been augmented with several new technologies to meet future emission- and performance targets. However, due to the often very ad-hoc fashion in which the control possibilities offered by the new technologies are utilized, the overall engine control picture becomes lost in the control strategy design phase. To improve focus on engine control essentials compact simplified engine models has gained great interest recently. Such models provided a way to test and debug control structures before actual implementation. However, the models are quite often based on look-up table interpolation or polynomial regression equations alone; The flexibility and scalability of such models are obviously poor. Hence, one of the objectives of this dissertation is to develop a unified way to model modern combustion engines. This has lead to the development of VES; an objective C code intended for use in the SIMULINK®/MATLAB® environment. The goal of this engine library is to offer an open and improved way to set up physically based zero dimensional engine models, since key engine components are basically treated just as LEGO bricks; key engine components can be added, removed and edited as required.

The development of VES has spawned several new contributions in the modelling field . First, the radial turbocharger has been carefully analyzed and broken down into three key elements: thermodynamic compressor and turbine behavior, and dynamic turbocharger wheel behavior. The compressor mass flow model has been statistically tested on three compressor maps and found optimal in all three cases i.e. the modelling error is normally distributed with mean value zero and is

relatively small. The turbine model is able to describe the mass flow through a turbine equipped with adjustable inlet nozzles, a so called VGT, within high accuracy. Furthermore, the model is able to provide a prediction of where the mass flow through the turbine reverses i.e. the turbine acts as a compressor.

Secondly, the introduction of EGR systems as a means to lower engine NO_X production renders the application of isothermal MVEMs for observer designs problematic due to the large temperature gradient between exhaust and intake air systems. This problem was first addressed in [75] and lead to model augmentation by a temperature state equation. This allowed for a dynamic description of the intake manifold temperature and thus more precise AFR control. However, an unavoidable mixing between the throttle body air and EGR will always exist when back flow conditions are present, making it impossible to assess the right mean value of the energy flow out the EGR system, $\mathrm{E}(\dot{m}_{egr}c_pT_{egr})$, in a MVEM framework. This statement was first predicted by a simplified EGR system model and later proven by measurements.

Third, precise EGR control is mandatory for optimal emissions control. However, after initial detailed system analysis it is here concluded that the EGR rate or rather the burnt mass fraction in the intake manifold can not be directly nor accurately estimated from either intake air flow, exhaust gas composition or temperature measurements. Hence, EGR control can only be controlled in an open loop fashion.

Fourth, engine control and estimation algorithms are run in an either time based or event based fashion. One of the arguments for doing the data sampling time based is the better utilization of sensor information since the anti-aliasing filters do not have to be designed for the lowest sampling frequency, while event based sampling may simplify certain engine observer designs. A new family of anti-aliasing filters is presented here which can provide optimal measurement bandwidth independently of the engine speed, and is thus optimal for event based engine control and estimation strategies.

Fifth, a new estimation methodology based on AM (Amplitude Modulation) techniques to locate sign reversal points in a systems input-output characteristics without the need for dynamic observer information is developed. This estimation method is later successfully applied in a simulation study to toggle the output sign of a MAF balancing controller on a bi-turbo equipped V6 engine model.

Dissertation organization

The dissertation is divided in five main chapters.

The first chapter introduces briefly some of the control problems encountered with the internal combustion engine. The advent of the MVEM (Mean Value Engine Model) framework in the late 1980's has been shown to ease and simplify the design of both estimation and control strategies. The good modelling qualities

offered by this framework are confirmed by two applications included in this dissertation concerning AFR control of SI engines. The first controller is based on a $\mathcal{H}_\infty$ control design, while the second AFR controller utilizes an event based predictive control design. The large difference in the control philosophy behind the AFR controllers and the successful experimental application in both cases supports the vast number of possibilities offered by the MVEM framework. This chapter is the introduction to and the motivation behind the rest of dissertation.

Chapter 2 discusses the engine modelling concepts which have been either developed or utilized in this text. Attention has especially been put on the turbocharger, EGR system and phenomenological combustion modelling.

In chapter 3 different EGR rate estimation schemes are analyzed. First the necessary dynamic state equations are found and combined to prepare the basics for a later steady state analysis of relative sensor measurement errors' influence on EGR estimation performance. Furthermore, a new family of anti-aliasing filters is presented, which can provide event based estimation schemes with the optimal amount of sensor information independent of engine speed.

Chapter 4 presents and discusses the results obtained with a newly developed sign-reversal detection algorithm. The algorithm can locate points of sign reversal in a dynamic system's characteristics, and thereby toggle the controller output sign. In this way it is possible to maintain the control direction desired. The sign-reversal estimation algorithm is later validated and confirmed by simulations.

Chapter 5 closes the dissertation with final conclusions and recommendations for future work.

Chapter 1

Recent MVEM based control developments

The purpose of this chapter is to provide the motivation for the research in simplified modelling of the internal combustion engine presented in this dissertation. The motivation is established by a presentation of two air-fuel ratio controllers for spark ignition engines. The controllers are both designed by utilizing the MVEM (Mean Value Engine Model) framework. However, the controllers designed originate from two very different control philosophies. The successful experimentally evaluation of both controllers and the significant diversity in the underlying control philosophy motivate the research in extensions to the MVEM framework.

1.1 Introduction

Control of IC (Internal Combustion) engines has become a more and more challenging task. In the early days of IC engines up to the time where the automobile had become almost universal possession in the West, engine control was merely limited to compensate for the SI engine's hesitation to accelerator pedal tip-ins and engine knocking. The first control problem was accomplished by the carburetor with the latter being achieved by a pneumatically controlled servomechanism mounted on the spark distributor; Both mechanisms are of the pure feed-forward control type. The Diesel engine was in theory even easier to control from a dynamic point of view since there was generally speaking only one control problem, the air-to-fuel ratio control problem. This control problem was in principle limited to an adjustment of the fuel control screw on the Diesel pump such that excessive exhaust smoke and extensive engine wear at full load were avoided. The actual speed control of the engine was done directly by the driver (and is for many commercial passenger cars available today still left to the driver) or the speed-governor (mostly used in heavy-duty applications), with the latter being adjustable through

one or more calibration screws. Hence, the only really closed engine control loop was until the recent past the driver–engine speed control loop.

The invention of a number of new technologies to reduce emissions and increase engine performance has rendered the simplified engine control picture presented above obsolete. Key elements from this list of new automotive technologies and the corresponding advantages/disadvantages associated are presented in more detail in chapter 2. A more elaborate list and discussion will therefore not be given here. The general rule is that the state space needing control actions grows in size as various technologies are moved from the list of possible engine components to the list of standard engine components. An example is the adoption of electronic fuel injection systems and three-way catalysts to reduce the emissions of SI engines. Gasoline fuel injection systems were already in the middle 1950's available as a power option (see [31]), but were later reintroduced as a mandatory equipment necessary to meet the strict fuelling requirements required by the TWC; a requirement not achievable with the standard fitted carburetor at that time. The fuelling strategy was in parallel to this transformed from a pure mechanically implemented system into software code and implemented with the wonder of the century; the microprocessor. However, the fuelling strategy implemented was normally just a number of different lookup tables in engine speed and intake manifold pressure; thus it was merely a static picture of the engine's behavior. These tables defined the steady state fuelling strategy for the engine. Engine hesitation due to throttle tip-ins was compensated for with a differentiating network controlled by the size of the throttle angle derivative, and possible stationary AFR errors were removed by a feedback loop around the EGO (Exhaust Gas Oxygen) sensor fitted to the exhaust manifold. Although it was possible to control the engine fuelling more precisely, more time and money were now needed for the calibration process of the individual tables to achieve acceptable drivability and engine emissions. Furthermore, as new tables were added to existing strategies to improve performance in an incremental way, the control picture became in general only more blurred and fuzzy (see e.g. [30]).

A strong attack on the problems and the complications with conventional AFR control strategies for SI engines briefly presented above was in 1990 given in the article *"Mean Value Modeling of Spark Ignition Engines"* by *E. Hendricks and S. C. Sorenson*, see [49]. The research in [49] defined a framework for simplified SI engine modelling; an extension to the MVEM terminology introduced earlier in the article *"The Analysis of Mean Value Engine Models"* by *E. Hendricks*, see [43][1]. It can be argued that the modelling framework behind the MVEM concept was outline as early as 1980 by *D. Dobner*, see [28]. This research presents a discrete engine model with an isothermal description of the intake manifold pressure. However, investigation of the simulation results presented in [28] obtained with a mathematical mean value model of an 5.7 liter carbureted SI engine indicates

[1]The research presented in [43] was motivated by the good modelling accuracy of a large, two-stroke Diesel engine obtained earlier in [42]

that the mass exchange computation is erroneous; the air mass flow basically stays constant after a throttle tip-out although the intake manifold pressure level has not stabilized. This is not physically realistic and would thus make a model based observer design difficult. Hence, it was at first with the presentation of the SI MVEM in [49] that observer based control of e.g. the AFR has been tractable.

Since the introduction of the MVEM framework, numerous investigations and applications using this framework have been reported to the engineering community, and the list of articles is today of an impressive length[2]. Two recent articles written by the author and co-authors attacking the AFR control problem of SI engines and belonging to the list mentioned are included in this dissertation. The first article is entitled *"Towards robust H-infinity control of an SI engine's air/fuel ratio"* and the second is entitled *"Predicting the port air mass flow of SI engines in air/fuel ratio control applications"*. Both articles were presented at the annual SAE (Society of Automotive Engineers) conference in Detroit in 1999 and 2000, respectively.

Although the control concepts behind the final AFR controllers developed in the two articles are very different they both utilize an observer derived from the MVEM framework to achieve the AFR control targets set. Hence, both articles utilize the vast number of possibilities offered by the MVEM framework, and the strategies developed are later confirmed by experimental results.

1.2 $\mathcal{H}_\infty$ air-to-fuel ratio control

The SAE paper *"Towards robust H-infinity control of an SI engine's air/fuel ratio"*, based on some of the research carried out earlier in [103], attacks the AFR control problem of SI engines in a rather untraditional way. Here, the intake air flow is regarded as a perturbation of the engine's AFR and the $\mathcal{H}_\infty$ controller developed thus attempts to attenuated (reject) the effects of the intake port mass flow changes as much as possible. The intake port mass flow is well described in transients as well as in steady state by the engine speed, the cycle averaged intake pressure, the engine's volumetric efficiency (see section 2.7), and the intake manifold temperature. Thus, neglecting the intake temperature dynamics, the final control design should be made robust against changes in the three variables remaining. Such an AFR controller design is very interesting and is worth pursuing since it would eliminate the need for an intake manifold pressure sensor and the implementation and calibration of a lookup table of the engine's volumetric efficiency in the AFR control algorithm.

The observer behind the final control design is derived by at first establishing a dynamic description of the AFR signal path from the fuel injection to the measurement point. This nonlinear model is then later utilized to create the λ-object; a linear state space model of the AFR signal path. The development of the nonlinear

[2] A list of articles authored by the ECG (Engine Control Group) at Technical University of Denmark may be found online at http://www.iau.dtu.dk/~eh/elb_pub.html

AFR model is based on the isothermal MVEM described in [50] and [47], and the fuel film model presented in [52].

The final AFR feedback controller utilizes two measurement signals: The λ exhaust sensor signal and the MAF measurement obtained upstream of the throttle body. The λ measurement is required to insure that the overall system is detectable (see e.g. [41]). The MAF measurement is optional. However, if it is included in the final control design the transient performance of $\mathcal{H}_\infty$ AFR control strategy may be improved considerably. This is quite logical since if this measurement is omitted, then the $\mathcal{H}_\infty$ controller can only counteract AFR perturbations after they have been registered by the λ sensor in the exhaust pipe. The bandwidth of this loop is significantly limited by the time delays introduced between the fuel injection and the λ measurement. However, if the observer incorporated in the controller is augmented with a MAF input, possible AFR perturbations may registered earlier and thereby improve transient control performance. Unfortunately, series production MAF sensors based on hot-film or hot-wire technology are after some service time known to be troubled by significant stationary measurement errors (see [94]). Hence, the final controller uses only a bandwidth filtered version of the MAF signal to avoid steady state AFR control problems.

The final controller was designed, digitally implemented, and experimentally tested by the author and one of the co-authors, *M. Struwe*, on one of the engine test-beds available to the ECG (Engine Control Group) at DTU. Some of the experimental results obtained are included in the paper.

1999-01-0854

Towards Robust H-infinity Control of an SI Engine's Air/Fuel Ratio

Christian Winge Vigild
Karsten P. H. Andersen
Elbert Hendricks
Technical University of Denmark

Michael Struwe
Sander-Hansen

ABSTRACT

Long term stoichiometric Air/Fuel Ratio (AFR) control of an SI engine is at the present mainly maintained by table mapping of the engine's fresh air intake as a function of the engine operating point. In order to reduce a stationary error in the AFR to zero the table based control normally works in conjunction with a PI feedback from a HEGO sensor. The effective bandwidth of this feedback loop is quite small and seldom exceeds 2 Hz. This is altogether too small for accurate transient AFR control.

This paper presents a new λ (normalized Air/Fuel Ratio) control methodology ($\mathcal{H}_\infty$control) which has a somewhat larger bandwidth and can guarantee robustness with respect to selected engine variable and parameter variations.

1 INTRODUCTION

A modern engine control system consists presently of two main parts: a "base" fuel calculation and a λ or Φ control loop, see figure 1. The variables λ and Φ are defined in equation (1).

$$\lambda = \frac{\dot{m}_{ap}}{L_{th}\dot{m}_f} \qquad \Phi = \frac{L_{th}\dot{m}_f}{\dot{m}_{ap}} \tag{1}$$

Most often the base fuel calculation is determined by the air mass flow to an engine from a table lookup. The index for the table lookup is calculated from engine sensor measurements. A more advanced method to estimate the air mass flow is by use of an observer technique, like the MVEM (Mean Value Engine Model) observer presented in [1] and [2]. The base fuel loop normally operates around the stoichiometric air/fuel operating point in order to achieve maximum Three Way Catalyst (TWC) efficiency. Since the base fuel calculation most often is done in open loop, the AFR (Air/Fuel Ratio) will have a tendency to drift from the desired operating point due to effects like fuel film formation, fuel injector heating [3] and changes in the volumetric efficiency η_{vol} [4]. In order to maintain the desired λ or Φ operating point it is necessary to incorporate an active λ-feedback loop from an exhaust air/fuel sensor[1] to the fuel algorithm. The active λ-feedback loop must be capable of keeping λ within a $\pm\frac{1}{2}\%$ window around the reference point ($\lambda = 1$) in the mean in order to assure a good TWC efficiency. The λ-feedback loop is seen as the lower loop in figure 1. The total fuel command (base fuel calculation and correction term from the λ-loop) is sent through a NTFC filter [5] in order to compensate for the effects of the fuel film dynamics in the intake manifold before it is converted into a pulse width signal appropriate for the fuel injector driver.

The control structure described above has one main disadvantage: no measure of its stability and/or performance is available, especially with respect to variations in the engine's parameters (due to either changes in the operating point or ageing effects). One way to overcome these problems is to formulate a complete model of the entire system which is required for the fuelling calculation. If this step is successful, one can then proceed with designing a λ-controller for the overall model which takes engine operating point and parameter variations into account.

Once the model is available, a linearised version of it can be derived which is suitable for application of the $\mathcal{H}_\infty$control methodology. System nonlinearities can be handled as model parameter uncertainties. To the authors knowledge, this is the first application of modern robust $\mathcal{H}_\infty$control techniques to practical internal combustion engine control.

The remainder of this paper is split up into three main parts:

- Engine modeling
- A new λ $\mathcal{H}_\infty$controller design
- Stability and performance analysis

This paper is typeset in LaTeX 2_ε

[1] HEGO or most recently a UEGO sensor is used.

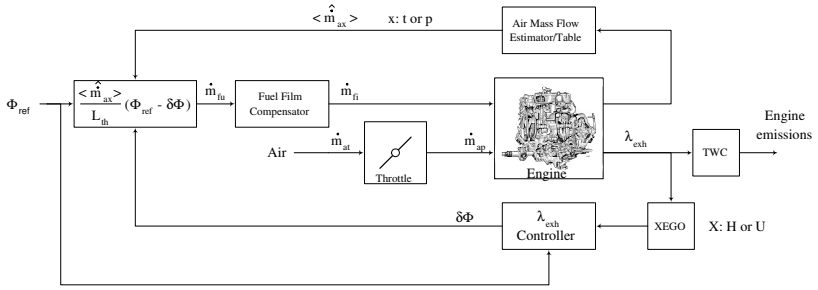

Figure 1: Block diagram of an engine control system. The upper loop in the figure is the base fuel calculation. The base fuel calculation can either be based on an air charge table lookup (conventional control strategy) or an estimate of the air mass flow (observer control strategy). Other necessary loops in the engine control strategy (for example the idle speed control loop) have been omitted for the sake of clarity.

2 ENGINE MODEL

This section describes a MVEM for an SI engine equipped with a MPI fuel injection system. The purpose of this engine model is to describe the signal path from the fuel injection to the λ measurement in the exhaust pipe. This model is then to be linearised in order that the standard $\mathcal{H}_\infty$framework can be applied. This engine model will be referred to here as the λ object.

The model to be presented is based on the MVEM engine equations presented in [1], [5] and [6].

2.1 Fuel Mass Flow in the Intake Manifold.

A model of the fuel mass flow to the cylinders is necessary since not all of the injected fuel mass is in gaseous form when the intake valves opens. A fraction of the injected fuel mass remains vaporized and is mixed with the air before it is sucked into the combustion chamber. The remaining fuel mass is deposited on the intake manifold wall as a fuel film. The fuel mass flow is schematically shown in figure 2 for an engine equipped with MPI. The evaporation of the fuel film introduces dynamics into the fuel injection system. The evaporation flow from the fuel film, $\dot{m}_{ff}$, is described by a first order ordinary differential equation. The time constant in the ODE (Ordinary Differential Equation) is the evaporation time constant for the fuel film, τ_f. The input to this subsystem is the fraction of the fuel mass flow, X, that is deposited on the wall. The vaporized portion of the fuel mass flow, $\dot{m}_{fv}$, is described by an algebraic equation. The total fuel mass flow to the engine, $\dot{m}_f$, is the sum of $\dot{m}_{fv}$ and $\dot{m}_{ff}$. The total MVEM model [5] for the fuel mass flow is shown in equation (2),

$$\boxed{\begin{aligned} \dot{m}_{ff} &= \frac{1}{\tau_f}\left(-\dot{m}_{ff} + X\dot{m}_{fi}\right) \\ \dot{m}_{fv} &= (1-X)\dot{m}_{fi} \\ \dot{m}_f &= \dot{m}_{fv} + \dot{m}_{ff} \qquad \text{mass conservation} \end{aligned}} \tag{2}$$

The variables X and τ_f are normally mapped for the specific engine as a function of engine speed n and intake manifold pressure p_i.

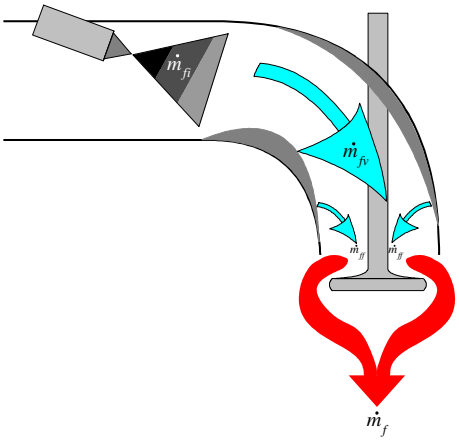

Figure 2: Fuel mass flow at the intake port.

2.2 Normalized AFR in the Intake Manifold.

The normalized AFR at the intake port is calculated as shown in equation (1). $\dot{m}_{ap}$ and $\dot{m}_f$ in equation (1) are now replaced by their corresponding MVEM equations as in equation (3),

$$\lambda(\dot{m}_{fi}, n, p_i) = \frac{V_d \eta_{vol}}{120 L_{th} R T_i (\dot{m}_{ff} + (1-X)\dot{m}_{fi})} n p_i \tag{3}$$

The state equation for λ can be found by differentiation, equation (4),

$$\begin{aligned} \dot{\lambda} &= \frac{1}{L_{th}\dot{m}_f}\ddot{m}_{ap} - \frac{\dot{m}_{ap}}{L_{th}\dot{m}_f^2}\ddot{m}_f \\ &= \frac{1}{\dot{m}_f}\left(\frac{\ddot{m}_{ap}}{L_{th}} - \lambda\ddot{m}_f\right) \end{aligned} \tag{4}$$

Equation (4) shows that $\dot{\lambda}$ is a function of the derivative of the port air mass flow, $\ddot{m}_{ap}$, and the derivative of the fuel mass flow, $\ddot{m}_f$. An equation for $\ddot{m}_{ap}$ can be found by differentiating the well known speed density equation [4], [6], equation (5),

$$\begin{aligned} \dot{m}_{ap} &= \frac{\eta_{vol} V_d n p_i}{120 R T_i} \qquad \text{Speed Density Eq.} \\ &\Updownarrow \\ \ddot{m}_{ap} &= \frac{V_d}{120 R T_i} \eta_{vol} \left(\dot{n} p_i + \dot{p}_i n \right) \end{aligned} \tag{5}$$

It is assumed that the process is isothermal, thus $\dot{T}_i \equiv 0$.

Now by substituting the manifold pressure state equation, $\dot{p}_i = \frac{RT_i}{V_i}(-\dot{m}_{ap} + \dot{m}_{at})$, for $\dot{p}_i$ in equation (5) and assuming that $\dot{n} \equiv 0$,

$$\begin{aligned} \ddot{m}_{ap} &= \frac{V_d}{120 R T_i V_i} \eta_{vol} n \frac{R T_i}{V_i} \left(-\dot{m}_{ap} + \dot{m}_{at} \right) \\ &= \frac{V_d}{120 L_{th} V_i} \eta_{vol} n \left(\frac{-V_d}{120 R T_i} \eta_{vol} n p_i + \dot{m}_{at} \right) \end{aligned} \tag{6}$$

The assumption $\dot{n} \equiv 0$ is justifiable, since the crankshaft dynamics are much slower than those of the intake manifold pressure, $\dot{p}_i$.

$\ddot{m}_f$ is found by differentiation of the fuel film model, equation (7).

$$\begin{aligned} \ddot{m}_f &= \ddot{m}_{fv} + \ddot{m}_{ff} \\ &= (1 - X) \ddot{m}_{fi} + \frac{1}{\tau_f} \left(-\dot{m}_{ff} + X \dot{m}_{fi} \right) \end{aligned} \tag{7}$$

The state equation for λ as a function of MVEM states and inputs is now found by inserting equations (6) and (7) into equation (4), which yields,

$$\begin{aligned} \dot{\lambda} = &- \left(\frac{\eta_{vol} V_d}{120 V_i} n \right. \\ &\left. + \frac{(1 - X) \ddot{m}_{fi} + \frac{1}{\tau_f} \left(-\dot{m}_{ff} + X \dot{m}_{fi} \right)}{\dot{m}_{fv} + \dot{m}_{ff}} \right) \lambda \\ &+ \frac{\eta_{vol} V_d}{L_{th} 120 V_i \left(\dot{m}_{fv} + \dot{m}_{ff} \right)} \dot{m}_{at} n \end{aligned} \tag{8}$$

Collecting terms, this equation can finally be reduced to

$$\boxed{\begin{aligned} \dot{\lambda} = &- \left(\frac{\eta_{vol} V_d}{120 V_i} n \right. \\ &\left. + \overbrace{\frac{(1 - X) \ddot{m}_{fi} + \frac{1}{\tau_f} \left(-\dot{m}_{ff} + X \dot{m}_{fi} \right)}{(1 - X) \dot{m}_{fi} + \dot{m}_{ff}}}^{:=0 \text{ Stationary}} \right) \lambda \\ &+ \frac{\eta_{vol} V_d}{120 V_i} n \underbrace{\frac{\dot{m}_{at}}{L_{th} \left((1 - X) \dot{m}_{fi} + \dot{m}_{ff} \right)}}_{:=\lambda \text{ for } \dot{m}_{at} = \dot{m}_{ap} \text{ (Stationary)}} \end{aligned}} \tag{9}$$

2.3 Normalized AFR in the Exhaust Manifold.

The AFR at the λ sensor, λ_{exh}, is ideally a time delayed version of the λ signal in the intake manifold. However in a real system this relation might be modified by the following problems:

- The combustion is not necessarily perfect.
- Unmodeled dynamics in the intake process (for example back flow, temperature variations, resonance phenomenons, etc.)
- Fuel injector model uncertainty.

Since these effects are more or less impossible to model correctly, it is necessary that their influence is minimized. In order to accomplish this, one can take the following precautions:

- The combustion is nearly ideal if λ is kept in reasonable operating area, ($\lambda \in [0.8; 1.05]$ for the BL (British Leyland) test engine).
- The final controller must have an integral term in order to minimize the effect of fuel injector uncertainties.
- The fuel is sprayed on closed valves as soon as possible in order to achieve good fuel evaporation. This will of course increase the effective time delay.

If the precautions above are taken, λ_{exh} can be modeled using a pure time delay, equation (10),

$$\lambda_{exh} = \lambda e^{-\tau_d s} \tag{10}$$

where τ_d is the time delay between fuel injection and the λ measurement. τ_d can be split up into three contributions,

τ_{d1}: The time delay between fuel injection and the intake valve opening.

τ_{d2}: Combustion time.

τ_{d3}: The exhaust transport time delay between the exhaust valve and the λ sensor.

Formulas for the three time delay contribution are given below. Representative values for the British Leyland test engine are given for convenience.

Fuel Injection on Closed Valve Time Delay.

The time delay between fuel injection and intake valve opening is a function of the engine speed, n, and the crank angle between injection and valve opening, $\Delta\theta_1$.

$$\begin{aligned} \tau_{d1} &= \frac{60 \Delta\theta_1}{360° n} \\ &\text{where} \\ &\Delta\theta_1 \in]0; 490]° \qquad \text{for the BL engine} \end{aligned} \tag{11}$$

$\frac{\Delta\theta_1}{360°}$ is the fraction of an engine cycle where the fuel injection has taken place until the intake valve opens. The time delay for the BL test engine is in worst-case,

$$\tau_{d1,\ wc} = \frac{60 \frac{s}{min} \cdot 490°}{600 \text{min}^{-1} 360°} = 136 ms \tag{12}$$

Combustion Time Delay.

The time delay introduced by the combustion is expressed as a function of the crank angle between intake valve opening and exhaust valve opening, $\Delta\theta_2$, and engine speed, n. The combustion time delay expression is,

$$\tau_{d2} = \frac{60\Delta\theta_2}{n360^\circ} \quad \text{where} \quad \Delta\theta_2 = 492^\circ \qquad \text{BL engine} \tag{13}$$

and will be in the set

$$\tau_{d2} \in \left[\frac{60\frac{s}{min}\cdot 492^\circ}{6000min^{-1}\cdot 360^\circ}; \frac{60\frac{s}{min}\cdot 492^\circ}{600min^{-1}\cdot 360^\circ}\right] = [14;136]ms \tag{14}$$

for normal engine operating points.

Transportation Time Delay.

The time delay introduced by the transportation of the exhaust matter from the exhaust valve to the λ sensor is modeled as a plug propagating through the exhaust pipe. The plug model for the transportation time delay, τ_{d3}, is an algebraic function of the pressure in the exhaust pipe, p_{exh}, the distance between valve and sensor, l_{exh}, the temperature in the exhaust pipe, T_{exh}, the effective area of the exhaust pipe, A_{exh}, and the mass flow in the exhaust pipe, $\dot{m}_{exh}$. By mass conservation the mass flow, $\dot{m}_{exh}$, in the pipe is about the same as the flow at the intake port, $\dot{m}_{ap}$, in the MVEM. The final formulae for the transportation time delay is then

$$\tau_{d3} = \frac{\rho_{exh} l_{exh} A_{exh}}{\dot{m}_{ap}} = \frac{\frac{p_{exh}}{RT_{exh}} l_{exh} A_{exh}}{\dot{m}_{ap}} \tag{15}$$

The transportation time delay, τ_{d3}, will be in the set below for normal operating points of the BL test engine,

$$\tau_{d3} \in [2;25]ms \tag{16}$$

The total time delay is the sum of the three time delay contributions. The time delay, τ_d, will be in the following set for the BL test engine equipped with SEFI,

$$\text{SEFI:} \quad \tau_d \in [16;297]ms \tag{17}$$

2.4 λ Sensor Model

The test engine is equipped with an AFRecorder 2400E UEGO λ sensor from ECM [7]. This sensor is linear for $\lambda \in [0.5;1.5]$ and can be modeled as a first order state equation with good approximation, equation (18).

$$\frac{\lambda_m(s)}{\lambda_{exh}(s)} = \frac{1}{\tau_\lambda s + 1} \tag{18}$$

The λ-sensor's time constant is dependent on the temperature in the exhaust pipe [8]. For normal operating points of the BL test engine, the time constant will be in interval set,

$$\tau_\lambda \in [50_{670^\circ C}; 94_{400^\circ C}]\ ms \tag{19}$$

2.5 Engine Control Model

The model for the propagation of λ through the engine to the sensor now has to be linearised in order to apply the standard $\mathcal{H}_\infty$-framework.

2.5.1 Linearisation of the λ State Equation.

The state equation for λ is linearised in appendix A with respect to the states $\dot{m}_{ff}$, λ, $\dot{m}_{fi}$ and the inputs n, $\dot{m}_{fi}$, $\dot{m}_{at}$.

2.5.2 Approximation of the Engine Time Delay.

The engine's time delay is for physical reasons linked to the crankshaft speed, n, as can be seen in equations (11), (13) and (15). The total engine time delay for the BL test engine can with good approximation be modeled as,

$$\tau_d = \frac{\xi}{n} = \frac{0.187krpm\cdot s}{n} \tag{20}$$

This time delay approximation was found by regression.

The time delay above has to be approximated before application of the standard $\mathcal{H}_\infty$-framework. The phase shift of the time delay is often approximated by either an ordinary low pass filter or a Padé filter. The choice of order and/or type of the time delay approximation is dependent on the application, see appendix C. It is shown in [3] that a second order Padé filter is sufficient, when modeling the time delay. The structure of the time delay approximating Padé filter is shown in figure 3, see appendix C.

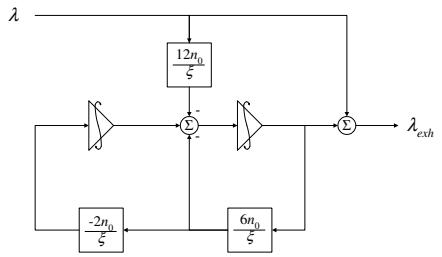

Figure 3: Padé approximation of the engine's time delay

The term n_0 in figure 3 is the nominal value for the crankshaft speed in the A/F control design.

2.5.3 λ-Object Control Model.

The overall λ-object which was used in the $\mathcal{H}_\infty$-design of the AFR controller is a sixth order model. The model consist of: two states modeling the fuel injection dynamics, one state modeling λ, two states approximating the engine time delay, and finally one state modeling the dynamics of the UEGO sensor. The block diagram of the control object is shown in figure 4. The corresponding state space system equations can be found in appendix B.

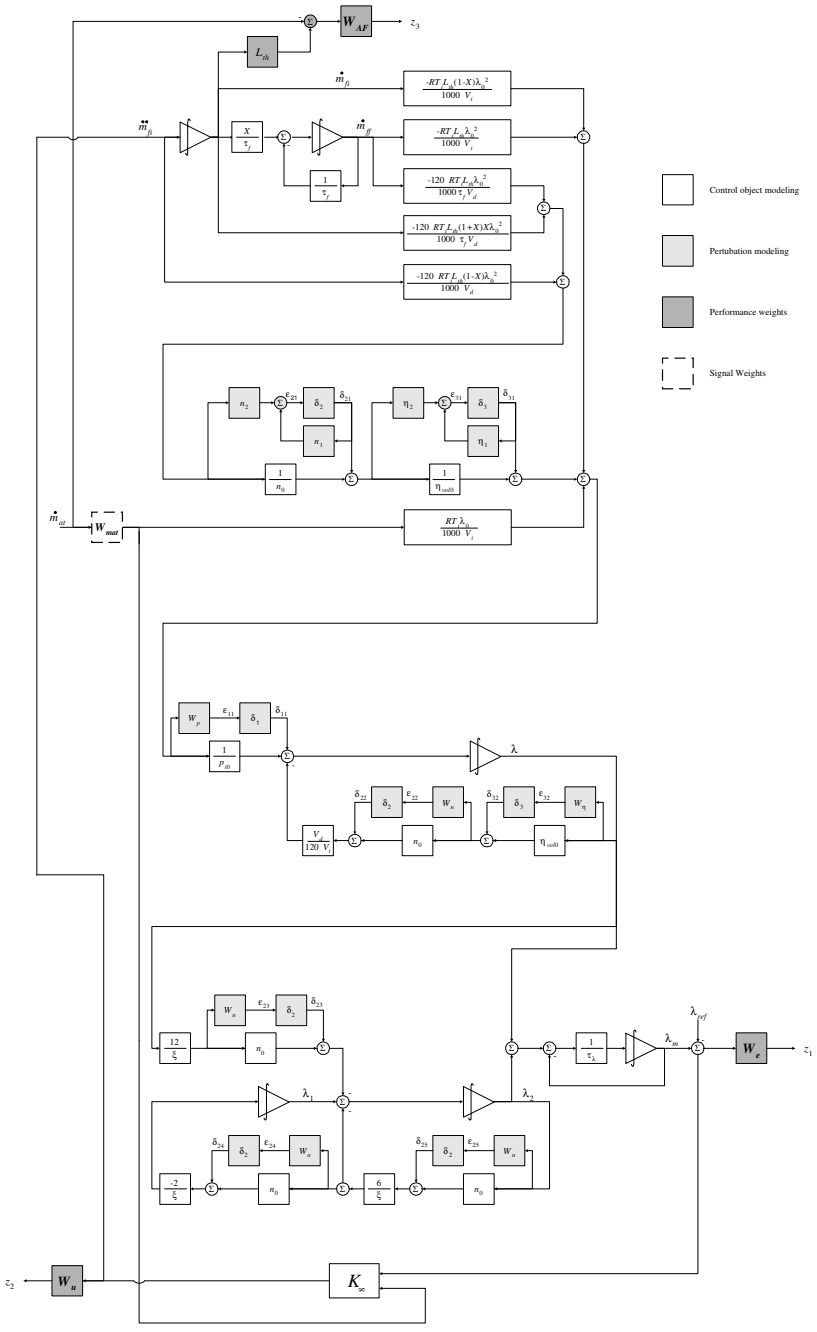

Figure 4: Block diagram for the linearised λ object with perturbation modeling, performance/signal weights and λ controller, K_∞. $\dot{m}_{ff}$ is the fuel film state, λ is the normalized AFR at the intake port, λ_1 and λ_2 are the states in the Padé filter, and finally λ_m is the UEGO sensor's state.

3 CONTROL DESIGN

The purpose of this section is to describe the system setup and the controller design. The system setup shows an easy and comprehensive way to model the most important perturbations in the λ model. The section then addresses control design for AFR engine control. The reader is referred to appendix D in order to obtain a quick overview of the formalism used in the design and analysis of the $\mathcal{H}_\infty$controller. If a more thorough overview of the formalism is needed, the reader is referred to [9].

3.1 Perturbation Model.

In order to avoid making the final $\mathcal{H}_\infty$-controller design too conservative, negligible uncertainties should not be modeled. In this paper it has been decided to address only the uncertainties in the engine's volumetric efficiency, η_{vol}, and the operating point dependencies of p_i and n.

3.1.1 Modeling the p_i Uncertainty.

Figure 4 shows that the manifold pressure p_i has a reciprocal dependency in the λ object. This dependency originates from the replacement of $\dot{m}_{fi0}$ with it's equivalent speed density equation, see appendix B. The manifold pressure may vary between 0.3 bar and 1 bar. $\frac{1}{p_i}$ will thus vary between 1 bar^{-1} and 3.33 bar^{-1}. This variation is modeled as an additive uncertainty in the λ object. The uncertainty is a linear function of the real perturbation $\delta_1 \in [-1;1]$. The uncertainty weight W_p and nominal operating point $\frac{1}{p_{i0}}$ are found as in equation (21).

$$\begin{aligned} W_p &= \frac{\frac{1}{p_{i,min}} - \frac{1}{p_{i,max}}}{2} \\ \frac{1}{p_{i0}} &= \frac{\frac{1}{p_{i,min}} + \frac{1}{p_{i,max}}}{2} \end{aligned} \tag{21}$$

3.1.2 Modeling the n Uncertainty.

The crankshaft speed, n, is found both to have a linear and reciprocal dependency in the state equation for λ in the intake manifold. Furthermore the parameters in the Padé filter time delay approximation are modeled as functions of n for the reasons mentioned in section 2.5.2. In order to avoid conservatism in the design of the variations around the nominal values n_0 and $\frac{1}{n_0}$ are modeled as functions of the same perturbation, δ_2. Since it is the same real perturbation δ_2 that is involved in the uncertainty modeling of the variations, one of the uncertainty models will have to be a nonlinear function of δ_2. It was decided to model the uncertainty in the quantity $\frac{1}{n_0}$ as a nonlinear function of δ_2. This was accomplished by a Linear Fractional Transformation (LFT) of the uncertainty's reciprocal dependency in δ_2. The LFT is shown in equation (22) and (23).

$$\begin{aligned} n &= n_0 + \delta_2 W_n \\ &= \frac{n_{max}+n_{min}}{2} + \delta_2 \frac{n_{max}-n_{min}}{2} \\ &= \frac{1+\delta_2 \frac{n_{max}-n_{min}}{n_{max}+n_{min}}}{\frac{2}{n_{max}+n_{min}}} \\ &\Updownarrow \\ \frac{1}{n} &= \frac{\frac{2}{n_{max}+n_{min}}}{1+\delta_2 \frac{n_{max}-n_{min}}{n_{max}+n_{min}}} \end{aligned} \tag{22}$$

The result from equation (22) is transformed into a LFT,

$$\begin{aligned} \frac{1}{n} &= n_{22} + \frac{n_{12}\delta_2 n_{21}}{1-n_{11}\delta_2} \\ &= \frac{n_{22} - \delta_2(n_{12}n_{21} - n_{11}n_{22})}{1-n_{11}\delta_2} \end{aligned}$$

which leads to

$$\begin{aligned} n_{11} &= -\frac{n_{max}-n_{min}}{n_{max}+n_{min}} = n_1, \\ n_{22} &= \frac{2}{n_{max}+n_{min}} = n_0, \\ n_{12}n_{21} &= -\frac{n_{max}-n_{min}}{(n_{max}+n_{min})^2} = n_2 \end{aligned} \tag{23}$$

The LFT is realised by the block diagram in figure 5.

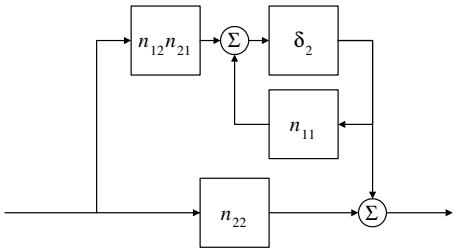

Figure 5: Block diagram representing the LFT in equation (22) and (23).

The variation around n_0 is modeled in the same way as $\frac{1}{p_{i0}}$ as an additive uncertainty. This yields the following values for W_n and n_0,

$$\begin{aligned} W_n &= \frac{n_{max}-n_{min}}{2} \\ n_0 &= \frac{n_{max}+n_{min}}{2} \end{aligned} \tag{24}$$

3.1.3 Modeling the Volumetric Efficiency, η_{vol}, Uncertainty.

The state equation for λ has both linear and reciprocal dependency with respect to the volumetric efficiency, η_{vol}, as was the case with n. The modeling of the uncertainty in η_{vol} is therefore straight forward since it follows the

methodology that was used in the n and $\frac{1}{n}$ perturbation modeling.

The constants involved in modeling the variation around the quantities η_{vol0} and $\frac{1}{\eta_{vol0}}$ are given in equation (25).

$$\begin{aligned} &\text{LFT} \\ \frac{1}{\eta_{vol0}} &= \frac{2}{\eta_{vol,max}+\eta_{vol,min}} \\ \eta_1 &= -\frac{\eta_{vol,max}-\eta_{vol,min}}{\eta_{vol,max}+\eta_{vol,min}} \\ \eta_2 &= -\frac{\eta_{vol,max}-\eta_{vol,min}}{(\eta_{vol,max}+\eta_{vol,min})^2} \end{aligned} \tag{25}$$

$$\begin{aligned} &\text{Additive uncertainty} \\ \eta_{vol0} &= \frac{\eta_{vol,max}+\eta_{vol,min}}{2} \\ W_\eta &= \frac{\eta_{vol,max}-\eta_{vol,min}}{2} \end{aligned}$$

The size of the perturbation is controlled by δ_3 which is a real value as for δ_1 and δ_2.

3.1.4 The Structured Δ-Block.

From the additive and LFT uncertainty models described above, the final structured perturbation matrix in equation (26) is obtained.

$$\Delta = \begin{bmatrix} \delta_1 & 0 & 0 \\ 0 & \delta_2 I_{5\times5} & 0 \\ 0 & 0 & \delta_3 I_{2\times2} \end{bmatrix} \tag{26}$$

$$\delta_1, \delta_2, \delta_3 \in \mathbb{R}\backslash\{\,\} - \infty; 1[\cup \,]1; \infty[\,\},$$
$$\|\Delta\|_\infty \leq 1$$

This structured perturbation governs the size of the perturbation inputs to the λ object.

3.2 Signal- and Performance Weights.

The $\mathcal{H}_\infty$-setup in figure 4 has one input signal weight W_{mat} and three performance weights W_e, W_u and W_{AF}. The amplitude characteristic of the weights are seen in figure 6. The design and choice of structure of the individual weights will be described in the next sections.

3.2.1 Signal Weight W_{mat}.

The input weight is realised as a 30 Hz low pass filter with unity gain at zero frequency. W_{mat} has the transfer function in equation (27)

$$W_{mat}(s) = \frac{10^{-4}s + 60\pi}{s + 60\pi} \tag{27}$$

The placement of the pole in the filter is a compromise between the wish to follow transient changes in $\dot{m}_{at}$ and at the same time maintain a mean value measurement of $\dot{m}_{at}$ without too great an influence from the pumping fluctuations. The reason for the high frequency zero in the transfer function is to fulfill the standard $\mathcal{H}_\infty$requirements of the control object.

3.2.2 Performance weight W_e.

The purpose of the weight W_e is to punish errors in the AFR. That is, an undesired steady state error in the AFR is to be minimized as soon and as much as possible. The structure of W_e's amplitude characteristic is thus much like that of an integrator. The transfer function for W_e is

$$W_e(s) = \frac{100}{s + 1 \cdot 10^{-6}} \tag{28}$$

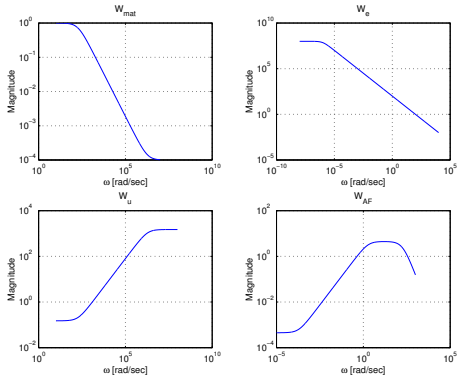

Figure 6: The signal and performance weights used in the $\mathcal{H}_\infty$control design.

3.2.3 Performance Weight W_u.

In order to minimize high frequencies (noise) in the control signal, the control setup has been augmented with a high pass filter for the control signal $\ddot{m}_{fi}$. The filter is implemented so it punishes control signal frequency content above 1240 $\frac{rad}{s}$. Equation (29) shows the transfer function for W_u.

$$W_u(s) = 1.5 \cdot 10^3 \frac{s + 60\pi}{s + 60 \cdot 10^4\pi} \tag{29}$$

3.2.4 Performance Weight W_{AF}.

The performance weight W_{AF} is inserted in the $\mathcal{H}_\infty$control setup in order to improve the control strategy transient response (tip-in and tip-out throttle response). Thus W_{AF} is a weight on the error signal $L_{th}\dot{m}_{fi} - \dot{m}_{at}$. Since the measurement of the steady state air mass flow past the throttle plate might be erroneous, the performance weight is designed so that it has a small weight on the zero frequency content. At higher frequencies the weight has a small gain, again in order to minimize the effects from the pumping fluctuation in the $\dot{m}_{at}$ signal. Thus the performance weight W_{AF} has to have band pass structure. The transfer function selected for W_{AF} in the control setup is

$$\begin{aligned} &W_{AF}(s) \\ &= 2.487 \cdot 10^5 \frac{s + 6 \cdot 10^{-5}\pi}{(s + 0.6\pi)(s + 60\pi)(s + 60\pi)} \end{aligned} \tag{30}$$

3.3 $\mathcal{H}_\infty$ Control Design.

The signal weight and the performance weights are now included in the system setup for P. For this system setup a 5% suboptimal $\mathcal{H}_\infty$ controller is designed for engine operating points in the range $n \in [1.5; 2.5]$ krpm and $p_i \in [0.4; 1]$ bar. The $\mathcal{H}_\infty$ controller is found by an iterative process so that the requirement in equation (31) is fulfilled.

$$\|F_l(P,K)\|_\infty < 1,05\gamma_{min} \quad \text{where} \quad \gamma_{min} = \min_K(\|F_l(P,K)\|_\infty) \tag{31}$$

Introduction of a 5% gab between γ_{min} and the γ used in the $\mathcal{H}_\infty$ control design insures existence of a small gain gab between the maximum transfer gain between the inputs and outputs of the closed loop system and the requirements specified by the performance weights. Thus assuring that none of the closed loop poles of the system tends towards infinity. Poles tending towards infinity might cause numerical problems. Fulfillment of the performance requirements can be checked by comparing the amplitude characteristics of the individual inputs to the outputs of the system to that of the inverted performance weights multiplied with γ. If the controller fulfills the requirements in equation (31) the characteristics from inputs to the specific output will be below γW_x^{-1}. W_x is the performance weight attached to the output which is analysed.

In the $\mathcal{H}_\infty$ controller which is reviewed here, a robust observer is automatically included. The feedback gain matrix for this observer is $Z_\infty X_\infty$. The state feedback gain matrix from the observer states to the control input vector is F_∞. A block diagram of the overall system as well as further explanation is given in appendix D.

3.4 μ Analysis

The goal of μ analysis is to test for certain desired system properties. The system properties which are normally tested are Nominal Performance, Robust Stability and Robust Performance.

The system is formulated as an upper LFT before the analysis is carried out. The LFT is given by

$$F_u(N,\Delta) = N_{22} + N_{21}\Delta(I - N_{11})^{-1}N_{12} \tag{32}$$

As mentioned above the properties of control system which normally are analysed are:

1. Nominal Stability (NS). The nominal ($\Delta = 0$) closed loop system is stable.
2. Nominal Performance (NP). The nominal closed loop system can fulfill the demands inherent in the performance weights.
3. Robust Stability (RS). The closed loop system is stable even when worst case perturbation of the system is present.
4. Robust Performance (RP). The closed loop system fulfills the performance specifications even then the worst case perturbation of the system is present.

The above requirements can be tested by an structured singular value analysis. The structured singular value is given by the following definition [9]

DEFINITION 1 (THE STRUCTURED SINGULAR VALUE μ) *Let M be a given complex matrix, an let Δ be a set of complex matrices with $\bar{\sigma}(\Delta) \leq 1$ and a given block diagonal structure (where some of the Δ_i might be repeated and/or real). The real non-negative function $\mu(M)$ is defined by,*

$$\mu(M) \triangleq \frac{1}{\min\left\{ \begin{array}{c} k_m \,|\, \det(I - k_m N\Delta) = 0, \\ \text{for } \Delta \text{ structured and } \bar{\sigma}(\Delta) \leq 1 \end{array} \right\}} \quad \text{where} \quad \Delta = \begin{bmatrix} \Delta_1 & \cdots & 0 \\ \vdots & \ddots & \vdots \\ 0 & \cdots & \Delta_n \end{bmatrix} \tag{33}$$

The performance weights W_e, W_u, W_{AF} are changed according to equation (34) before the Nominal Performance and Robust Performance analysis of the λ control is carried out.

$$W_{x,\mu} = \frac{1}{1,05\gamma} W_x \tag{34}$$

This equation says that NP and a proceeding RP analysis is fulfilled if the individual amplitude characteristics do not exceed the maximal specified amplitudes by more than 5%.

3.4.1 Robust Stability Analysis.

Figure 7 shows that the control system fulfills Robust Stability for operating points in the range of, $p_i \in [0.4; 1]$ *bar* and $n \in [1.15; 4.5]$ *krpm*.

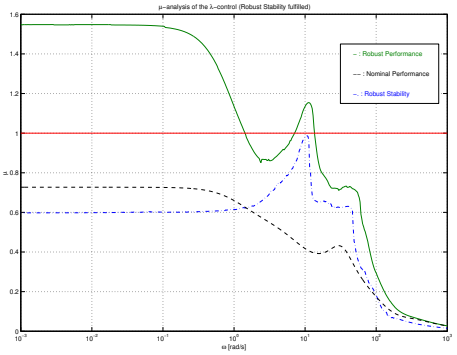

Figure 7: Robust Stability fulfilled. The operating range of the SI engine is here, $p_i \in [0.4; 1]$ *bar* and $n \in [1.15; 4.5]$ *krpm*.

3.4.2 Robust Performance Analysis.

Figure 8 shows that the control system fulfills Robust Performance for operating points in the range of, $p_i \in [0.4; 0.85]$ bar and $n \in [1.75; 2.25]$ $krpm$.

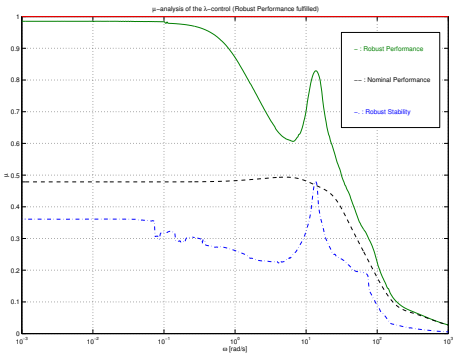

Figure 8: Robust Performance fulfilled. The operating range of the SI engine is here, $p_i \in [0.4; 0.85]$ bar and $n \in [1.75; 2.25]$ $krpm$.

4 Experimental Results

The $\mathcal{H}_\infty$controller designed was discretized and implemented in the ECDS (Engine Control Development System) software [10]. The ECDS is a multitasking sofware package developed at the Technical University of Denmark for engine control. Figure 9 shows a sample of the results obtained.

The first three plots in the figure show the measured α, n and p_i responses as functions of time. The engine is being driven over a large part of its operational range and through most of the design range of the λ controller.

The fourth subplot shows the normalised air mass flow at the throttle, $\frac{\dot{m}_{at}}{L_{th}}$, and the fuel mass flow command from the controller, $\dot{m}_{fi}$. The difference between the two mass flows in the steady state has been shown to be mainly due to the inaccurate operation of the fuel injectors. At the time the experiments reviewed here where conducted, the injection scheme available in the ECDS hardware was one injection per cylinder per event. This meant that the pulse width command given to the injector driver was very small (typical below 3 ms), thus the injectors were operated in the nonlinear portion of their characteristics [3]. This introduced some significant unmodelled nonlinearities in their operation. Even though the injectors were operated in the nonlinear portion of their characteristics, the $\mathcal{H}_\infty$controller was nearly capable of keeping λ within the window $1 \pm \frac{1}{L_{th}}$ ($\pm$ 1 AFR) during the throttle angle transients as seen in the final plot in figure 9. In steady state the controller kept λ within the window $1 \pm \frac{1}{2L_{th}}$ ($\pm\frac{1}{2}$ AFR). These results have been obtained in spite of the fact the controller has been designed for operation in a large portion of the engine's operating range instead of being tuned at closely

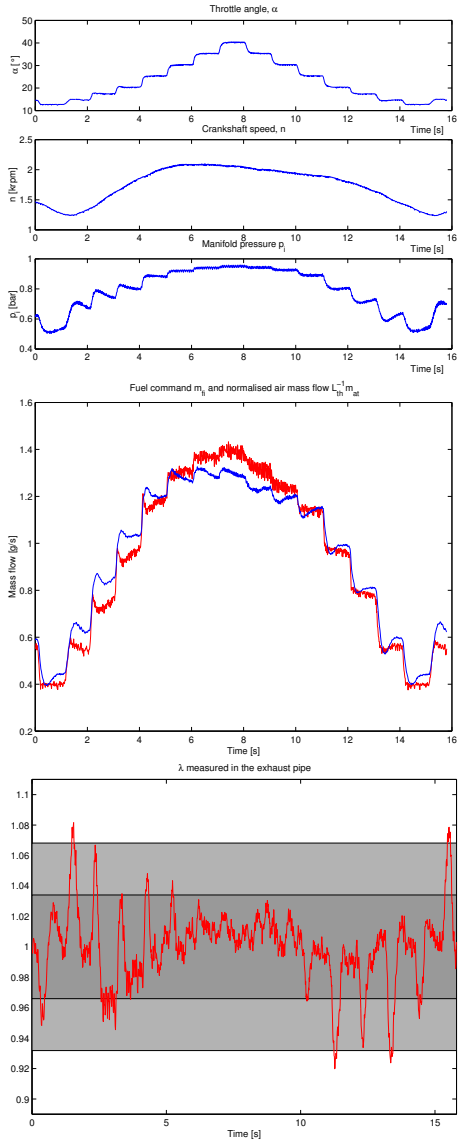

Figure 9: The first three plots shows the throttle angle, α, the engine's rpm, n and the pressure in the intake manifold p_i as functions of time. The steps in α is low pass filtered with a 100ms time constant. The fourth plot is the fuel flow command $\dot{m}_{fi}$ together with the normalised air mass flow $\frac{\dot{m}_{at}}{L_{th}}$. The final plot depicts the measured normalised air/fuel ratio in the exhaust pipe. The large window shows the $\pm$AFR window and the small window shows the $\pm\frac{1}{2}$AFR window.

spaced and carefully mapped operating points. This shows the basic robustness of the $\mathcal{H}_\infty$method and its main advantage in comparison to more conventional control methods. Moreover the steady state and transient operating modes have been optimized in concert rather than separately.

5 CONCLUSIONS

An $\mathcal{H}_\infty$control methodology has been applied to the problem of SI engine air/fuel ratio control. This has been one of the first practical applications of this method to a nonlinear system and to internal combustion engine control. Nonlinearity of the engine has been treated as a system uncertainty in the same way as parameter uncertainty is handled in conventional linear $\mathcal{H}_\infty$applications. The entire air/fuel ratio control system, from fuel injection to exhaust, has been treated as one control object. This makes it possible to obtain an overview of the control process which is unusual in its scope and effectiveness. Analytical methods can be applied to analyse fulfillment of stability and performance guarantees. It is also possible to balance different, often conflicting, control objectives against each other without cut and try methods.

It has been possible to obtain reasonably accurate AFR control even though a very accurate system model has not been derived first. This suggests that with further development, the use of $\mathcal{H}_\infty$control can reduce significantly the calibration time necessary to put a global engine control into place on a given engine.

Further future developments include the use of multiple nonlinearity uncertainty zones spaced over the entire operating range of the engine. When coupled with gain scheduling, it is thought that this approach will lead to less conservative zone controls while maintaining the overall robustness of the underlying control methodology.

6 NOMENCLATURE

Acronyms.

AFR: Air Fuel Ratio.

BL: British Leyland.

ECDS: Engine Control Development System.

EFI: Electronic Fuel Injection.

HEGO: Heated Exhaust Gas Oxygen sensor (switching type).

LFT: Linear Fractional Transformation.

MVEM: Mean Value Engine Model.

MPI: Multi Point Injection.

NTFC: Nonlinear Transient Fuel film Compensation.

ODE: Ordinary Differential Equation.

RHP: Right Half Plane.

SEFI: Sequential Electronic Fuel Injection.

SI: Spark Ignition.

TWC: Three Way Catalyst.

UEGO: Universal Exhaust Gas Oxygen sensor (linear type).

Engine Symbols and States.

η_{vol}: Volumetric efficiency.

Φ: Normalized fuel/air ratio at intake port.

λ: Normalized air/fuel ratio at intake port.

λ_{exh}: Normalized air/fuel ratio in exhaust manifold.

λ_m: Measured normalized air/fuel ratio at intake port.

$\dot{m}_{ap}$: Fresh air mass flow at intake port, $[\frac{kg}{s}]$.

$\dot{m}_{at}$: Fresh air mass flow at throttle plate, $[\frac{kg}{s}]$.

$\dot{m}_{exh}$: Mass flow in the exhaust pipe, $[\frac{kg}{s}]$.

$\dot{m}_f$: Vaporized fuel mass flow at intake port, $[\frac{kg}{s}]$.

$\dot{m}_{ff}$: Vaporized fuel mass flow from fuel film, $[\frac{kg}{s}]$.

$\dot{m}_{fi}$: Injected fuel mass flow, $[\frac{kg}{s}]$.

$\dot{m}_{fv}$: Vaporized fuel mass flow from injectors, $[\frac{kg}{s}]$.

n: Crankshaft revolutions per minute, $[rpm]$.

p_i: Intake manifold pressure, $[bar]$.

p_{exh}: Exhaust manifold pressure, $[bar]$.

ρ_{exh}: Air density in the exhaust manifold, $[\frac{kg}{m^3}]$.

s: Complex variable, $\jmath\omega$

τ_f: Evaporation time constant for the fuel film, $[s]$

λ_λ: The λ sensor's time constant, $[s]$.

T_i: Intake manifold gas temperature, $[K]$.

T_{exh}: Exhaust manifold gas temperature, $[K]$.

X: Fraction of $\dot{m}_{fi}$, that hits the intake manifold wall.

Constants.

A_{exh}: Cross sectional area of exhaust pipe, $3.24 \cdot 10^{-4} \pi m^2$.

l_{exh}: Distance between exhaust valve and λ sensor, 0.32 m.

L_{th}: Stoichiometric air/fuel ratio, 14.67.

R: Gas constant for dry air, $287.09 \cdot 10^{-5} \frac{bar \cdot m^3}{kg \cdot K}$

V_d: Displacement volume, $1.275 \cdot 10^{-3} m^3$

V_i: Intake manifold volume, $1.700 \cdot 10^{-3} m^3$

References

[1] Hendricks, E. and Sorenson, S. C., "SI Engine Controls and Mean Value Engine Modelling," *SAE Technical Paper*, no. 910258, 1991.

[2] Hendricks, E., Vesterholm, T., and Sorenson, S. C., "Nonlinear, Closed Loop, SI Engine Control Observers," *SAE Technical Paper*, no. 920237, 1992.

[3] Struwe, M. and Vigild, C. W., "Robust $\mathcal{H}_\infty$ Control of a SI Engine's A/F-ratio, in danish," Master's thesis, The Technical University of Denmark, Institute for Automation, Aug. 1997.

[4] J. B. Heywood, *Internal Combustion Engine Fundamentals*. McGraw-Hill, Inc., 1 ed., 1989.

[5] Hendricks, E., Jensen, M., Kaidantzis, P., Rasmussen, P., and Vesterholm, T., "Nonlinear transient fuel film compensation (NTFC)," *SAE Technical Paper*, no. 930767, 1993.

[6] Hendricks, E., Jensen, M., Chevalier, A., Sorenson, S. C., Trumphy, D., and Asik, J., "Modelling of the intake manifold filling dynamics," *SAE Technical Paper*, no. 960037, 1996.

[7] ECM, *Engine Control and Monitoring*. 101 First Street, Suite 365, Los Altos, CA 94022, U.S.A.

[8] Poulsen, J. S., "Identification of SI engine submodels, in danish," Master's thesis, The Technical University of Denmark, Institute for Automation, Mar. 1997.

[9] Sigurd Skogestad and Ian Postlethwaith, *Multivariable feedback control*. John Wiley & Sons, 1996.

[10] Jan Lillelund, "Design of an Engine Control Development System, in danish," Master's thesis, The Technical University of Denmark, Institut for Automation, 1991.

APPENDIX

A Linearisation of the λ State Equation

The λ state equation is repeated in equation (35).

$$\begin{aligned}\dot{\lambda} = &-\left(\frac{\eta_{vol}V_d}{120V_i}n + \frac{(1-X)\,\ddot{m}_{fi} + \frac{1}{\tau_f}\left(-\dot{m}_{ff} + X\dot{m}_{fi}\right)}{(1-X)\,\dot{m}_{fi} + \dot{m}_{ff}}\right)\lambda \\ &+ \frac{\eta_{vol}V_d}{L_{th}120V_i\left((1-X)\,\dot{m}_{fi} + \dot{m}_{ff}\right)}\dot{m}_{at}n\end{aligned} \tag{35}$$

The state equation for λ is now linearised with respect to $\dot{m}_{ff}$, λ, n, $\dot{m}_{at}$, $\dot{m}_{fi}$ and $\ddot{m}_{fi}$. The final linearised state equation is shown in equation (36).

$$\begin{aligned}d\dot{\lambda} = &\left(\frac{-\frac{1}{\tau_f}\dot{m}_{fi0} - (1-X)\ddot{m}_{fi0}}{\left((1-X)\dot{m}_{fi0} + \dot{m}_{ff0}\right)^2}\lambda_0 - \frac{\eta_{vol}V_d\dot{m}_{at0}n_0}{120L_{th}V_i\left((1-X)\dot{m}_{fi0} + \dot{m}_{ff0}\right)^2}\right)d\dot{m}_{ff} \\ &+ \left(-\frac{\eta_{vol}V_dn_0}{120V_i} - \frac{(1-X)\ddot{m}_{fi0} + \frac{1}{\tau_f}(-\dot{m}_{ff0} + X\dot{m}_{fi0})}{(1-X)\dot{m}_{fi0} + \dot{m}_{ff0}}\right)d\lambda \\ &+ \left(-\frac{\eta_{vol}V_d}{120V_i} - \frac{\eta_{vol}V_d\dot{m}_{at0}}{120L_{th}V_i\left((1-X)\dot{m}_{fi0} + \dot{m}_{ff0}\right)}\right)dn \\ &+ \frac{\eta_{vol}V_dn_0}{120L_{th}V_i\left((1-X)\dot{m}_{fi0} + \dot{m}_{ff0}\right)}d\dot{m}_{at} \\ &+ \left(\frac{-\frac{X}{\tau_f}\dot{m}_{ff0} + (1-X)^2\ddot{m}_{fi0} - \frac{1}{\tau_f}\dot{m}_{ff0}}{\left((1-X)\dot{m}_{fi0} + \dot{m}_{ff0}\right)^2}\lambda_0\right. \\ &\left.- \frac{(1-X)\eta_{vol}V_d\dot{m}_{at0}n_0}{120L_{th}V_i\left((1-X)\dot{m}_{fi0} + \dot{m}_{ff0}\right)^2}\right)d\dot{m}_{fi} \\ &+ \frac{(1-X)\lambda_0}{(1-X)\dot{m}_{fi0} + \dot{m}_{ff0}}d\ddot{m}_{fi}\end{aligned} \tag{36}$$

B State Space Representation of the Linearised λ Object

The state space representation of the linearised λ object is shown in equation (37),

$$\begin{bmatrix}\delta\ddot{m}_{ff}\\ \delta\dot{\lambda}\\ \delta\dot{\lambda}_1\\ \delta\dot{\lambda}_2\\ \delta\dot{\lambda}_m\end{bmatrix} = \begin{bmatrix}\frac{-1}{\tau_f} & 0 & 0 & 0 & 0\\ a_{21} & -a_{22} & 0 & 0 & 0\\ 0 & 0 & 0 & \frac{-12}{\tau_d^2} & 0\\ 0 & \frac{-12}{\tau_d} & 1 & \frac{-6}{\tau_d} & 0\\ 0 & \frac{1}{\tau_\lambda} & 0 & \frac{1}{\tau_\lambda} & \frac{-1}{\tau_\lambda}\end{bmatrix}\begin{bmatrix}\delta\dot{m}_{ff}\\ \delta\lambda\\ \delta\lambda_1\\ \delta\lambda_2\\ \delta\lambda_m\end{bmatrix} + \begin{bmatrix}0 & 0 & \frac{X}{\tau_f} & 0\\ b_{21} & b_{22} & b_{23} & b_{24}\\ 0 & 0 & 0 & 0\\ 0 & 0 & 0 & 0\\ 0 & 0 & 0 & 0\end{bmatrix}\begin{bmatrix}\delta n\\ \delta\dot{m}_{at}\\ \delta\dot{m}_{fi}\\ \delta\ddot{m}_{fi}\end{bmatrix} \tag{37}$$

$$y = \begin{bmatrix}0 & 0 & 0 & 0 & 1\end{bmatrix}\begin{bmatrix}\delta\dot{m}_{ff}\\ \delta\lambda\\ \delta\lambda_1\\ \delta\lambda_2\\ \delta\lambda_m\end{bmatrix}$$

The constants a_{xx} og b_{xx} are seen in equation (38).

$$
\begin{aligned}
a_{21} &= \frac{-\frac{1}{\tau_f}\dot{m}_{fi0} - (1-X)\ddot{m}_{fi0}}{\left((1-X)\dot{m}_{fi0} + \dot{m}_{ff0}\right)^2}\lambda_0 - \frac{\eta_{vol}V_d\dot{m}_{at0}n_0}{120L_{th}V_i\left((1-X)\dot{m}_{fi0} + \dot{m}_{ff0}\right)^2} \\
a_{22} &= \frac{\eta_{vol}V_dn_0}{120V_i} + \frac{(1-X)\ddot{m}_{fi0} + \frac{1}{\tau_f}(-\dot{m}_{ff0} + X\dot{m}_{fi0})}{(1-X)\dot{m}_{fi0} + \dot{m}_{ff0}} \\
b_{21} &= -\frac{\eta_{vol}V_d}{120V_i}\lambda_0 + \frac{\eta_{vol}V_d\dot{m}_{at0}}{120L_{th}V_i\left((1-X)\dot{m}_{fi0} + \dot{m}_{ff0}\right)} \\
b_{22} &= \frac{\eta_{vol}V_dn_0}{120L_{th}V_i\left((1-X)\dot{m}_{fi0} + \dot{m}_{ff0}\right)} \\
b_{23} &= \frac{-\frac{X}{\tau_f}\dot{m}_{ff0} + (1-X)^2\ddot{m}_{fi0} - \frac{1}{\tau_f}\dot{m}_{ff0}}{\left((1-X)\dot{m}_{fi0} + \dot{m}_{ff0}\right)^2}\lambda_0 \\
&\quad - \frac{(1-X)\eta_{vol}V_d\dot{m}_{at0}n_0}{120L_{th}V_i\left((1-X)\dot{m}_{fi0} + \dot{m}_{ff0}\right)^2} \\
b_{24} &= -\frac{(1-X)\lambda_0}{(1-X)\dot{m}_{fi0} + \dot{m}_{ff0}}
\end{aligned}
\tag{38}
$$

These constants are now reorganized to ease the implementation and/or design of the final $\mathcal{H}_\infty$controller. The reorganization follows the rules below.

- $\dot{m}_{fi}$ is now a state in the model. The control signal will instead be the "acceleration in fuel mass flow", $\ddot{m}_{fi}$. This is done for the following two reasons: First, by using $\ddot{m}_{fi}$ as the control signal and then calculating $\dot{m}_{fi}$ as $\int_0^t \ddot{m}_{fi}(\tau)d\tau$ internally in the control computer, one get a "filtered" control signal. Second, the physically relationship between $\ddot{m}_{fi}$ and $\dot{m}_{fi}$ is preserved. The final control signal for the engine is of course $\dot{m}_{fi}$.

- $\dot{m}_{fi0}$ is the steady state fuel mass flow in the linearised model. Since the magnitude of this signal is given by the speed density equation it suggests that one should replace $\frac{\eta_{vol}V_dn_0p_{i0}}{120L_{th}RT_i\lambda_0}$ for $\dot{m}_{fi}$. In this way the physically relationship between $\dot{m}_{fi}$ and n, p_i, η_{vol} and T_i is maintained. Especially when addressing the modeling of the perturbations it is very critical that the uncertainty space is minimized in order not to obtain a too conservative design.

- The inputs $\dot{m}_{fi}$ and $\dot{m}_{at}$ are in $\frac{g}{s}$ units instead of $\frac{kg}{s}$. This is to prevent numerical problems when using the μ and $\mathcal{H}_\infty$tools provided in the MATLAB environment.

From the above statements the constants a_{xx} and b_{xx} can be rearranged as in equation (39).

$$
\begin{aligned}
a_{21} &= a_{21_1} + a_{21_2} \\
a_{21_1} &= -\frac{120RT_iL_{th}}{1000\tau_fp_{i0}n_0\eta_{vol0}V_d}\lambda_0^2 \\
a_{21_2} &= -\frac{RT_iL_{th}}{1000p_{i0}V_i}\lambda_0^2 \\
a_{22} &= \frac{\eta_{vol0}n_0V_d}{120V_i}
\end{aligned}
\qquad
\begin{aligned}
b_{21} &= 0 \\
b_{22} &= \frac{RT_i}{1000V_ip_{i0}}\lambda_0 \\
b_{23} &= b_{23_1} + b_{23_2} \\
b_{23_1} &= -\frac{120RT_iX(1+X)L_{th}}{1000n_0p_{i0}\eta_{vol0}V_d\tau_f}\lambda_0^2 \\
b_{23_2} &= -\frac{(1-X)RT_iL_{th}}{1000p_{i0}V_i}\lambda_0^2 \\
b_{24} &= -\frac{120(1-X)RT_iL_{th}}{1000n_0p_{i0}\eta_{vol0}V_d}
\end{aligned}
\tag{39}
$$

The final state space representation of the λ object is shown in equation (40). One can see that λ's dependence with respect to the engine's crankshaft speed n has vanished.

$$\begin{bmatrix} \delta\ddot{m}_{fi} \\ \delta\ddot{m}_{ff} \\ \delta\dot{\lambda} \\ \delta\dot{\lambda}_1 \\ \delta\dot{\lambda}_2 \\ \delta\dot{\lambda}_m \end{bmatrix} = \begin{bmatrix} 0 & 0 & 0 & 0 & 0 & 0 \\ \frac{X}{\tau_f} & \frac{-1}{\tau_f} & 0 & 0 & 0 & 0 \\ b_{23} & a_{21} & -a_{22} & 0 & 0 & 0 \\ 0 & 0 & 0 & 0 & \frac{-12}{\tau_d^2} & 0 \\ 0 & 0 & \frac{-12}{\tau_d} & 1 & \frac{-6}{\tau_d} & 0 \\ 0 & 0 & \frac{1}{\tau_\lambda} & 0 & \frac{1}{\tau_\lambda} & \frac{-1}{\tau_\lambda} \end{bmatrix} \begin{bmatrix} \delta\dot{m}_{fi} \\ \delta\dot{m}_{ff} \\ \delta\lambda \\ \delta\lambda_1 \\ \delta\lambda_2 \\ \delta\lambda_m \end{bmatrix} + \begin{bmatrix} 0 & 1 \\ 0 & 0 \\ b_{22} & b_{24} \\ 0 & 0 \\ 0 & 0 \\ 0 & 0 \end{bmatrix} \begin{bmatrix} \delta\dot{m}_{at} \\ \delta\ddot{m}_{fi} \end{bmatrix} \tag{40}$$

$$y = \begin{bmatrix} 0 & 0 & 0 & 0 & 0 & 1 \end{bmatrix} \begin{bmatrix} \delta\dot{m}_{fi} \\ \delta\dot{m}_{ff} \\ \delta\lambda \\ \delta\lambda_1 \\ \delta\lambda_2 \\ \delta\lambda_m \end{bmatrix}$$

C Choosing the Order and/or Type of Time Delay Approximation.

The aim of this appendix is to give a control engineer rough guidelines of how to choose an appropriate approximation of a time delay. The appendix will discuss two approximation types: a low pass filter and a Padé filter approximation. It is assumed in the following that the nature of the control object is SISO. Figure 10 shows the behaviour of the two approximation types

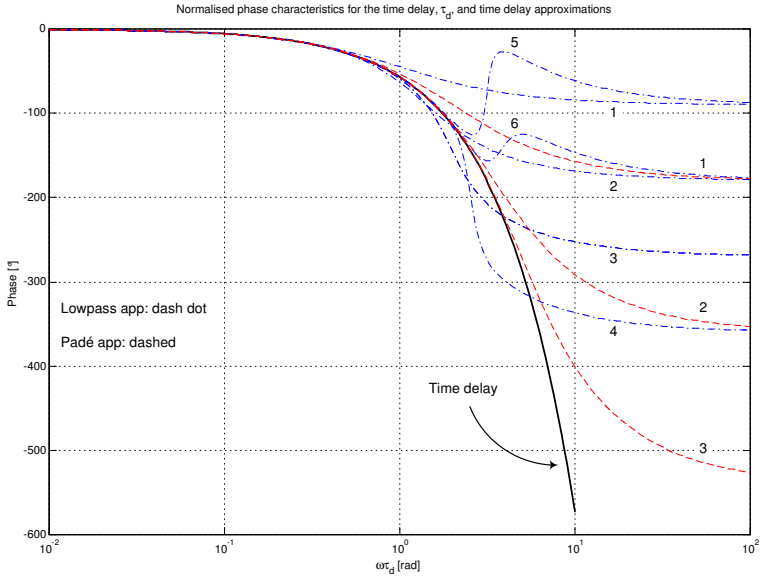

Figure 10: Phase characteristics of the low pass and Padé filter time delay approximations as functions of normalised frequency, $\omega\tau_d$. Characteristics are shown for low pass filter approximations up to sixth order and for Padé filter approximations up to third order. The solid line is the phase characteristic of the time delay, $e^{\tau_d s}$.

phase characteristics compared with those of a real time delay. The choice of type and order of the approximation method is strongly linked to the desired cross over frequency, ω_c, of the open loop system. Using figure 10 the choice of approximation can be split up into two categories:

$\omega_c \leq \frac{1}{\tau_d}$: For frequencies below $\frac{1}{\tau_d}$ the phase characteristics of the time approximations are more or less independent of type and order. It is thus natural to chose a first order low pass filter approximation to the time delay. The low pass

filter approximation does not introduce any zeroes i the right half plane (RHP) like a Padé approximation and a control strategy based on plant inversion may still be used.

$\omega_c > \frac{1}{\tau_d}$: If a cross over frequency larger $\frac{1}{\tau_d}$ is desired the first order low pass approximation should be discarded. Instead a low pass approximation of a higher order or a Padé approximation should be used. If it is desired to maintain the control object minimum phase, low pass approximations up to fourth order are usable for cross over frequencies below $\frac{4}{\tau_d}$. Using low pass approximations of higher order than 4 yields unstable approximations. Using an unstable filter as a time delay approximation is not intuitively correct since a time delay in its self does not make the open loop system unstable. Instead a Padé approximation can be used if zeroes in the RHP are acceptable. Introducing zeroes in the RHP may have an effect that is desirable. RHP zeroes can not be canceled out by poles and will thus have a limiting effect on the achievable control performance. Another good property of the Padé approximation is that it does not change the amplitude characteristics of the control object since it is a all pass filter. So for desired cross over frequencies higher than $\frac{2}{\tau_d}$ a Padé filter of second order or higher may be used.

D System Setup and $\mathcal{H}_\infty$Controller Structure

In the design of an $\mathcal{H}_\infty/\mathcal{H}_2$-regulator and robust analysis it is often advantageous to use a generalised system description. The generalised method used here is depicted in figure 11. K is the controller, P is the plant with uncertainty model and

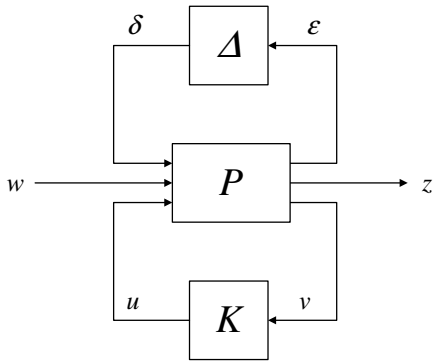

Figure 11: Generalised system setup

performance- and signal weights, and Δ is a structured perturbation matrix. The individual signals in the setup is: u, control signals, v, measurement signals, w, exogenous inputs, z, controlled signals, ϵ, perturbation output vector to Δ and finally δ is the perturbation input vector to the plant. The signal vector z contains those signals, which are to be controlled. When designing a controller the system is described by,

$$\left[\begin{array}{c}\epsilon\\ z\\ \hline v\end{array}\right] = \left[\begin{array}{c|c}P_{11}(s) & P_{12}(s)\\ \hline P_{21}(s) & P_{22}(s)\end{array}\right]\left[\begin{array}{c}\delta\\ w\\ \hline u\end{array}\right] \qquad u = K(s)v \tag{41}$$

P has the following state-space realisation,

$$P = \left[\begin{array}{c|cc}A & B_1 & B_2\\ \hline C_1 & D_{11} & D_{12}\\ C_2 & D_{21} & D_{22}\end{array}\right] \tag{42}$$

When designing $\mathcal{H}_\infty/\mathcal{H}_2$ controllers the closed loop transfer function from $\left[\begin{smallmatrix}\delta\\ w\end{smallmatrix}\right]$ to $\left[\begin{smallmatrix}\epsilon\\ z\end{smallmatrix}\right]$ is minimized. The transfer function from $\left[\begin{smallmatrix}\delta\\ w\end{smallmatrix}\right]$ to $\left[\begin{smallmatrix}\epsilon\\ z\end{smallmatrix}\right]$ is typically written as an LFT. This LFT is seen in equation (43).

$$\begin{bmatrix}\epsilon\\ z\end{bmatrix} = F_l(P,K)\begin{bmatrix}\delta\\ w\end{bmatrix} \qquad \text{where} \qquad N = F_l(P,K) = P_{11} + P_{12}K\left(I - P_{22}K\right)^{-1}P_{21} \tag{43}$$

The $\mathcal{H}_\infty$controller fulfilling $\|N(P,K)\|_\infty < \gamma$ has the structure,

$$K = \left[\begin{array}{c|c} A + \frac{1}{\gamma^2}B_1B_1^TX_\infty + B_2F_\infty + Z_\infty L_\infty C_2 & -Z_\infty L_\infty \\ \hline F_\infty & 0 \end{array}\right]$$

where

$$\begin{aligned} F_\infty &= -(D_{12}^TD_{21})^{-1}(B_2^TX_\infty + D_{12}^TC_1) \\ L_\infty &= -(Y_\infty C_2^T + B_1D_{21}^T)(D_{21}D_{21}^T)^{-1} \\ Z_\infty &= (I - \frac{1}{\gamma^2}Y_\infty X_\infty)^{-1} \end{aligned} \tag{44}$$

X_∞ and Y_∞ in equation (44) are the solutions to two matrix ricatti equations. These equations are,

$$\begin{aligned} 0 &= A^TX_\infty + X_\infty A + C_1^TC_1 + \frac{1}{\gamma^2}X_\infty B_1B_1^TX_\infty \\ &\quad - (X_\infty B_2 + C_1^TD_{12})(D_{12}^TD_{12})^{-1}(B_2^TX_\infty + D_{12}^TC_1) \\ 0 &= AY_\infty + Y_\infty A^T + B_1B_1^T + \frac{1}{\gamma^2}Y_\infty C_1^TC_1Y_\infty \\ &\quad - (Y_\infty C_2^T + B_1D_{21}^T)(D_{21}D_{21}^T)^{-1}(C_2^TY_\infty + D_{21}B_1^T) \end{aligned} \tag{45}$$

where

$$\rho(X_\infty Y_\infty < \gamma^2)$$

Figure 12 shows the block diagram for the $\mathcal{H}_\infty$controller. The location of the feedback gain matrix for the robust observer feedback vector and control signal vector are shown in the figure.

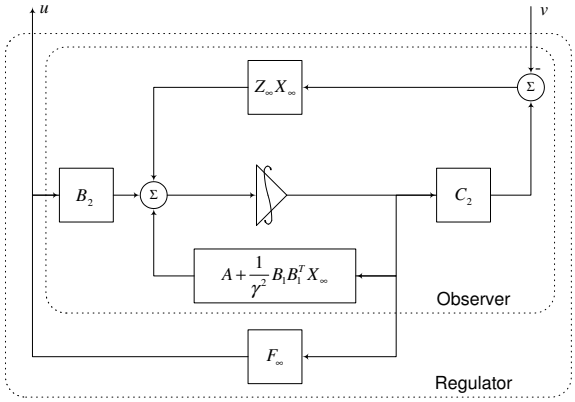

Figure 12: Block diagram for $\mathcal{H}_\infty$control structure.

In μ-analysis the closed loop system N is tested for stability/performance with respect to a structured perturbation. That is, the norm of $F_u(N,\Delta)$ is investigated. $F_u(N,\Delta)$ is given by the upper LFT in equation (46).

$$F_u(N,\Delta) = N_{22} + N_{21}\Delta(I - N_{11}\Delta)^{-1}N_{12} \tag{46}$$

1.3 Predictive air-to-fuel ratio control

The predictive AFR controller presented in the SAE paper entitled *"Predicting the Port Air Mass Flow of SI Engines in Air/Fuel Ratio Control Applications"*[3] is in many ways different from the $\mathcal{H}_\infty$ controller presented earlier even though the control objective is the same: control of the SI engine's AFR ratio. Where as the philosophy behind the $\mathcal{H}_\infty$ AFR controller presented previously was "Who far can one go with a *bad* model and a minimum set of sensor signals when one relies on feedback compensation" the topic in the following article is rather "How good a control performance can one achieve if one develops a very *good* model of the intake manifold filling dynamics and use this model to predict future control actions capable of eliminating some of the dynamical problems in a feed-forward strategy". This change of control philosophy requires some adjustments compared to the $\mathcal{H}_\infty$ AFR controller, some of which will be briefly introduced in the following.

One of the major Chinese walls of the port fuel injected SI engine is the significant time delay introduced in the signal path from the point of fuel injection to the AFR recorded by the λ sensor in the exhaust pipe. This time delay may be divided into two categories: *injection delay* and *transport delay*. The injection delay is the period of time between the sampling of the intake manifold signals relevant to the fuel injector pulse-width computation to the actual injection of the fuel, and the transport delay is the time between the end of fuel injection until the quality of the combustion process is measured by the λ sensor (and sampled). Of these two time delays, only the injection time delay may be compensated for or eliminated by a predictive control strategy. However, this requires that the time delay stays constant and that the fuel injection strategy is perfectly phased relative to the engine events. Hence, the predictor to be developed must be designed and implemented in the event domain.

Since the fuel injector pulse-width computed cannot be corrected/altered after the corresponding fuel algorithm has terminated[4] measures must be taken to insure that the signals/states used in the corresponding fuel calculation step either stay constant until the end of the induction event or that their trajectory during the period of induction are *known* in advance. The first case is obviously not possible since it is equivalent to limiting the engine operation to the steady state only and the latter calls for predictive control of the fuel injection. However, using a predictive strategy not only requires a model of the intake manifold dynamics relevant to the description of AFR, but also knowledge of all future exogenous control actions within the prediction horizon. Since the control problem in the following paper is limited to AFR control of port fuel injected NA (Natural Aspirated) SI engines without external exhaust gas recirculation, the only control variable of

[3] This article was also presented in [10].

[4] It is assumed that the fuel injection system is not capable of firing the fuel injector multiple times during an engine event. If this was possible, however, too lean mixtures could be compensated by a following fuel injection before and during the induction event.

interest is the throttle angle[5]. The throttle command was therefore postponed a fixed number of event samples and made possible a prediction of the air mass flow through the throttle system. Although this action necessitates a drive-by-wire control system, the throttle command was as mentioned before only time delayed and not controlled; Hence, the air-lead classification of the AFR control system was maintained.

When a predictive control strategy is designed, the underlying dynamic model must as previously mentioned be of high accuracy if the feed-forward compensation should be effective. This called for some adjustments of the IMVEM (Isothermal Mean Value Engine Model) proposed earlier in [47] to improve the level of model accuracy within the normal engine operation limits. First, the isothermal assumption for the intake filling dynamics was discarded and the model was exchanged for a polytrophic description of the intake pressure and the intake temperature dynamics. Second, a simple second order model of the DBW (Drive By Wire) system's dynamics was constructed. Using this model in parallel with the models of the intake pressure and the intake temperature, the response of the throttle plate position within the prediction horizon could be predicted. This offers valuable information for the throttle air mass flow model. Lastly, the air filter upstream of the throttle body introduces a small however noticeable pressure drop, i.e. the stagnated throttle body pressure level is offset from the ambient pressure level. Bearing this in mind and that the throttle mass flow model proposed in the following article is very sensitive not only to model errors in the intake manifold pressure model, but also to errors in the description of the stagnated pressure upstream of the throttle plate, measures must be taken such that the throttle body pressure level is corrected. However, since the air filter pressure loss is mainly a function of volumetric flow it will together with the algebraic description of the throttle model form an algebraic loop. To overcome this problem a simple iterative algorithm with a fixed number of steps was implemented in the final strategy.

Using a pure predictive feed-forward strategy the danger of model divergence is immense as various model errors are accumulated. In order to minimize the danger of such scenarios, the states of the predictive model are updated every event sample by an extended Kalman filter utilizing measurement innovation from the intake manifold pressure sensor and from the thermocouple mounted in the middle of the intake plenum. However, before the Kalman filter could be designed the predictive model just described needed several important augmentations. First, although the temperature sensor[6] used was fast, its time constant was still significant compared to the time constant of the intake temperature state equation. Hence, the temper-

[5]The throttle type used on the experimental engine was of an older type that did not feature any external air injection capabilities. Hence, the intake air mass flow was controlled completely by the throttle position.

[6]The temperature sensor used during the experimental work was a conventional K-type thermocouple. However, due to the small size of the sensing element this sensor type is 35 to 200 times faster than the thermistors and thermocouples normally used in mass production applications or conventional test cells.

ature sensor required modelling to insure a correct picture of the overall dynamic system. Thus, a simple linear first order model was designed and later found sufficiently descriptive from experimental results. Second, the pressure fluctuations in the intake manifold are deterministic and do not fulfill the requirement of being that of Gaussian white noise nature as required by the Kalman filter framework. Instead, the model was augmented further by a linear network of second order tuned to the frequency of the first harmonic of the pumping fluctuations. The output of this filter was thereafter added to the averaged intake pressure estimate provided by the pressure state equation. This signal along with the pressure measurement formed the signal innovation to the observer. In this way the distribution of the error between the pressure model and measurement was brought closer to a Gaussian noise distribution. Finally, to account for a possible steady state error between the throttle mass flow model and the port mass flow a *constant* (deviation) variable was added to the output of the throttle model in the temperature and pressure state equation.

The actual computation of the corresponding Kalman gains required of course not only a linearized version of the model briefly described above but also a priori knowledge of the individual state noise and measurement noise intensities. These were derived from experimental data using either conventional FFT (Fast Fourier Transform) techniques or soft assumptions on the process and measurement covariances along with an inverted version of the classical Lyapunov equation.

Needless to say, however,model errors will always exist and thus to prevent steady state AFR errors, a simple, but good PI control loop around the λ sensor fitted to exhaust manifold was designed. The control output of this compensator was later added to the AFR predictor output, and hence formed the final port fuel flow command.

Finally, the port fuel flow command was sent through a fuel film compensator to eliminate the dynamics of the fuel film. The fuel film compensator was designed according to the classic Aquino fuel film model with its two adjustment parameters stored in a speed–pressure map. The output of this filter is the final fuel injection command sent to the fuel injection unit. However, this filter or rather its calibration proved to be limited by great difficulties; the filter parameters maps could not be satisfactorily realized from experimental engine data using a off-line identification algorithm, hence the final parameters maps used in the experimental work were found in a trial-and-error manner.

The strategy presented in detail here was finally implemented in a version of the ECDS (Engine Control Development System) environment (see [58]) which had been updated earlier in a collaboration between A. Chevalier and the author. The functionality of the strategy developed was confirmed by several different transient experiments in one of the test cells available to the ECG, some of which are included in the article presented here.

2000-01-0260

Predicting the Port Air Mass Flow of SI Engines in Air/Fuel Ratio Control Applications

Alain Chevalier
Ford Motor Co.

Christian Winge Vigild
Ford Motor Co.

Elbert Hendricks
Technical University of Denmark

ABSTRACT

With the tightening of exhaust emission standards, wide bandwidth control of the air/fuel ratio (*AFR*) of spark ignition engines has attracted increased interest recently. Unfortunately, time delays associated with engine operation (mainly injection delays and transport delays from intake to exhaust) impose serious limitations to the achievable control bandwidth. With a proper choice of sensors and actuators, these limitations can be minimized provided the port air mass flow can be accurately predicted ahead in time.

While the main objective of this work is to propose a complete *AFR* controller, the main focus is on the problems associated with port air mass flow prediction.

1 INTRODUCTION

In order to achieve maximum conversion efficiency of the three-way catalyst (*TWC*), the engine management system needs to be able to keep the mass of fresh air, m_a and the mass of fuel, m_f, which are trapped in each cylinder, in a stoichiometric proportion (L_{th}, the ratio for complete combustion). If one defines the normalized *AFR*, λ, as

$$\lambda = \frac{m_a}{m_f \, L_{th}} \tag{1}$$

then the requirement of the controller is to maintain λ as close to 1 as possible, both during steady-state and transient operation. In the literature, this is known as the air/fuel ratio (*AFR*) control problem.

Conventional *AFR* strategies are based on look-up tables (non-dynamic map modeling). Associated with a feedback loop (from the λ oxygen sensor placed in the exhaust pipe), they can ensure that the *AFR* will remain in the vicinity of the stoichiometric point during steady-state operation (constant load and constant engine speed). However, the dynamic nature of air and fuel flows, the low pass characteristic of sensors, the delays required by the control system to respond to measurements and the driver's command (on tip-in or tip-out), and finally the transport time required by the air-fuel mixture to cross the engine and reach the oxygen sensor, make conventional feedback loop control strategies slow (with a small control bandwidth). They are thus unable to avoid large *AFR* excursions during transient operation (acceleration, deceleration, varying engine load, wind gusts etc.). This is a key problem when trying to address the problem of automobile induced pollution in cities: during rush-hour traffic, the engine is often operated in transient conditions, thus leading to large *AFR* excursions from stoichiometry and consequently poor *TWC* efficiency.

The purpose of this paper is to consider in detail not only the physical characteristics of the engine, but those of the sensors as well. In addition to these physical constraints, the details of the timing of the engine control microprocessor and the associated actuators are taken into account. The overall goal is thus to demonstrate experimentally the effectiveness of a nearly ideal theoretical solution to the *AFR* control problem on a practical system.

Before attempting to address the control problem, it is convenient to review the actual physical problems which engine controllers have to overcome if they are to be successful in controlling an engine.

2 *AFR* CONTROL PROBLEMS

The wall-wetting phenomenon[1] and the manifold filling phenomenon[2] have been known as the source of transient *AFR* problems for many years and will therefore not be discussed here. Readers who are not familiar with these phenomena, should refer to [1], [2], [3], [4], [5] and [6] for a thorough discussion. Here, the authors will discuss three problems which they consider to be just as important, but which have surpris-

This paper is typeset in LaTeX 2ε

[1] Some of the injected fuel is deposited on the manifold wall instead of entering the cylinders immediately.

[2] During transients, port air mass flow and throttle air mass flow differ because of the filling/emptying of the intake manifold volume.

ingly enough not enjoyed much attention in the existing literature. These are the limitations imposed on the controller by the presence of engine pumping fluctuations, poor sensor response characteristics and time delays.

2.1 Pumping Fluctuations

In the intake duct, pressures and flows oscillate because of the periodic motion of piston and valves. During the induction process, the engine operates as a pump, and the resulting periodic variations are often referred to as pumping fluctuations [7],[8]. The modulation depth of the fluctuations can be of the order of 15% of the average signal level for the pressure and more than 100%[3] of the average signal level for the air mass flow. The source of pumping noise is periodic and so are the pumping fluctuations which are frequency locked to the engine event frequency. This is illustrated in Figure 1 where a steady state manifold absolute pressure (*MAP*) signal (measured on an engine dynamometer) is shown both in the time domain and in the frequency domain. The fundamental frequency (marked f_0) is clearly locked to the event frequency (marked f_e), and power is also present in the first and second harmonics (marked f_1 and f_2). As shown in Equation 1, the mass of air that enters one

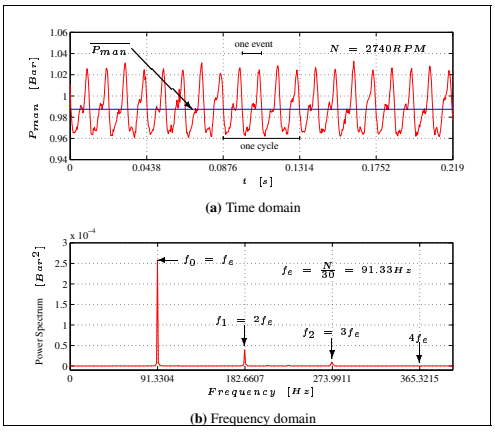

Figure 1: Intake pressure pumping fluctuations during steady-state operations

cylinder, m_a, and consequently the mean over one event of the air mass flow related (*AMFR*) signals, are the only variables of interest in multi-point injection (*MPI*) *AFR* control. What is actually desired in the conditioning of the signals from the *AMFR* sensors is to remove the large fluctuating component of the signals without damping out their mean value during transients and without introducing time lags and time delays which would impose limitations on the system bandwidth. In conventional fueling strategies, this is a problem which has often been ignored. Because of the discrete nature of microprocessor-based controllers and given the level of pumping noise, serious aliasing problems should be expected if no special measures are taken during the sampling/processing of the measurements. This is especially true in event-based sampling strategies where the noise spectrum and the sampling frequency are locked.

In Figure 2, the transient performance of a 4-step moving average filter (*EABS4*)[4] averaging algorithm is simulated during a fast (50 ms) tip-in and tip-out at constant idle-speed conditions (worst case). In order to emphasize the delay associated with the filter, the pressure is also filtered with a zero-phase *EABS4* digital filter (i.e. the input data are processed *off-line* in both the forward and reverse directions, so that the time lag introduced in the forward filtering is canceled by the time advance introduced in the backward filtering). The expected resulting transient λ trace is shown in Figure 2(b) where tip-in results in a lean and tip-out in a rich excursion. Note that because the filtering delay is inversely proportional to the engine speed, these excursions decrease with increasing engine speed down to 5% at 6000 RPM. However, it should be clear that this λ trace is in many ways ideal (and therefore optimistic) since the effects of manifold filling, fuel film dynamics and injection delays were not included in the simulation.

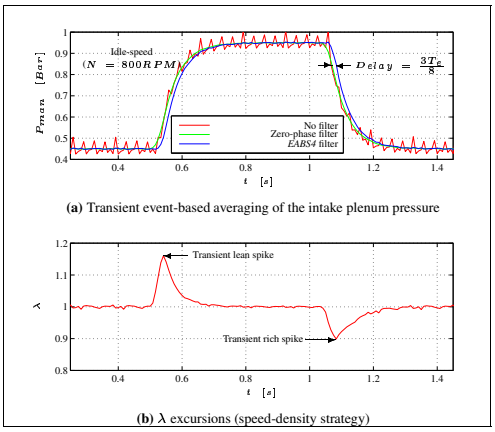

Figure 2: The impact of filtering delays/time-lags on transient *AFR* control. T_e is the event duration.

One way to circumvent this problem is to use model-based filters (extended Kalman filter (*EKF*)) which have built into them an a priori dynamic picture of the mean of the *AMFR* signals as well as a statistical description of the noise [9]. However, because pumping noise can in no way be approximated by white noise, special care should be taken in the design of these filters (choice of the observer structure, choice of the sampling frequency, and calculation of the Kalman gains) if they are to perform properly. This topic is treated in more detail in a later section.

[3] indicating backflow.

[4] 4^{th} Order Event Averaged Based Sampling. The signal is sampled 4 times per event and averaged over the last 4 measurements ([7], [8]).

2.2 Sensor Characteristics

The characteristics of the *AMFR* sensors must be taken into account in the design of an engine controller. In particular, the nonlinearity and the response time of the sensor can have a significant impact on the performance of the controller. Also, when possible, the structure of the controller should be adapted to take full advantage of a combination of sensors. To make the discussion more concrete, the typical characteristics of the most common sensors used in *AFR* control are listed in Table 1.

Despite its popularity in the automotive industry, the hot wire mass air flow (*MAF*) sensor is clearly a bad candidate for *AFR* control applications. It is also inadequate for direct port air mass flow measurements which might be corrupted by flow reversal and large pulsations. This is discussed in further detail in [7] and [8]. A *MAP* sensor (possibly combined with a potentiometer mounted on the throttle plate axle) is clearly the best choice among the *AMFR* sensors. Despite their accuracy, the common temperature sensors (usually thermistors) are usually too slow to catch any fast thermal effects which may occur during transient operation. The λ (or exhaust-gas-oxygen (*EGO*)) sensors are the only sensors which give a direct measure of the *AFR* signal and consequently are the only sensors which can guarantee the robust performance of *AFR* controllers. While the switching type *EGO* sensors are clearly nonlinear and bring only limited information to the *ECU*, production type universal exhaust-gas-oxygen (*UEGO*) (linear) sensors (which are slowly replacing *EGO* sensors) still suffer from drift problems and are quite slow compared to *MAP* sensors.

But the main drawback with λ sensors comes from the fact that they are placed in the exhaust manifold; as a consequence, the *AFR* signal is made available to the *ECU* only after a large transport delay which, in turn, limits the response time of the controller. This is the subject of the next section.

2.3 Bandwidth Limitations Imposed by Time Delays

From [4] it is known that the *AMFR* signals, during transients, respond at a speed very close to the throttle angle rise time and thus they can be assumed to have basically the same spectrum as the driver's input spectrum. In [8] measurements made on a vehicle driven on the road over various realistic road operating conditions show that the throttle angle is commonly changed on a minimum time scale of 50 to 100 ms. This suggests that the link between the driver's wishes and the throttle plate can be roughly characterized as a low pass filter with a cut-off frequency of 20 rad/s. In the limit, the driver's wishes tend toward white noise (series of rapid tip-in and tip-out with random amplitudes). The worst case operator input spectrum, and consequently the spectrum of the (mean) *AMFR* signals, can thus be approximated as a low pass filtered white noise with a bandwidth of 20 rad/s at -3 dB [8]. This value is very important because it indicates the requirements of the *AFR* controller in terms of bandwidth[5]; approximately, the controlled system should perform properly (the control should be tight) to frequencies up to a decade above the bandwidth of the operator spectrum (i.e. 100 to 200 rad/s) if λ errors are to be avoided during transients.

Whatever controller is used (even if designed with no penalty on the input), there are always limits to the performance the controlled system can achieve. These limits are imposed by the system to be controlled and by the structure of the controller itself. Again, it should be very clear that there is no point in trying to tune the controller to perform above these limits, since this is impossible. For engines, the bandwidth of the *AFR* system is strongly limited by delays. As illustrated in Figure 3, two delays need to be considered: the injection delay and the transport delay.

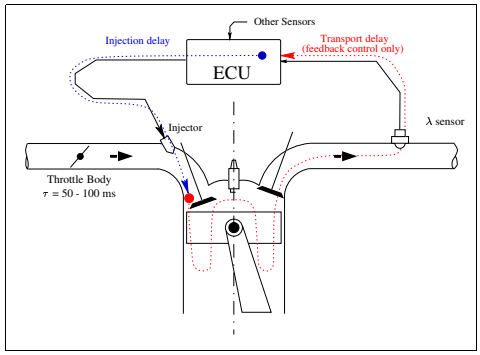

Figure 3: Injection and transport delays

2.3.1 Injection Delay and λ Feedback Transport Delay

The *injection delay* is the time between the sampling of the *AMFR* sensor signals by the *ECU* and the time at which the in-cylinder *AFR* builds up to its final value, i.e. during the induction of the fuel-air mixture at intake valve opening. This delay is important because any disturbance which may alter the flow during this period can not be compensated for by the controller and will immediately result in *AFR* excursions. The injection delay depends on three parameters:

1. Computation duration

   This is the time it takes for the *ECU* to compute one step of the control strategy. In a time-based strategy, this delay is usually about 15 ms long [13] (90 crankshaft degrees (*cdeg*) at 1000 RPM, 450 *cdeg* at 5000 RPM). In a crank

[5] It is common practice to characterize the performance of a controller in term of its frequency bandwidth. Intuitively, a large bandwidth corresponds to a faster rise time (high frequency signals are easily passed to the output). Strictly speaking, the concept of bandwidth only applies to linear systems for which Fourier transformation is defined. However, for nonlinear system, it is convenient to continue characterizing the system in terms of its bandwidth, though in this case, it should only be interpreted as the inverse of some settling time (in *AFR* control, the inverse of the time it takes for the λ signal to settle down to 1 $\pm$ some tolerance).

		Specifications				
		Sensing method	**Accuracy**	**Response time**	**Linearity**	**Comments**
Sensor type	**manifold absolute pressure (*MAP*)**	Piezoresistive silicon	$\pm 1\%$	1 ms	Excellent	Dynamic response deteriorates with long pneumatic transmission lines
	manifold air temperature (*MAT*)	Metal film or thermistor or thermocouple	$\pm 2\%$	1 - 10 sec.	Nonlinear, compensated	Time constant down to 200 ms with a very small thermocouple
	mass air flow (*MAF*)	Hot wire or hot film	$\pm 3\%$ in stationary flows	50 ms - 0.5 sec.	Nonlinear, compensated	Dynamics depends on engine operating conditions, unidirectional, very inaccurate during transients (tip-in/out, pumping fluctuations) [10]
	Throttle Position Sensor	Potentiometer	$\pm 3\%$	0.1 ms	Excellent	Several potentiometers may be used in series/parallel to increase locally the accuracy
	Crank/Cam-shaft timing/speed	Hall effect or variable reluctance	$> 1\%$	30 μs - 300 μs	Excellent	The primary goal of the sensors is to provide triggers signals to the timing processor unit of the electronic control unit (*ECU*)
	exhaust-gas-oxygen (*EGO*)	Zirconium dioxide ceramic	1 - 6%	50 ms	Highly nonlinear	Used as a switch between lean & reach air/fuel ratios
	universal exhaust-gas-oxygen (*UEGO*)	Zirconium dioxide ceramic with oxygen pumping device	1 - 6%	$>$ 50 ms	Nonlinear, compensated	Subject to drift, available as production type sensor since 1999

Table 1: Characteristics of the most used sensors in *AFR* control applications ([11], [12])

based strategy, the delay is usually 180 *cdeg* long (30 ms at 1000 RPM, 6 ms at 5000 RPM).

2. Injection duration

   The flow out of the injector is constant and it is the duration of the injection pulse which determines the quantity of fuel injected. This pulse is usually between 2 and 15 ms long (between 12 and 90 *cdeg* at 1000 RPM, and between 60 and 450 *cdeg* at 5000 RPM).

3. Injection timing (start of injection (*SOI*) delay)

   In order to achieve low emissions, tight control of the *AFR* is not the only requirement. The quality of the air-fuel mixture is also an important factor: as much fuel as possible should enter the cylinders in vapor form. As shown in [14], the wall-film evaporation dominates the mixture preparation process; because the heat from the intake air is negligible compared to the heat absorbed from the wall, injecting most or all the fuel on closed hot intake valves is a requirement of modern *MPI* systems. In [15] it is shown that heat-transfer rates are up to 50% higher with closed valve injection than with open valve injection; the fuel is trapped on the valve surface for the time the valve remains closed, thereby giving a longer time for evaporation.

   Similarly, in open valve injection, a large proportion of the unvaporized droplets follow the air stream into the cylinder instead of hitting the wall/valve. In [16] tests run on an engine show a significant increase in emission of hydrocarbons (HC) from injection on closed valves to injection on open valves. It is therefore necessary to provide enough *SOI* advance so that no or little fuel is sprayed on open valves; in order to guarantee the proper injection timing, a delay (the *SOI* delay) is required between the end of the computation of the strategy and the beginning of the injection pulse. As a consequence, the injection delay is increased. Note that for a time-based strategy where only the injection pulses are crank-synchronized (whereas the computation of the strategy and the sampling of the *AMFR* signals are time-synchronized) the *SOI* delay is varying continuously and can be equal, in the worst case, to the computational delay (15 ms).

In short, the injection delay varies between 17 ms (15+0+2) and 45 ms (15 + 15 + 15) for a time-based controller (between 102 *cdeg* at 1000 RPM and 900 *cdeg* at 5000 RPM). In a crank-based strategy (where all operations are crank-synchronized), the injection delay is fixed in the crank domain. To prevent injection on open valves, this delay should be at least 630 *cdeg* (180 *cdeg* for computation + 15 ms injection pulse at 5000 RPM, worst case). This gives a delay of 105 ms at 1000 RPM and 21 ms at 5000 RPM. For the sake of clarity, these results are illustrated in Figure 4.

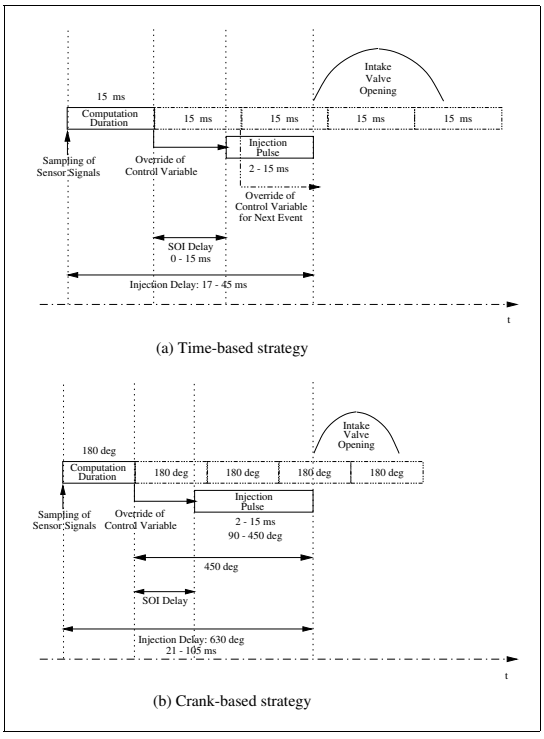

Figure 4: Injection delay in time-based and crank-based strategies

The *transport delay* is the time it takes for the controlled variable (the mass of injected fuel) to have an impact on the measured λ signals; in other words, it is the time between the injection of the fuel at the injectors and the reading of the λ sensor

signals by the *ECU*. Of course, the transport delay exists only in the case of λ-feedback *AFR* control. If fuel is injected on closed valves, it will take about 3 $\frac{1}{2}$ strokes (105 ms at 1000 RPM, 21ms at 5000 RPM) before it reaches (in burned form) the exhaust manifold. It will take another 2 to 20 ms before it reaches the λ sensor (transport time through the exhaust manifold). Clearly, no control reaction can occur before this transport delay and the injection delay have elapsed.

In [17], it is proved that for a stable plant with a time delay (Loop-delay), and whatever the integral square error (*ISE*)-optimal controller[6] which is used, the maximum achievable bandwidth of the controlled system is equal to:

$$\frac{1}{\text{Loop-Delay}}$$

This is the upper limit (right half plane zeros decrease this limit further) which can be achieved with an *ideal unrealizable* (no penalty on the input) controller; note that this applies to any type of controller, including pure feedforward.

In the case of exhaust λ-feedback, the loop-delay is equal to the sum of the injection delay and the transport delay:

Loop-Delay	=	*Injection Delay*	+	*Transport Delay*
(best case, time-based)	=	17 ms	+	23 ms
(worst case, time-based)	=	45 ms	+	125 ms
(best case, crank-based)	=	21 ms	+	23 ms
(worst case, crank-based)	=	105 ms	+	125 ms

In the case where the controller is based only on measurements made in the intake manifold, the loop-delay equals the injection delay only:

Loop-Delay	=	*Injection Delay*
(best case, time-based)	=	17 ms
(worst case, time-based)	=	45 ms
(best case, crank-based)	=	21 ms
(worst case, crank-based)	=	105 ms

The consequences in terms of bandwidth limitation of the controlled system are summarized in Table 2. It is seen that the optimal bandwidth of an ideal λ-feedback strategy never exceeds 25 rad/s. This is much too low compared to the 200 rad/s required for tight transient *AFR* control. Even for strategies based on intake manifold measurements only, the bandwidth is sometimes as low as 22.5 rad/s for an ideal time-based strategy and 9.5 rad/s for an ideal crank-based strategy. This latter value corresponds to low engine speed (1000 RPM) where most of the tip-ins happen, and is therefore the source of large transient errors during acceleration. However, even if none of the above strategies can satisfy the bandwidth requirements, strategies based on intake manifold measurements are clearly to be preferred to those based on exhaust measurements, as far as overall system bandwidth is concerned.

[6] a controller which minimizes the integral square error ($\int_0^\infty |y(t) - r(t)|^2 dt$) between the output y and the command r, [18].

2.3.2 Disturbances and Injection Delay

In the previous section it was shown that even strategies based only on ideal intake measurements are unable to meet the bandwidth requirements of a tight *AFR* controller; this is due to the large injection delay imposed on the controller by the hardware. Concretely, any disturbance which may occur between the measurement of the *AMFR* signals and the actual injection of the fuel may lead to a large mismatch between the amount of induced fuel and the amount of induced air.

Two types of disturbances, mainly, are possible: a change of external load (torque) on the crankshaft (and consequently a change of engine speed) and a change of throttle position (and consequently a change in air mass flow). The inertia of the vehicle/engine prevents the engine speed from changing on time scales smaller than a few seconds (much larger than the injection delay) and the disturbances associated with the varying external load can safely be discarded on the same basis. However, because of the fast dynamics associated with the intake manifold, any change in the throttle position after the *AMFR* measurements are made will immediately move the port air mass flow away from the value estimated (anticipated) in the *ECU* [19].

The resulting *AFR* excursions can be very large as illustrated in Figure 5. Note that in this simulation, the crank-based strategy is ideal in the sense that perfect knowledge of the port air mass flow at the sampling instants, no fuel-film and no pumping fluctuations are assumed; the transient λ excursions are solely due to the injection delay which is set to 630 crank degrees. The engine speed is kept constant and the only disturbance comes from the movement of the throttle.

3 MODELING THE INTAKE AIR DYNAMICS

In this section the Mean Value Engine Model (*MVEM*)[7], which forms the basis of the model-based controller described in Section 4, is presented. The validity of the model during transient operation is discussed in a companion paper by some of the authors [20]. The focus is on the validity of the dynamic air flow model which is normally used in control applications. Three points critical to accurate transient modeling are emphasized:

[7] A compact, but accurate, description of the mean values (no pumping fluctuations) of some engine variables, both during steady-state and transient operation

	Controller based on exhaust measurements		Controller based on intake measurements	
	Best Case	**Worst Case**	**Best Case**	**Worst Case**
Time-Based	25.0 rad/s	5.9 rad/s	58.8 rad/s	22.2 rad/s
Crank-Based	22.7 rad/s	4.3 rad/s	47.6 rad/s	9.5 rad/s

Table 2: Comparison of the approximate maximum bandwidth of different types of air/fuel ratio controllers. Note that these figures are largely over estimated since they apply to ideal unrealizable controllers with infinitely fast sensors. These figures should be compared to the required bandwidth of 200 rad/s.

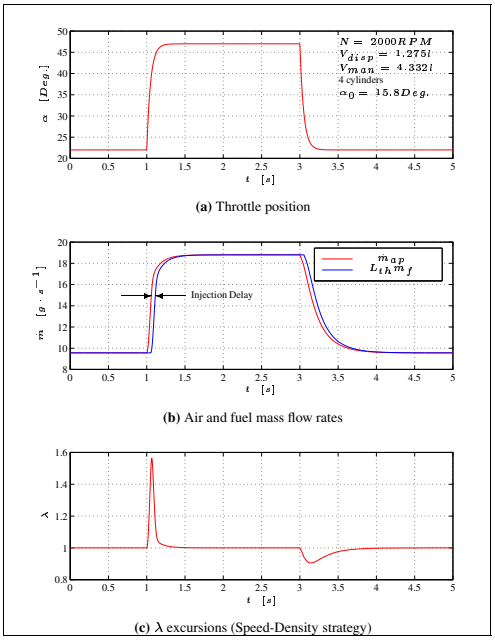

(a) Throttle position

(b) Air and fuel mass flow rates

(c) λ excursions (Speed-Density strategy)

Figure 5: The impact of injection delay on transient *AFR* control.

- Despite the complex nature of acoustic phenomena during transients (rapid throttle opening/closing, varying load on the crank), conventional steady-state volumetric efficiency maps are capable of describing the engine breathing performance with a remarkable accuracy also during fast transient operation; consequently, the so-called speed density equation (2) provides a very accurate description of the port air mass flow, provided the mean air density is known with equivalent accuracy in the intake manifold.

$$\dot{m}_{ap} = \eta_{vol}^{P_{amb},T_{man}}\left(\frac{N}{\sqrt{T_{man}}}, \frac{P_{man}}{P_{amb}}\right)\frac{N\,V_{disp}}{120}\frac{P_{amb}}{r\,T_{man}} \quad (2)$$

where $\eta_{vol}^{P_{amb},T_{man}}$ is the volumetric efficiency based on barometric pressure, P_{amb} and intake manifold temperature, T_{man}. For the sake of accuracy and speed, it is stored in a map table. Unlike η_{vol}^{man}, $\eta_{vol}^{P_{amb},T_{man}}$ depends almost linearly on the pressure ratio $P_r = \frac{P_{man}}{P_{amb}}$ and errors associated with linear interpolation between the points of the grid are minimized - this is the justification for using the latter of the two.

- The isentropic converging nozzle/sudden enlargement model, which is normally used to describe the throttle air mass flow, is too inaccurate for actual use. Because the flow splits along two paths across the plate (one large dominant flow, and one small residual flow), a more accurate two-channel model is proposed in [20]. This model is made up of two isentropic converging nozzle/sudden enlargement models in parallel. In the dominant channel, the pressure loss at the throat amounts to the total pressure loss across the throttle ($Pup - Pman$), whereas, in the residual channel, the pressure loss only amounts to a part, δ ($\delta \in [0,1]$) of the total pressure loss ($\delta\,(Pup - Pman)$). Finally, the contribution of the residual flow is ν times that of the dominant flow. The model is summarized below:

$$\dot{m}_{at}(\alpha, P_{man}, P_{up}, T_{amb}) = \frac{P_{up}}{\sqrt{T_{amb}}}\beta_1(\alpha)\left(\frac{1}{\nu+1}\beta_2(P_r) + \frac{\nu}{\nu+1}\beta_2\big(1-\delta\,(1-P_r)\big)\right) \quad (3)$$

where

$$P_r = \frac{P_{man}}{P_{up}}$$
$$\beta_2(x) = \frac{\sqrt{\max(x,P_{rc})^{\frac{1}{\gamma}} - \max(x,P_{rc})^{\frac{\gamma+1}{\gamma}}}}{\sqrt{P_{rc}^{\frac{1}{\gamma}} - P_{rc}^{\frac{\gamma+1}{\gamma}}}} \quad (4)$$
$$P_{rc} = \left(\frac{2}{\gamma+1}\right)^{\frac{\gamma}{\gamma-1}} \approx 0.5283$$

and

$$\beta_1(\alpha) = b_{10} + b_{11}\cos(\alpha) + b_{12}\cos^2(\alpha) + b_{13}\cos^3(\alpha) \quad (5)$$

P_r is the pressure ratio across the throttle plate. P_{rc} is the pressure ratio threshold below which the flow is sonic at a throat. β_2 and β_1 are functions which account for compressibility and effective throat area changes. δ, ν and $b_{10}\ldots b_{13}$ are fitting constants.

For pressure ratios above 0.9, the flow becomes extremely sensitive to pressure ratio variations:

$$\lim_{P_r \to 1}\frac{\partial \dot{m}_{at}}{\partial P_r} = -\infty \quad (6)$$

and it is therefore important to know accurately not only the pressure downstream the throttle, P_{man}, but also the pressure upstream, P_{up}. Usually, no pressure sensors are available upstream the throttle plate and this pressure is assumed to be equal to the barometric pressure, P_{amb}. However, because of the presence of an air filter, neglecting the air filter pressure loss can lead to very large throttle air mass flow modeling errors close to wide open throttle (*WOT*). It is therefore necessary to compensate for this pressure loss and the following model is proposed:

$$P_{up} = P_{amb} - K_{filt}\,\dot{m}_{at}^{\chi_1}\left(\frac{T_{amb}}{P_{amb}}\right)^{\chi_2} \tag{7}$$

where K_{filt}, χ_1 and χ_2 are fitting constants (in the present work, the air filter was replaced with a laminar flow meter and $\chi_1 = \chi_2 = 1$). Note that Equations (3) and (7) need to be solved simultaneously for $\dot{m}_{at}$ and P_{up} (implicit solution). An iterative solution is proposed in Appendix A.

This model was tested on a steady flow bench and was shown to describe the throttle air mass flow with an excellent accuracy (error $< 3\%$ of actual flow) over the entire operating region. On an engine where the flow is typically unsteady, the model describes the instantaneous flow with the same accuracy, since the throttle body is much smaller than the wave length of the pumping fluctuations. However, because of the strong nonlinearity of the flow for P_r close to 1 (see Equation (6)), the mean of the β_2 function applied to (instantaneous) P_r differs from the β_2 function applied to the mean of P_r (in short: $\overline{\beta_2}(P_r) \neq \beta_2(\overline{P_r})$) so that the model of Equation (3) is not very appropriate for Mean Value Engine Modeling (for P_r close to 1 only). This is illustrated in Figure 6 where errors up to 50% are unavoidable close to *WOT*.

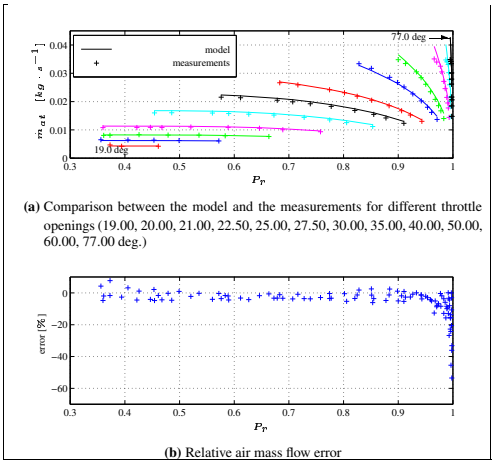

(a) Comparison between the model and the measurements for different throttle openings (19.00, 20.00, 21.00, 22.50, 25.00, 27.50, 30.00, 35.00, 40.00, 50.00, 60.00, 77.00 deg.)

(b) Relative air mass flow error

Figure 6: Two-channel throttle air mass flow model. Note the large error due to pumping fluctuations for pressure ratios close to 1.

- The isothermal assumption ($\dot{T}_{man} = 0$) which is normally used in the one-state manifold model[8] [21] leads to a somewhat inaccurate description of the intake air density during tip-ins and tip-outs. Mass conservation and energy conservation in the intake manifold should both be considered to properly describe the air dynamics. The difference between the isothermal model (single state) and the adiabatic model (two states) can be of up to 15% in port air mass flow, and it is therefore important that the right model is used in order to achieve tight *AFR* control.

  The following equations are for the two-state *MVEM*:

$$\begin{aligned}
\dot{P}_{man} = \;& P_{man}\,\frac{\gamma\, r\, T_{amb}}{V_{man}\, P_{man}} \\
& \left(\dot{m}_{at} - T_r\,\dot{m}_{ap} + \frac{\gamma - 1}{\gamma\, r}\,\frac{\dot{Q}_{ext}}{T_{amb}}\right) \\
\dot{T}_{man} = \;& T_{man}\,\frac{\gamma\, r\, T_{amb}}{V_{man}\, P_{man}} \\
& \left(\dot{m}_{at}\left(1 - \frac{1}{\gamma}T_r\right) - T_r\,\dot{m}_{ap}\left(1 - \frac{1}{\gamma}\right)\right. \\
& \left. + \frac{\gamma - 1}{\gamma\, r}\,\frac{\dot{Q}_{ext}}{T_{amb}}\right)
\end{aligned} \tag{8}$$

  where

$$\begin{aligned}
T_r &= \frac{T_{man}}{T_{amb}} \\
\dot{Q}_{ext} &= h\,(T_{amb} - T_{man})
\end{aligned} \tag{9}$$

  Heat transfer, $\dot{Q}_{ext}$, is also included in the model since it may play an important role during fast throttle openings and closings where compression/expansion effects result in large intake temperature spikes ([22], [20]). h is the heat transfer coefficient in $\left[\frac{J}{s\,K}\right]$. $\dot{m}_{at}$ and $\dot{m}_{ap}$ are given in Equations (3) and (2).

Note that in [20], it is also suggested that the pressure losses at the junctions between the intake plenum and the intake runners might not be negligible, and might therefore influence the time development of the pressure and the temperature in the runners. The solution which is proposed is to model the intake manifold as two control volumes (one for the plenum and one for the runners instead of one for the whole system) separated by an orifice. Each volume is described by two state equations (mass and energy conservation), one for pressure and one for temperature. Unfortunately, the orifice flow resistance varies significantly with the flow velocity; at low flows, the resistance is almost zero and the associated eigenfrequencies become infinite. The resulting stiffness of the 4-state model requires very small simulation steps which are impractical for real time applications and only one control volume (2-state model) will be used in this work. This simplification results in temperature differences in the order of 10 K during fast transients.

Finally, it should be clear that because the inertia of the vehicle/engine prevents the engine speed from changing on time

[8] A differential equation which describes the time development of the air pressure in the intake manifold of a naturally aspirated spark ignition (*SI*) engine.

scales smaller than a few seconds, and because the engine speed can be measured very accurately, N is treated in this work as a known, slowly varying parameter.

4 WIDE BANDWIDTH AIR/FUEL RATIO CONTROL

In Section 2, an attempt was made to make a list of all the limitations, physical and practical, which make wide bandwidth *AFR* control a challenging task. It should now be clear that there are not many methods available to overcome these limitations. The one proposed in this research is quite similar to the ones found in conventional transient strategies[9], except that the port air mass flow is predicted ahead in time instead of being simply estimated at the current instant. In this way, the limitation imposed by injection time delays can be removed. The structure of this model-based wide-bandwidth predictive controller is depicted in Figure 7. The derivation of this controller is discussed in details in the following sections.

4.1 Choice of Sensors

Because of the bandwidth limitations imposed by the transport delay associated with λ-feedback control and because of the large time constant of oxygen sensors, the new strategy is primarily based on intake manifold measurements. Among all the sensors which can be mounted on an intake manifold, a *MAP* sensor (time constant $<$ 1 ms) was preferred to the popular *MAF* sensor which is too slow, too inaccurate, too nonlinear and more costly. Also mounted on the intake manifold are a throttle position sensor and a fast 0.4 mm Nickel/Chromium-Nickel/Aluminium type K thermocouple with a time constant of 200 ms. The engine is also instrumented with an engine speed (and position) sensor and barometric pressure and temperature sensors. Finally, a *UEGO* sensor is mounted in the exhaust pipe to guarantee some robustness of the controller (this is explained later). The engine setup is illustrated in Figure 8.

4.2 Choice of Actuators

Because it is impossible to predict what the driver intends to do with the accelerator pedal, the bandwidth limitations imposed by the injection delay associated with conventional *AFR* controllers is a critical issue. One solution to this problem was suggested more than 20 years ago by *Stivender* [23] where the idea of controlling not only the fuel path but also the air path was first introduced as an alternative solution to *AFR* management control. The solution followed in this work complements the conventional fuel injectors with an electrically controlled throttle actuator (also known as drive by wire (*DBW*)). In this way, the injection delay can be compensated for.

[9]Fuel flow is treated as a dependant variable; intake air flow is first measured or estimated, then fuel injectors are operated to meter the proper amount of fuel into the engine.

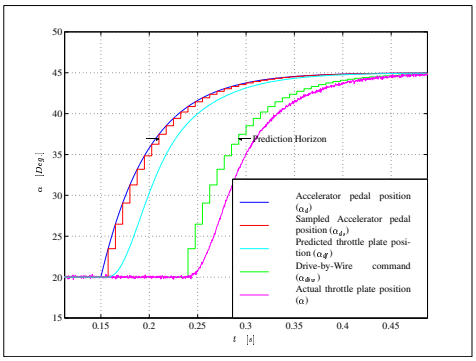

Figure 9: Delaying the driver's throttle command. The driver's command α_d is sampled, held and delayed (stored in a buffer) in the *ECU* (α_{d_s}). After a time equivalent to the prediction horizon, this sampled signal is sent to the *DBW* actuator (α_{dbw}). Note that, because of the time response of the *DBW*, the actual throttle plate position α differs from α_{dbw}. In particular, the resulting time lag can be large enough so that the *DBW* dynamics cannot be ignored in the prediction algorithm. With a good model of the *DBW* dynamics, the throttle position can be predicted accurately (α_{df}). As explained later, the prediction horizon is set to 495 crank degrees (0.0825 sec. at 1000 RPM and 0.0165 sec. at 5000 RPM). This delay introduced between the driver's pedal command and the throttle plate is short enough to be imperceptive to the driver, although this is still to be evaluated in a vehicle under real driving conditions.

By buffering the sampled driver command into the memory of the *ECU*, the throttle motion can be delayed for a time equal to the injection delay, see Figure 9. Consequently, the throttle position is known sufficiently in advance so that the controller can safely predict the amount of air to be sucked in during the next induction event. For this reason, the injection delay will also be referred to as the prediction horizon in the remainder of this paper.

However, because the *DBW* actuator is not infinitely fast, the commanded throttle position and the actual throttle position can differ greatly. For example, the *DBW* used in this work behaves as a well damped second order system with an undamped natural frequency, ω_{dbw}, of 76.9 rad/s and a damping factor, ζ_{dbw}, of 0.675. As can be seen in Figure 9, the resulting time lag is too large to be ignored during transients. In order to predict accurately enough the actual throttle position, the dynamics of the actuator must thus be taken into account in the predictor as well. To this end, a second-order low-pass filter is used to model the *DBW* dynamics:

$$\frac{\alpha(s)}{\alpha_{dbw}(s)} = \frac{\omega_{dbw}^2}{s^2 + 2\zeta_{dbw}\omega_{dbw}s + \omega_{dbw}^2} \tag{10}$$

where s is the Laplace operator. α_{dbw} is the command signal to the *DBW* actuator and α is the actual throttle position (see Figure 9). Because the controller is implemented in discrete

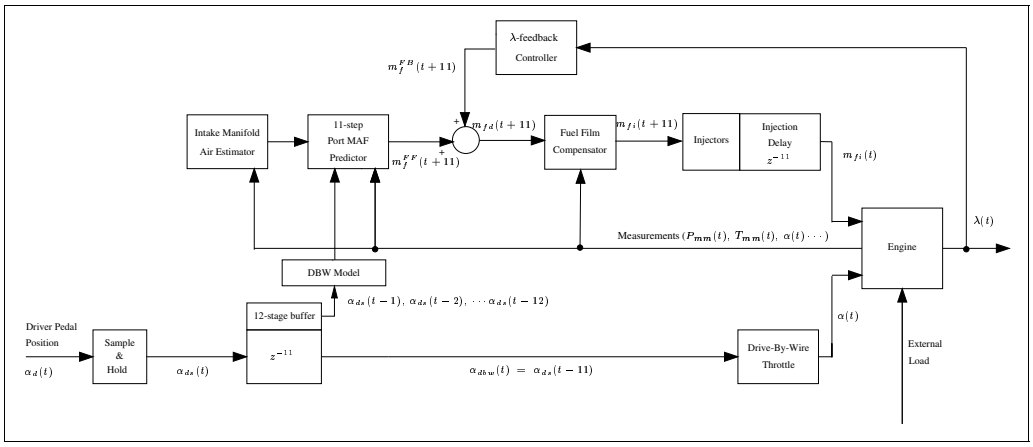

Figure 7: The model-based wide-bandwidth predictive controller structure

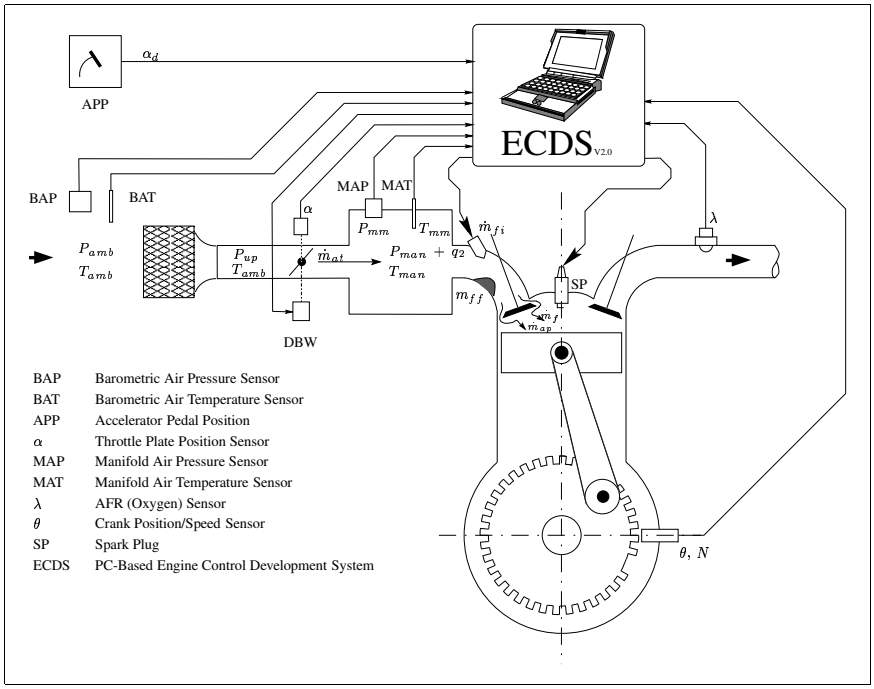

Figure 8: Engine description

time (explained later), the *DBW* model is discretized as follows

$$\alpha(t+1) = -dbw_{d1}\,\alpha(t) - dbw_{d2}\,\alpha(t-1) + dbw_{n1}\,\alpha_{dbw}(t) + dbw_{n2}\,\alpha_{dbw}(t-1) \quad (11)$$

where

$$\begin{aligned} dbw_{d1} &= -2\,dbw_c \\ dbw_{d2} &= dbw_e^2 \\ dbw_{n1} &= 1 - dbw_c - dbw_s \\ dbw_{n2} &= dbw_{d2} - dbw_c + dbw_s \end{aligned} \quad (12)$$

and where

$$\begin{aligned} dbw_e &= \exp(-aT_s) \\ dbw_c &= dbw_e\,\cos(\omega_0 T_s) \\ dbw_s &= dbw_e\,\frac{a}{\omega_0}\,\sin(\omega_0 T_s) \\ \omega_0 &= \omega_{dbw}\sqrt{1-\zeta_{dbw}^2} \\ a &= \zeta_{dbw}\omega_{dbw} \end{aligned} \quad (13)$$

and T_s is the sampling period (explained later) and t is the normalized discrete time.

4.3 Choice of Operating Domain

One of the requirements of a delayed-throttle strategy is that the prediction horizon must be deterministic. With time-based strategies, the injection delay is randomly varying and cannot satisfy the above requirement. A crank-based strategy is therefore adopted. From a practical point of view, the fact that the prediction horizon is fixed in the crank domain makes the implementation of the strategy much easier; for instance, the size of the buffer for the *DBW* delaying mechanism is fixed. In the same way, the number of states required by the predictor is also fixed.

4.4 Choice of Sampling Period

The choice of the sampling period is dictated by four criteria:

- 720 deg should be an integer multiple of the sampling period (in crank degrees). This is to keep the phasing of the strategy fixed with respect to the position of the crankshaft.
- It has been seen that the rise time of the throttle plate can be as small as 50 ms. In [24], *Åström* and *Wittenmark* suggest that the sampling interval be chosen 4 to 10 times smaller than the rise time, that is 5 - 12.5 ms. At 1000 RPM (worst case), this corresponds to 30 - 75 crank degrees.
- In order to avoid aliasing of the pressure signal, the sampling frequency should be at least twice the maximum frequency of the measured signal. It has been seen in Section 2.1 that the pressure signal contains significant energy only in the fundamental (the event frequency) and in the first harmonic (twice the event frequency). The sampling frequency should therefore be at least four times the event frequency, which corresponds to a sampling interval of maximum 45 crank degrees.
- The smaller the sampling period, the higher the number of steps required by the predictor and hence the higher the computational burden.

As a consequence of the above criteria, the sampling period, θ_s is set at 45 crank degrees ($\frac{1}{16}$ of a cycle). In the time domain, the sampling period, T_s, varies with the engine speed.

$$T_s = \frac{\theta_s}{6\,N(t)} \quad \text{where} \quad \theta_s = 45\,cdeg \quad (14)$$

4.5 Choice of Prediction Horizon

The prediction horizon should be an integer multiple of the sampling period so that the predictor can contain a whole number of steps. In order to overlap the injection delay, it should be at least 45 crank degrees (computational duration) + 15 ms (injection duration, i.e. 450 crank degrees at 5000 RPM). Finally, it should be as short as possible to minimize the prediction error. The prediction horizon is therefore set to 495 crank degrees, that is, 11 sampling periods.

4.6 Port Air Mass Flow Prediction

Despite the *DBW*, the controller is still of the fuel management type, that is the fuel is treated as a dependant variable. No attempt is made to control the air path and the *DBW* is only used as a way to compensate for the injection delay. In order to meter the proper amount of fuel into the engine, port air mass flow must be predicted 11 steps ahead of the induction process. This is of course made possible thanks to the a priori knowledge available of the throttle position. Because a predictor is nothing more than an open-loop estimator (there are no measurement updates), a highly accurate dynamic model of the intake air path is required. The model should be compact enough so that it can be run efficiently on a microcontroller (in the present case, it should be able to run 11 times faster than real time, as explained in the next section), without sacrificing the required accuracy (1% error in port air mass flow prediction leads to 1% error in λ). Air path modeling is treated in detail in [20]. For the sake of completeness, the model used in this research is also described in Section 3.

One possible way to implement the predictor is to have a model running completely open-loop 11 steps ahead of the real engine. In that way, modeling errors can accumulate, and the predictor may slowly diverge. However, the computational burden for this type of predictor is very low since for each sampling event, the predictor is updated only one step ahead. Another approach is to have the predictor recompute the estimates/states over the entire prediction horizon at each and every sampling event. In this way, the states of the predictor can be re-initialized

every sampling event according to the latest available measurements (i.e. the latest available information is extrapolated into the future for the purpose of prediction). Clearly, this measurement update should minimize the prediction error. The drawback of this approach is that the calculation burden is greatly increased since, within each sampling event, the model's response needs to be computed over 11 time steps (in terms of the computer burden, one 11-step predictor is equivalent to 11 one-step-ahead predictors running in parallel!). For the sake of clarity, the modus operandi of the predictor is illustrated in Figure 10.

Because accuracy is the primary requirement of modern *AFR* controllers, the 11-step predictor with measurement update is used in this research. This also establishes a limit for the best possible performance.

If it is assumed that, at the current instant t, estimates of the mean of the intake pressure and temperature ($\hat{P}_{man}(t)$, $\hat{T}_{man}(t)$) are available (see next section), as well as measurements of $P_{amb}(t)$, $T_{amb}(t)$, $N(t)$, $\alpha(t-1)$, $\alpha(t)$, $[\alpha_{ds}(t-12)\cdots\alpha_{ds}(t-2)]$ (eventually buffered in the *ECU*), then the 11-step port air mass flow predictor can be derived as in Equations (15) and (16).

$$\begin{aligned}
\check{P}_{man}(t+1) &= \hat{P}_{man}(t) + \hat{\dot{P}}_{man}(t)\cdot T_s \\
\check{T}_{man}(t+1) &= \hat{T}_{man}(t) + \hat{\dot{T}}_{man}(t)\cdot T_s \\
\check{\alpha}(t+1) &= -dbw_{d1}\,\alpha(t) - dbw_{d2}\,\alpha(t-1) \\
&\quad + dbw_{n1}\,\alpha_{ds}(t-11) + dbw_{n2}\,\alpha_{ds}(t-12) \\
\check{P}_{man}(t+2) &= \check{P}_{man}(t+1) + \check{\dot{P}}_{man}(t+1)\cdot T_s \\
\check{T}_{man}(t+2) &= \check{T}_{man}(t) + \check{\dot{T}}_{man}(t+1)\cdot T_s \\
\check{\alpha}(t+2) &= -dbw_{d1}\,\check{\alpha}(t+1) - dbw_{d2}\,\alpha(t) \\
&\quad + dbw_{n1}\,\alpha_{ds}(t-10) + dbw_{n2}\,\alpha_{ds}(t-11) \qquad (15) \\
&\vdots \\
\check{\alpha}(t+10) &= -dbw_{d1}\,\check{\alpha}(t+9) - dbw_{d2}\,\alpha(t+8) \\
&\quad + dbw_{n1}\,\alpha_{ds}(t-2) + dbw_{n2}\,\alpha_{ds}(t-3) \\
\check{P}_{man}(t+11) &= \check{P}_{man}(t+10) + \check{\dot{P}}_{man}(t+10)\cdot T_s \\
\check{T}_{man}(t+11) &= \check{T}_{man}(t+10) + \check{\dot{T}}_{man}(t+10)\cdot T_s
\end{aligned}$$

The hats ($\hat{}$) denote estimated states and the inverted hats ($\check{}$) denote predicted states. The speed-density equation (Equation (2)) gives the predicted port air mass flow (11 steps ahead) as a function of the predicted intake manifold conditions.

$$\dot{m}_{ap}(t+11) = \dot{m}_{ap}(\check{P}_{man}(t+11)\,,\,\check{T}_{man}(t+11)\,,\, N(t)\,,\,P_{amb}(t)) \qquad (16)$$

The (desired) amount of fuel which should be injected at any given instant and enter the cylinders 11 steps later (m_f^{FF}, in unit mass per sampling period) is given in Equation (17).

$$m_f^{FF}(t+11) = \frac{120\,\check{\dot{m}}_{ap}(t+11)}{L_{th}\,16\,N(t)}\,\frac{1}{\lambda_{ref}} \qquad (17)$$

where the reference λ, λ_{ref} is in principle set to 1 for current *TWC*'s.

In Equation (15), the state derivatives are calculated according to Equations (2), (3), (7) and(8) in which the dependant variables are determined as follows:

$$\begin{aligned}
\hat{\dot{P}}_{man}(t) &= \dot{P}_{man}(\hat{P}_{man}(t),\,\hat{T}_{man}(t) \\
&\qquad T_{amb}(t),\,P_{amb}(t),\,N(t),\,\alpha(t)) \\
\hat{\dot{T}}_{man}(t) &= \dot{T}_{man}(\hat{P}_{man}(t),\,\hat{T}_{man}(t) \\
&\qquad T_{amb}(t),\,P_{amb}(t),\,N(t),\,\alpha(t)) \\
\check{\dot{P}}_{man}(t+1) &= \dot{P}_{man}(\check{P}_{man}(t+1),\,\check{T}_{man}(t+1) \\
&\qquad T_{amb}(t),\,P_{amb}(t),\,N(t),\,\check{\alpha}(t+1)) \\
\check{\dot{T}}_{man}(t+1) &= \dot{T}_{man}(\check{P}_{man}(t+1),\,\check{T}_{man}(t+1) \\
&\qquad T_{amb}(t),\,P_{amb}(t),\,N(t),\,\check{\alpha}(t+1)) \\
&\vdots \qquad (18) \\
\check{\dot{P}}_{man}(t+10) &= \dot{P}_{man}(\check{P}_{man}(t+10),\,\check{T}_{man}(t+10) \\
&\qquad T_{amb}(t),\,P_{amb}(t),\,N(t),\,\check{\alpha}(t+10)) \\
\check{\dot{T}}_{man}(t+10) &= \dot{T}_{man}(\check{P}_{man}(t+10),\,\check{T}_{man}(t+10) \\
&\qquad T_{amb}(t),\,P_{amb}(t),\,N(t),\,\check{\alpha}(t+10))
\end{aligned}$$

Note that $\alpha(t)$, $\alpha(t-1)$, $\hat{P}_{man}(t)$ and $\hat{T}_{man}(t)$ are used to initialize the predictor. For the pressure and temperature state equations, simple Euler integration is used. This is to keep the computer burden to an acceptable level (compared to the solution which consists in linearizing then discretizing - *on line* - the model, and which involves the computation of many matrix exponential functions). Given the relatively small size of the sampling period, no significant accuracy penalty could be observed for this (tested off-line).

The throttle position predictor is based on Equation (11) where $\alpha_{dbw}(t)$ has been replaced by $\alpha_{ds}(t-11)$ (buffered in the *ECU*).

$$\alpha_{dbw}(t) = \alpha_{ds}(t-11) \qquad (19)$$

4.7 Intake Air Observer

As mentioned previously, the states of the predictor (T_{man}, P_{man}) need to be re-initialized for every sampling event (measurement update). However, because not all the states of the predictor can be measured directly (mean intake manifold pressure) or with the required bandwidth (intake manifold temperature) and because the measurements are corrupted with large noise contributions (mainly pumping noise), an intake air observer is required to estimate/filter the variables of interest. Because of the nonlinear nature of the intake air dynamics, an extended Kalman filter (*EKF*) [25] is used in this research. It uses

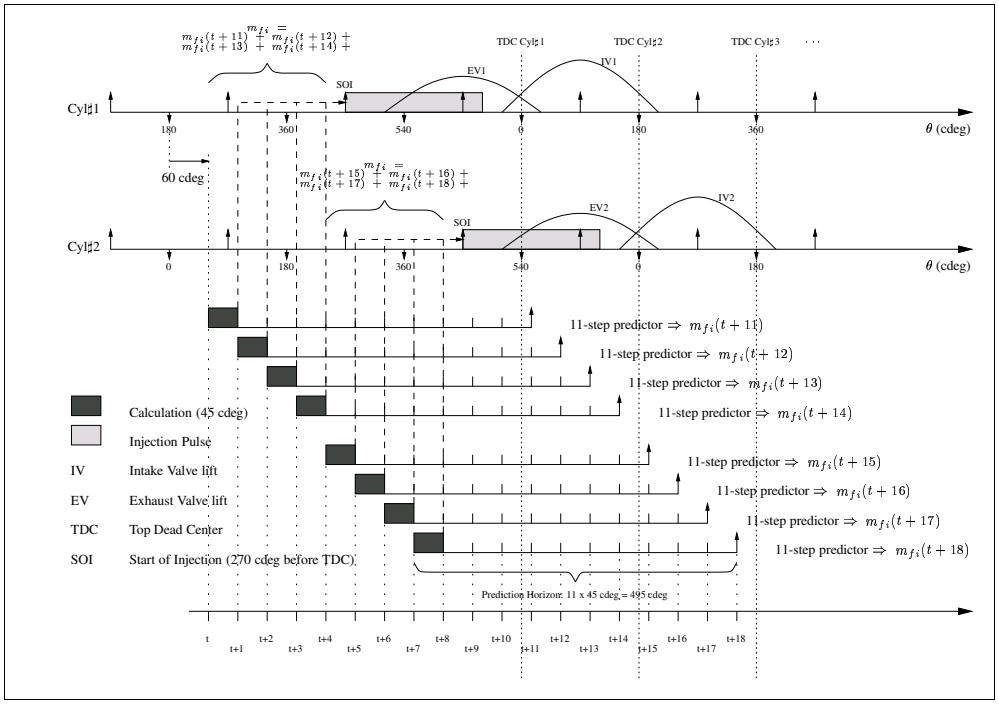

Figure 10: Modus operandi of the 11-step model-based predictor with measurement update. Note how the quantity of fuel to be injected, m_{fi}, is updated on the basis of the last 4 outputs ($\Leftrightarrow$ 1 stroke) of the predictor/controller.

the measured intake pressure and temperature as the innovation terms.

The challenges of using *EKF*'s for engine applications are:

1. the presence of deterministic pumping fluctuations (which in no way can be considered as stochastic white noise) normally prevents the use of the Kalman-Bucy's method [26] to calculate the observer gains (Riccati equations can only be used to determine how Gaussian white noise propagates through the model).
2. finding the intensity of the process noise. The intensity of this noise determines the uncertainty in the different parts of the model. It is the comparison between the model uncertainties and the confidence level of the measurements (measurement noise intensities) which determines the size of the observer gains, and it is therefore important to use appropriate noise intensities.

The design procedure for the observer can be split in four phases: modeling, a priori selection or calculation of noise intensities, determination of the gains and finally implementation of the observer. These four phases are discussed below (although in a different order).

Modeling The model behind the observer is given in the continuous domain in Equation (20).

$$\dot{P}_{man} = P_{man}\frac{\gamma\, r\, T_{amb}}{V_{man}\, P_{man}}\Big(\dot{m}_{at} + \delta_{mat} - T_r\,\dot{m}_{ap} + \frac{\gamma-1}{\gamma\, r}\frac{\dot{Q}_{ext}}{T_{amb}}\Big) + \mathcal{V}_{P_{man}} \tag{20a}$$

$$\dot{T}_{man} = T_{man}\frac{\gamma\, r\, T_{amb}}{V_{man}\, P_{man}}\Big(\big(\dot{m}_{at} + \delta_{mat}\big)\big(1 - \frac{1}{\gamma}T_r\big) - T_r\,\dot{m}_{ap}\big(1 - \frac{1}{\gamma}\big) + \frac{\gamma-1}{\gamma\, r}\frac{\dot{Q}_{ext}}{T_{amb}}\Big) + \mathcal{V}_{T_{man}} \tag{20b}$$

$$\dot{T}_{ms} = -\frac{1}{\tau_t}\big(T_{ms} - T_{man}\big) + \mathcal{V}_{T_{ms}} \tag{20c}$$

$$\dot{\delta}_{mat} = -\frac{1}{\tau_\delta}\delta_{mat} + \mathcal{V}_{\delta_{mat}} \tag{20d}$$

$$\dot{q}_1 = -2\,\zeta_q\,\omega_e\,q_1 - \omega_e^2\,q_2 + \mathcal{V}_{q_1} \tag{20e}$$

$$\dot{q}_2 = q_1 \tag{20f}$$

and

$$P_{mm} = P_{man} + q_2 + \mathcal{V}_{P_{mm}} \tag{20g}$$

$$T_{mm} = T_{ms} + \mathcal{V}_{T_{mm}} \tag{20h}$$

where P_{mm} and T_{mm} are the measured intake manifold pressure and temperature respectively. $\mathcal{V}_{P_{man}}$, $\mathcal{V}_{T_{man}}$, $\mathcal{V}_{T_{ms}}$, $\mathcal{V}_{\delta_{mat}}$

and $\mathcal{V}_{q_1}$ are the state excitation (or process) noises; $\mathcal{V}_{P_{mm}}$ and $\mathcal{V}_{T_{mm}}$ are measurement noises. All noise sources are assumed white. The signification of the new states T_{ms}, δ_{mat}, q_1, q_2 are explained below.

As can be seen, this model is based on the model developed for the predictor (see Equations (2), (3), (7) and(8) for details), augmented with selected important sub-models:

- A model of the temperature sensor (state T_{ms}).

  As explained before,the temperature sensor has a time constant, τ_{Temp} around 200 ms which is too large compared to the 50 ms which is required to open the throttle. A first order low-pass filter is used to model the temperature sensor dynamics.

- A low-pass filter (acting almost as an integrator) to compensate for the inaccuracy of the throttle air mass flow model close to *WOT* (state δ_{mat}).

  In the manifold temperature and pressure state equations, the throttle air mass flow, $\dot{m}_{at}$, is offset by δ_{mat}, a slowly varying constant (the output of a low-pass filter driven by white noise) which represents the error between the actual throttle air mass flow and the modeled throttle air mass flow (Equation (3)). The purpose of this correction term is to compensate for steady-state errors rather than transient errors. The time constant of the low-pass filter is therefore selected small enough so that the size of the estimated error, $\hat{\delta}_{mat}$, can change rapidly enough from one steady-state operating point to another, but large enough so that it does not follow the measurement noise. τ_δ is set to 300 ms.

- A model of the pumping fluctuations ("deterministic noise") (states q_1 and q_2, output q_2).

  Because the pumping fluctuations are deterministic, the measurement noise entering the model is suppressed and effectively whitened with the help of a model of the pumping fluctuations. In this way, a more rigorous derivation of the Kalman gains is possible (compared to a derivation where the unmodeled pumping fluctuations enter the observer as unrealistic Gaussian white noise). As shown in Section 2.1, the amplitude of the deterministic pumping fluctuations decays rapidly with increasing frequency. Most of the noise energy is found at the fundamental frequency whereas the first harmonic contains only a small part of the total energy. An empirical model (the physics behind the pumping noise is much too complex [20] to be included directly) of the fundamental component of the pumping fluctuations is therefore included in the observer. It is a tuned filter (a poorly damped - oscillatory - second order filter) with its undamped natural frequency tuned to the event frequency ω_e:

$$\omega_e = \frac{2\pi N}{30} \tag{21}$$

  In order to pick up only the fundamental component of the pumping fluctuations, the resonant spike of the filter should be extremely narrow (very low damping factor) as illustrated in Figure 11. However, in order for the reconstructed pulsations to be able to change rapidly enough from one amplitude to another, the damping ratio should not be too small (with a damping ratio of 0, the amplitude of the reconstructed pumping pulsations would grow infinitely). A "large" damping ratio is also required for the phase of the reconstructed pulsations to be able to lock itself to the phase of the real pulsations. After some testing, a damping ratio, ζ_q, of 0.01 was adopted here.

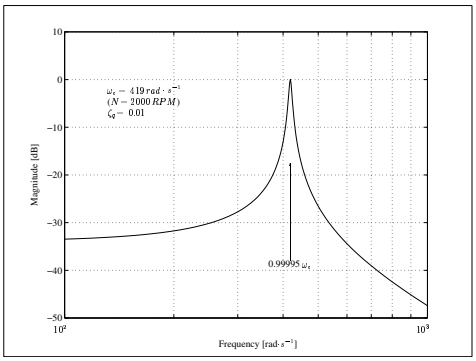

Figure 11: The frequency response of the pumping fluctuations model. Note that the frequencies away from the engine event frequency will be attenuated. For the sake of clarity, the magnitude has been amplified by a factor of $2\,\zeta_q\,\omega_e^2$ compared to the actual filter of Equations (20d) and (20f)

.

Implementation In order to derive the discrete *EKF*, the model of Equation (20) must be discretized. As for the predictor, Euler integration is used for the first two nonlinear state equations. The four remaining linear state equations are discretized using conventional techniques. This leads to the estimator of Equation (22) below.

Time Update

$$\tilde{P}_{man}(t) = \hat{P}_{man}(t-1) + \hat{\dot{P}}_{man}(t-1)\cdot T_s \tag{22a}$$
$$\tilde{T}_{man}(t) = \hat{T}_{man}(t-1) + \hat{\dot{T}}_{man}(t-1)\cdot T_s \tag{22b}$$
$$\tilde{T}_{ms}(t) = A_t\,\hat{T}_{ms}(t-1) + (1-A_t)\,\hat{T}_{man}(t-1) \tag{22c}$$
$$\tilde{\delta}_{mat}(t) = A_\delta\,\hat{\delta}_{mat}(t-1) \tag{22d}$$
$$\tilde{q}_1(t) = A_q\big[-\zeta_q\,\hat{q}_1(t-1) - \omega_e\,\hat{q}_2(t-1)\big] \tag{22e}$$
$$\tilde{q}_2(t) = A_q\big[\frac{1}{\omega_e}\,\hat{q}_1(t-1) + \zeta_q\,\hat{q}_2(t-1)\big] \tag{22f}$$

where

$$\begin{aligned} A_t &= \exp\big(\frac{-T_s}{\tau_t}\big) \\ A_\delta &= \exp\big(\frac{-T_s}{\tau_\delta}\big) \\ A_q &= \exp\big(\frac{-\pi\xi}{2}\big) \end{aligned} \tag{23}$$

and where the tildes (˜) denote one-step ahead predictions of the states. In Equations (22a) and (22b), $\hat{\dot{P}}_{man}(t-1)$ and

$\hat{\tilde{T}}_{man}(t-1)$ are calculated as in Equations (20a) and (20b) (but now as functions of the previous estimates). The compact Equations (22e) and (22f) are obtained using the approximation $\sqrt{1-\zeta_q^2} = \sqrt{1-0.01^2} = 0.99995 \approx 1$.

The measurement update now becomes:

$$\begin{aligned}
\hat{P}_{man}(t) &= \tilde{P}_{man}(t) + k_{11}\,\Delta P_{mm} + k_{12}\,\Delta T_{mm} \\
\hat{T}_{man}(t) &= \tilde{T}_{man}(t) + k_{21}\,\Delta P_{mm} + k_{22}\,\Delta T_{mm} \\
\hat{T}_{ms}(t) &= \tilde{T}_{ms}(t) + k_{31}\,\Delta P_{mm} + k_{32}\,\Delta T_{mm} \\
\hat{\delta}_{mat}(t) &= \tilde{\delta}_{mat}(t) + k_{41}\,\Delta P_{mm} + k_{42}\,\Delta T_{mm} \\
\hat{q}_1(t) &= \tilde{q}_1(t) + k_{51}\,\Delta P_{mm} + k_{52}\,\Delta T_{mm} \\
\hat{q}_2(t) &= \tilde{q}_2(t) + k_{61}\,\Delta P_{mm} + k_{62}\,\Delta T_{mm}
\end{aligned} \tag{24}$$

where ΔP_{mm} and ΔT_{mm} are the two innovation terms:

$$\Delta P_{mm} = P_{mm}(t) - [\tilde{P}_{man}(t) + \tilde{q}_2(t)] \tag{25}$$

$$\Delta T_{mm} = T_{mm}(t) - \tilde{T}_{ms}(t) \tag{26}$$

and where

$$K = K\big(\tilde{P}_{man}(t),\, N(t)\big) = \begin{pmatrix} k_{11} & k_{12} \\ k_{21} & k_{22} \\ k_{31} & k_{32} \\ k_{41} & k_{42} \\ k_{51} & k_{52} \\ k_{61} & k_{62} \end{pmatrix} \tag{27}$$

is the gain matrix of the observer. Each element is stored in the *ECU* in table form (as a function of N and P_{man}).

Kalman gains For the sake of clarity, the continuous, nonlinear, state space model of Equation (20) is rewritten in the more general form of Equation (28).

$$\begin{aligned}
\dot{X} &= F(X,U) + W \\
Y &= G(X) + V
\end{aligned} \tag{28}$$

where $X = [P_{man}\, T_{man}\, T_{ms}\, \delta_{mat}\, q_1\, q_2]^T$ is the state vector, $U = \alpha$ is the input variable, $Y = [P_{mm}, T_{mm}]^T$ is the output vector, F is a nonlinear vector function (derived from the state equations), G is a linear vector function, $W = [\mathcal{V}_{P_{man}}\, \mathcal{V}_{T_{man}}\, \mathcal{V}_{T_{ms}}\, \mathcal{V}_{\delta_{mat}}\, \mathcal{V}_{q_1}]^T$ and $V = [\mathcal{V}_{P_{mm}}\, \mathcal{V}_{T_{mm}}]^T$ are the vector state excitation noise and measurement noise respectively, with matrix intensities I_w and I_v. It is assumed that W and V are uncorrelated white noise processes. I_w and I_v are usually dependant on the engine operating conditions. In the remainder of this paragraph, it is assumed that I_w is a known function of N and P_{man} (as will be explained in next paragraph).

The Kalman gains (see Equation (27)) are calculated off-line for different stationary engine conditions (X_0, U_0) and then stored in table form in the *ECU* as a function of N and P_{man}. The procedure to calculate the gain is outlined below. The model of Equation (28) is first linearized about X_0 and U_0 and then discretized.

$$\begin{aligned}
X_{t+1} &= A_d X_t + B_d U_t + W_d(t) \\
Y_t &= C_d X_t + V_d(t)
\end{aligned} \tag{29}$$

where

$$\begin{aligned}
A_d &= e^{T_s \cdot \frac{\partial F(X,U)}{\partial X}\Big|_{\substack{X=X_0 \\ U=U_0}}} \\
B_d &= \Big(\int_0^{T_s} e^{\tau \cdot \frac{\partial F(X,U)}{\partial X}\Big|_{\substack{X=X_0 \\ U=U_0}}} d\tau\Big) \cdot \frac{\partial F(X,U)}{\partial U}\Big|_{\substack{X=X_0 \\ U=U_0}} \\
C_d &= \frac{\partial G(X)}{\partial X}\Big|_{X=X_0}
\end{aligned} \tag{30}$$

and where $W_d(t)$ and $V_d(t)$, $t = 0, 1, 2, \cdots$, are two uncorrelated sequences of mutually uncorrelated zero-mean, vector-valued stochastic variables with variance matrices Q_w and Q_v.

Note that the system of Equation (29) was found to be observable (the observability matrix formed from A_d and C_d has full rank) over the entire operating range. This would not be the case if, for instance, the temperature measurement was not available.

The measurement noise variance, Q_v, is a (2x2) matrix with the off-diagonal elements set to zero. The first diagonal element is set to the variance of the measured intake pressure signal when the engine is not running plus the variance of the (residual) first harmonic of the pumping fluctuations (measured for different engine operating conditions using a Fast Fourier Transform (*FFT*) technique). The fundamental component of the pumping fluctuation does not contribute to the measurement noise since it is now a state of the observer. The second diagonal element is set to the variance of the measured intake temperature signal (again, measured for different engine operating conditions). Quite clearly, Q_v is operating point dependant.

The process noise variance, Q_w is deduced from I_w [27]

$$Q_w = \int_0^{T_s} e^{\tau \cdot \frac{\partial F(X,U)}{\partial X}\Big|_{\substack{X=X_0 \\ U=U_0}}} I_w e^{\tau \cdot \left(\frac{\partial F(X,U)}{\partial X}\Big|_{\substack{X=X_0 \\ U=U_0}}\right)^T} d\tau \tag{31}$$

For each operating point, the stationary Kalman gain matrix is given by

$$K = Q_d C_d^T [C_d Q_d C_d^T + Q_v]^{-1} \tag{32}$$

where Q_d is the covariance matrix of the predictive (one step ahead) estimation error and is the solution of the Riccati Equation:

$$\begin{aligned}
&A_d Q_d A_d^T - Q_d - \\
&\quad A_d Q_d C_d^T [C_d Q_d C_d^T + Q_v]^{-1} C_d Q_d A_d^T + Q_w = 0
\end{aligned} \tag{33}$$

where I is the identity matrix. As mentioned previously, the elements of K are stored in the *ECU* in table form as a function of N and P_{man} (the mapping grid variables).

Process noise intensity In order to calculate the gain matrix, it has been seen that the process noise intensity matrix, I_w is

required. Usually, finding this intensity is a difficult task. However, the performance of the observer depends directly on the choice of I_w, and it is therefore important to choose it appropriately (it indicates the accuracy of the model compared to the measurements). In this work, the intensity is assessed on the basis of steady-state considerations only. First of all, I_w is assumed to have the following structure

$$I_w = \begin{pmatrix} I_{P_{man}} & I_{12} & 0 & 0 & 0 & 0 \\ I_{12} & I_{T_{man}} & 0 & 0 & 0 & 0 \\ 0 & 0 & 0 & 0 & 0 & 0 \\ 0 & 0 & 0 & I_{\delta_{mat}} & 0 & 0 \\ 0 & 0 & 0 & 0 & I_{q_1} & 0 \\ 0 & 0 & 0 & 0 & 0 & 0 \end{pmatrix} \tag{34}$$

The model can be decomposed in 4 parts: the intake plenum model (2 states, P_{man} and T_{man}), the temperature sensor model (1 state, T_{ms}), the flow error model (1 state, δ_{mat}) and the pumping fluctuations model (2 states, q_1 and q_2). Because the phenomena behind each part are physically independent, it makes sense to assume that the process noise sources (of each part) are uncorrelated. The "off-diagonal" elements of I_w are therefore set to zero. However, the physical coupling between the elements (P_{man} and T_{man}) of the intake plenum model suggest that cross-coupling (I_{12}) between $\mathcal{V}_{P_{man}}$ and $\mathcal{V}_{T_{man}}$ is possible. The second order model of the pumping fluctuations only requires one process noise source with intensity I_{q_1} (see Equation (20)). Finally, the temperature sensor model is assumed to be ideal (compared to the intake plenum model) and the intensity of $\mathcal{V}_{T_{ms}}$ (3^{rd} diagonal element) is set to zero.

Not only should the modeled fundamental pumping fluctuations have the right frequency, but they should also have the right amplitude. The intensity I_{q_1} of $\mathcal{V}_{q_1}$ is therefore selected so that the power of the signal out of the tuned filter (Equations (20d) and (20f)) equals the power in the fundamental of the pumping fluctuations. This leads to

$$I_{q_1} = 2(A_{pf0}\,\zeta_q\,\omega_e^2)^2 \tag{35}$$

where A_{pf0} is the amplitude of the fundamental component of the pumping fluctuations, measured using *FFT* techniques.

In steady-state, the process noise intensities propagate through the model into the states according to the Lyapunov equation

$$A\,Q + Q\,A^T + I_W = 0 \tag{36}$$

where A

$$A = \left.\frac{\partial F(X,U)}{\partial X}\right|_{\substack{X=X_0 \\ U=U_0}} \tag{37}$$

is the Jacobian of F (see Equation (28)) and Q is the covariance matrix (symmetric) of the state vector X

$$Q = \begin{pmatrix} q_{P_{man}} & q_{12} & q_{13} & q_{14} & q_{15} & q_{16} \\ q_{12} & q_{T_{man}} & q_{23} & q_{24} & q_{25} & q_{26} \\ q_{13} & q_{23} & q_{T_{ms}} & q_{34} & q_{35} & q_{36} \\ q_{14} & q_{24} & q_{34} & q_{\delta_{mat}} & q_{45} & q_{46} \\ q_{15} & q_{25} & q_{35} & q_{45} & q_{55} & q_{56} \\ q_{16} & q_{26} & q_{36} & q_{46} & q_{56} & q_{66} \end{pmatrix} \tag{38}$$

If it is now assumed that $q_{P_{man}}$, $q_{T_{man}}$, $q_{T_{ms}}$ and $q_{\delta_{mat}}$ are known (see below), then it is possible to find the four remaining intensities by solving the Lyapunov Equation (36) (a linear system of 21 equations with 21 unknowns, the 4 intensities plus the 17 q_{ij}'s). The equation is solved for each operating point of the (N, P_{man}) mapping grid.

$q_{P_{man}}$ is set to the covariance of the measured intake pressure, minus the first diagonal element, $Q_v(1,1)$ of the measurement noise variance, minus the covariance of the fundamental part of the pumping fluctuations (measured using *FFT* techniques)

$$q_{P_{man}} = \mathrm{Cov}(P_{man}) - Q_v(1,1) - \frac{A_{pf0}^2}{2} \tag{39}$$

In other words, $q_{P_{man}}$ comes from the variance of the manifold pressure (including sensor noise and pumping fluctuations), minus the variance of the pressure measurement noise, minus the variance of the pumping fluctuations (which instead contributes to the intensity of $\mathcal{V}_{q_1}$, see Equation (35)).

$q_{T_{man}}$ and $q_{T_{ms}}$ are set equal to the second diagonal element, $Q_v(2,2)$ of the measurement noise variance

$$q_{T_{man}} = Q_{T_{ms}} = Q_v(2,2) \tag{40}$$

In other words, it is assumed that the uncertainty in the temperature (a-priori) estimates and the uncertainty in the temperature measurements are of the same order of magnitude. In this way, the temperature related gains are forced to be tuned so that model and measurements contribute equally to the final temperature estimates (this is the best solution given that no exact statistical information about the process and the measurement noises is available).

It is assumed that δ_{mat} is a zero-mean gaussian stochastic process, with 99% probability that any value is less than the steady-state error between the throttle *MAF* model and the port *MAF* model then

$$q_{\delta_{mat}} = \left(\frac{\dot{m}_{ap} - \dot{m}_{at}}{2.5758}\right)^2 \tag{41}$$

where $\dot{m}_{ap}$ and $\dot{m}_{at}$ are given in Equations (2) and (3) respectively. This is of course a crude approximation since δ_{mat} is a deterministic, not a stochastic process. The fact that the steady-state solution of Equations (20a) and (20b) (without the process noise) leads to $\delta_{mat} = \dot{m}_{ap} - \dot{m}_{at}$ may help the reader understanding Equation (41).

The result of the Kalman gain calculation procedure is illustrated in Figure 12 where the gains are shown as a function of P_{man} or N (depending on which has the greatest influence on the corresponding gain). For the ease of comparison, the gains in Figure 12 are non-dimensional (the dimensional scaling factors are 10^5 Pa for pressures, 400 K for temperatures and 10^{-3} kg$\cdot s^{-1}$ for mass flows)[10].

4.8 Fuel-Film Compensator

In an *MPI* system, some of the fuel which is injected at the intake port does not enter the cylinders immediately and is de-

[10] Actually the entire derivation and implementation of the observer/controller was conducted non-dimensional, since this is recommended for numerical reasons.

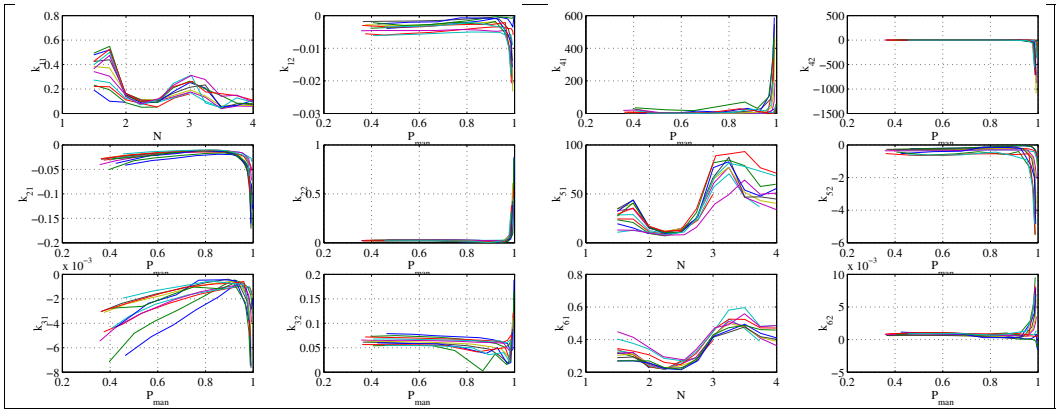

Figure 12: Kalman gains (non-dimensional) as a function of P_{man} and N. Note that if P_{man} is used as the abscissa, each line of the plot correspond to a constant N (and viceversa). The gains have been scaled so that they can be compared within a pair (i.e. k_{i1} and k_{i2} for $i = 1 \cdots 6$ can be compared). As could be expected, the estimates of P_{man}, q_2 and q_1 depend more on the pressure measurement, P_{mm}, than on the temperature measurement, T_{mm}. On the other hand, the estimate of T_{ms}, depends more on the temperature measurement, T_{mm}, than on the pressure measurement, P_{mm}. It is also interesting to see how some of the gains become large for P_{man} close to 1. This is partially due to Equation (6) and partially due to the inaccuracy of the throttle plate model in this region (see Figure 6).

posited instead in liquid form on the manifold wall. In *AFR* control, this is known as the fuel-film problem, and leads to large λ excursion if it is not properly compensated for. In this research, a technique known as *Nonlinear Fuel-Film Compensation* ([28],[29]) is used to address this fueling dynamics problem.

The compensator used here is based on a model due to Aquino [1], which is widely accepted in the literature. The input to the model is the (mean) injected fuel mass flow, $\dot{m}_{fi}$, and the output is the (mean) fuel mass flow at the intake port, $\dot{m}_f$. A fraction, X_f, of the injected fuel creates a fuel puddle (or film) in the intake port, the remaining fraction, $1-X_f$, stays suspended in the air stream as fuel vapor, $\dot{m}_{fv}$. Simultaneously, the fuel puddle evaporates at a rate which is proportional to puddle mass, m_{ff}. The factor τ_f has the dimension of time and is often referred to as the fuel puddle (film) evaporation time constant. The evaporated fuel then combines with the fuel vapor flow to give the total fuel flow which actually enters the cylinders, $\dot{m}_f$. Note that this model satisfies mass conservation and therefore makes no contribution during steady-state operation. In equation form the Aquino model is:

$$\begin{aligned} \dot{m}_{ff}(t) &= -\frac{1}{\tau_f} m_{ff}(t) + X_f\, \dot{m}_{fi}(t) \\ \dot{m}_{fv}(t) &= (1 - X_f)\, \dot{m}_{fi}(t) \\ \dot{m}_f(t) &= \dot{m}_{fv}(t) + \frac{1}{\tau_f} m_{ff}(t) \end{aligned} \tag{42}$$

X_f is of the order of 0.1 - 0.5 and τ_f of the order of 0.25 - 0.75 sec, depending on engine operating conditions.

This model can easily be discretized assuming linearity:

$$\begin{aligned} m_{ff}(t+1) &= \big(1 - \kappa_f(t)\big)\, m_{ff}(t) \\ &\quad + \big(1 - \mu_f(t)\big)\, m_{fi}(t) \\ m_f(t) &= \kappa_f(t)\, m_{ff}(t) + \mu_f(t)\, m_{fi}(t) \end{aligned} \tag{43}$$

where

$$\begin{aligned} \kappa_f(t) &= 1 - \exp\Big(\frac{-T_s(t)}{\tau_f}\Big) \\ \mu_f(t) &= 1 - X_f \frac{\tau_f}{T_s(t)} \kappa_f \end{aligned} \tag{44}$$

where T_s is the sampling time given in Equation(14). It is important to note that m_{fi} and m_f are the quantity of fuel injected in the manifold and the quantity of fuel inducted in a cylinder *during one sampling period* (45 cdeg) respectively. An identification technique such as Maximum Likelihood Estimation [30] is used to identify the fueling parameters κ_f and μ_f.

By inverting the fueling dynamics model of Equation (43), a nonlinear discrete feed-forward compensator can be derived:

$$m_{fi}(t+11) = \frac{m_{fd}(t+11) - \kappa_f(t)\, \hat{m}_{ff}(t)}{\mu(t)} \tag{45a}$$

$$\begin{aligned} \hat{m}_{ff}(t+1) &= \big(1 - \kappa_f(t)\big)\, \hat{m}_{ff}(t) \\ &\quad + \big(1 - \mu_f(t)\big)\, m_{fi}(t+11) \end{aligned} \tag{45b}$$

where Equation (45b) is a simple open-loop estimator of the mass of fuel which is stored in the fuel film. $m_{fd}(t+11)$ is the quantity of fuel which should enter the cylinders 11 steps ahead in time, and $m_{fi}(t+11)$ the corresponding quantity of fuel which needs to be injected immediately (*during one sampling period*). Note that

$$m_{fd}(t+11) = m_f^{FF}(t+11) + m_f^{FB}(t+11) \tag{46}$$

where m_f^{FF} is the output of the feedforward controller (predictor, see Equation (17)) and m_f^{FB} is the output of the feedback controller (see the next section).

Placed between the air predictor and the injector, this compensator modifies the injected fuel quantity so as to compensate for the amount of fuel stored in and released by the fuel film. The fueling parameters κ_f and μ_f are stored in table form in the *ECU* as functions of the engine speed and intake manifold pressure.

4.9 Bandwidth Versus Robustness: ϕ-feedback

In theory, provided a very accurate model of the air and fuel dynamics exists, the bandwidth of the above proposed controller is infinite (or more rigorously, equals the sampling frequency). The fueling dynamics is assumed to be canceled and the delay of the plant has been compensated for, so that no λ error should be observed neither during steady-state nor during transient operation.

In practice, of course, modeling errors are unavoidable and λ excursions are to be expected. Although the transient excursions should be much smaller than those observed with conventional controllers, the steady-state errors may be larger because of the lack of direct *AFR* feedback. In order to make the proposed controller more robust against modeling errors, a *UEGO* sensor is mounted in the exhaust and a simple ϕ[11]-feedback controller is introduced.

The output of this controller, $\delta\phi_{int}$, which is proportional to the ϕ-error ($\delta\phi_{exh} = \frac{1}{\lambda_{ref}} - \frac{1}{\lambda_{exh}}$) and to the integral of $\delta\phi_{exh}$ (for 0 static error), is used to offset the output of the model-based predictive controller (see Figure 7) with a fuel quantity m_f^{FB}.

$$m_f^{FB}(t+11) \;=\; \frac{120\,\check{m}_{ap}(t+11)}{L_{th}\,16\,N(t)} \cdot \delta\phi_{int}(t) \qquad (47)$$

where $\delta\phi_{int}$ is the correction term from the feedback controller. For the sake of completeness, the ϕ-feedback controller used in this research is detailed in Appendix B.

Note that the presence of the transport delay associated with ϕ-feedback does not decrease the overall bandwidth of the controller. One should instead consider two bandwidths: one for the model-based predictive controller (ideally infinite), and one for the ϕ-feedback controller. The latter characterizes how fast the feedback controller can compensate for the errors of the predictive feedforward controller. This bandwidth is of course limited by the transport delay, but only applies to small deviations (ϕ excursions) which occur when the feedforward part is inaccurate.

Ideally, if the model-based predictive controller is perfect, the lambda error remains zero and the λ-feedback controller does not influence the quantity of injected fuel. In practice, the larger the λ excursions (poor predictor), the longer it takes for the ϕ-feedback controller to bring λ back to λ_{ref} (small bandwidth). On the other hand, the smaller the λ excursions (good predictor), the shorter time it takes for the ϕ-feedback controller to bring λ back to λ_{ref} (large bandwidth). Quite clearly, the impact of the ϕ-feedback loop on the overall bandwidth increases with increasing *AFR* errors. This should again stress that modeling is a fundamental aspect of the work presented here.

For the sake of completeness, the input to the fuel film compensator is repeated in Equation (48).

$$\begin{aligned} m_{fd}(t+11) \;&=\; m_f^{FF}(t+11) + m_f^{FB}(t+11) \\ &=\; \frac{120\,\check{m}_{ap}(t+11)}{L_{th}\,16\,N(t)} \cdot \Big(\frac{1}{\lambda_{ref}} \;+\; \delta\phi_{int}(t)\Big) \end{aligned} \qquad (48)$$

Note however that, in principle, ϕ-feedback only applies to residual deviations; therefore, it does not need to be switched off during transient. This is unusual and represents a great simplification compared to conventional fueling strategies.

5 EXPERIMENTAL RESULTS

5.1 Experimental setup

In order to test the above controller, a series of experiments was performed on a engine dynamometer at the Technical University of Denmark (*DTU*). The engine is a 1275 cc British Leyland engine, with the original cylinder head (2 siamesed intake ports) replaced with a custom made head (4 independent intake ports) more suitable for *MPI* operation. A new intake manifold was built for this project. It consists of 4 straight runners (approx. 10 cm long and 350 cc each) with a plenum (approx 3000 cc). Four injectors sprayed directly onto each intake valve. The exact manifold volume (from valves to throttle plate) is 4332 cc. The engine is throttled upstream of the plenum with an electronically controlled actuator (*DBW*, whose characteristics are described in Section 4).

The engine is instrumented with the sensors necessary for the controller (intake pressure and temperature sensors, barometric pressure and temperature sensors, throttle position sensor, engine position and engine speed sensor, λ sensor) as described in Section 4. The λ sensor is a *UEGO* type sensor from NTK, with a time constant of 50 ms approximately. A laminar air flow meter is also mounted on the engine, upstream of the throttle plate, in place of the conventional air filter. Note that this laminar flow element is mounted only for the purpose of calibration and validation of the controller; it is not a part of the controller itself.

Before logging any data, all sensors and actuators were carefully calibrated. The predictor/controller was implemented using a PC-based Engine Control Development System built at *DTU* [31]. This system is built around a multi-tasking scheduler which allows the use of a normal PC as a real-time computer. All calculations are handled by the microprocessor of the PC itself. Interface with the sensors and actuators is via A/D and

[11] The normalized excess of fuel. It is convenient to derive the controller around ϕ instead of λ since $\phi = \frac{1}{\lambda}$ is proportional to the controlled variable (the fuel quantity) whereas λ is inversely proportional to it.

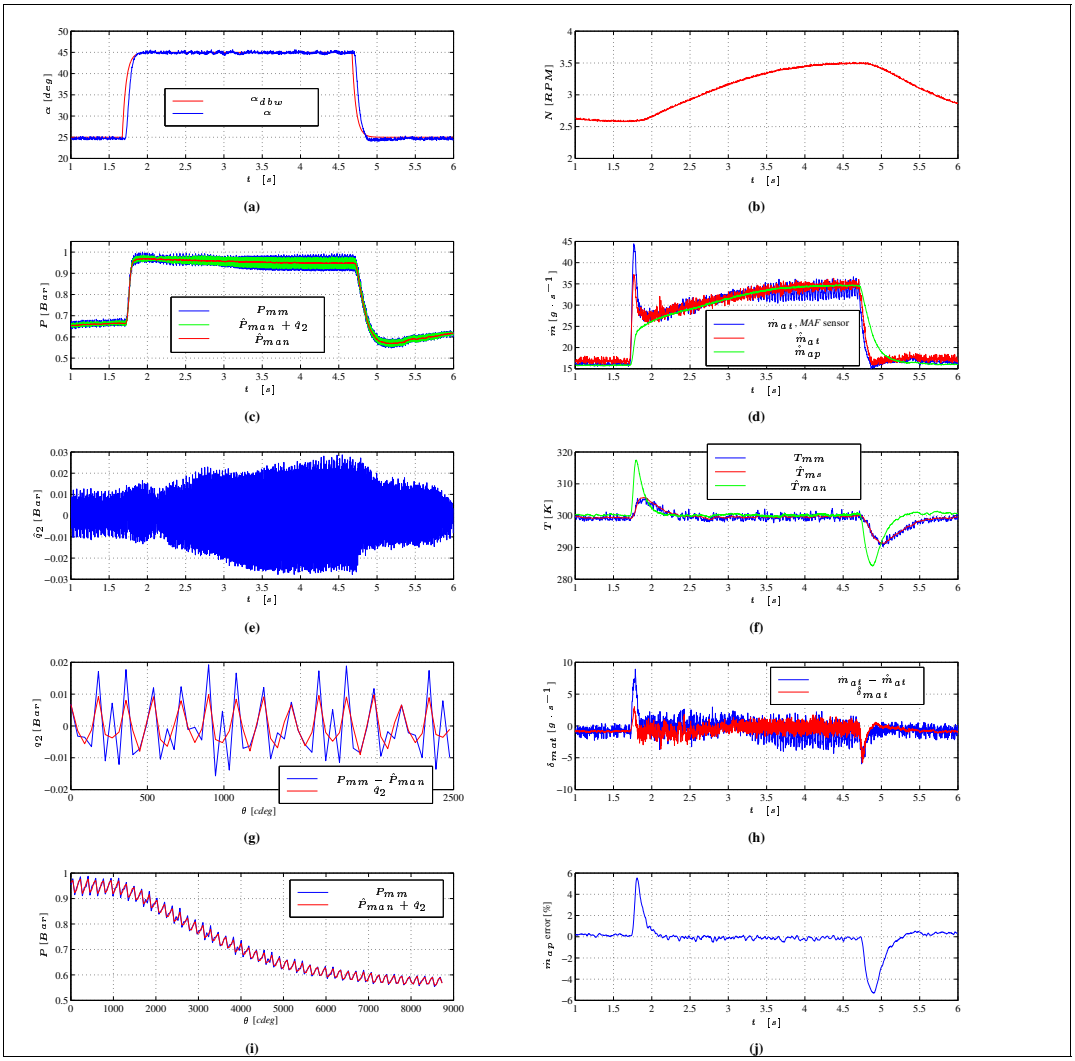

Figure 13: Testing the 6-state observer. Notice the time lag between the *DBW* command and the actual throttle position in Figure 13(a).

D/A cards (from ComputerBoards) in the expansion slots of the PC. Because of the special requirements of this project, both the hardware and software part of the Engine Control Development System (*ECDS*) had to be modified.

In order to meet the increased computer power demand, the whole system was migrated to a 200MHz Pentium PC. Because of the high sampling frequency required during calibration (especially for the *FFT*'s), a timing board was added in the expansion slot of the PC so that the scheduler can now be interrupted up to 30000 times per second.

Possibility for preemption from an external interrupt line was also added. In this way, the pulse signal from a 72-teeth wheel mounted on the crankshaft could be used to interrupt the scheduler every 45 *cdeg*, as required by the *AFR* controller (or any other value). On-line data-processing capability was added, and monitoring features were improved as well as user friendliness (the entire system is configurable in one "config" file written in Pascal and assembly code programming is no longer necessary).

The *AFR* controller was implemented in Pascal as one task of the *ECDS*. The outputs of the controller, the *DBW* command (α_{dbw}) and the fuel quantity (m_{fi}) are sent, via the A/D board

to the *DBW* unit and to the injection unit respectively.

Because the timing of the injection (control of injection delay) is a critical issue in this project, a special PC-based sequential electronic fuel injection (*SEFI*) injection unit was developed. A second PC, with an A/D board (to communicate with the *ECDS* and interface with the additional required sensors) and a timing board (10 16-bit counters) from ComputerBoards were installed in the expansion slots. It was programmed to drive sequentially the four injectors (the beginning of each injection pulse is phased 270 *cdeg* before top-dead-center of the corresponding cylinder).

5.2 Testing the observer

Figure 13 shows the performance of the estimator both during steady-state and fast transient operation. The throttle plate is opened 20 deg with a rise time of 50 ms and the engine speed varies between 2500 RPM and 3500 RPM. Despite the large level of pumping fluctuation, the observer is capable of reconstructing all the states with a remarkable accuracy. It is interesting to note that the observer is capable of picking up the fundamental component of the pumping fluctuations, q_2 (see Figures 13(c) and 13(e)), while rejecting the higher harmonics components (see Figure 13(g)), both during steady-state and transient operation (see Figure 13(i)).

In Figure 13(d) the estimated throttle air mass is compared with measured throttle air mass flow. Again, the accuracy is excellent, also during the initial filling spike. Note that the level of noise on the estimated throttle air mass flow has nothing to do with the pumping fluctuations (at least directly). It is pure noise which comes from the amplification (see Equation (6)) of the noise on the estimated manifold pressure, $\hat{P}_{man}$. This noise is however a good indicator that the Kalman gains are properly tuned. (Too little noise would indicate that the gains are too low, and that the estimator is running almost open loop). Note also how δ_{mat} (see Figure 13(h)) is capable of picking up the throttle air mass flow estimation error. Again, it should be clear that the throttle air mass flow measurement is not part of the observer, and that it is shown here for the purpose of validation only.

The temperature estimates are shown on Figure 13(f). It is interesting to see that despite a measured temperature excursion during tip-in of only 5 K, the estimated actual temperature excursion is up to 18 K. To the authors' knowledge, this is the first time that such transient temperature excursions are measured (estimated) and the measurements reported in the literature.

Figure 13(j) illustrates the implication of these temperature excursions on the error of the port air mass flow estimate, compared to an estimate based on a speed density equation where the transient temperature variation is ignored (isothermal assumption). As can be seen in this case, the error is up to 6%; this is unacceptably large for efficient *TWC* operation. For larger throttle openings, the error can be up to 10% (temperature variation of 30 K).

In Figure 14, the experiment of Figure 13 is repeated with the Kalman gains k_{41} and k_{42} set to zero. In this way, $\hat{\delta}_{mat}$ is forced to zero. As can be shown, the throttle air mass flow estimation error at small throttle openings remains uncompensated, which leads to a static error on the temperature estimate (physically, the throttle flow, and consequently the inflowing enthalpy, is over estimated).

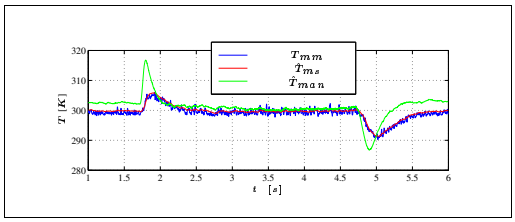

Figure 14: Temperature estimates for the observer without any compensation for the throttle air mass flow error ($\hat{\delta}_{mat} = 0$).

5.3 Testing the model-based predictive *AFR* controller

In Figure 15 the performance of the *AFR* controller is demonstrated over a large operating range. For each step, the throttle is operated with a 100 ms rise time. Most of the important engine variables are plotted so that the operating range of the engine during the test can be judged. The parallel lines on the lambda plot represent the $\pm 3\%$ normalized *AFR* limits. The λ achieved clearly lies within these bounds. The correction term, $\delta\phi_{int}$, from the ϕ-feedback controller is also shown in Figure 15(e). It should be pointed out that, due to a bad combustion chamber, the background level of noise (measured at 3 standard deviations) on the λ-signal is around 1% (as can be seen in the last three seconds of Figure 15(d)).

A typical conventional *AFR* control system will show λ peaks on the order of +/- 6-20% for a control input like that used in this work. A sliding mode control system presented recently in the literature shows peaks on the order of or +/-3.5% with throttle angle inputs about the size of those demonstrated here [32]. An adaptive *AFR* control system published in 1995 with a similar amplitude control input but around one input level and constant engine speed has residual λ noise like that in Figure 15(e) [19]. Neural network *AFR* control was investigated in [33] with a control input like that used here. The *AFR* control accuracy possible was of +/- 6%. Earlier work at *DTU* using special port air mass flow sensors and observer technologies gave a performance close to that found in this work [34].

In order to demonstrate the effectiveness of the model-based predictive *AFR* controller, a series of severe transient tests was conducted on the engine, and the results are compared with a non-predictive *AFR* controller (the controller is exactly the same as the model-based predictive controller except that fueling is based on the estimated port air mass flow rather than on the predicted port air mass flow , i.e. $\check{m}_{ap}(t+11)$ is replaced by $\hat{m}_{ap}(t)$ in Equation (48)).

In Figure 16, the throttle is repeatedly opened and closed between 25 deg and 35 deg, with a rise time of 100 ms and a period of 0.5 s. The engine is operated at a constant speed of 2430 RPM. In spite of the severity of the test, the model-based predictive controller is still capable of maintaining λ within the $\pm 3\%$ limits. On the other hand, the non predictive controller exhibits excursions up to 15%.

In Figure 17, the test is even more severe. The throttle is now repeatedly opened end closed between 25 deg and 45 deg, with a rise time of 50 ms and a period of 0.5 s. The model-based predictive controller still gives acceptable performance whereas the non-predictive controller drives the engine into regions where combustion becomes unstable.

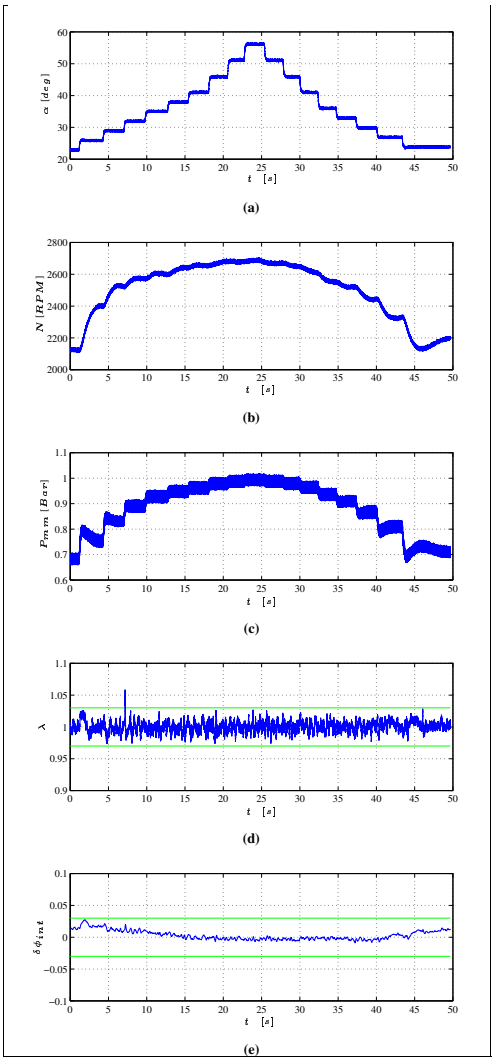

Figure 15: Test of the model-based predictive *AFR* controller over a large operating region.

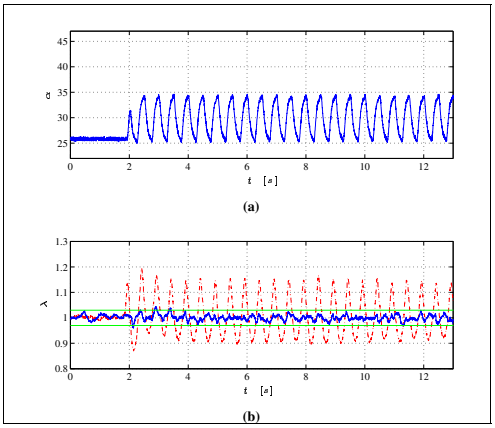

Figure 16: Comparison between model-based predictive (solid trace) and non-predictive (dashed trace) *AFR* controllers under severe transient operation.

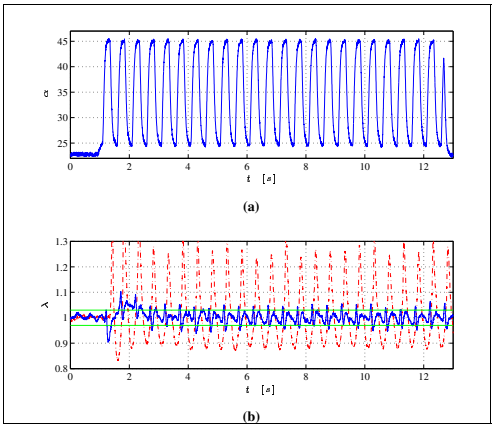

Figure 17: Comparison between model-based predictive (solid trace) and non-predictive (dashed trace) *AFR* controllers under even more severe transient operation.

6 CONCLUSIONS

Some of the limitations imposed on *AFR* controllers have been carefully reviewed. In particular, it is shown how deterministic pumping fluctuations (periodic noise due to the reciprocating nature of the engine) and time delays (injection and transport delays) can strongly penalize the achievable performance (bandwidth) of *AFR* controllers during transients (no matter how complex and how expensive the engine management system is). The only way to circumvent these limitations is through a proper choice of sensors and actuators, combined with the use

of a model-based strategy. Careful control of the timing of the strategy within the engine cycle was also found important.

The controller proposed in this paper is made up of three parts:

1. A **non-causal feedforward controller** which uses information about the future accelerator pedal position to predict the port air mass flow. In order to minimize the prediction error, an Extended Kalman Filter based on the latest intake manifold and temperature measurements serves as a means to initialize the states of the predictor and to extrapolate (the most recent) past information into the future. This estimator is new, not only because of the model on which it is based, but also because of the way the observer gains are calculated. Since a large proportion of the measurement noise is deterministic, a model of the pumping fluctuations is also included in the estimator. In this way, all the noise entering the observer can satisfactorily be approximated as white noise. By inverting a Lyapunov equation, the process noise intensities are calculated so as to match the noise level observed on the measured variables. The controller also includes integral action to minimize steady-state estimation errors due to modeling inaccuracy.
2. While the predictive feedforward controller provides the necessary bandwidth during transient operation, a slower **λ-feedback controller** is used to compensate for unavoidable long term steady-state *AFR* deviations.
3. Before injecting the fuel, the fueling dynamics is canceled using an inverted model of the fuel puddling process.

The controller derived was tested on an engine dynamometer and transient *AFR* traces were presented. The performance of the estimator was successfully demonstrated over the entire operating region with the calculated Kalman gains (fine tuning the gains during dynamometer testing was not required). The benefits of the predictive controller over non-predictive strategies were also demonstrated.

However, it is felt that the fuel film compensator did not always work properly and that the predictor should therefore be tested in more detail. It would be interesting to test the controller on engines where the fuel film problem is absent, i.e. in direct injection or gaseous fuel engines.

While the observer/controller which has been developed is complex, it has been derived nearly without compromise as a limiting example of what can practically be accomplished. It is also true that if a proper fuel film compensator is available, it will nearly always work as shown here. In contrast to many other *AFR* control systems in the literature, proper account is taken for the effects of compression, expansion and heat transfer in the intake manifold. This ordinarily can lead to somewhat erratic behavior during large rapid throttle inputs, especially if the intake manifold is large compared to the engine displacement volume.

Clearly, for production applications, some simplifications and compromises will be necessary in the algorithm presented. Nevertheless it is thought that the work which has been presented sets a lower limit for what can be accomplished given the variability of combustion, common production tolerances and unavoidable engine noise.

References

[1] C. F. Aquino, "Transient A/F Control Characteristics of the 5 Liter Central Fuel Injection Engine," *SAE Technical Paper*, no. 810494, 1981.

[2] E. Hendricks and S. C. Sorenson, "Mean Value Modeling of Spark Ignition Engines," *SAE Technical Paper*, no. 900616, 1990.

[3] E. Hendricks and S. C. Sorenson, "SI Engine Controls and Mean Value Engine Modeling," *SAE Technical Paper*, no. 910258, 1991.

[4] E. Hendricks and T. Vesterholm, "The Analysis of Mean Value SI Engine Models," *SAE Technical Paper*, no. 920682, 1992.

[5] P. Maloney and P. Olin, "Pneumatic and Thermal State Estimations for Production Engine Control and Diagnostics," *SAE Technical Paper*, no. 980517, 1998.

[6] P. Maloney, "An Event-Based Transient Fuel Compensator with Physically Based Parameters," *SAE Technical Paper*, no. 1999-01-0553, 1999.

[7] E. Hendricks, M. Jensen, A. Chevalier, and T. Vesterholm, "Conventional Event Based Engine Control," *SAE Technical Paper*, no. 940377, 1994.

[8] E. Hendricks, A. Chevalier, and M. Jensen, "Event Based Engine Control: Practical Problems and Solutions," *SAE Technical Paper*, no. 950008, 1995.

[9] E. Hendricks and A. Chevalier, "Emerging Engine Control Technologies," *29th ISATA Conference on Automotive Electronics*, June 1996. Florence, Italy.

[10] E. Hendricks, "Errors in Hot Wire MAF Measurement Systems." Revised Interim Report, the Technical University of Denmark, 1992.

[11] H.-M. Wiedenmann, G. Hötzel, H. Neumann, J. Riegel, and H. Weyl, "Exhaust Gas Sensors," in *Automotive Electronics Handbook* (R. K. Jurgen, ed.), chapter 6, McGraw-Hill, Inc., 1995.

[12] M. H. Westbrook and J. D. Turner, *Automotive Sensors*. Institute of Physics Publishing, Bristol and Philadelphia, 1994.

[13] L. Trajkovski, "Computer Controlled Engine Management System," Master's thesis, the Technical University of Denmark, Institute of Automation, 1997. In danish.

[14] G. Chen, *Study of Fuel-Air Mixture Formation in a Port-Injected Gasoline Engine*. Ph.D. dissertation, University of Illinois at Chicago, 1995.

[15] J. J. G. Martins and I. C. Finlay, "Fuel Preparation in Port-Injected Engines," *SAE Technical Paper*, no. 920518, 1992.

[16] T. Nogi, Y. Ohyama, T. Yamauchi, and H. Kuroiwa, "Mixture Formation of Fuel Injection Systems in Gasoline Engines," *SAE Technical Paper*, no. 880558, 1988.

[17] S. Skogestad and I. Postlethwaith, *Multivariable Feedback Control, Analysis and Design*. John Wiley & Sons, 1996.

[18] M. Morari and E. Zafiriou, *Robust Process Control*. Prentice-Hall, Inc., 1989. Englewood Cliffs, N.J.

[19] N. Fekete, J. Powell, U. Nester, and I. Gruden, "Model Based Air-Fuel Ratio Control of a Lean Multi-Cylinder Engine," *SAE Technical Paper*, no. 950846, 1995.

[20] A. Chevalier and M. Müller, "On the Validity of Mean Value Engine Models During Transient Operation," *SAE Technical Paper*, no. 2000-01-1261, 2000.

[21] E. Hendricks, M. Jensen, A. Chevalier, S. C. Sorenson, D. Trumphy, and J. Asik, "Modelling of the Intake Manifold Filling Dynamics," *SAE Technical Paper*, no. 960037, 1996.

[22] M. Müller, "Mean Value Modelling of Turbocharged Spark Ignition Engines," Master's thesis, The Technical University of Denmark, Institute of Automation and Department of Energy, 1997.

[23] D. L. Stivender, "Engine Air Control - Basis of a Vehicular Systems Control Hierarchy," *SAE Technical Paper*, no. 780346, 1978.

[24] K. J. Åström and B. Wittenmark, *Computer-Controlled Systems: Theory and Design*. Prentice-Hall International, Inc., 2nd ed., 1990.

[25] A. Gelb, ed., *Applied Optimal Estimation*. The M.I.T. Press, 12th printing, 1992.

[26] R. E. Kalman and R. S. Bucy, "New Results in Linear Filtering and Prediction Theory," *Journal of Basic Engineering, Trans. ASME*, vol. 83D, pp. 95–108, 1961.

[27] H. Kwakernaak and R. Sivan, *Linear Optimal Control Systems*. Wiley-Interscience, first ed., 1972.

[28] United States Patent No. 4,939,658, July 3, 1990. Assignee: Hitachi Ltd., Tokyo, Japan.

[29] E. Hendricks, T. Vesterholm, P. Kaidantzis, P. Rasmussen, and M. C. Jensen, "Nonlinear Transient Fuel Film Compensation," *SAE Technical Paper*, no. 930767, 1993.

[30] H. Melgaard, E. Hendricks, and H. Madsen, "Continuous Identification of a Four-Stroke SI Engine," *American Control Conference (ACC)*, no. TP10, 5:30, 1990. San Diego, CA.

[31] J. Lillelund, "Design of an Engine Control Development System," Master's thesis, The Technical University of Denmark, Institute of Automation, 1991.

[32] S. Choi, M. Won, and J. Hedrick, "Fuel Injection Control of SI Engines," *Proceedings of the 33rd IEEE Conference on Des. and Control (CDC)*, dec 1994. Lake Buena Vista, Florida.

[33] P. Shayler and M. Goodman, "Mixture Control with Air-Flow Anticipation Using Neural Networks," *29th ISATA Conference on Automotive Electronics*, June 1996. Florence, Italy.

[34] P. Jensen, M. Olsen, J. Poulsen, E. Hendricks, M. Føns, and C. Jepsen, "A New Family of Nonlinear Observers for SI-Engine Air-Fuel Ratio Controls," *SAE Technical Paper*, no. 970615, 1997.

[35] J. Lillelund and E. Hendricks, "A PC Engine Control Development System," *SAE Technical Paper*, no. 910259, 1991.

ACRONYMS

AFR .... Air/Fuel Ratio

AMFR... Air Mass Flow Related

cdeg .... Crankshaft Degrees

DBW.... Drive by Wire

DTU .... Technical University of Denmark

EABS4 .. 4^{th} Order Event Average Based Sampling ([7], [8])

ECDS... Engine Control Development System, [35]

ECU .... Electronic Control Unit

EGO.... Exhaust-Gas-Oxygen

EKF .... Extended Kalman Filter

FFT .... Fast Fourier Transform

HC..... Hydrocarbons

ISE ..... Integral Square Error

MAF.... Mass Air Flow

MAP.... Manifold Absolute Pressure

MAT.... Manifold Air Temperature

MPI .... Multi-Point Injection

MVEM.. Mean Value Engine Model

PI ..... Proportional Integral

RPM ... Revolutions Per Minute

SEFI.... Sequential Electronic Fuel Injection

SI ..... Spark Ignition

SOI ..... Start Of Injection

TWC .... Three-Way Catalyst

UEGO .. Universal Exhaust-Gas-Oxygen

WOT .... Wide Open Throttle

VARIABLES

A ..... Jacobian of F with respect to X

A_d ..... State matrix of the discretized linearized model

α ..... Throttle plate angle (position), $[deg.]$

α_d ..... Accelerator pedal position (desired throttle position), $[deg.]$

α_{dbw} .... *DBW* command (α_{ds} delayed), $[deg.]$

α_{df} ..... Predicted throttle plate position, $[deg.]$

α_{ds} ..... Sampled accelerator pedal position, $[deg.]$

A_{pf0} .... Amplitude of the fundamental of the pumping fluctuations $[Pa]$

B_d ..... Input matrix of the discretized linearized model

β_1 ..... Discharge coefficient at the throttle plate

β_2 ..... Compressibility coefficient at the throttle plate

C_d ..... Output matrix of the discretized linearized model

dbw_{d1} ... Coefficient of the discrete *DBW* model

dbw_{d2} ... Coefficient of the discrete *DBW* model

dbw_{n1} ... Coefficient of the discrete *DBW* model

dbw_{n2} ... Coefficient of the discrete *DBW* model

δ_{mat} .... Throttle air mass flow model error, $[kg \cdot s^{-1}]$

$\dot{m}_{ap}$ ..... Port air mass flow rate, $[kg \cdot s^{-1}]$

$\dot{m}_{at}$ ..... Throttle air mass flow rate, $[kg \cdot s^{-1}]$

$\dot{m}_f$ ..... Cylinder port fuel mass flow, $[kg \cdot s^{-1}]$

$\dot{m}_{fi}$ ..... Injected fuel mass flow, $[kg \cdot s^{-1}]$

$\dot{m}_{fv}$ .... Fuel vapor mass flow, $[kg \cdot s^{-1}]$

$\delta\phi_{exh}$ ... ϕ-feedback control input ($= \frac{1}{\lambda_{ref}} - \frac{1}{\lambda_{exh}}$)

$\delta\phi_{int}$ .... ϕ-feedback control output (fueling correction term)

ΔP_{mm} .. Intake pressure reconstruction error, $[Pa]$

$\dot{Q}_{ext}$ .... Rate of heat transfer $[j \cdot s^{-1}]$

ΔT_{mm} .. Intake temperature reconstruction error, $[K]$

$\eta_{vol}^{P_{amb}, T_{man}}$ Volumetric efficiency based on barometric pressure, P_{amb} and intake manifold temperature, T_{man}

η_{vol}^{man} .... Volumetric efficiency based on intake manifold conditions

F ..... Differential system function

f_0 ..... Fundamental frequency, $[Hz]$

f_1 ..... First harmonic frequency, $[Hz]$

f_2 ..... Second harmonic frequency, $[Hz]$

f_e ..... Engine event frequency, $[Hz]$

G ..... Output function

I_v ..... Measurement noise intensity matrix

I_w ..... State excitation (process) noise intensity matrix

K ..... Kalman gain matrix

κ_f ..... Fuel film parameter (discrete model)

K_Π ..... A gain in the ϕ-PI controller (depends of N)

λ ..... Normalized air/fuel ratio

λ_{exh} .... Measured λ in the exhaust manifold

λ_{int} ..... λ at the intake port (non measurable)

m_a ..... Mass of fresh air trapped in a cylinder, $[kg]$

m_f ..... Mass of fuel trapped in a cylinder, $[kg]$

m_{fd} .... Desired mass of fuel at the intake port $[kg]$

m_{ff} .... Fuel puddle mass, $[kg]$

m_f^{FB} .... Fuel mass quantity (output of the feedback controller), $[kg]$

m_f^{FF} .... Fuel mass quantity (output of the feedforward controller), $[kg]$

m_{fi} ..... Mass of injected fuel $[kg]$

μ_f ..... Fuel film parameter (discrete model)

N ..... Engine speed, [RPM]

P_{amb} .... Atmospheric manifold pressure, $[Pa]$

ϕ ..... Normalized excess of fuel ($\frac{1}{\lambda}$)

P_{man} ... Mean intake manifold pressure, $[Pa]$

P_{mm} .... Measured intake manifold pressure, $[Pa]$

P_r ..... Pressure ratio

P_{up} ..... Pressure upstream the throttle plate, $[Pa]$

Q ..... Variance matrix of the state vector X

q_1 ..... State of the pumping fluctuation model

q_2 ..... Output (and state) of the pumping fluctuation model

Q_d ..... Variance matrix of the estimation error

$q_{\delta_{mat}}$ .... Covariance of the δ_{mat}-state, $[kg^2 \cdot s^{-1}]$

$q_{P_{man}}$ ... Covariance of the P_{man}-state, $[Pa^2]$

$q_{T_{man}}$ ... Covariance of the T_{man}-state, $[K^2]$

$q_{T_{ms}}$ .... Covariance of the T_{ms}-state, $[K^2]$

Q_v ..... Measurement noise variance matrix

Q_w ..... Process noise variance matrix

t ..... Time $[s]$ or normalized time [sampling period]

T_{amb} .... Atmospheric manifold temperature, $[K]$

τ_d ..... Loop delay (injection + transport delay) (depends of N) $[s]$

τ_f ..... Fuel film evaporation time constant, $[s]$

T_e ..... Engine event duration, $[s]$

θ ..... Crankshaft position, $[cdeg]$

T_{man} ... Mean intake manifold temperature, $[K]$

T_{mm} .... Measured intake manifold temperature, $[K]$

T_{ms} ..... Intake temperature sensor state variable, $[K]$

T_r ..... $= \frac{T_{man}}{T_{amb}}$ Normalized intake manifold temperature

T_s ..... Sampling period $[s]$

U ..... Input vector (state space model)

V ..... Continuous measurement noise

V_d ..... Discrete measurement noise

$\mathcal{V}_{\delta_{mat}}$ ... Process noise of the δ_{mat}-state equation

$\mathcal{V}_{P_{man}}$ ... Process noise of the P_{man}-state equation

$\mathcal{V}_{P_{mm}}$ ... Measurement noise of the P_{mm}

$\mathcal{V}_{q_1}$ ..... Process noise of the q_1-state equation

$\mathcal{V}_{T_{man}}$ ... Process noise of the T_{man}-state equation

$\mathcal{V}_{T_{mm}}$ ... Measurement noise of the T_{mm}

$\mathcal{V}_{T_{ms}}$ .... Process noise of the T_{ms}-state equation

W ..... Continuous state excitation (process) noise

W_d ..... Discrete state excitation (process) noise

ω_e ..... Engine event frequency, $[rad \cdot s^{-1}]$

X ..... State vector (state space model)

X_f ..... Fraction of the injected fuel which is deposited on manifold as fuel film

Y ..... Output vector (state space model)

ζ_q ..... Damping ratio (pumping fluctuations model)

CONSTANTS

α_0 ..... Throttle plate angle at closed throttle position, $[deg.]$

$b_{10} \ldots b_{13}$ Fitting constant for the throttle air mass flow model

χ_1 ..... Fitting constant for the air filter flow model

χ_2 ..... Fitting constant for the air filter flow model

δ ..... Fitting constant for the throttle air mass flow model

γ ..... $= \frac{c_p}{c_v}$ Ratio of specific heats, 1.40 for air

h ..... Heat transfer coefficient $[j \cdot s^{-1} \cdot K^{-1}]$

K_{filt} .... Air filter flow resistance coefficient

λ_{ref} .... Reference λ (1 for *TWC* optimal conversion efficiency)

L_{th} ..... Stoichiometric mass air/fuel ratio, 14.67

ν ..... Fitting constant for the throttle air mass flow model

P_{rc} ..... Critical pressure ratio (at which a throat becomes sonic)

r ..... Specific gas constant, 287.0 $j \cdot kg^{-1} \cdot K^{-1}$ for air

τ_δ ..... Time constant of the δ_{mat}-model

τ_{Temp} ... Time constant of the intake temperature sensor $[s]$

τ_{uego} .... Time constant of the *UEGO* sensor $[s]$

θ_s ..... Sampling period in the crank domain, $45cdeg$

V_{disp} .... Engine displacement, $[m^3]$

V_{man} ... Intake manifold volume, $[m^3]$

ω_{dbw} .... *DBW* undamped natural frequency $[rad \cdot s^{-1}]$

ζ_{dbw} .... *DBW* damping ratio

OPERATORS

s ..... Laplace operator

$\hat{x}$ ..... Estimate of x

$\overline{x}$ ..... Mean of x

$\check{x}$ ..... Prediction of x

$\tilde{x}$ ..... One-step ahead prediction of x

x^T ..... Transpose of x

APPENDIX

A Numerical solution to the implicit ($\dot{m}_{at}$, P_{up}) problem

In order to calculate $\dot{m}_{at}$ and P_{up}, a system of 2 algebraic nonlinear equations must be solved. These two equations are repeated in Equations (49) and (50).

$$\dot{m}_{at}(\alpha, P_{man}, P_{up}, T_{amb}) = \frac{P_{up}}{\sqrt{T_{amb}}}\beta_1(\alpha)\Big(\frac{1}{\nu+1}\beta_2(P_r) + \frac{\nu}{\nu+1}\beta_2\big(1-\delta\,(1-P_r)\big)\Big) \tag{49}$$

$$P_{up} = P_{amb} - K_{filt}\,\dot{m}_{at}^{\chi_1}\left(\frac{T_{amb}}{P_{amb}}\right)^{\chi_2} \tag{50}$$

A simple iterative solution, suitable for real-time control applications, is given below:

1. $P_{up} = P_{amb}$ (initial guess)
2. Calculate $\dot{m}_{at}$ with Equation (49) (1^{st} approximation)
3. Calculate P_{up} with Equation (50) (1^{st} approximation)
4. Calculate $\dot{m}_{at}$ with Equation (49) (2^{nd} approximation)
5. Calculate P_{up} with Equation (50) (2^{nd} approximation)
6. Calculate $\dot{m}_{at}$ with Equation (49) (3^{rd} approximation)
7. Calculate P_{up} with Equation (50) (Estimated P_{up})
8. Calculate $\dot{m}_{at}$ with Equation (49) (Estimated $\dot{m}_{at}$)

Further iterations do not give any significant improvement of the estimates.

B ϕ-feedback controller

The ϕ-feedback controller used in the work presented is a simple proportional integral (*PI*) controller, designed using loop-shaping techniques. No attempt has been made to achieve a very sophisticated controller and the objective of this Appendix is simply to document how the *PI* controller used was tuned.

In order to be able to apply loop-shaping techniques, a simple linear model of the engine was used. If it is assumed that the fuelling dynamics are almost compensated for by the transient fuel film compensator and that the air dynamics are almost compensated for by the port air mass flow predictor, the plant can be modelled as the combination of a low-pass filter (with a time constant $\tau_{uego} = 100\ ms$) representing the *UEGO* sensor dynamics, and a delay ($\tau_d \cong 1300\ cdeg$) representing the injection and transport delay. This is illustrated in Figure 18 where the uncompensated fuel and air dynamics (due to errors in the predictor and in the fuel film compensator) enter the system as a disturbance d. The transfer function for the model is given in Equation (51).

$$\frac{\phi_{exh}}{\phi_{int}}(s) = \frac{\exp(-\tau_d\,T_s)}{1 + \tau_{uego}\,s} \tag{51}$$

where

$$\begin{aligned} \phi_{exh} &= \frac{1}{\lambda_{exh}} \\ \phi_{int} &= \frac{1}{\lambda_{int}} \end{aligned} \tag{52}$$

and where λ_{exh} is the measured λ in the exhaust, and λ_{int} is the (unmeasurable) λ at the intake port.

The transfer function of the *PI* controller is shown in Equation (53).

$$\frac{\delta\phi_{int}}{\delta\phi_{exh}}(s) = K_{\text{II}}\frac{1 + 5\,\tau_{uego}\,s}{s\,(1 + \tau_{uego}\,s)} \tag{53}$$

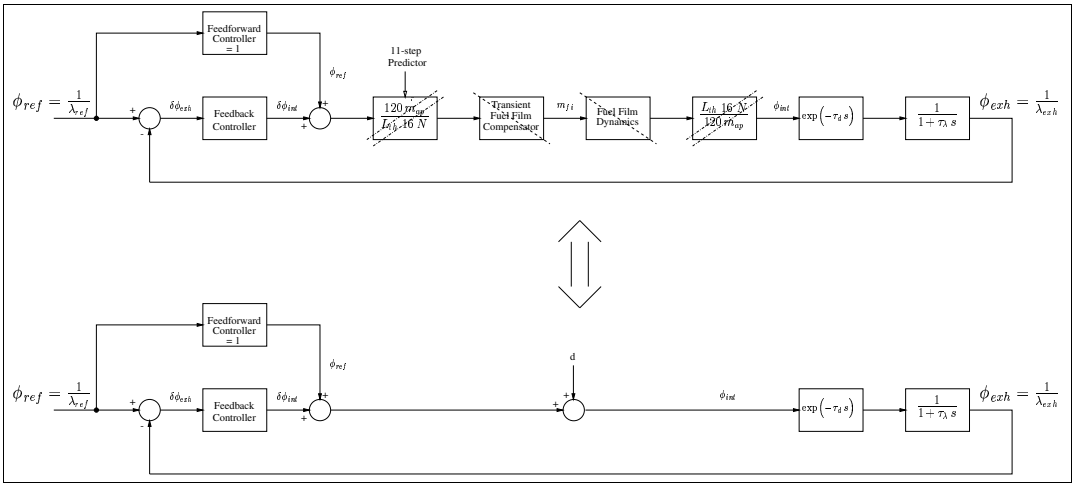

Figure 18: A model of the engine suitable for tuning the *PI* ϕ-feedback controller. The diagonal lines show which parts of the system approximately compensate for each other. Note that the fuel and air dynamics are cancelled out by the fuel-film compensator and the port air mass flow predictor respectively.

where $\delta\phi_{int}$ is the output of the controller and $\delta\phi_{exh} = \frac{1}{\lambda_{ref}} - \frac{1}{\lambda_{exh}}$ is the input. K_Π is chosen to give a 60 degree phase margin and is a function of the engine speed (since the loop delay, τ_d, is a function of N).

The discrete realization of this controller is given in Equation (54).

$$\delta\phi_{int}(t) \;=\; -\Pi_{d1}\,\delta\phi_{int}(t-1) \;-\; \Pi_{d2}\,\delta\phi_{int}(t-2) \;+\; K_\Pi(t)\,\left[\Pi_{n1}\,\delta\phi_{exh}(t-1) \;+\; \Pi_{n2}\,\delta\phi_{exh}(t-2)\right] \tag{54}$$

where

$$\begin{aligned}
\Pi_{d2} &= \exp\Big(-\frac{T_s}{\tau_{uego}}\Big)\\
\Pi_{d1} &= -\,(1+\Pi_{d2})\\
\Pi_{n1} &= T_s \;+\; (1-\Pi_{d2})\,4\,\tau_{uego}\\
\Pi_{n2} &= -\big(T_s\,\Pi_{d2} \;+\; (1-\Pi_{d2})\,4\,\tau_{uego}\big)\\
K_\Pi(t) &= K_\Pi\big(N(t)\big)
\end{aligned} \tag{55}$$

This is the form of the controller actually used in the work presented.

1.4 A basic validation of the MVEM framework

The MVEM framework is based on a simplified physical picture of IC engine utilizing as few regression based equations as possible. However, since physics unlike mathematics cannot be proven, but only experimentally validated such a thing as a proof for the MVEM framework does not exist. Hence, an effort to *prove* the MVEM conception will not be conducted here, instead it will argued that the MVEM framework provides a favorable and suitable way of engine modelling for control applications.

The two articles previously presented probably represent the limits imaginable for MVEM based AFR control of a port fuel injected SI engine for the following reasons:

- The $\mathcal{H}_\infty$ controller is realized by applying a lumped version of the isothermal MVEM presented in [50, 47] and the fuel film model presented in [52]. This model was linearized and augmented with fictional inputs representing the model variation introduced by variations in the volumetric efficiency, the intake pressure and the engine speed. The AFR controller was finally verified by experiments and exhibited an acceptable AFR control performance. Hence, this *low-fidelity model* manifests the possibilities available with simplified MVEMs, a minimum need for engine mapping, and feedback control strategies.

- The predictive AFR controller presented in the SAE-paper number 2000-01-0260 utilizes a high-accuracy model to predict the time response of the intake manifold dynamics. Comparing this AFR control strategy to the $\mathcal{H}_\infty$ strategy, it is clear that the predictive control algorithm with the extended Kalman filter initialization procedure is superior in terms of AFR performance. The downside of the strategy is the extensive calibration (mapping) of the engine required by the control design. Furthermore, due to the relatively long predictive horizon required (11 steps!) by the control design, causes danger of a significant degradation in the control performance due to engine ageing effects and tolerances exists. One obvious example is the possible presence of model and/or map interpolation errors, or unforseen external perturbations. The effect of such scenarios will become more pronounced as the horizon of prediction is extended due to error accumulation. The predictive feed-forward control design is therefore more fragile than $\mathcal{H}_\infty$ feedback control design. The predictive controller thus represents the other extreme made possible with a *high-fidelity* MVEM and feed-forward control.

Following the arguments presented above it is clear that the MVEM framework offers good modelling capabilities and scalability for a variety for different control designs. Hence, it is of great interest to encourage the research in model extensions to the MVEM framework and thereby making it easier to include many of the recently introduced or emerging engine technologies. The extension of the

MVEM framework with models of some of these new technologies is the topic of the following chapter.

Chapter 2

Engine Modelling

This chapter will present the most important modelling work carried out during this project. First, a new variable geometry turbocharger model is presented and compared to manufacturer maps, followed by the EGR and combustion modelling contributions. The EGR model is a simplified dynamic model just advanced enough that the influence of engine pumping may be investigated. The combustion modelling contribution is based on a locally weighted regression methodology. Together with several other automotive sub-models this forms the basis for the development of an objective based C library intended for the SIMULINK® *environment.*

2.1 Introduction

The last twenty years have enjoyed a dramatic interest increase in engine modelling for control purposes and with good reason. The automotive industry stands today, and in the recent past, faced with the problems of providing the market with IC engines meeting the government emission legislation while still being able to provide the customer with acceptable engine performance. In order to meet these demands both the SI and CI (Compression Ignition) engines have undergone some significant changes. Of these changes the most noticeable ones have probably been made in the engine's air path some of which are summarized below.

Modern standard SI engines are now equipped with EGR, electronic fuel injection of the GDI or MPI (Multi Point Injection) types, exhaust gas after treatment components like the TWC, and DBW control of the engine throttle. The list of components for more exotic engines is further augmented by auxiliaries like compressors, turbochargers, and throttle-less mass flow control through VVT (Variable Valve Timing) or VVL (Variable Valve Lift) technologies among others.

The development of and research in Diesel engines have not standing still either. Some would even claim that the basic Diesel engine design has been changed more radically than the SI engine. What used to be a noisy, smoking but robust

engine mostly used in heavy duty vehicles has now attacked the SI engine's main terrain – namely the passenger car market. This has mainly been achieved through new diesel injection technologies like the TDI (Turbo Direct Injection) system from Volkswagen and the common–rail system, VGT/VNT (Variable Nozzle Turbine) turbocharger technology, and HSDI (High Speed Direct Injection) engine designs. The future diesel engine is thus approaching 70 $\frac{kW}{liter}$, almost a factor 3 larger than engines 20 years ago, while still providing an unbeatable fuel economy compared to the SI engine. But trees do not grow into heaven; the diesel engine is generally speaking still more polluting than the MPI SI engine with comparable displacement volume in terms of NO_X and soot emissions, and disregarding CO_2 emissions. These problems the engine manufactures are trying to counteract by increasingly tighter control of the EGR, the boost pressure and the fuel injection timing and structure. Recycling a portion of the exhaust gas back to the intake manifold is known to lower the combustion temperature mainly due to a higher thermal heat capacity of the intake gas. However as EGR is also known to increase PM (Particulate Matter) production, which lately has received much public attention, since soot particles apparently are cancer provocative. Thus in order to meet both the tighter NO_X and PM legislation some new diesel cars are being provided with exhaust filters, known as DPF (Diesel Particle Filter). The long term efficiency and environmental impact of such filters, however, still remains unverified. A schematic layout of a modern diesel engine showing of the engine technologies mentioned is shown in figure 2.1.

With this short overview of engine technologies already introduced or being introduced in future passenger cars it is clear that the control burden has also experienced an almost exponentially growth. So far most automotive control algorithms are developed using ad-hoc methodologies and often disregarding control loops which are already implemented. This way natural interactions between engine states might be disrespected and thereby lead to unfortunate control actions (internal competing controllers). Hence, engine control source codes have grown into a tremendously size which is both hard to understand and overview.

In the author's opinion the only safe way to solve or ease the future control burden is by using simple comprehensible engine modelling structures. Only such structures can provide the control engineer with the necessary level of model complexity such that natural physical couplings are respected, and still be abstract enough to provide an overall picture of the dynamic engine behavior.

1. Fuel injection pump
2. Pump Control unit (PCU)
3. Fuel filter
4. Electric fuel lift pump
5. Crankshaft position sensor
6. Port deactivation position sensor
7. Port deactivation vacuum actuator
8. Port deactivation vacuum regulator
9. EGR throttle position sensor
10. EGR throttle vacuum actuator
11. EGR throttle vacuum regulator
12. EGR valve position sensor
13. EGR valve vacuum actuator
14. EGR valve vacuum regulator
15. Glow plug
16. Fuel injector
17. Cylinder head temperature sensor
18. Vacuum pump
19. Engine coolant temperature sensor
20. Manifold absolute pressure sensor
21. Air charge temperature sensor
22. EGR cooler
23. Intercooler
24. Mass air flow sensor
25. Air filter
26. Turbocharger compressor
27. Turbocharger turbine
28. Turbocharger wastegate
29. Catalytic converter
30. Instrument cluster
31. Accelerator pedal
32. Ignition key

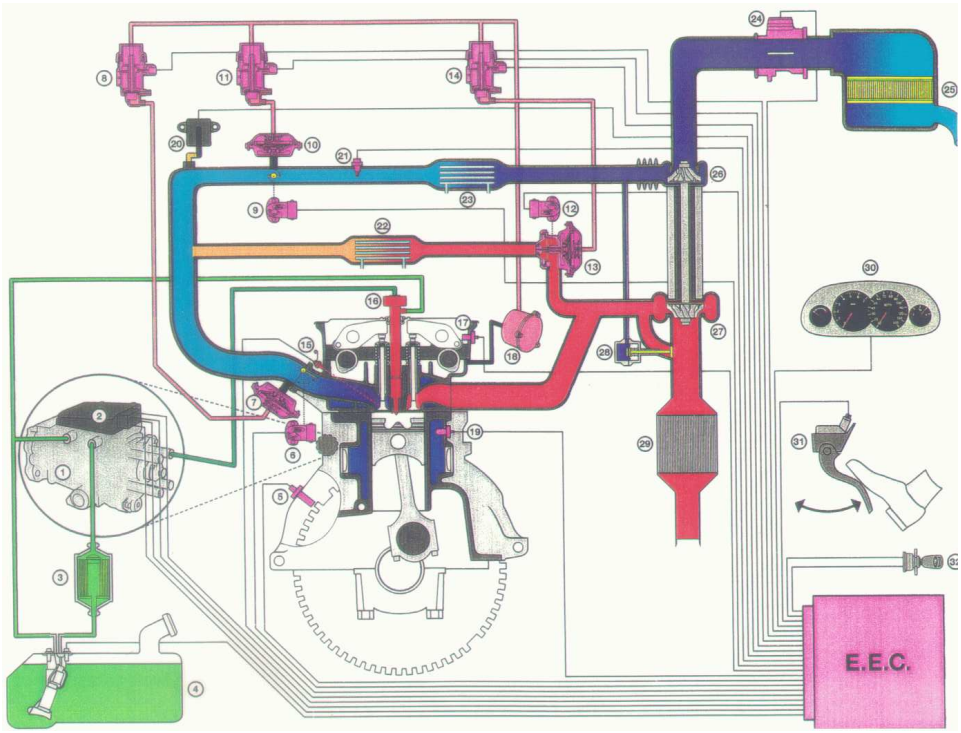

Figure 2.1: Layout schematic of a modern Diesel engine equipped with EGR and a waste-gate controlled turbocharger (courtesy of Ford Motor Company).

2.2 Explanatory remarks

The specific *stagnation* or *total* enthalpy of a gas, h_0, will here be defined as the sum of the *static* enthalpy, h, kinetic energy and potential energy,

$$h_0 = h + \frac{C^2}{2} + sg \tag{2.1}$$

where C is the gas velocity, s is the height, and g is the gravitational acceleration. The potential energy contribution is often of minor importance in most engine modelling aspects and can thus safely be neglected. Hence equation 2.1 reduces to,

$$h_0 = h + \frac{C^2}{2} \tag{2.2}$$

Furthermore it will be assumed that the gas properties pressure p, temperature T and volume V relation can be described by the ideal gas law:

$$pV = mRT \tag{2.3}$$

where m is the mass of the gas, and R is the gas constant. This assumption is reasonable for moderate pressures and temperatures [87].

The specific heat capacities at constant volume, c_v, and constant pressure, c_p, are derived from the the internal gas energy u and the enthalpy, h, in the following manner,

$$\begin{aligned} c_v &= \left(\frac{\partial u}{\partial T}\right)_v = \frac{du}{dT} = c_v(T) \\ c_p &= \left(\frac{\partial h}{\partial T}\right)_p = \frac{dh}{dT} = c_p(T) \end{aligned} \tag{2.4}$$

since the specific internal energy and the specific enthalpy are functions of temperature only.

The difference in the specific heats equals the gas constant, R

$$R = c_p - c_v \tag{2.5}$$

while heat capacity ratio is defined as,

$$\gamma = \frac{c_p(T)}{c_v(T)} = \gamma(T) \tag{2.6}$$

The specific heats will in this text be assumed constant, if this is not explicitly stated, since most of the temperature changes experienced in the engine air path[1]

[1]The combustion processes excepted

are moderate. Hence, descriptive values of γ, c_v and c_p will be used.

$$\begin{aligned} \overline{c}_v &= E\left(\, c_v(T) | \, T\right) \\ \overline{c}_p &= E\left(\, c_p(T) | \, T\right) \\ \overline{\gamma} &= E\left(\, \gamma(T) | \, T\right) \end{aligned} \tag{2.7}$$

with

$$T = \{t \in \mathbb{R}_+ \, | T_{min} \leq t \leq T_{max} \}$$

The mean value notation will be in the following be omitted for the sake of convenience.

The gas temperature and pressure are for an isentropic[2] process related as

$$p_0^{1-\gamma} T_0^{\gamma} = p_1^{1-\gamma} T_1^{\gamma} \tag{2.8}$$

The stagnation pressure and temperature can now be found from the definitions and functions given above,

$$\begin{aligned} T_0 &= T + \frac{C^2}{2c_p} \\ p_0 &= p\left(1 + \frac{C^2}{2c_p T}\right)^{\frac{\gamma}{\gamma-1}} \end{aligned} \tag{2.9}$$

if the gas is isentropically brought to rest.

2.3 Turbocharger modelling

2.3.1 Introduction

A buzz word in the automotive industry today is engine downsizing. This is not so much derived from an economic point of view but rather from a packaging/performance point of view. The list of auxiliary components in a standard car's engine compartment has clearly increased over the last decade. Components like the air conditioning coolant pump, closed coupled TWC, hydraulic steering assistance, air/pollen filters for the cabin air, not to mention all the added sensors and actuators, are all parts of a standard middle class car today. Meanwhile, the engine compartment size has decreased to meet the increased customer requirements for cabin and trunk space while keeping the overall size of the car the same. Thus designing an engine compartment containing all the necessary components is nowadays often a very challenging task for the designers. Lastly, engine downsizing is also a way to reduce the weight of the car, whence improving car handling and mileage.

Downsizing a NA engine while maintaining the same engine performance in terms of torque and power over the entire operating range of the engine though is

[2] Adiabatic and reversible process

not an easy task. The maximum power a given engine can deliver is limited by how much fuel it can burn efficiently. This is of course dependent upon how much fresh air the engine can induct per cycle.

A way to maintain engine torque and power as the engine displacement volume decreases, at least in a steady state sense, is by intake air supercharging, i.e increasing the intake manifold air density. The basic methods of supercharging are *mechanical supercharging*, *turbocharging* and *pressure wave supercharging*.

Mechanical supercharging is most often done by a separate air compressor directly driven by the engine through a belt/chain drive or gear[3].

Turbocharging implies the use of an exhaust manifold mounted turbine to extract energy from the exhaust gas. The turbine is directly coupled to the compressor through a shaft, thus a part of the exhaust energy extracted is returned to the intake manifold in terms of an air density increase.

The last method mentioned, which is highly uncommon today, is pressure wave supercharging. This method is probably best known as Comprex supercharging. The Comprex devices make use of the fact that the pressure equalisation happens a lot faster than the temperature equalisation if two fluids with different pressures and temperatures are brought together in a long narrow pipe. The schematics of such a device together with a brief introduction of the elementary theory behind the Comprex compressor can be found in [54].

The idea of supercharging the intake air on IC engines is not new, but has in the past mostly been used on stationary CI engines operating at constant speed or in race cars. Fitting a turbocharger to a normal SI car is quite clearly not an easy task for the following reasons. First, one major problem when fitting to a turbocharger on a SI engine is engine knocking (fuel mixture detonation). This problem can by minimized by increasing the quality of the fuel e.g. increasing the gasoline octane number and/or by fuel additives like lead. Increasing the octane number is costly and lead additives are now prohibited for environmental reasons. Hence, the only really effective method to avoiding engine knocking is by engine compression ratio reduction. However, the engine's fuel efficiency is thereby also reduced. Secondly, it is only recently that the turbocharging technology has reached such level of maturity that the wide flow range experienced in CI/SI engines for private transportation can be attained, while at the same time maintaining a reasonable compressor efficiency. Third, the automotive industry is very cost sensitive. Overall earnings per car in the range of 1% of the sales price in this industry is rather the rule than the exception. Thus, a costly component like a turbocharger or compressor is only introduced in middle class cars if it is really necessary from the competitive point of view.

Thus, it is only in recent years that downsized supercharged SI/CI engines in larger numbers are starting to emerge in the automotive market. The growth in the diesel market has been so dramatic, though, that turbocharged diesel engines are

[3] A clutch is sometimes included in the compressor transmission for noise and/or fuel consumption reasons.

ruling the CI engine market today.

For the reasons presented above turbocharger modelling is becoming more and more necessary in off-line simulations and for engine control system design. It has here been decided to investigate turbomachinery with variable nozzle geometry since this seems to be the turbocharger technology for the present and near future.

2.3.2 Turbocharger parameters

The characteristics of a turbine or compressor are often provided in maps. These maps relate turbomachinery quantities like isentropic efficiency, mass flow rate, pressure ratio and rotational speed together. An example of a compressor map is shown in figure 2.2. The actual mapping process itself is normally carried out at constant rotational speeds as implied by figure 2.2. These lines of constant speed will in this text, adopted from [83], be referred to as 'speedlines'.

Turbocharger flow rate ($\dot{m}_c$ or $\dot{m}_t$) and rotational speed (N_c or N_t) are in the maps normally corrected with respect to upstream conditions. This is done in order that the characteristics of the turbocharger can be represented by just one map (loss temperature dependencies are however neglected).

It is customary to correct the parameters in one of the following two ways,

$$N_{c/t,c} = \frac{N_{c/t}}{\sqrt{T_{01}}} \qquad \dot{m}_{c/t,c} = \frac{\dot{m}_{c/t}\sqrt{T_{01}}}{p_{01}} \tag{2.10}$$

or

$$N_{c/t,c} = \frac{N_{c/t}}{\sqrt{\frac{T_{01}}{T_{01,ref}}}} \qquad \dot{m}_{c/t,c} = \frac{\dot{m}_{c/t}\sqrt{\frac{T_{01}}{T_{01,ref}}}}{\frac{p_{01}}{p_{01,ref}}} \tag{2.11}$$

where the subscript 01 refers to upstream stagnation conditions. The latter correction method, used by Garrett[4] (see e.g. [14]), will be adopted here.

2.3.3 Centrifugal compressor model

2.3.3.1 Compressor elementary

The centrifugal (radial) compressor consists of four basic components or sections:

- A stationary inlet casing (vaned or vaneless).
- A rotating impeller.
- A stationary diffuser (vaned or vaneless)
- Collector/Volute

Figure 2.3 shows a sketch of a centrifugal compressor with a vaneless inlet and diffuser. These components have the following functions:

[4]Now part of Allied Signal

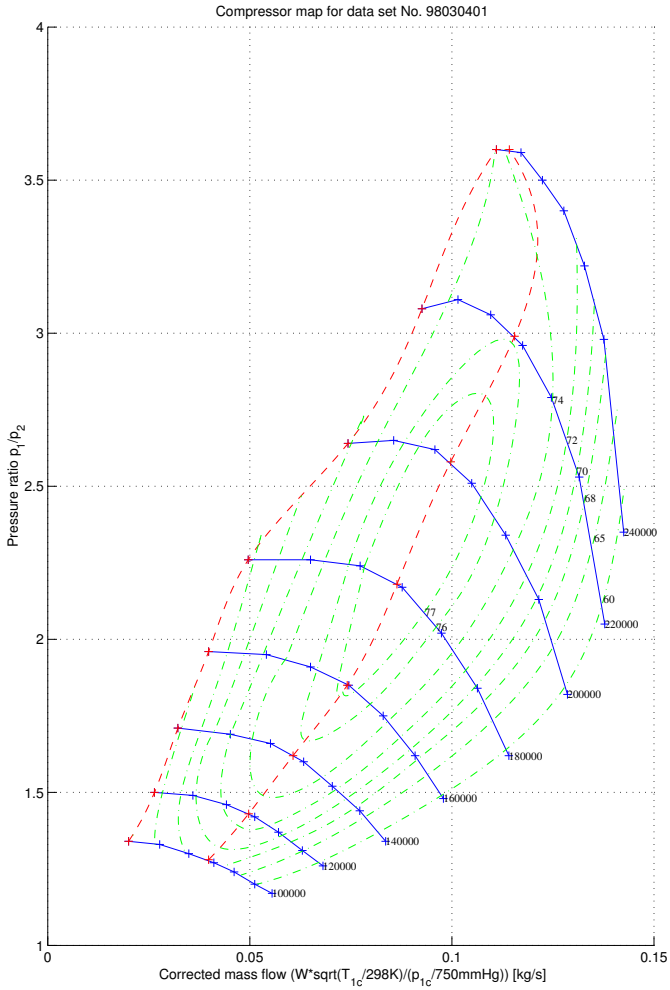

Figure 2.2: Compressor map of a Allied Signal centrifugal compressor with back-sweep impeller, splitter blades, and vaneless diffuser. The two dashed lines are the surge line and maximum efficiency line, respectively, left to right.

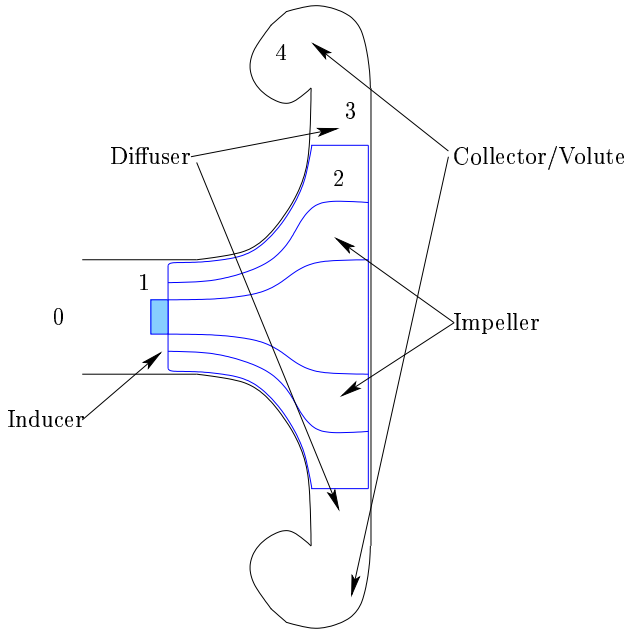

Compressor components/sections	
0:	Inlet casing
1:	Inducer
2:	Impeller
3:	Diffuser
4:	Collector/Volute

Figure 2.3: Centrifugal compressor components.

First, the inlet casing is responsible for guiding the air to the inducer (impeller inlet). Since the compressor efficiency is strongly affected by the air flow inlet angle relative to the blade angle some inlet casings are equipped with guide vanes such that the flow inlet angle is as optimal as possible. The optimal vane angle is however a function of the inlet gas velocity (see figure 2.20 on page 90). Hence, inlet vanes are normally omitted in automotive turbochargers due to the large inlet flow velocity variation experienced in an engine.

Second, the impeller is normally the only moving part in an automotive compressor and is probably the most important compressor component. This component is responsible for lowering the gas velocity relative to the impeller blades i.e. turning velocity (kinetic energy) into a static pressure as close as possible to the adiabatic compression curve, while accelerating the gas with as few losses as possible in the rotational direction.

Third, the diffuser's job is to turn the high exit gas velocity into static pressure by slowing the gas carefully down to an acceptable level. The conversion is accomplished due to the increase of the cross sectional area. This component is in some cases, like the inlet casing, equipped with guide vanes to improve the diffusion process. However, the efficiency is highly dependent upon the inlet angle. Hence the diffuser used is normally of the vaneless type.

Finally, the gas is collected in the collector and sent to the compressor outlet. The cross sectional area is increased along the flow path, hence the name volute, leading to further diffusion.

The gas process described can be depicted in an enthalpy-entropy diagram. An illustrative example of such a diagram is depicted in figure 2.4. The enthalpy-entropy diagram enables inspection of the different departures from isentropic compression in the stage. Station 00 represents ambient conditions. The gas is first speeded up on its way to the inducer thus lowering the dynamic enthalpy by the quantity $\frac{C_1^2}{2}$. The actual energy transfer taking place in the impeller is indicated by the path 1-2. The departure from isentropic compression is mainly due to collision and friction losses in the impeller channels when the compressor is operated in the stable region of the compressor map. The path 2-3-4 describes the gas diffusion process from impeller outlet to collector outlet. If the diffusion process were ideal the stagnation pressure would be raised by $\frac{C_2^2}{2}$ to the p_{02} level. The diffusion is however not accomplished isentropically, and the some kinetic energy still remains at the stage exit (e.g. due to mass conservation). Hence the static pressure delivered at the compressor outlet is p_4.

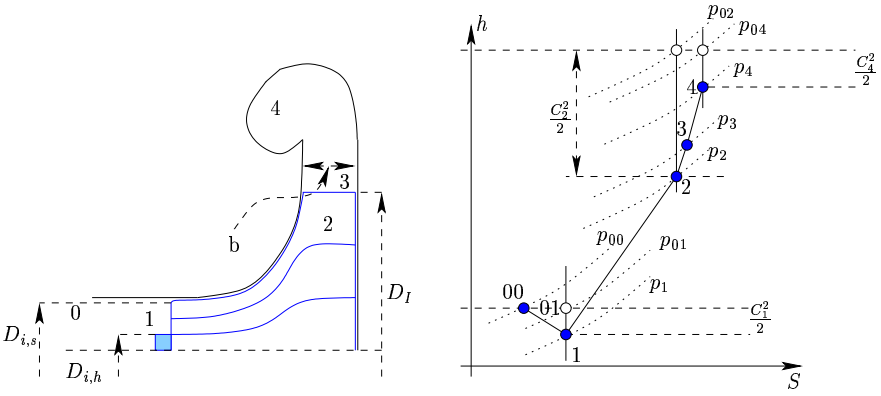

Figure 2.4: Centrifugal compressor entropy–enthalpy diagram

The impeller, as mentioned previously, is the only component in the compressor stage where mechanical energy is transformed into thermodynamic energy. The total increase in specific enthalpy thus is

$$\Delta h_{0c} = h_{04} - h_{00} = h_{02} - h_{00} = h_{02} - h_{01} \tag{2.12}$$

This specific energy consumption can be derived by investigating the changes in gas velocity from impeller eye (inducer) to impeller tip. Figure 2.5 illustrates the velocity distribution at the impeller eye.

Since the blade speed between hub and shroud differs it is in the literature customary to use the blade diameter, D_1 ,that divides the inlet area into two annuli

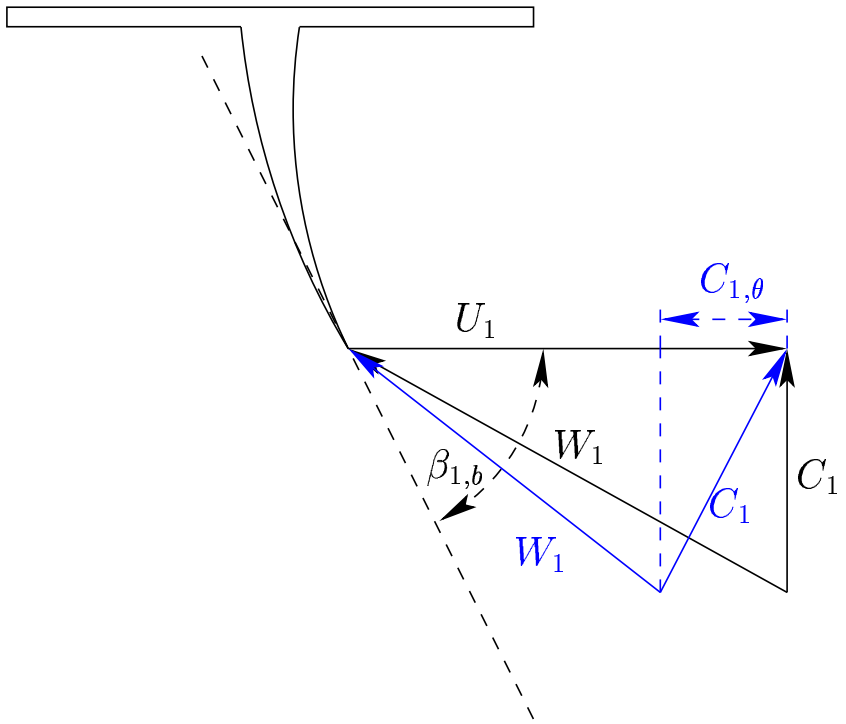

Figure 2.5: Inducer velocity triangles. The blue triangle and the black triangles show the velocity distribution with and without pre-whirl, respectively

of equal area for speed calculations, thus

$$D_1^2 = \frac{1}{2}\left(D_{i,h}^2 + D_{i,s}^2\right) \tag{2.13}$$

where $D_{i,h}$ and $D_{i,s}$ are the hub and shroud diameter of the inducer, respectively. Whence, the tangential speed of the impeller eye, U_1, at this diameter is

$$U_1 = \frac{D_1}{2} \times \omega_C = \frac{\pi D_1 N_c}{60} \tag{2.14}$$

The air is entering the inducer at this diameter with the absolute velocity C_1. Given the blade and gas velocities the gas velocity relative to the impellers blades, W_1, can found from the following vectorial relationship[5],

$$W = U - C \tag{2.15}$$

The torque exerted on the impeller on the inlet side can thus be found to be,

$$\tau_1 = \frac{\dot{m}_c D_1 C_{1,\theta}}{2} \tag{2.16}$$

since the angular momentum of the gas is the moment of linear momentum. Hence, the torque exerted is the product of the mass flow $\dot{m}_c$, radius and the tangential velocity component, $C_{1,\theta}$.

The energy transfer to the impeller on the inducer side is found as the product of the torque and angular speed, ω_c,

$$P_1 = \tau_1 \omega_c = \dot{m}_c U_1 C_{1,\theta} \tag{2.17}$$

The velocity triangle at the impeller tip is shown in figure 2.6.

The figure shows the ideal velocity triangle (no slip) together with the actual velocity triangle. The term *slip factor* expresses the ratio between the tangential component of the absolute velocity and either one of the tangential velocities; under ideal conditions or the impeller tip speed. Thus, slip, σ, is defined as

$$\sigma \triangleq \frac{C_{2,\theta}}{C_{2,\theta b}} \qquad \text{or} \qquad \sigma \triangleq \frac{C_{2,\theta}}{U_2} \tag{2.18}$$

The slip phenomenon is discussed in more detail in section 2.3.3.2.

The torque exerted on the air by the impeller, τ_2, is again found from angular momentum considerations to be

$$\tau_2 = \frac{\dot{m}_c D_2 C_{2,\theta}}{2} \tag{2.19}$$

and the power consumed is

$$P_2 = \tau_2 \omega_c = \dot{m}_c U_2 C_{2,\theta} \tag{2.20}$$

[5]The subscripts are omitted, since velocity triangles are in general constructed according to equation 2.15.

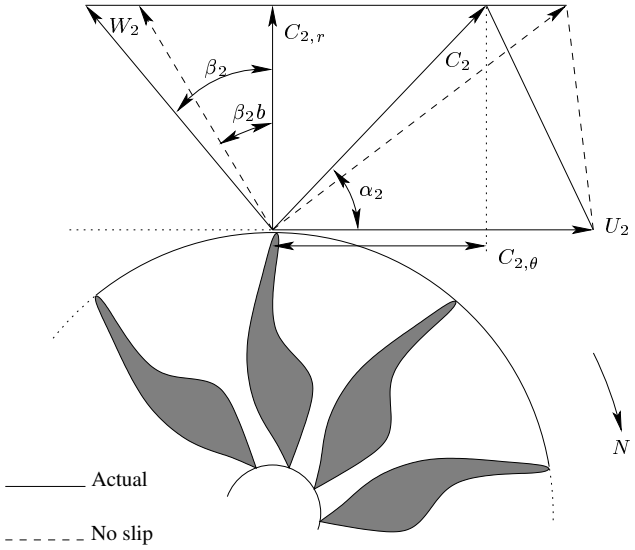

Figure 2.6: Velocity triangle at the impeller tip.

The impeller power consumption, P_c, can now derived from equation 2.17 on the facing page and 2.20 on the preceding page to be

$$\boxed{P_c = \dot{m}_c \Delta h_{0,c} = P_2 - P_1 = \dot{m}_c \left(U_2 C_{2,\theta} - U_1 C_{1,\theta}\right)} \tag{2.21}$$

This formula is also known as the Euler equation. In order to shed more light on the energy transfer, one must revert to the velocity triangles drawn in figure 2.5 and in figure 2.6. The relative velocity, W, at impeller exit or inlet is given by

$$W^2 = U^2 + C^2 - 2UC_\theta \tag{2.22}$$

Using this expression the Euler equation can be rewritten as

$$P_c = \dot{m}_c \frac{1}{2} \left[\underbrace{\left(C_2^2 - C_1^2\right)}_{\text{Absolute kinetic energy change}} + \underbrace{\left(U_2^2 - U_1^2\right)}_{\text{Centrifugal energy change}} + \underbrace{\left(W_1^2 - W_2^2\right)}_{\text{Relative kinetic energy change}} \right] \tag{2.23}$$

The first term in this alternative form of the Euler equation represents the absolute kinetic energy change in the impeller. The second term represents the change in centrifugal energy as the gas is moved from one radius of rotation to another. This rotational energy raises the static pressure in the impeller. Finally, the static impeller pressure is also changed as the velocity relative to the impeller changes. This contribution is represented by the third term in equation 2.23

Most of the compressors, if not all, in automotive turbochargers are constructed without stationary pre-whirl vanes in front of the inducer. Pre-whirl vanes enhance

the compressor efficiency around some mass flow design point. The efficiency outside the design region, however, will be tempered dramatically. This hampers the employment of pre-whirl vanes in compressors experiencing large mass flow variations e.g. automotive compressors. The theory presented in the literature (see [83], [87] and [40]) states that the tangential component (whirl) of the air approaching the inducer is negligible. Thus, the enthalpy transfer described by the Euler formula in equation 2.21 on the page before reduces to

$$\Delta h_{0,c} = \frac{P_c}{\dot{m}_c} = U_2 C_{\theta,2} \tag{2.24}$$

Using the slip definition $\sigma \triangleq \frac{C_{2,\theta}}{U_2}$ this equation may be rewritten as

$$\boxed{\Delta h_{0,c} = \sigma U_2^2} \tag{2.25}$$

Thus, the specific energy transfer is dependent on the impeller speed alone if the slip factor is assumed constant.

2.3.3.2 Slip

The slip phenomenon is experienced under all normal flow conditions, since the inertia (mass) of the gas prevents the tangential gas velocity from matching the tangential blade velocity. The gas will thus rotate relative to the impeller channel, but in the opposite direction. Whence the tangential velocity of the gas, $C_{2,\theta}$, leaving the impeller will be smaller than the ideal tangential velocity (U_2 for a radial designed impeller) due to this relative rotation. The phenomenon is sought illustrated by the impeller tip schematics in figure 2.7.

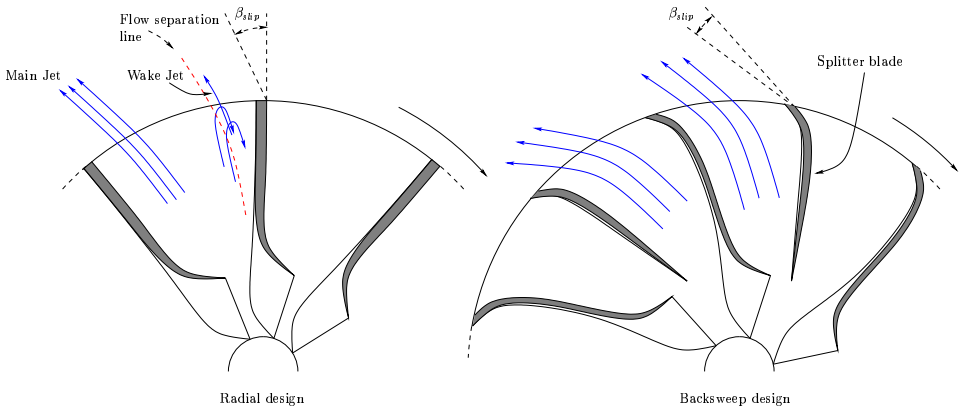

Figure 2.7: Relative flow conditions for a radial impeller without splitter blades and an impeller of the backsweep type with splitter blades, along with an illustration of the flow separation at the impeller outlet

The figure shows the schematics of an impeller with radial design and a backsweep impeller with splitter blades, respectively, together with the relative gas velocity along the blades. The problem of using radial impellers vs. backsweep impellers in automotive applications is clear from the figure. Due to the harder radial acceleration of the gas in the radial case the pressure difference between the pressure side (blade front side) and the suction side (blade backside) is larger. Hence, the chance of flow separation and thus compressor surge is greater. The backsweep impeller, however, accelerates the gas more gently[6], and together with the use of splitter blades the pressure difference between the pressure- and suction side of the impeller blade is smaller. Thus, the surge region of backsweep impeller compressors is smaller providing the backsweep impeller with a larger stable operating range compared to that of the radial type. The maximum energy transfer for a backsweep impeller, however, will be lower due to the lower tangential gas velocity at the impeller tip.

The existence of this pressure difference between the pressure- and suction side of the impeller leads to an obvious velocity difference between the gas exiting the impeller at the suction side and pressure side, respectively. The existing flow is so to say split in a "main jet stream" and a "wake jet stream". It is stated in [87] that the "wake jet flow" comprises approximately 15% of the mass flow but occupies 35% of the impeller exit area for a radially vaned impeller close to the surge region. This, of course, complicates the mean velocity computation of the gas leaving the impeller.

An empirical attempt to describe the speed conditions at the impeller tip within the confines of one-dimensional modelling is by the use of the *slip factor* definition. This factor is explained below.

It is customary in the literature (see [83], [87] and [40]) to express the idealness of the compressor as the ratio between the actual tangential gas velocity, $C_{\theta,2}$, and the ideal absolute exit velocity, $C_{2,\theta b}$, or the impeller tip speed, U_2. This ratio is known as the *slip factor* and is, as mentioned, defined by

$$\sigma \triangleq \frac{C_{2,\theta}}{C_{2,\theta b}} \tag{2.26}$$

or

$$\sigma \triangleq \frac{C_{2,\theta}}{U_2} \tag{2.27}$$

The slip factor, σ, can be increased by increasing the number of impeller blades. The added viscous drag from the blades will hamper the relative gas rotation at the cost of larger frictional losses and added manufacturing complexities. Numerous models for the slip factor exist in the literature, [117] and [36]. Most of these models are based solely on design parameters. One such fixed slip factor formula,

[6]The effective channel path of a backsweep impeller is longer compared to a radial impeller for the same impeller diameter

which can be applied to both backsweep type and radial vaned impellers, is presented in [87] and is repeated here,

$$\sigma = \frac{1}{1 + \frac{\pi}{2(1-\epsilon)Z\left(1-\frac{D_{i,s}}{D_I}\right)\cos\beta_{2,b}}} \tag{2.28}$$

with ϵ = 0.3 for a radial vaned impeller and 0.2 for a backsweep impeller.

However, the slip factor is known to vary with mass flow, [87], [115] and [15]. A mass flow dependent slip factor formulation is presented in [15] (see also [83]). The formula, known as the Reffstrup slip factor, is repeated in equation 2.29.

$$\boxed{\sigma = \frac{C_{\theta,2}}{U_2} = 1 + \phi\tan\beta_{2,b} - \frac{1}{2}\left(1 - e^{\frac{-2\pi\cos\beta_{2,b}}{Z}}\right)} \tag{2.29}$$

where ϕ is the ratio between radial gas velocity, $C_{2,r}$, and impeller tip speed,

$$\phi = \frac{C_{r,2}}{U_2} = \frac{\dot{m}_c}{\rho_2\pi D_I b U_2} \tag{2.30}$$

Z is the number of impeller blades, D_I impeller outlet diameter, b impeller outlet width, and ρ_2 is the static outlet gas density.

The Reffstrup slip formula will be used throughout the rest of the compressor modelling work in this text, since it includes a dependency on the mass flow rate. The eminent importance of this mass flow dependency will become clear in section 2.3.3.5 on page 79.

Remark: The slip angle, β_2, and impeller blade angle, $\beta_{2,b}$, are defined counterclockwise. Hence, both angles are negative for backsweep type impellers.

2.3.3.3 Total energy transfer or Δh_{0c} modelling

The total energy transfer to the compressor can be found by combining equation 2.25 on page 72 and the Reffstrup slip factor. Thus, the following structure of the Euler equation is obtained

$$P_c = \dot{m}_c\Delta h_{0c} = \dot{m}_c U_2^2\left(1 + \phi\tan\beta_{2,b} - \frac{1}{2}\left(1 - e^{\frac{-2\pi\cos\beta_{2,b}}{Z}}\right)\right) \tag{2.31}$$

The factor multiplying the squared impeller tip speed may be split in a constant and mass flow dependent part, thus the specific energy transfer takes the following form

$$\Delta h_{0c} = U_2^2\left(a + b\frac{\dot{m}_C}{U_2}\right) \tag{2.32}$$

where

$$a = 1 - \frac{1}{2}\left(1 - e^{\frac{-2\pi\cos\beta_{2,b}}{Z}}\right) \qquad \text{and} \qquad b = \frac{\tan\beta_{2,b}}{\rho_2\pi D_I b} \tag{2.33}$$

Since it is assumed that all gases can treated as perfect gases the enthalpy rise across the compressor stage may formulated as

$$\Delta h_{0c} = h_{02} - h_{01} = c_p \left(T_{02} - T_{01} \right) \tag{2.34}$$

The "total to total" isentropic efficiency[7], $\eta_{c,TT}$, is defined as the ratio between the total specific energy transfer and the specific energy transfer required for an isentropic compression, thus

$$\eta_{c,TT} \triangleq \frac{\Delta h_{0c,i}}{\Delta h_{0c}} = \frac{T_{02,s} - T_{01}}{T_{02} - T_{01}} \tag{2.35}$$

The relation between pressure and temperature for an isentropic process is repeated in equation 2.36

$$p_r = \frac{p_{02}}{p_{01}} = \left(\frac{T_{02,s}}{T_{01}} \right)^{\frac{\gamma}{\gamma - 1}} \tag{2.36}$$

The expression for the total specific energy transfer as function of ambient conditions, stage efficiency and pressure ratio may now be found by combining equations 2.34, 2.35 and 2.36.

$$\Delta h_{0c} = \frac{c_p T_{01}}{\eta_{c,TT}} \left(p_r^{\frac{\gamma - 1}{\gamma}} - 1 \right) \tag{2.37}$$

Utilizing the equations 2.32 and 2.37, the impeller speed, stage efficiency, mass flow and pressure ratio may be related.

$$\boxed{\Delta h_{0c} = \frac{c_p T_{01}}{\eta_{c,TT}} \left(p_r^{\frac{\gamma - 1}{\gamma}} - 1 \right) = U_2^2 \left(a + b \frac{\dot{m}_c}{U_2} \right)} \tag{2.38}$$

2.3.3.4 Compressor data

Having developed the background for one dimensional compressor modelling in the preceding sections the one dimensional compressor model's accuracy with real data will now be examined. It has been decided to evaluate the final physical compressor model, to be finalized in the coming sections, based on data for three different compressors to prove the model's generality. The intermediate results obtained for compressor A, however, will only be presented for the sake of clarity and convenience. The data for the compressors, all manufactured by Allied Signal Ltd., are listed in table 2.1.

All the compressors have the same design except for the trim size ($D_{i,s}$–D_I ratio, see [14] and figure 2.4). Although the difference on the outer diameter of the inducer, $D_{i,s}$, seems negligible, the effect on the compressor characteristic is

[7]The difference between "total to total" and "total to static" efficiency is often negligible for most compressors calculations, since the volute exit velocity is small

	Compressor A	Compressor B	Compressor C
Manufacture	Allied Signal Ltd.	Allied Signal Ltd.	Allied Signal Ltd.
Compressor Type No.	C101 E(44)	C101 E(44)	C101 E(44)
Impeller diameter [mm]	44	44	44
Trim	55	50	45
A/R	0.33	0.33	0.33
Main blade No.	6	6	6
Splitter blade No.	6	6	6
Impeller tip width* [mm]	4	4	4
Inducer dia. (hub)* [mm]	12	12	12
Inducer dia. (shroud) [mm]	32.6	31.1	29.5
Impeller tip angle* [°]	-45	-45	-45
Inducer blade angle* [°]	-40	-40	-40

Table 2.1: Experimental compressor specifications. **Remark**: Measures marked with * are found by local dismantling of the turbocharger and should such be treated of more descriptive than accurate.

tremendous. The importance of trim setting is evident when comparing the characteristics of the compressors in figure 2.8, 2.9 and 2.10. A trim decrease loosely speaking moves the whole of the compressor map closer to the abscissa. An interesting effect of a trim decrease is the movement of the so called stonewall (maximum mass flow for a given impeller speed). However, the effect is as expected since the inducer by design is the flow limiting component of the compressor, and hence a natural consequence of the radial gas velocity deceleration/radial stage area enlargement. Whence, the radial area must increase along the impeller channel to convert the radial kinetic energy into pressure.

Another interesting observation, confirming a typical problem, is the notorious lack of data points at low pressure ratios[8].

The use of the compressor data presented in the figures 2.8, 2.9 and 2.10 is complicated by the fact that the efficiency data point and speedline data point indices do not coincide. To overcome this problem interpolated efficiency values are computed for each speedline point. Speedline data points necessitating an efficiency extrapolation are omitted.

The computation of the interpolated efficiency surface is outline in the following. First a data grid is constructed by Delaunay data triangulation, see [32] and [80], such that each data point is connected to its natural neighbors. This set of triangles based on the scattered compressor data are then used to define what data points are appropriate in a subsequent identification procedure. This way of defining properness for an interpolation point is fortunate, since interpolation indices that are not contained within a triangle may be discarded i.e. data extrapolation can be avoided; a property clear from figure 2.11. Having defined interpolation point properness and identification data a cubic interpolation is carried out forcing the efficiency surface through each data point.

[8]Compressor map points at lower impeller speed are often not provided by the manufacturer. The reason is rather obvious; the small temperature increase across the stage at such operating point makes it difficult to assess the compressor accurately.

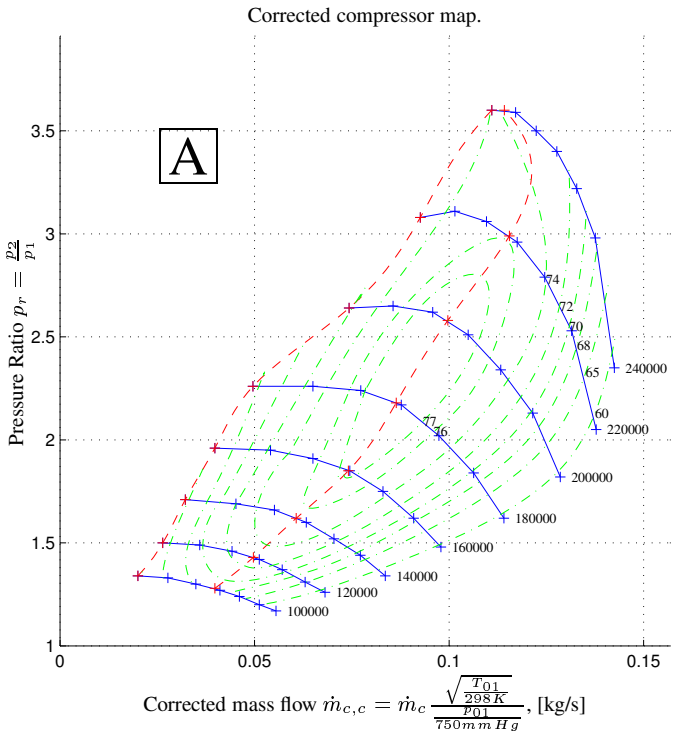

Figure 2.8: Compressor A efficiency and flow characteristics together with surge line and maximum efficiency line. The data points are marked with '+'

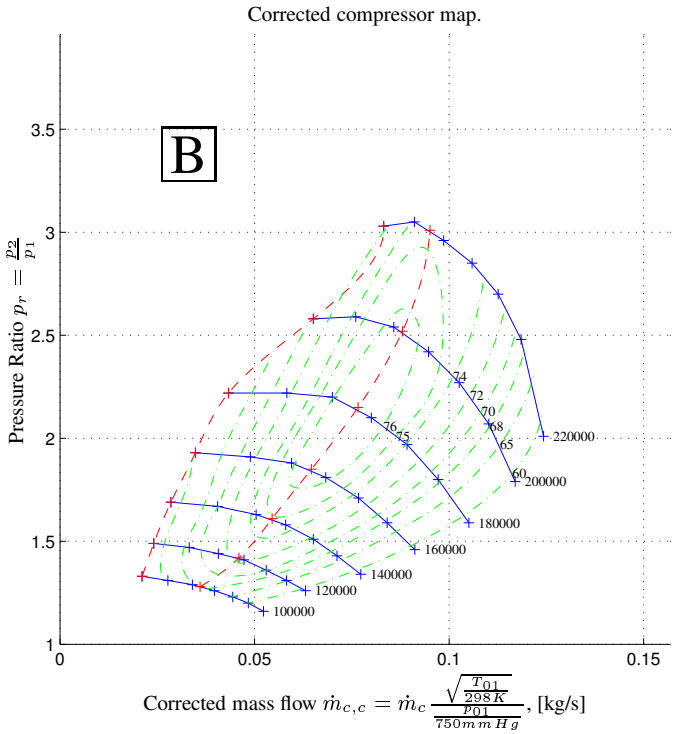

Figure 2.9: Efficiency and flow characteristics for compressor B

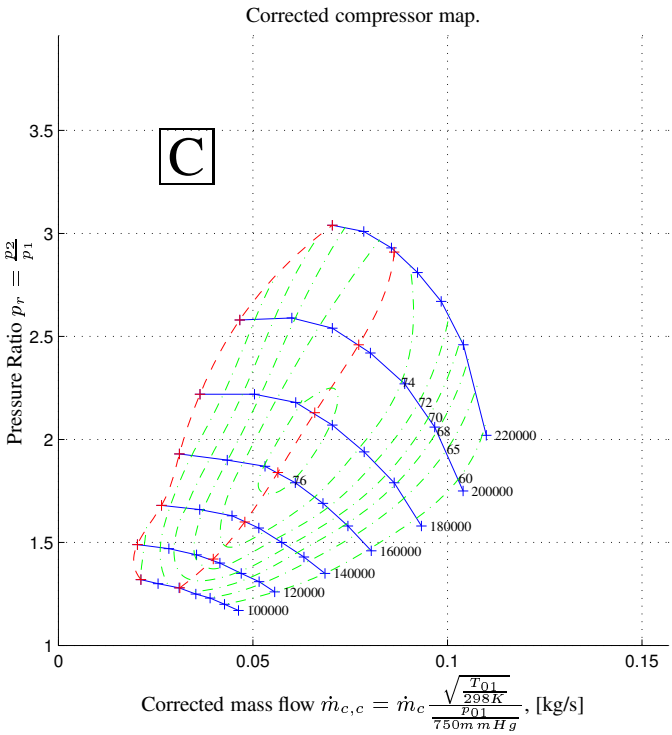

Figure 2.10: Efficiency and flow characteristics for compressor C

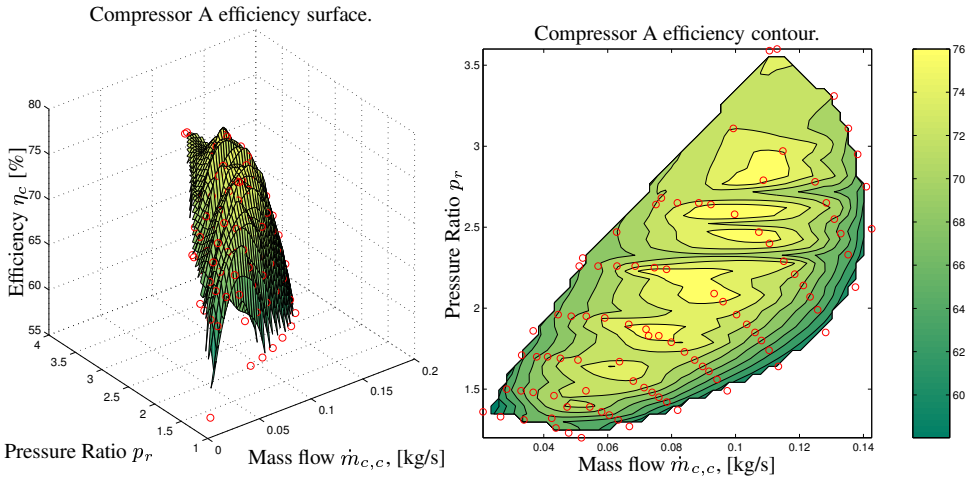

Figure 2.11: Interpolated efficiency surface and contour for compressor A.

2.3.3.5 Δh_{0c} model deduction from data

The specific enthalpy speedlines may be derived by using equation 2.37 on page 75. The computed enthalpy speedlines are plotted in figure 2.12. Looking at the speedlines in the left plot the importance of a correct efficiency estimation is evident. The difference between the speedlines based on interpolated efficiency data and the speedlines derived using the mean value of the efficiency data is not negligible.

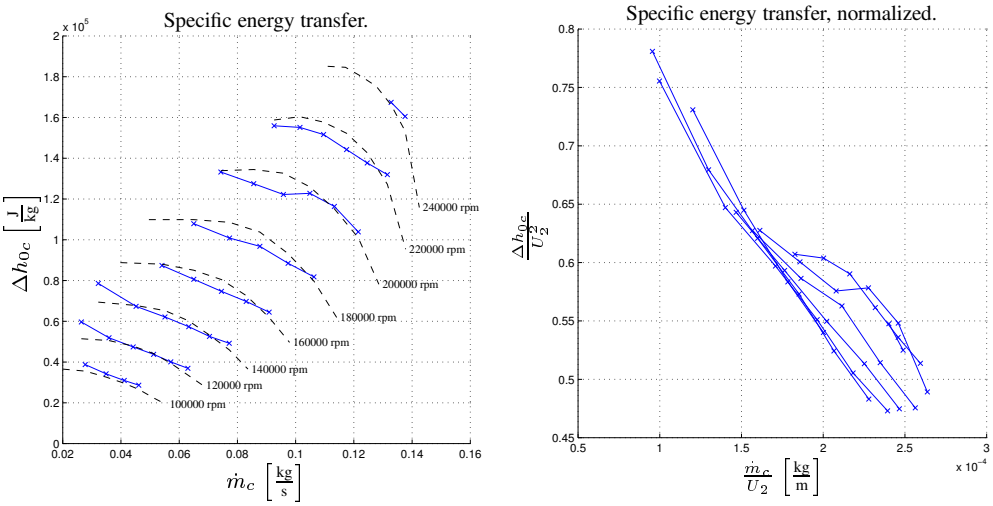

Figure 2.12: The left plot, on basis of the interpolated efficiency surface computed, shows the specific enthalpy speedlines. Speedline points necessitating efficiency extrapolation are omitted. The dashed enthalpy speedlines are derived using the efficiency mean value. The normalized enthalpy speedlines are plotted in the right figure.

It was found in section 2.3.3.3 on page 74, equation 2.32, that the total specific energy transfer can also be deduced from the impeller speed and mass flow. This equation is repeated below for the sake of convenience.

$$\Delta h_{0c} = U_2^2 \left(a + b \frac{\dot{m}_c}{U_2} \right) \tag{2.39}$$

According to [83] the coefficients a and b may be regarded as constants for a given speed under the assumption that the gas density stays constant throughout the impeller channel. The validity of this statement is to some extent confirmed by the structure of the speedlines in the right plot in figure 2.12, since the the individual speedlines are almost linear functions of $\frac{\dot{m}_c}{U_2}$. The statement may, however, be tested since a is given by geometric data alone and the varying parameter in b is static density at the impeller tip, ρ_2. Hence, the only assumption which has to be tested is the validity of the $\rho_2 \equiv \rho_1$ assumption. This will be tested in the following.

The enthalpy at the impeller tip and volute exit are related in the following manner

$$c_p T_c + \frac{C_c^2}{2} = c_p T_4 + \frac{C_4^2}{2} = c_p T_2 + \frac{C_2^2}{2} \tag{2.40}$$

The density at the impeller tip, ρ_2, may be derived as

$$\rho_2 = \rho_c \left(\frac{T_c}{T_2} \right)^{\frac{1}{1-\gamma}} \tag{2.41}$$

under the assumption that the diffuser and volute are lossless i.e. the kinetic energy available at the impeller tip is transformed into pressure isentropically. This assumption is justifiable for the whole operating range of a compressor with vaneless diffuser, since the diffuser and volute losses together only comprise a maximum of 5% of the total enthalpy losses according to [87] and [40].

The specific kinetic energy at the impeller tip, E_k, may be found by using the velocity triangle in figure 2.6 and the slip factor definition

$$\begin{aligned} E_k &= \frac{1}{2} \left(C_{2,r}^2 + C_{2,\theta}^2 \right) \\ &= \frac{1}{2} \left(\left(\frac{\dot{m}_c}{\rho_2 \pi D_I b} \right)^2 + \sigma^2 U_2^2 \right) \end{aligned} \tag{2.42}$$

The kinetic energy remaining at stage exit is often of minor importance i.e. the exit velocity is negligible. Hence, the enthalpy equation in equation 2.40, may be reduced without any loss of generality to

$$c_p T_c = c_p T_0 4 = c_p T_2 + \frac{C_2^2}{2} \tag{2.43}$$

The temperature T_2 may now implicitly be computed from equation 2.41, 2.42 and 2.43 by computing the minimum quadratic criterion

$$J_{min} = \min_{T_2} \left(T_2 - T_c + \frac{E_k}{c_p} \right)^2 \tag{2.44}$$

Figure 2.13 depicts the iteratively computed impeller temperature, T_2, and impeller density,ρ_2. The stage outlet temperature T_c is derived from compressor data as

$$T_c = T_{01} \left[1 + \frac{1}{\eta_{c,TT}} \left(p_r^{\frac{\gamma-1}{\gamma}} - 1 \right) \right] \tag{2.45}$$

and the density as

$$\rho_c = \frac{p_r p_{01}}{R T_c} \tag{2.46}$$

and are include in the figure as boundary conditions. The figure clearly shows that the assumption $\rho_2 = \rho_1$ used in [83] is not valid. The static impeller tip density

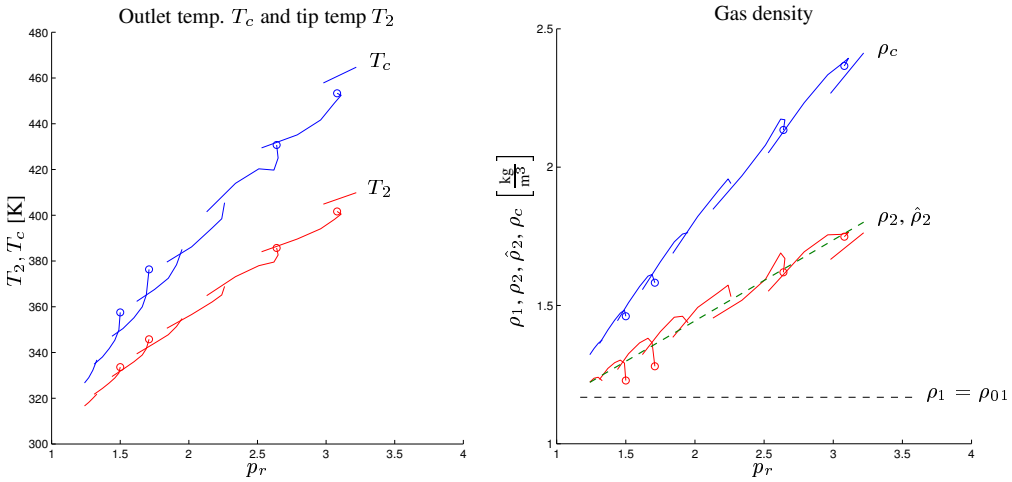

Figure 2.13: The left plot shows the iteratively computed impeller tip temperature, T_2, speedlines together with the outlet temperature, T_c. Using these temperatures the gas densities ρ_2 and ρ_c may be found. The computed densities are illustrated in the plot to the right together with a linear fit of the impeller density, $\hat{\rho}_2$. Computations utilizing surge data are marked with $\circ$.

is approximately 50% larger than ρ_1 in the high pressure region of the compressor map.

The question is how this knowledge can be include in a model for the total specific energy transfer, h_{0c}. The kinetic energy available at the impeller tip can from the above discussion be derived based on the impeller velocity triangle. Having computed this energy, the temperature T_2 may be found analogous to equation 2.43. But since the triangle itself is temperature dependent, the solution to T_2/ρ_2 will be of implicit nature if this method of calculation is chosen. To overcome this hurdle it is decided here to utilize the apparently linear relationship in figure 2.13 between the pressure ratio p_r and the impeller tip density ρ_2. Whence, a descriptive value for ρ_2 is found as

$$\boxed{\rho_2 = \alpha_{\rho 2} p_r + \xi_{\rho 2}} \tag{2.47}$$

The identified parameters for all three compressors are listed in table 2.2.

	$\alpha_{\rho 2}$ $\left[\frac{\text{kg}}{\text{m}^3}\right]$	$\xi_{\rho 2}$ $\left[\frac{\text{kg}}{\text{m}^3}\right]$	$(\alpha_{\rho 2} + \xi_{\rho 2})\vert_{p_r=1}$ $\left[\frac{\text{kg}}{\text{m}^3}\right]$	ρ_{01} $\left[\frac{\text{kg}}{\text{m}^3}\right]$	$\sigma^2 \cdot 10^{-3}$ $\left[\frac{\text{kg}^2}{\text{m}^6}\right]$
Compressor A	0.2924	0.8359	1.1283	1.1680	1.348
Compressor B	0.2971	0.8680	1.1651	1.1680	0.652
Compressor C	0,3181	0,8359	1.1540	1.1680	0.990

Table 2.2: Identified parameter for $\hat{\rho}_2 = \text{f}\,(p_r)$.

The generality of the functional dependency found between p_r and ρ_2 is confirmed by the small variance around the identified line, and by the fact that the ρ_2

estimate for the boundary condition $p_r = 1$ is very close to the ambient gas density, $\rho_1 = \rho_{01}$.

The ordinate in figure 2.12's right plot is normalized by the identified $\hat{\rho}_2$ function. The result is illustrated in figure 2.14. The normalization leads to a further regularization of the normalized enthalpy speedlines.

The green dashed line in Figure 2.12 shows the best linear fit for the $\left(\frac{\dot{m}_c}{\hat{\rho}_2 U_2}, \frac{\Delta h_{0c}}{U_2^2}\right)$ data set. The identified slope, $\hat{a}$, and constant, $\hat{b}$, of the line are estimates of a and b in a rewritten form of equation 2.32 on page 74

$$\boxed{\Delta h_{0c} = U_2^2 \left(a + b\frac{\dot{m}_c}{\rho_2 U_2}\right)} \tag{2.48}$$

with

$$a = 1 - \frac{1}{2}\left(1 - e^{\frac{-2\pi \cos \beta_{2,b}}{Z}}\right) \qquad \text{and} \qquad b = \frac{\tan \beta_{2,b}}{\pi D_I b} \tag{2.49}$$

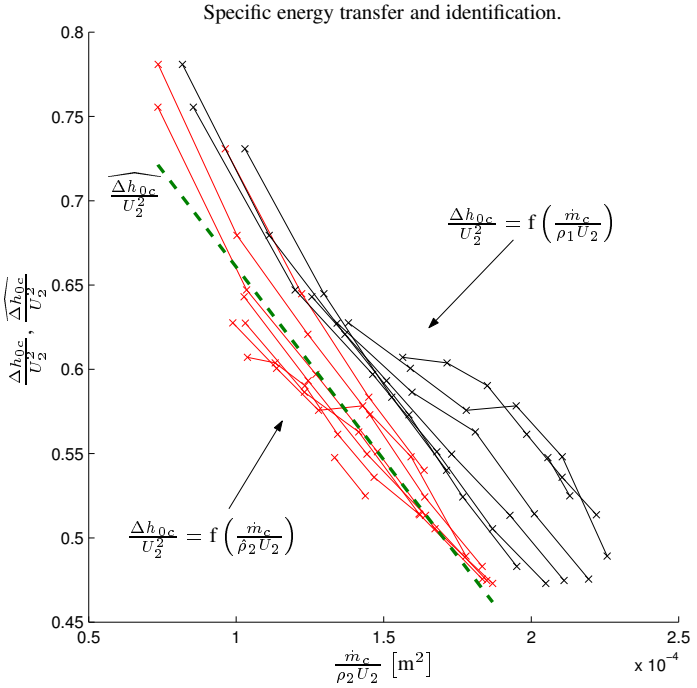

Figure 2.14: Non- (black solid) and ρ_2 (red solid) normalized energy curves. The dashed green line is the best general fit forced through the ρ_2 normalized energy speed curves.

In contrast to equation 2.32, the a and b parameters in equation 2.48 are only dependent upon geometrical compressor specifications. This is thus a identification procedure which is no longer operating point dependent.

	$\hat{a}$	$\hat{b} \cdot 10^3 \left[\frac{1}{\mathbf{m}^2}\right]$
Compressor A	0.8893	-2.2865
Compressor B	0.8443	-2.2102
Compressor C	0.8280	-2.4138
	a	$b \cdot 10^3 \left[\frac{1}{\mathbf{m}^2}\right]$
Geometric	0.8571	-2.1554

Table 2.3: Identified a and b parameters for the three compressors.

The identified parameters for all compressors are listed in table 2.3 together with the coefficients based on geometrical specifications.

The agreement between theory and data is good. The linear description found in equation 2.48 can estimate the total specific energy transfer to the compressor with good accuracy.

The Δh_{oc} model validity is confirmed further by figure 2.15. Furthermore, the convex effect of the impeller tip density, ρ_2, on the speedlines is evident on the high speed curves ($N_c \geq 180$ krpm).

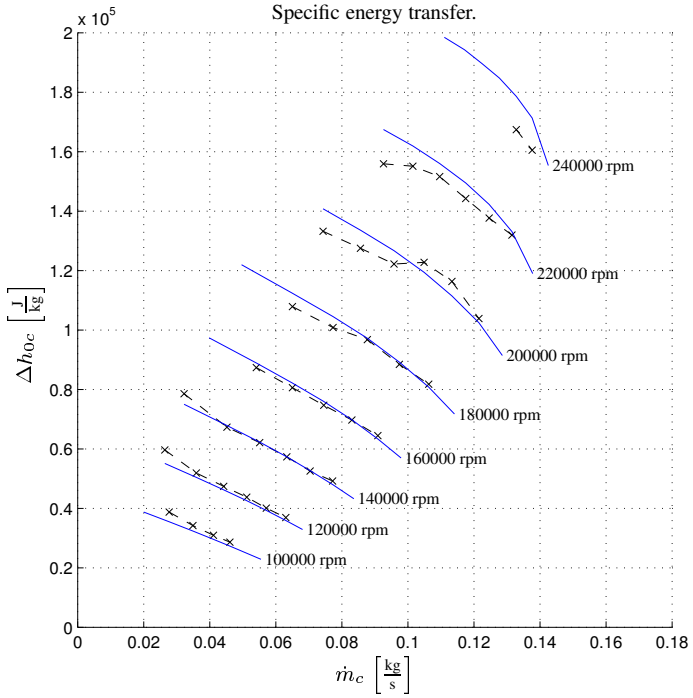

Figure 2.15: Δh_{0c} speedlines for compressor A. The dashed black speedlines are measurement data and the blue lines are derived using equation 2.48.

The slip phenomenon is revisited as an addition to this section. In the iterative search procedure for T_2 it is necessary to compute the slip factor, σ. The slip factor

is derived from the measurements as

$$\sigma = \frac{\Delta h_{0c}}{U_2^2} \tag{2.50}$$

The tangential gas velocity, $C_{2,\theta}$, can be found by trigonometry as[9],

$$C_{2,\theta} = U_2 + C_{2,r} \tan \beta_2 \tag{2.51}$$

Inserting equation 2.50 in 2.51 and using the mass conservation law β_2 is found to be

$$\beta_2 = \arctan\left(\frac{\pi(\sigma - 1)U_2 \rho_2 D_I b}{\dot{m}_c}\right) \tag{2.52}$$

Equation 2.52 makes it possible to study compressor slip as the mass flow through the compressor is varied. This is seen in the plot to the left in figure 2.16. The general tendency independent of impeller speed is a β_2 increase as the compressor mass flow is increased. The plot right in the figure depicts the calculated slip factor. The slip factor decreases here in agreement with the theory developed as the mass flow increases.

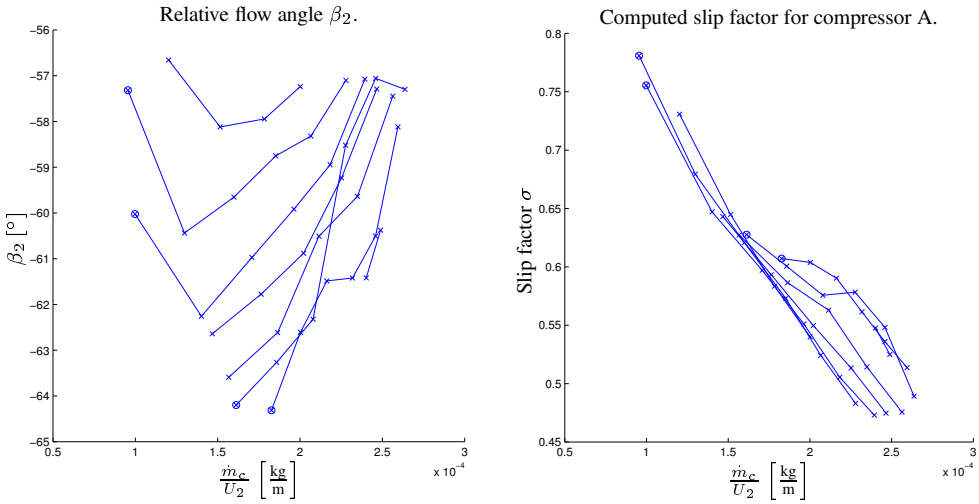

Figure 2.16: The left plot depicts the computed angle, β_2, of the relative outlet velocity W_2. The corresponding computed slip factors are illustrated in the plot to the right. Computations utilizing surge data are marked with ∘.

2.3.3.6 Speedline shapes

The previous section provides an important paradigm in understanding the shape of the speedlines based on geometry alone. It was found that the specific energy consumed by the compressor, Δh_{0c}, may be described by two parameters, a slip

[9]Remark: β_2 is negative for a backsweep impeller.

factor, σ, and the squared impeller tip velocity, U_2^2. The level of slip is very important in predicting the specific energy consumed, Δh_{0c}, by the compressor, and is fundamentally speaking a measure of the ratio between the tangential velocity of the gas leaving the impeller and the impeller tip speed. Whence, the slip should not be mistaken for a loss, but rather the compressor's ability to transfer energy. The slip level is found to be dependent upon two geometrically given constants a and b, and one operating point dependent parameter $\frac{\dot{m}_c}{\rho_2 U_2}$.

The pressure ratio p_r across the the stage can be found from equations 2.37 and 2.48 to be

$$p_r = \left(\frac{\eta_{c,TT} \Delta h_{0c}}{c_p T_{01}} + 1 \right)^{\frac{\gamma}{\gamma-1}} = \left(\frac{\eta_{c,TT} U_2^2 \left(a + b \frac{\dot{m}_c}{\rho_2 U_2} \right)}{c_p T_{01}} + 1 \right)^{\frac{\gamma}{\gamma-1}} \tag{2.53}$$

where the parameter a is a positive constant. The sign of b is impeller blade angle dependent

$$\begin{aligned} b > 0, &\quad \text{forward sweep impeller, } \beta_{2,b} > 0 \\ b = 0, &\quad \text{radial impeller, } \beta_{2,b} = 0 \\ b < 0, &\quad \text{backsweep impeller, } \beta_{2,b} < 0 \end{aligned} \tag{2.54}$$

Note that the solution to p_r is implicit due to the functional dependence between ρ_2 and p_r.

The transformation of enthalpy into pressure for a radial and backsweep impeller, respectively, are illustrated in figure 2.17 and figure 2.18. According to equation 2.48 the enthalpy rise across a radial stage during stable compressor operation (no choke and surge operation) is only rotational speed dependent. These constant enthalpy speedlines are transformed into constant p_r speedlines if the stage efficiency is assumed constant. However, the actual structure is convex since the enthalpy losses grow rapidly as the surge region or stonewall is approached.

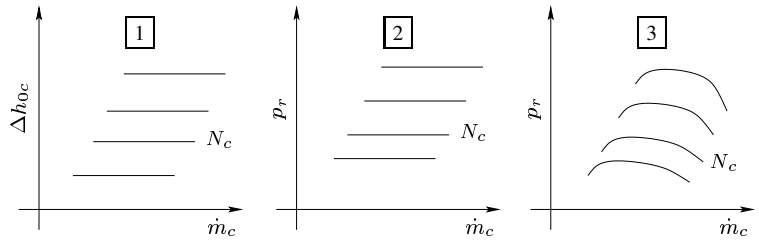

Figure 2.17: Energy transfer illustration for compressor with radial impeller. 1 The enthalpy speedlines are constant since $b = 0$. 2 Assuming fixed compressor efficiency the enthalpy speedlines are mapped into constant p_r speedlines. 3 Typical characteristics of a compressor with a radial impeller.

The enthalpy speedlines for a backsweep impeller, neglecting the convex effect of ρ_2, are linearly decreasing with the mass flow, $\dot{m}_c$. Hence, p_r will be concave in

the idealized case due to the exponent $\frac{\gamma}{\gamma-1}$. The actual shape is convex though due to the characteristics of the enthalpy losses.

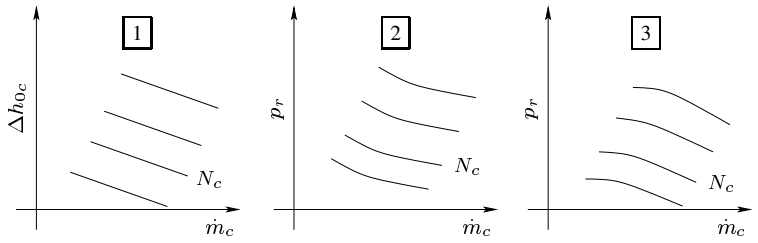

Figure 2.18: Illustration of energy transfer for a compressor with backsweep impeller. 1 The enthalpy speedlines are approximately linear decreasing functions of the compressor mass flow $\dot{m}_c$. 2 Assuming fixed compressor efficiency the enthalpy speedlines are mapped into concave p_r speedlines due to the exponent $\frac{\gamma}{\gamma-1}$. 3 Typical characteristics of a compressor with backsweep impeller design.

The qualitative effect of the compressor efficiency can be seen from the diagrams i.e. the energy losses increase rapidly as the mass flow moves higher (approaching the stonewall) or lower (approaching the surge region) away from the point of maximum efficiency with the latter being the most aggressive of the two. Thus, the missing link in a quantitative understanding of the compressor behavior is a loss model.

2.3.3.7 Energy losses or Δh_{loss} modelling

The compressor pressure- and efficiency characteristics are often modelled separately (see [63], [91], [108] and [61]). However, applying this methodology, the connection between the two models is lost i.e. the total error level when combining the models may be unacceptable due to an unfortunate mathematical interfacing of the models. Hence, it is decided here to develop an efficiency model as close to the level of physics allowed by one-dimensional modelling such that the compressor may be understood from a comprehensive picture instead of just a collection of arbitrary equations. A positive side effect to this approach is the simultaneous creation of a rough design tool compressor.

The stage efficiency definition in equation 2.35 on page 75 can be expressed in terms of specific energies

$$\eta_{c,TT} = \frac{\Delta h_{0c,i}}{\Delta h_{0c,i} + \Delta h_{loss}} \tag{2.55}$$

where

$$\begin{aligned} \Delta h_{0c} &= \Delta h_{0c,i} + \Delta h_{loss} \\ \Delta h_{0c,i} &= c_p T_{01} \left(p_r^{\frac{\gamma-1}{\gamma}} + 1 \right) \end{aligned} \tag{2.56}$$

The total compressor loss given by the specific energy Δh_{loss} originates from several sources. Some of the sources are listed below:

Clearance: A small clearance, l_{cl}, between impeller wheel and the shroud side of the housing exist due to manufacturing tolerances and temperature variations. Due to this clearance some mixing between the channels will occur. An approximative value of the mixing loss in terms of efficiency degradation is given below (see [40] and [92]).

$$\eta_{cl} = 0.3 \frac{l_{cl}}{b}$$

where b is the impeller tip width. However, the clearance is normally so small that clearance losses can safely be neglected.

Back flow: Due to the acceleration of the fluid across the stage a pressure gradient between the suction side and pressure side of the impeller blade exist (see the discussion in section 2.3.3.2 on page 72). Hence, some of the fluid leaving the impeller will be re-injected if the local kinetic energy level is too low to overcome this suction force. One-dimensional modelling of the losses due to this reprocessing process of some of the fluid are sparse in the literature. However, [87] suggests a typical efficiency degradation on the order of 3% points during stable compressor operation.

Volute: A inevitable loss exists due to the volute's inability to convert all the radial kinetic energy out of the diffuser. The approximative value of this loss is within 2–5% points of efficiency [40].

Collision/Incidence: Collision losses are unavoidable in compressors due to off-design angles between the velocity vectors of the impeller respectively fluid. Hence, a fraction of the fluid's kinetic energy will be dissipated.

Friction: Frictional losses are unavoidable with viscous fluids when a speed differences between boundary (surface) and fluid exists.

Heat transfer: An energy leakage to the ambient can not be avoided when a temperature difference between turbocharger housing and the surroundings exists. However, this loss is of minor importance.

According to [87], [83] and [40] the shape of the efficiency characteristic is mainly controlled by

- Incidence losses in the impeller.[10]
- Fluid friction losses in impeller and diffuser.

Therefore, it is decided here to only address the origin and modelling of these two sources.

2.3.3.8 Incidence loss

The biggest collision loss without doubt occurs in the inducer and is most widely modelled by one of the following two approaches [87]:

- The total tangential velocity component of the inlet air is assumed destroyed. This model is referred as the ”NASA shock loss theory”. It should be noted here that the term ”shock” is misleading since that nothing akin to shock waves occurs (supersonic velocities). Instead the expression should be understood as a simple notion used to describe the shape of the compressor characteristic.
- The fluid is deviated from its original direction to the impeller channel inlet normal, just inside the impeller eye following a constant pressure process.

However, the difference between these widely used loss models is negligible when applied to centrifugal compressor modelling according to [87]. The difference mainly lies in the zero loss angle prediction i.e. the angle between the fluid velocity relative to the impeller blades and the inducer velocity at which the loss vanishes. This angle is assumed equal to the inlet blade angle in the ”NASA shock loss theory” model.

Based on the simplicity of the ”NASA shock loss theory” model and the reported the loss estimation accuracy indifference between the two models, the NASA model will be adopted here.

However, a few words of caution should be said before the inducer losses are modelled as incidence loss alone. Depending on the inducer flow conditions and impeller speed another loss may develop and coexist together with the incidence loss - namely stall[11] [87]. Stall, or flow separation, occurs when the magnitude of the kinetic inlet energy falls below a specific point such that the adverse pressure between the pressure- and suction side of the impeller channel cannot be overcome. In the event of this separation, vortices along the suction side develop i.e boundary layer separation occurs. This flow separation is illustrated in figure 2.19. The separated fluid is then re-injected into the main jet (see the discussion of back flow at the impeller tip on page 87). This reprocessing of the fluid naturally introduces a loss. This loss may in some cases actually be audible; the re-injection of the

[10] If a vaned instead of an annular diffuser is used the collision losses here may be of a considerable size during off-design compressor operation and hence call for separate modelling.

[11] Stall may also be experienced in the vaneless diffuser when the adverse pressure gradient cannot be overcome by the kinetic energy of the fluid leaving the impeller.

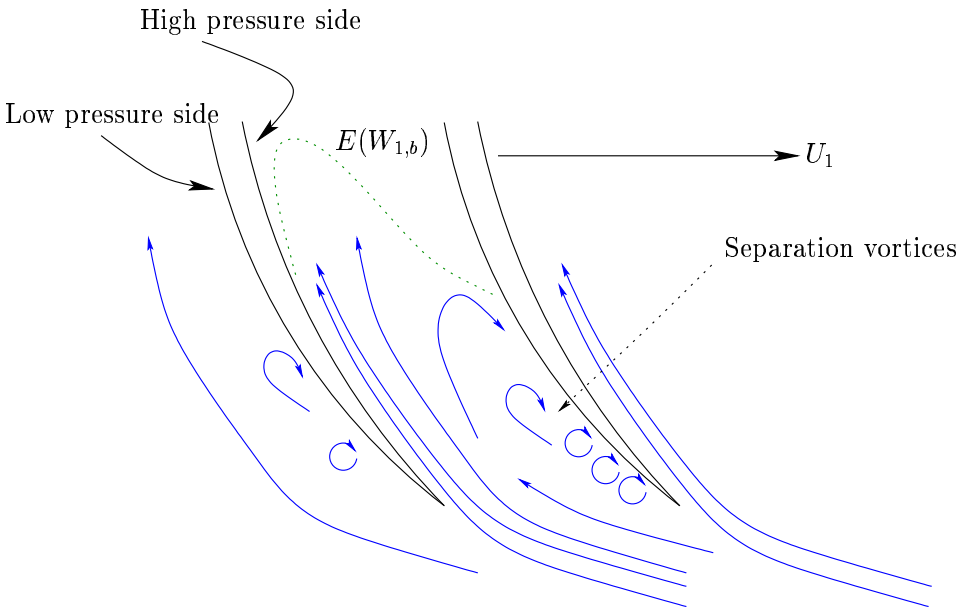

Figure 2.19: Illustration of the flow separation at the inducer

fluid introduces aerodynamically induced vibration in the stage, thus leading to an increase in the noise level.

Inducer stall may contribute to a complete stage stall - surge, but may also occur, depending on the inducer design, in nominally stable operating modes. Further analysis of inducer stall, than presented above, is complicated by the fact that no generic model of this loss exists in the literature [40]. However, stall losses are minimal within the compressor map (see [83]) and will be encompassed by the following incidence modelling work.

Figure 2.20 illustrates velocity triangles at the inducer.

According to the "NASA shock loss theory" the incidence loss, $\Delta h_{loss,inc}$, may be described by

$$\Delta h_{loss,inc} = \frac{1}{2} W_{1,\theta}^2 \tag{2.58}$$

The tangential velocity component, $W_{1,\theta,r}$, is in [83] found to be

$$W_{1,\theta,r} = \frac{1}{\cos\beta_1}\left(\sqrt{U_1^2 + C_1^2} + \frac{\cos\left(\beta_1 - \beta_{1,opt}\right)}{\sin\beta_{1,opt}} C_1\right) \tag{2.59}$$

The subscript r indicates the tangential velocity's radial dependence.

Equation 2.59 may after some mathematical manipulation (see appendix A on page 251) be rewritten as

$$W_{1,\theta,r} = U_1 + C_1 \cot\beta_{1,opt} \tag{2.60}$$

The tangential velocity, $W_{1,\theta}$, and thus the incidence loss $\Delta h_{loss,inc}$, is most often in the literature derived at the diameter that splits the inducer (impeller eye)

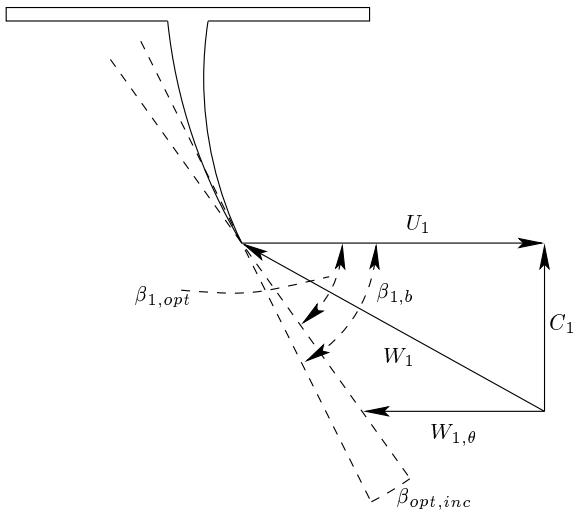

Figure 2.20: Inducer velocity triangles in the no inlet pre-whirl case.

in two circles of equal area, $D_1^2 = \frac{1}{2}\left(D_{i,s}^2 + D_{i,h}^2\right)$, (see e.g. [83], [87] and [40]). In this work a more generic approach, which will outlined in the following, will be introduced.

The inflow conditions are shown diagrammatically in figure 2.21 together with a frontal view of the impeller eye. The green dashed line in front illustrates the assumed turbulent velocity profile of the fluid approaching the impeller blades.

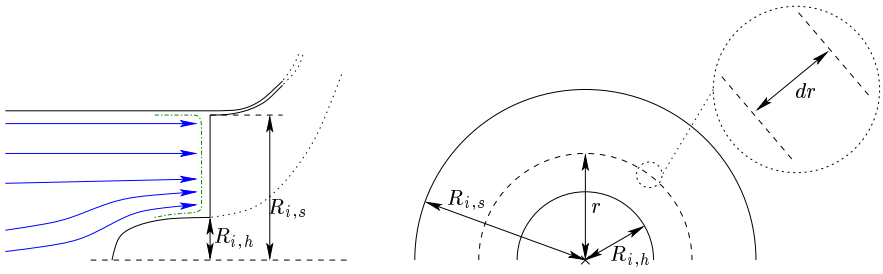

Figure 2.21: A sketch of the inducer flow conditions is seen to the left. A frontal view of the impeller together with dimensions are depicted to the right.

Instead of applying the area averaging diameter an area averaging function is sought. This function may be found based on the impeller eye diagram to the right in figure 2.21.

The area of the ring with thickness dr is given by

$$\begin{aligned} dA &= \pi \left((r + dr)^2 - r^2 \right) \\ &= \pi \left(2r dr + dr^2 \right) \end{aligned} \tag{2.61}$$

and constitutes the following fraction of the effective inducer inlet area

$$\mathrm{f}(r) = \frac{dA}{\pi \left(R_{i,s}^2 - R_{i,h}^2 \right)} = \frac{2r\,dr + \overbrace{\left(dr^2 \right)}^{\nearrow (=0)}}{R_{i,s}^2 - R_{i,h}^2} \tag{2.62}$$

The total enthalpy loss due to incidence may now be found by averaging the local incidence loss over the impeller eye inlet area. Hence, equation 2.58, 2.60 and 2.62 are combined to find that

$$\Delta h_{loss,inc} = \frac{1}{R_{i,s}^2 - R_{i,h}^2} \int_{r=R_{i,h}}^{R_{i,s}} r \left(U_1(r) + C_1(r) \cot \beta_{1,opt}(r) \right)^2 dr \tag{2.63}$$

Assuming that the velocity profile of the inflow is turbulent, the spatial radial velocity variation of C_1 may be neglected. This assumption is reasonable in light of the turbulence created by the impeller blades. Thus, a solution to the integral in equation 2.63 is found as

$$\begin{aligned} \Delta h_{loss,inc} = \frac{1}{R_{i,s}^2 - R_{i,h}^2} \Bigg(& \frac{\pi^2 N_c^2 \left(R_{i,s}^4 - R_{i,h}^4 \right)}{60^2} + \frac{\pi N_c C_1 \cot \beta_{1,opt} \left(R_{i,s}^3 - R_{i,h}^3 \right)}{45} \\ & + \frac{C_1^2 \cot^2 \beta_{1,opt} \left(R_{i,s}^2 - R_{i,h}^2 \right)}{2} \Bigg) \end{aligned} \tag{2.64}$$

by substituting the tangential inducer velocity, U_1, with

$$U_1(r) = \frac{2\pi r N_c}{60} \tag{2.65}$$

In the solution to equation 2.63 the blade angle, flow angle, β_1, and hence optimal inlet angle, $\beta_{1,opt}$ are assumed constant. An interesting consequence of this assumption is that an incidence loss independent of the operating mode will always be present (see appendix B on page 253). Hence the conclusion given in [83] stating that incidence and friction losses can be treated separately is not valid.

2.3.3.9 Frictional loss

Viscous friction will always be present when a fluid moves relative to a surface. Hence, a large amount of frictional loss can be expected in turbo machinery due the complex bends and turns experienced by the fluid as it flows through the stage.

The frictional loss is in the literature mainly attributed to be mass flow, $\dot{m}_c$, or relative velocity, W_1, dependent. In [40] and [87] the specific energy loss in the impeller due to friction is modelled as a turbulent flow in a smooth circular pipe. Thus

$$\begin{aligned} \Delta h_{loss,fric} &= 4f\frac{l}{D}\frac{W_1^2}{2} \\ f &= 0.3164\,(Re)^{-0.25}, \qquad \text{Blasius' formula} \end{aligned} \tag{2.66}$$

where D is the mean hydraulic diameter of the channel ($D = \frac{4\text{Area}}{\text{Perimeter}}$), l is the mean length of the impeller channel, and Re is the Reynolds number

$$Re = \frac{\rho D W_1}{l\mu} \tag{2.67}$$

Müller modelled in [83] the loss in specific energy due to friction, $\Delta h_{loss,fric}$, by a simple power function of the mass flow.

$$\Delta h_{loss,fric} = c_1 \dot{m}_c^{c_2} \tag{2.68}$$

Both models were applied in a global search for the total enthalpy loss, but in vain.

The same unsuccessful behavior of the mass flow dependent friction model was also observed in [83]. When applied in a global search routine on single speedlines in a KKK (Kühnle, Kopp & Kausch) compressor map the predicted frictional loss became in some cases negative. This unfortunate behavior was attributed to a erroneous level of the estimated energy transfer Δh_{0c}. However, the estimated values of the coefficients c_1 and c_2 for the individual speedlines vary a great deal, and the quality of the proposed friction model in [83] is thus dubious. The reason should rather be found in the following:
Separation losses in the inducer were in [83] sought included in the incidence loss by a single coefficient K, hence

$$\Delta h_{loss,inc} = K\frac{W_{1,\theta}^2}{2} \tag{2.69}$$

The value of K was derived for the speedlines of a KKK backsweep compressor and found to vary between 2.12 (60 krpm) and 4.02 (180 krpm). This would mean that the separation loss should account for 53% to 75% of the total incidence loss according to the incidence loss definition. These values are altogether too large considering the sensitivity of stable compressor operation to separation losses.

The reason for the dubious incidence loss level should rather be attributed to the form of the friction model given in [83] than the separation loss level. The assumption of spatial uniform turbulent impeller flow is not valid for the following reasons:

- Except for the energy transfer explained by the Euler equation other mechanical energy to thermodynamical energy transfer mechanisms takes place. One such energy transformation is due to the viscous friction between the shroud wall and fluid enclosed in the impeller channel. This energy transfer will be referred to as *Shroud side energy transfer*. The energy transfer is best pictured in a scenario where the impeller inlet and outlet are closed. As the impeller turns some mechanical energy will be converted into rotational energy and the enclosed fluid will begin to rotate around an axis along the impeller channel. However, since only the shroud side wall is moving a frictional force between the fluid and the remaining three impeller walls will exist. This frictional loss may in specific energy be roughly modelled like $\Delta h_{loss,fric,1} = \alpha_1 U_2^2$.

- Due to the impeller rotation the fluid experiences heavy tangential acceleration on its way through the impeller channel. Hence, the velocity profile does not correspond to that of a steady turbulent pipe flow, but rather reassembles the profile sketched in figure 2.19. Furthermore, the normal force perpendicular to the impeller blade differs between the pressure side and suction side of the channel and the fluid will begin to rotate around axis parallel to the turbo shaft i.e. some of the translational energy is transformed into rotational energy. However, due to the inertia of the fluid, a speed difference between surface and fluid, and therefore also friction, will exist. A rough model of this friction is $\Delta h_{loss,fric,2} = \alpha_2 W_{1,b} U_2$, since the friction force, which is a function of the normal force, depends on the rotational speed and the level of friction on the velocity relative to the blade.

- Hub friction. This friction is best understood if the impeller does not rotate. The fluid enters inducer, travels along the channel and enters the diffuser. Thus, the fluid leaves the impeller with a vector perpendicular to the compressor axis. The fluid experiences in this scenario a difference in the normal force perpendicular to the impeller hub wall and impeller shroud wall, respectively, due to conservation of momentum. Thus, some of the kinetic energy will be transformed into rotational energy. However, the transformation is not perfect and some of the energy will be lost as friction. A simple rough model of this loss is $\Delta h_{loss,fric,3} = \alpha_3 W_{1,b}^2$.

The three modes of energy transfer are sketched in figure 2.22. It should be noted here that the radius of the eddies described not necessarily occupy the whole control volume, but may be separated in several large and small scale motions.

It is clear from the discussion above that other energy transfers, than explained by the Euler equations, occur. However, these energy transfers are included in the

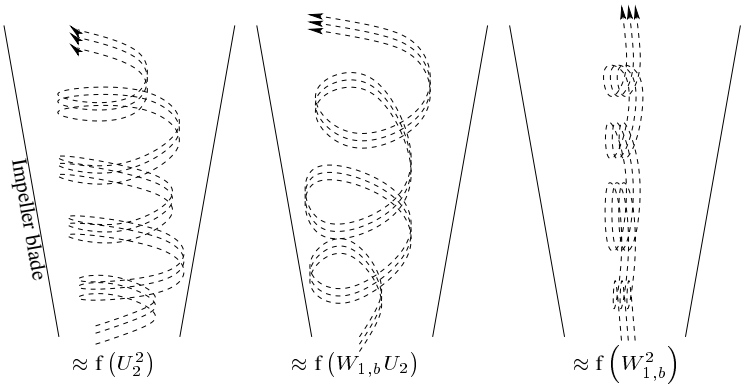

Figure 2.22: Illustrative sketches of the rotational energy components in the impeller flow.

slip factor. Hence, a global acceptable model of the friction loss is

$$\begin{aligned}\Delta h_{loss,fric} &= \Delta h_{loss,fric,1} + \Delta h_{loss,fric,2} + \Delta h_{loss,fric,3} \\ &= \alpha_1 U_2^2 + \alpha_2 W_{1,b} U_2 + \alpha_3 W_{1,b}^2\end{aligned} \tag{2.70}$$

2.3.3.10 Δh_{loss} model deduction from data

The specific energy loss, Δh_{loss}, may be derived from the data in the following manner

$$\Delta h_{loss} = \frac{1-\eta_c}{\eta_c} c_p T_{01} \left(p_r^{\frac{\gamma-1}{\gamma}} - 1 \right) \tag{2.71}$$

It should be noted again that the compressor efficiency is found by map interpolation (see section 2.3.3.4 on page 75)

The according to equation 2.71 computed energy losses are illustrated in figure 2.23.

The total specific energy loss may be modelled according to the last two sections as

$$\Delta h_{loss} = \Delta h_{loss,fric} + \Delta h_{loss,inc} \tag{2.72}$$

The incidence and friction loss models are repeated below for the sake of convenience.

$$\begin{aligned}\Delta h_{loss,inc} =& \frac{1}{R_{i,s}^2 - R_{i,h}^2} \left(\frac{\pi^2 N_c^2 \left(R_{i,s}^4 - R_{i,h}^4 \right)}{60^2} + \frac{\pi N_c C_1 \cot \beta_{1,opt} \left(R_{i,s}^3 - R_{i,h}^3 \right)}{45} \right. \\ &\left. + \frac{C_1^2 \cot^2 \beta_{1,opt} \left(R_{i,s}^2 - R_{i,h}^2 \right)}{2} \right)\end{aligned} \tag{2.73}$$

$$\Delta h_{loss,fric} = \alpha_1 U_2^2 + \alpha_2 W_{1,b} U_2 + \alpha_3 W_{1,b}^2$$

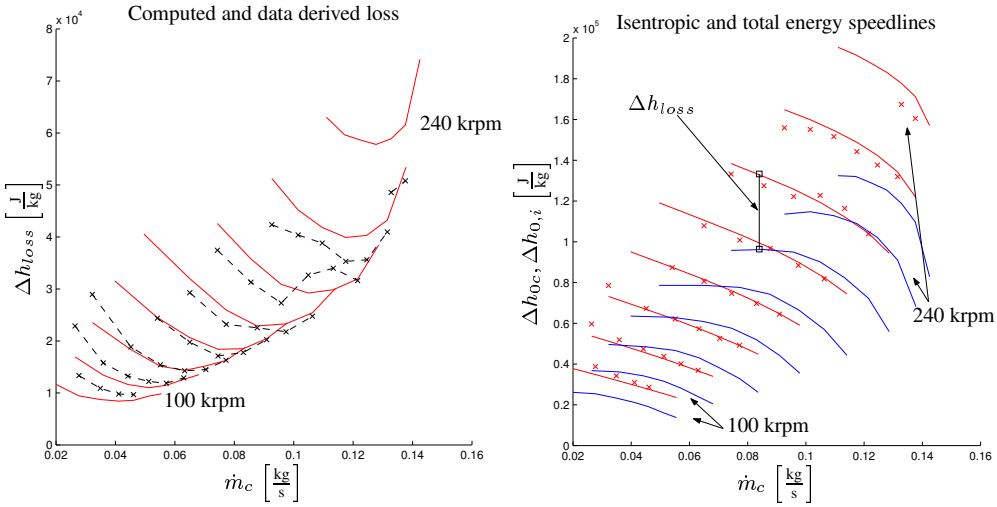

Figure 2.23: The energy losses according to the data for compressor A is in the plot to the left drawn together with the model based deduced losses ($\Delta h_{loss} = \Delta h_{0c} - \Delta h_{0,i}$). The right plot shows the Δh_{0c} model (red solid curves) together with the corresponding data points. The blue curves illustrate the energy required by isentropic compression, $\Delta h_{0,i}$.

The optimal entry angle for the air, $\beta_{1,opt}$, together with the friction coefficients, α_1, α_2 and α_3, are unknown. In order to estimate the coefficients a minimization routine was constructed in MATLAB®, and the cost function numerically minimized was

$$J_{min} = \min_{\theta=\{\beta_{1,opt},\alpha_1,\alpha_2,\alpha_3\}} \left(\frac{\Delta h_{loss}\left(\theta, p_r, N_c, \dot{m}_c\right) - \Delta h_{loss,m}\left(p_r, N_c, \dot{m}_c\right)}{U_2^2} \right)^2 \tag{2.74}$$

The estimation error is normalized with respect to the squared impeller velocity such that the high speed data points are not weighted too much in the computation of J_{min}. The parameters identified for the individual compressor are listed in table 2.4.

	Compressor A	**Compressor B**	**Compressor C**
$\hat{\beta}_{1,opt}$ [°]	-34.7411	-37.4640	-37.4635
$\hat{\alpha}_1$	0.4534	0.3924	0.3811
$\hat{\alpha}_2$	-1.4216	-1.1689	-1.1289
$\hat{\alpha}_3$	1.4999	1.2573	1.2466

Table 2.4: The by equation 2.74 identified compressor parameters.

The optimal entry angle for the fluid is computed to be approximately -36°. This corresponds remarkably well with the findings in [87], where the optimal entry angle according to experiments was found to approximately 9° ahead of the inducer

blade angle. Thus, the computed blade angle is approximately -45° compared to the measured angle of -40°.

Figure 2.24 depicts the incidence- and friction loss curves obtained for compressor A. The two losses are collected in the lower plot and compared to the total enthalpy loss derived from data. The agreement between model and data is reasonable.

Having demonstrated the loss model's ability to describe the incidence- and friction losses, the loss model may be simplified since the friction component and incidence component share the same structure. Therefore, without loss of generality the total loss model may be transformed into

$$\Delta h_{loss} = U_2^2 \left(\kappa_1 \left(\frac{\dot{m}_c}{U_2} \right)^2 + \kappa_2 \frac{\dot{m}_c}{U_2} + \kappa_3 \right) \tag{2.75}$$

However, using the equation above the ability to attribute the loss to different sources is naturally lost.

Table 2.5 shows the parameters, κ_1, κ_2 and κ_3, identified by forcing the enthalpy loss function in equation 2.75 through the loss data set. It is noticed that the

	Compressor A	**Compressor B**	**Compressor C**
$\hat{\kappa}_1 \cdot 10^6$ $\left[\frac{\mathbf{m}^2}{\mathbf{kg}^2}\right]$	9.8313	9.3874	11.9660
$\hat{\kappa}_2 \cdot 10^3$ $\left[\frac{\mathbf{m}}{\mathbf{kg}}\right]$	-4.2866	-3.8306	-4.1834
$\hat{\kappa}_3$	0.6095	0.5360	0.5122

Table 2.5: Identified compressor loss parameter.

loss function apparently gets more mass flow and less rotational speed dependent as the compressor trim setting decreases. The enthalpy loss curve identified for compressor A is shown in figure 2.25. The agreement between data and model is reasonable.

2.3.3.11 Mass flow model

Filling and emptying model structures necessitate description of the incoming and outgoing mass flows in a control volume. Since these models for engine control purposes have proven their versatility in simple engine modelling for control and/or estimation purposes (see e.g. [69, 63, 45, 49, 51, 19, 50], [53], [107], [13], [103], [112] or [22]), it is of course natural to investigate the possibilities in establishing a general model of the compressor mass flow. This way the mandatory description of the inlet mass is provided, and the existing engine model structures based on the filling and emptying model approach may be reused.

A formula for the mass flow through the compressor may be found by combining equation 2.48 on page 82, 2.56 on page 87, 2.47 on page 81,and 2.75 on

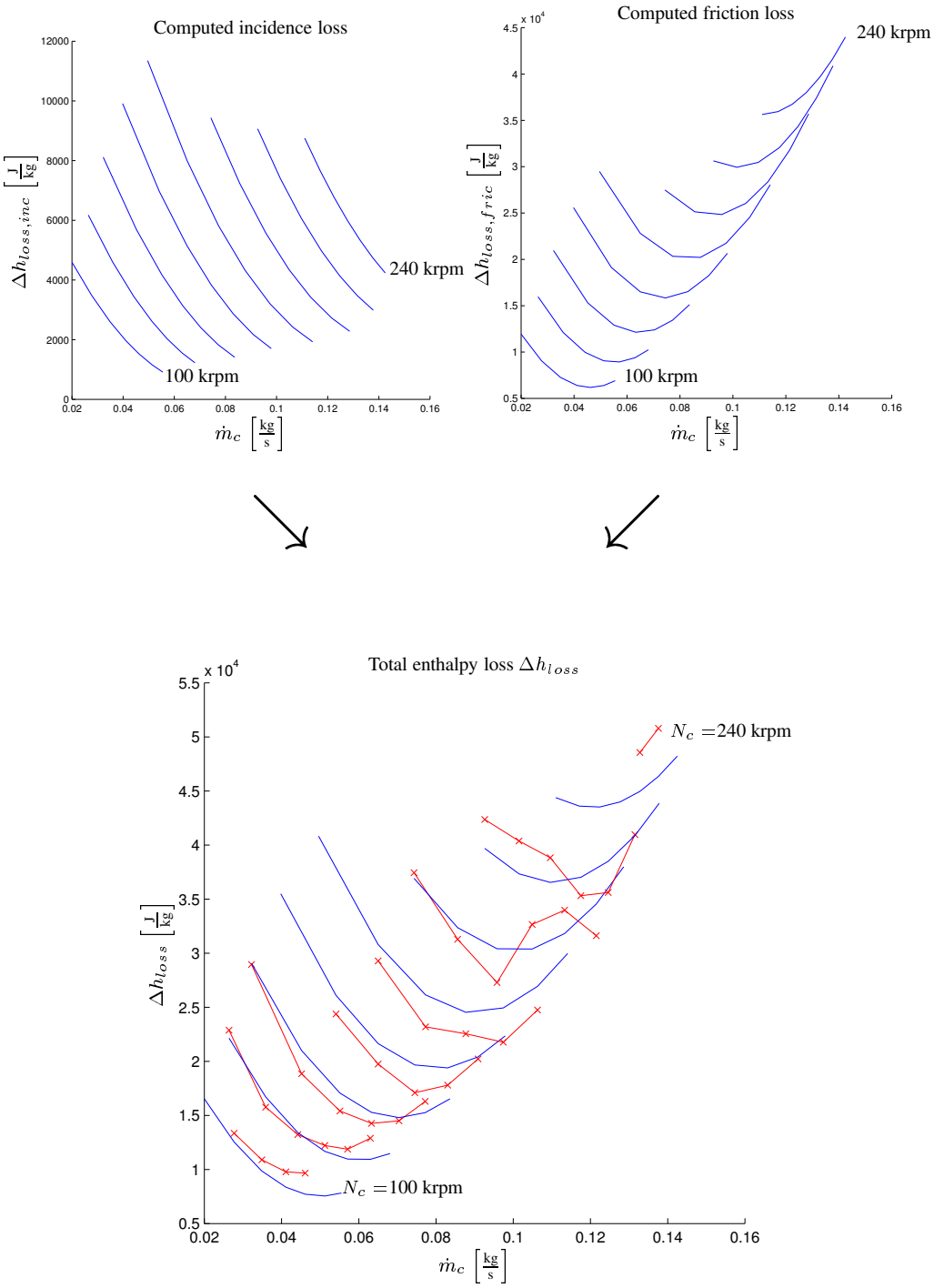

Figure 2.24: The incidence and friction energy losses computed for compressor A. The total enthalpy loss (sum of collision and friction loss) speedlines are compared with measurements in the lower plot. The measurement speedlines are seen as solid red curves with the individual data point marked as '×'.

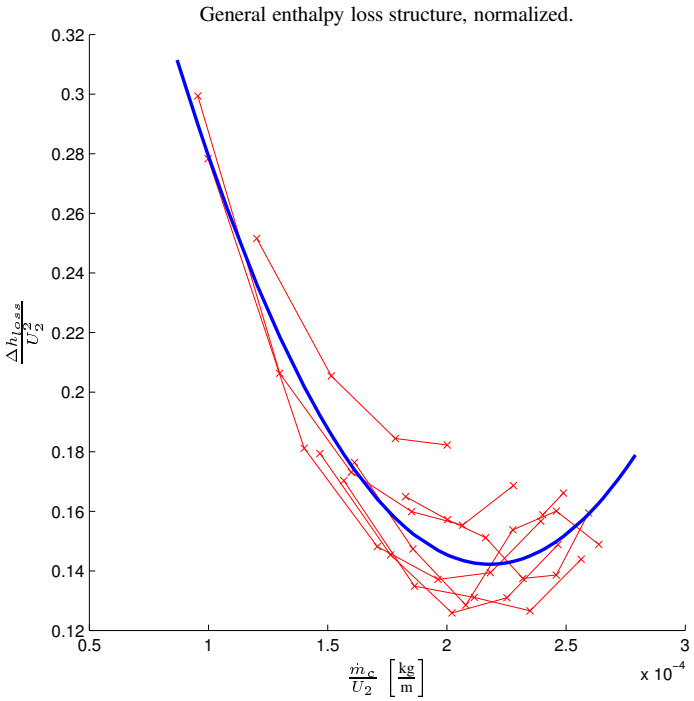

Figure 2.25: Plot of the data point derived loss speedlines, normalized together with the data fitted loss model (Blue solid curve). Data points are marked with $\times$.

page 96.

$$\kappa_1 \left(\frac{\dot{m}_c}{U_2}\right)^2 + \left(\kappa_2 - \frac{b}{\hat{\rho}_2}\right)\frac{\dot{m}_c}{U_2} + \kappa_3 - a + \frac{\Delta h_{0c,i}}{U_2^2} = 0 \tag{2.76}$$

leading to

$$\boxed{\begin{aligned} \dot{m}_c &= \frac{\left(\frac{b}{\alpha_{\rho_2} p_r + \xi_{\rho_2}} - \kappa_2\right) \pm \Phi}{2\kappa_1} U_2 \\ &\text{where} \\ \Phi &= \sqrt{\left(\kappa_2 - \frac{b}{\alpha_{\rho_2} p_r + \xi_{\rho_2}}\right)^2 - 4\kappa_1 \left(\frac{c_p T_{01}\left(p_r^{\frac{\gamma-1}{\gamma}} - 1\right)}{U_2^2} + \kappa_3 - a\right)} \end{aligned}} \tag{2.77}$$

The mass flow model derived gives two solutions for a given (p_r, N_c) operation point, and consequently is of an implicit nature. The physical explanation for this behavior is clear from the speedline shape discussion in section 2.3.3.6 and the loss model which has been derived i.e. the total normalized energy transfer $\frac{\Delta h_{0c}}{U_2^2}$ is primarily found to be a linear function of $\frac{\dot{m}_c}{U_2}$, and the loss model, $\frac{\Delta h_{loss}}{U_2^2}$, is

quadratic in $\frac{\dot{m}_c}{U_2}$. Furthermore, the implicit characteristic is clear from the high speed speedlines in the compressor characteristics presented in section 2.3.3.4 on page 75.

However, the compressor is a *follower* i.e. the steady state compressor mass flow is determined by the pipe system downstream of compressor[12]. Hence the quasi-steady state mass flow may be found using an auxiliary mass flow function. Examples of such auxiliary mass flow functions are

- Throttle mass flow in the SI engine scenario (see eg. [83]).
- Intake port mass flow (minus possible EGR mass low) in a DI/IDI Diesel engine scenario.
- Connecting pipe mass flow in a Bi-Turbo – connected throttle body scenario.

Hence the unique solution to the compressor mass flow is

$$\boxed{\dot{m}_c = \min_{\dot{m} \in \left\{\dot{m}_c^-, \dot{m}_c^+\right\}} |\dot{m} - \dot{m}_{aux}|} \tag{2.78}$$

The three models constituting the mass flow model have been identified separately, and a possible model deterioration due to accumulated estimation errors in the individual models may exist. Hence, a identification routine readjusting the 9 model coefficients such that the criterion below is minimized is implemented in MATLAB.

$$J_{\dot{m}_c}(\iota) = \left(\dot{m}_c(p_r, N_c) - \hat{\dot{m}}_c(p_r, N_c; \theta; \iota)\right)^2 \tag{2.79}$$

The parameter vector ι is a gain vector, which readjusts the compressor parameter vector θ in the following manner

$$\tilde{\theta} = \theta \odot \iota = \left[\iota_1 a \ \iota_2 b \ \iota_3 \alpha_{\rho_2} \iota_4 \xi_{\rho_2} \ \iota_5 \kappa_1 \ \iota_6 \kappa_2 \ \iota_7 \kappa_3\right]^T \tag{2.80}$$

The gain vector identified, ι, is listed in table 2.6. The table confirms that the

	Compressor A	**Compressor B**	**Compressor C**
ι_1	1.0341	0.9961	0.9354
ι_2	0.7869	0.7912	0.6656
ι_3	0.9708	0.9105	0.9450
ι_4	1.0972	1.3032	1.3908
ι_5	1.1009	1.1142	1.1933
ι_6	0.9050	0.9116	0.9736
ι_7	0.9757	1.0024	1.0378

Table 2.6: Readjusted gains belonging to the individual elements in the compressor parameter vector θ.

[12]Stable compressor operation is assumed.

error on the different parameters generally is small since the gains identified deviate modestly from the expected value of 1. However, interestingly enough, the slope, $\frac{b}{\alpha_{\rho_2} p_r + \xi_{\rho_2}}$, of the total normalized energy transfer, $\frac{\Delta h_{0c}}{U_2^2}$, is the parameter undergoing the biggest relative change of the compressor parameters and should be attributed to the base mass flow model's overestimation for the high speed speedlines. This tendency is general for all three compressors and is graphically visible in the maps to the left in figure 2.26. The three maps to the right depict the predicted compressor mass flow and measurements. It is evident that a relatively small readjustment of the individual elements in θ can improve the model prediction performance significantly.

It should be noted that the prediction to the left of the surge line should only be seen as a best guess of the compressor mass flow mean value since they belong to an uncharted part of the compressor characteristics. However, the predictions show a high degree of resemblance with surge area speedlines presented in [40], and it is believed that the model derived together with a simple restriction model for the negative mass flow region may also be used in basic surge area simulation studies.

2.3.3.12 Mass flow model validation

The mass flow model derived in the last section shows a high degree of estimation accuracy. However, can it be concluded or somehow tested that the derived model grasps the essentials of the compressor mass flow behavior? Hence, the purpose of this section is the investigation of the hypothesis below

$$\begin{aligned} H_0: &\quad \dot{m}_c\left(p_r, N_c\right) = \hat{\dot{m}}_c\left(p_r, N_c; \tilde{\theta}\right) + \epsilon + \nu \\ H_1: &\quad \dot{m}_c\left(p_r, N_c\right) \neq \hat{\dot{m}}_c\left(p_r, N_c; \tilde{\theta}\right) + \epsilon + \nu \end{aligned} \tag{2.81}$$

where ϵ is a steady stochastic error on the mass flow prediction $\hat{\dot{m}}_c$ with the following distribution

$$\epsilon \in \mathrm{N}(0, \sigma_\epsilon^2) \tag{2.82}$$

The variable ν is the measurement noise. However, all the measurements are carried out with state of the art equipment in the compressor manufacture's laboratories, and the assumption $\nu \equiv 0$ is viable.

The relative error in the mass flow predictions is computed for all three compressors and graphically illustrated in Figure 2.27. The relative errors are generally kept within an acceptable $\pm 10\%$ interval. A couple of outliers are encountered in the low mass flow region due to the increased relative error sensitivity in this region. The plots to the right in figure 2.27 are the corresponding estimated error distribution shown together with the normal error distributions, $\mathrm{N}\left(\mu_\epsilon, \sigma_\epsilon^2\right)$. The corresponding identified mean value, $\mu_\epsilon = \mathrm{E}(\epsilon)$, is clearly of a negligible significance. Hence the mean value assumption presented in equation 2.82 seems valid.

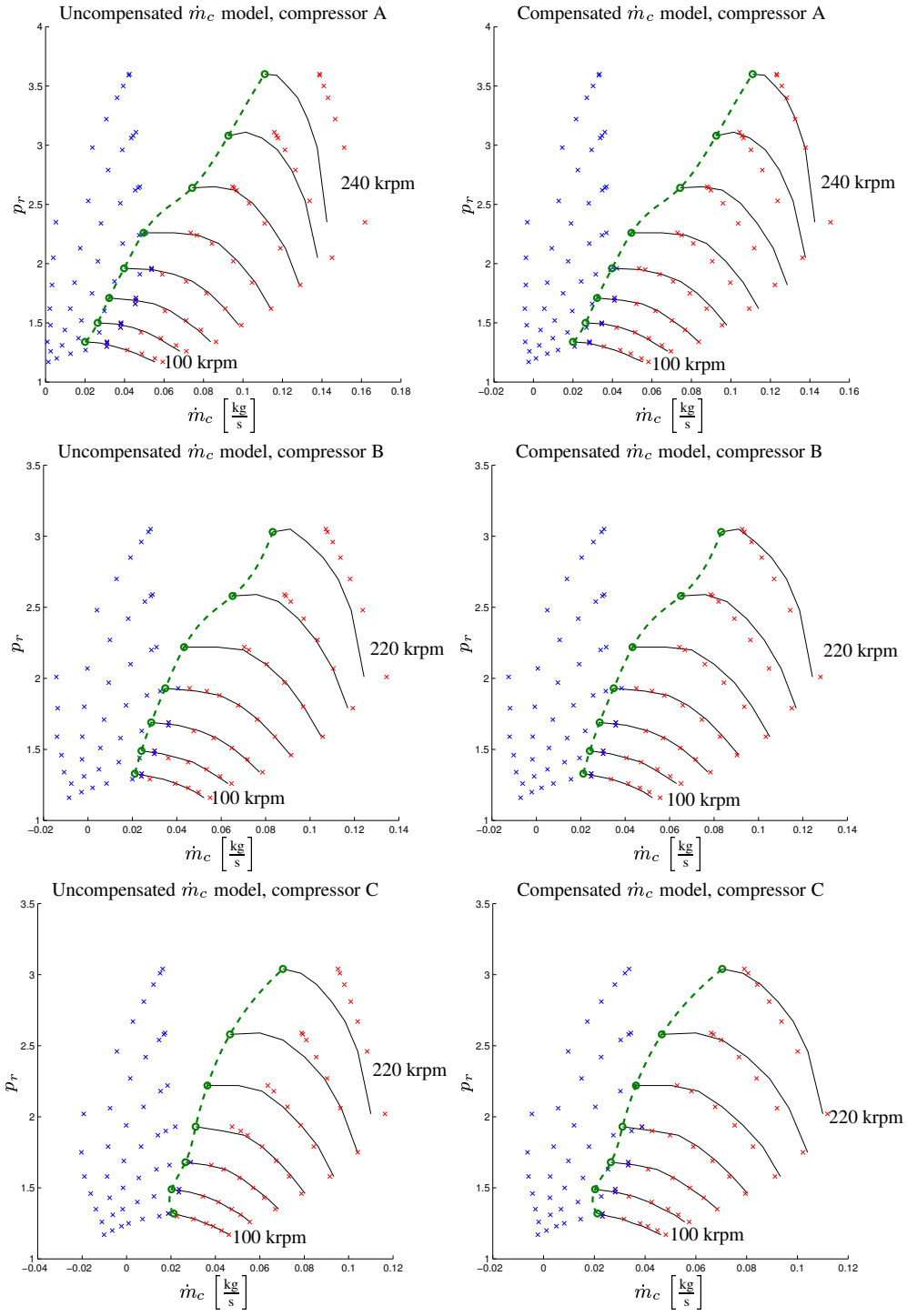

Figure 2.26: Comparison between base model and parameter adjusted compressor mass flow model. The solid black lines illustrates the measured speedlines for the three compressors, blue and red $\times$ are positive and negative solutions to equation 2.77, respectively, and the green dashed curves are the compressor surge lines.

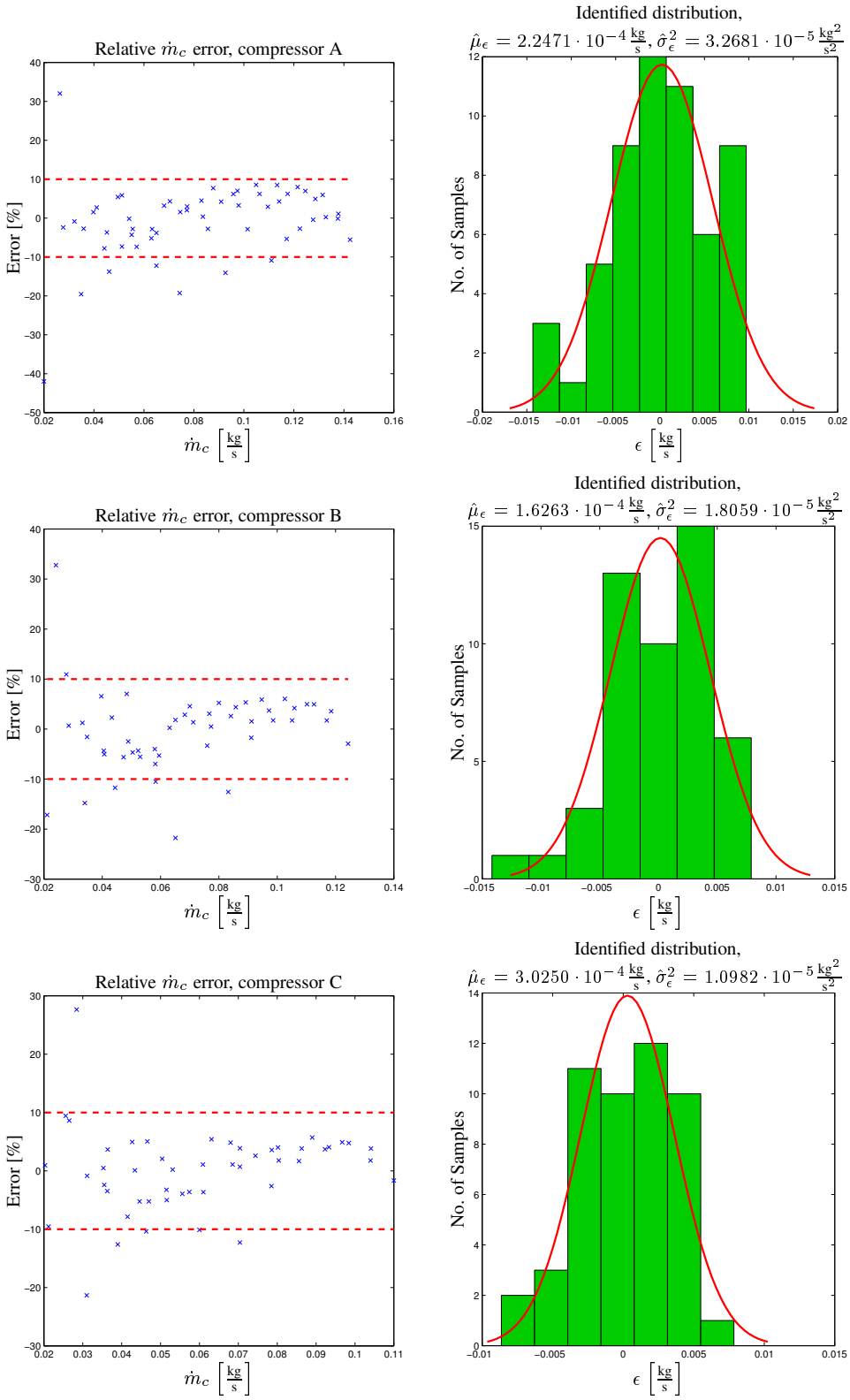

Figure 2.27: Relative mass flow error together with the estimated normal error distribution, N $\left(\mu_\epsilon, \sigma_\epsilon^2\right)$

This conclusion naturally leads to the question – "*does the variable* $\frac{\epsilon}{\sigma_\epsilon}$ *follow a N(0,1) distribution?*". In order to answer the question an Anderson–Darling test is conducted.

The Anderson-Darling test is designed to test goodness-of-fit in the tails of a probability density function based on a weighted-average of the squared difference between the observed and expected cumulative densities. Because of its relative high emphasis on fit quality in the tails, the Anderson–Darling statistic may be particularly useful in statistically goodness-of-fit tests. The reader is directed to [88] or [101] for a more elaborate treatment of the Anderson–Darling test.

The Anderson–Darling test size is defined by

$$\begin{aligned} A^2 &= -N - S \\ &\text{where} \\ S &= \sum_{i=1}^{N} \frac{2i-1}{N} \left(\ln \left(\mathrm{F}\left(y_i \right) \right) + \ln \left(1 - \mathrm{F}\left(y_{N-i+1} \right) \right) \right) \end{aligned} \tag{2.83}$$

where N is the number of samples, y_i is the ordered variable i.e. $y_1 \leq y_2 \leq \ldots \leq y_N$, and $\mathrm{F}(y)$ is the cumulative distribution function to be tested, here the normal cumulative distribution function.

Table 2.7 shows the computed A^2 values together with the critical value for the test, [88]. The test value, A^2, is for all compressors below the critical value of 1.321, and the H_0 hypothesis presented in equation 2.81 can with a confidence level of 95% not be overruled – the distribution of ϵ may be described by a normal distribution.

	A^2	**p-value**$_{\alpha=0.05}$	$\frac{\epsilon}{\sigma_\epsilon} \in \mathbf{N}(0,1) \Leftrightarrow A^2 < p$
Compressor A	0.4433	1.3210	✓
Compressor B	0.6634	1.3210	✓
Compressor C	0.7948	1.3210	✓

Table 2.7: Anderson–Darling test values.

It should be noted that the ϵ data set was not detrended prior to the Anderson–Darling, but only scaled with the estimated standard deviation $\hat{\sigma}_\epsilon$, to strengthen the test confidence. Whence, the assumption $\mu_\epsilon = 0$ is viable since all tests terminated successfully.

Finally as a final stage of model validation, the estimated cumulative distribution function for ϵ is compared to the theoretical cumulative normal distribution $\mathrm{F}(\epsilon)$. The results for the three compressors are shown graphically in figure 2.28. The figure shows that the general variance of the EDF (Empirical Distribution Function) around the theoretical CDF (Cumulative Distribution Function) is of acceptable level, however with an increasing degradation when moving from compressor A to compressor C; a conclusion supported by the Anderson–Darling test. However, the general curve tendency is linear, hence it can not from the plots be

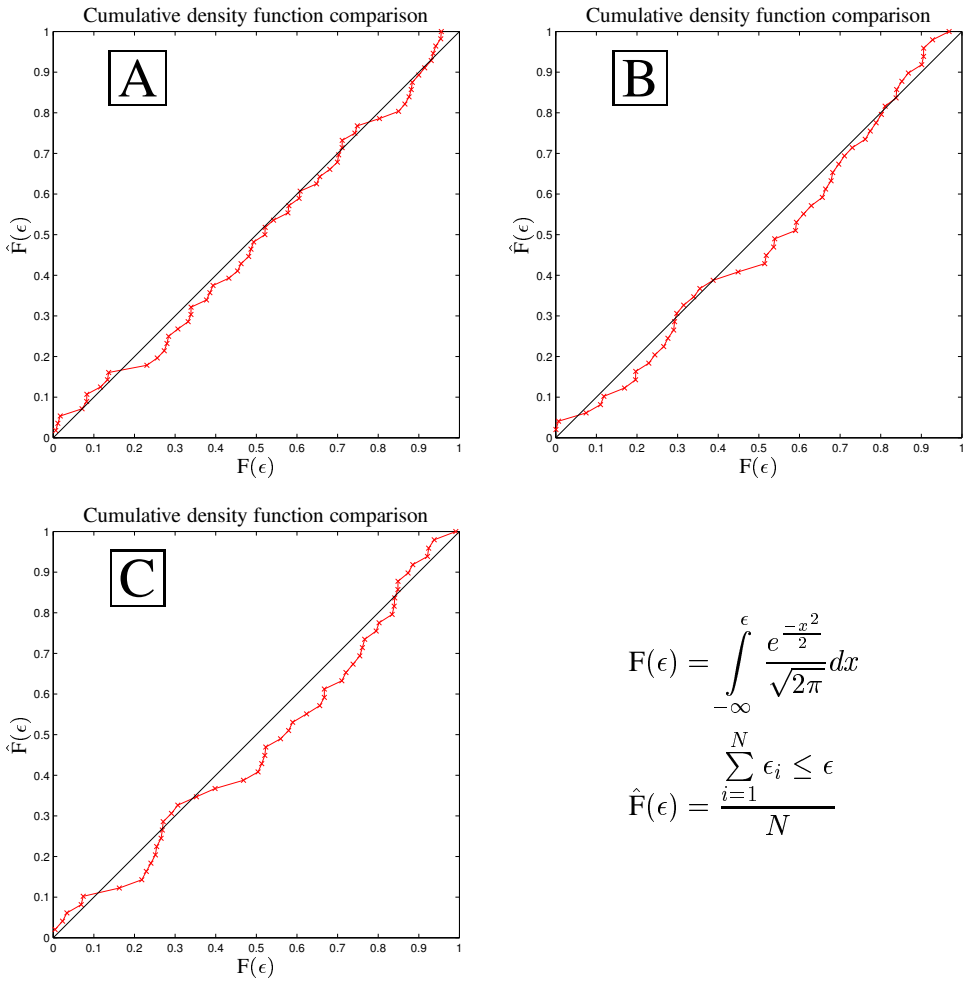

Figure 2.28: Comparison of the estimated cumulative density to that of the theoretical N(0,1) distribution.

concluded that the normal distribution hypothesis may be overruled. Hence, the graphical comparison of the cumulative distribution functions supports the conclusion of the EDF test.

On basis of the graphic test results given along with the positive conclusion of the Anderson–Darling EDF test it is here stated that the derived compressor model, within the limits of the manufacturer compressor map, is able to capture the essentials in compressor flow modelling.

2.3.3.13 Summary

The section describes the development of a one-dimensional compressor mass flow model based on physical considerations. The derived mass flow model is repeated below for the sake of convenience.

$$\boxed{\begin{aligned}\dot{m}_c &= \frac{\left(\frac{b}{\alpha_{\rho 2} p_r + \xi_{\rho 2}} - \kappa_2\right) \pm \Phi}{2\kappa_1} U_2 \\ &\text{where} \\ \Phi &= \sqrt{\left(\kappa_2 - \frac{b}{\alpha_{\rho 2} p_r + \xi_{\rho 2}}\right)^2 - 4\kappa_1 \left(\frac{c_p T_{01}\left(p_r^{\frac{\gamma-1}{\gamma}} - 1\right)}{U_2^2} + \kappa_3 - a\right)}\end{aligned}} \tag{2.84}$$

The implicit equation structure is turned into an explicit solution by

$$\boxed{\dot{m}_c = \min_{\dot{m} \in \left\{\dot{m}_c^-, \dot{m}_c^+\right\}} |\dot{m} - \dot{m}_{aux}|} \tag{2.85}$$

where $\dot{m}_{aux}$ is an auxiliary mass flow describing the general flow out of a selected control volume.

The mass flow model consists of 7 operating point independent parameters: a, b, $\alpha_{\rho 2}$, $\xi_{\rho 2}$ describing the total energy transfer in the model, and κ_1, κ_2, κ_3 describing the compressor energy loss. The number of coefficients may be reduced to 6 since the parameters a and κ_3 may be collected as one variable in the total model. However, the ability to split the energy transfer in total specific energy and specific loss energy is lost.

The mass flow model was on a statistical basis found descriptive throughout the map supplied for three different compressors, all manufactured by Allied Signal. Hence, the model derived is a good candidate in the selection of compressor models for robust modelling in the sense that the model also scales well outside of the compressor map.

2.3.4 Radial variable geometry turbine model

2.3.4.1 Modus operandi

The automotive turbine, today dominated by the the radial flow turbine, is similar in appearance to the centrifugal compressor, but with the flow in the inward direction. Figure 2.29 shows a photograph of a sectioned VGT. The adjustable inlet nozzles are seen located around the rotor circumference. The nozzle position may be altered by the pneumatically operated actuator seen positioned below the scroll. The trend in the industry however is a replacement of the pneumatically actuator by electrical torque controlled motors. The added cost is justified by smaller response time, less dead band width and symmetric actuation.

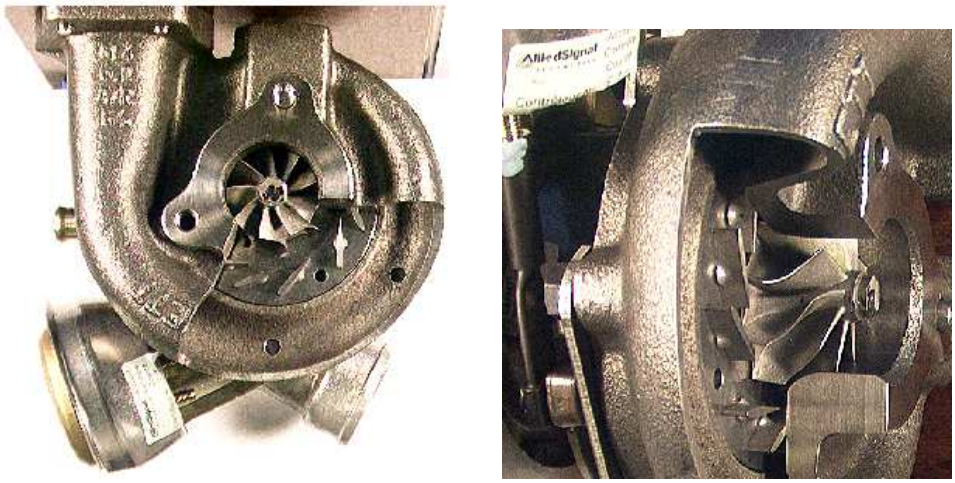

Figure 2.29: Pneumatically actuated VGT turbo from Allied Signal (courtesy of Ford Motor Company).

The operating principle is the inverse of the compressor - work is extracted through gaseous expansion. The extracted work is transferred as mechanical energy through a shaft to external power consumers e.g. the centrifugal compressor or generator in the case of power assisted turbochargers (see e.g. [106]). The turbine may fundamentally speaking be operated in two modes: constant pressure mode or pulse mode. The working principle of the two modes is briefly addressed here.

Constant pressure turbocharging The principle behind constant pressure turbocharging is conversion of the high kinetic energy of the gaseous matter leaving the engine exhaust ports into pressure. This diffusion process necessitates carefully designed exhaust runners enhancing the diffusion and a large connecting volume capable of damping the fluctuations to an acceptable level. This ensures a high efficiency of a properly matched turbine. However, due to this big exhaust volume the transient response of the engine is rather slow. Hence, the constant pressure

turbocharging principle is mainly use on stand alone engines operating at a fixed speed e.g. power generators. Furthermore, the back pressure will be relatively high, and an increased pumping loss may be expected, especially in the case of a throttled engine.

Pulse mode turbocharging The other extreme of turbine operation is the pulse mode operation. Here the exhaust flow is sought stagnated as little as possible before turbine entry i.e. kinetic energy preservation. The pulse mode exhaust manifold is thus characterized by separate relatively thin short runners. The pressure ratio across the turbine is characterized by a high narrow pressure burst followed by a long period with a stage pressure ratio close to unity until the next pressure burst arrives, [87, 54]. The penalty is evidently a degradation of the turbine efficiency. It is actually fortunate that the turbine is able to function at all under these conditions. However, if the exhaust runners are grouped carefully, an acceptable level of turbine operating efficiency can be achieved. Furthermore, the small exhaust volume gives the pulse mode strategy a much faster transient response compared to the constant pressure strategy.

The pulse mode strategy is quite clearly the relevant choice for automotive applications due to the better transient response and ease of packaging.

2.3.4.2 VGT elementary

The VGT consists of the four base components listed below.

- Inlet casing or scroll
- Variable inlet nozzles.
- Rotor
- Exducer (Rotor eye) and outlet pipe.

A sketch of a VGT depicting the key elements mentioned is shown in figure 2.30.

The job of the scroll is purely to deliver a uniform flow to the nozzle entry. The flow is then accelerated through the nozzles due to the radial area decrease i.e. pressure is converted into kinetic energy. The actual energy transfer occurs in the rotor. The rotor should be designed so that the kinetic exit energy is minimized as much as possible. This process description is pictured schematically in the enthalpy-entropy diagram such that the loss sources may be understood individually. Station 01 refers here to scroll inlet stagnation conditions. However, the flow enters the nozzle with absolute velocity C_1, and the static enthalpy is thereby a quantity $\frac{C_1^2}{2}$ smaller than the stagnation enthalpy. Between station 1 and 2 the flow is accelerated due to the area decrease mentioned above and the flow will leave the nozzles with absolute velocity C_2. However, some of the thermodynamic energy

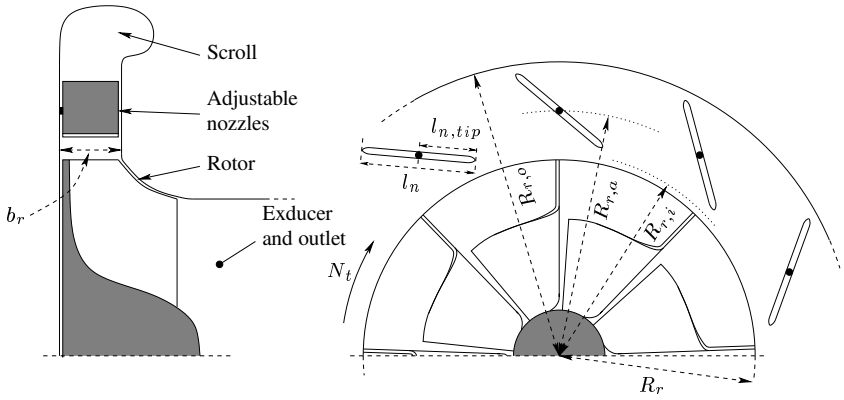

Figure 2.30: Variable geometry turbine diagram.

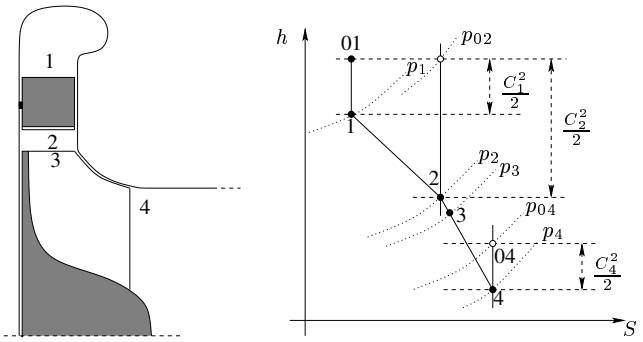

Figure 2.31: VGT Entropy–Enthalpy diagram.

is lost mainly due to the collision between nozzles and fluid during flow entry and the inevitable nozzle passage friction. This leads to a significant entropy increase. The line connecting station 2 to 3 describes the process between nozzle exit and rotor entry. Since this space is relatively small the distance between station 2 and 3 normally negligible. The path 3 to 4 describes the actual energy extraction. This path is not ideal either mainly due to collision and friction losses. Finally, since a fair amount of the kinetic energy can not be extracted fully the stagnation pressure, p_{04}, will be higher than the static pressure p_4. Since no work takes place in the scroll and nozzles the total work extraction may be found to be

$$P_t = \dot{m}_t \left(\Delta h_{01} - \Delta h_{04}\right) = \dot{m}_t \left(\Delta h_{03} - \Delta h_{04}\right) \tag{2.86}$$

Similar to the compressor case this energy transfer may also be derived from an investigation of the inlet and outlet fluid velocities. Figure 2.32 shows the fluid velocity conditions at the rotor entry and exducer, respectively.

The torque extracted may be derived dual to the compressor description. Thus, the rate of change of angular momentum equals the sum of external torques. Since the change of angular momentum corresponds to the change of the moment of linear momentum, the effective torque, τ_t, is found to

$$\tau_t = \dot{m}_t \left(R_r C_{3,\theta} - R_4 C_{4,\theta}\right) \tag{2.87}$$

The radius, R_4, is normally selected as the radius of the circle splitting the exducer area in two annuli of equal area i.e. $R_4 = \frac{1}{4}\sqrt{D_{4,h}^2 + D_{4,s}^2}$. Multiplying equation 2.87 with the rotor angular speed the extracted power is found to

$$P_t = \dot{m}_t \omega_t \left(R_r C_{3,\theta} - R_4 C_{4,\theta}\right) = \dot{m}_t \left(U_3 C_{3,\theta} - U_4 C_{4,\theta}\right) \tag{2.88}$$

Combining equations 2.88 and 2.86 the effective work extracted in terms of specific energy may be expressed as

$$\Delta h_{0,t} = \left(U_3 C_{3,\theta} - U_4 C_{4,\theta}\right) \tag{2.89}$$

However, since the absolute exit velocity C_4 is desired to be small for efficiency reasons, the rotor design is optimized so that swirl is minimized i.e. $C_{4,\theta} \approx 0$, and the previous equation may be reduced even further to

$$\Delta h_{0,t} = U_3 C_{3,\theta} \tag{2.90}$$

The enthalpy released due to the expansion on a total-to-total basis is given by the isentropic relation below

$$\Delta h_{0t,i} = c_p T_{01} \left(1 - \left(\frac{p_{01}}{p_{04}}\right)^{\frac{1-\gamma}{\gamma}}\right) \tag{2.91}$$

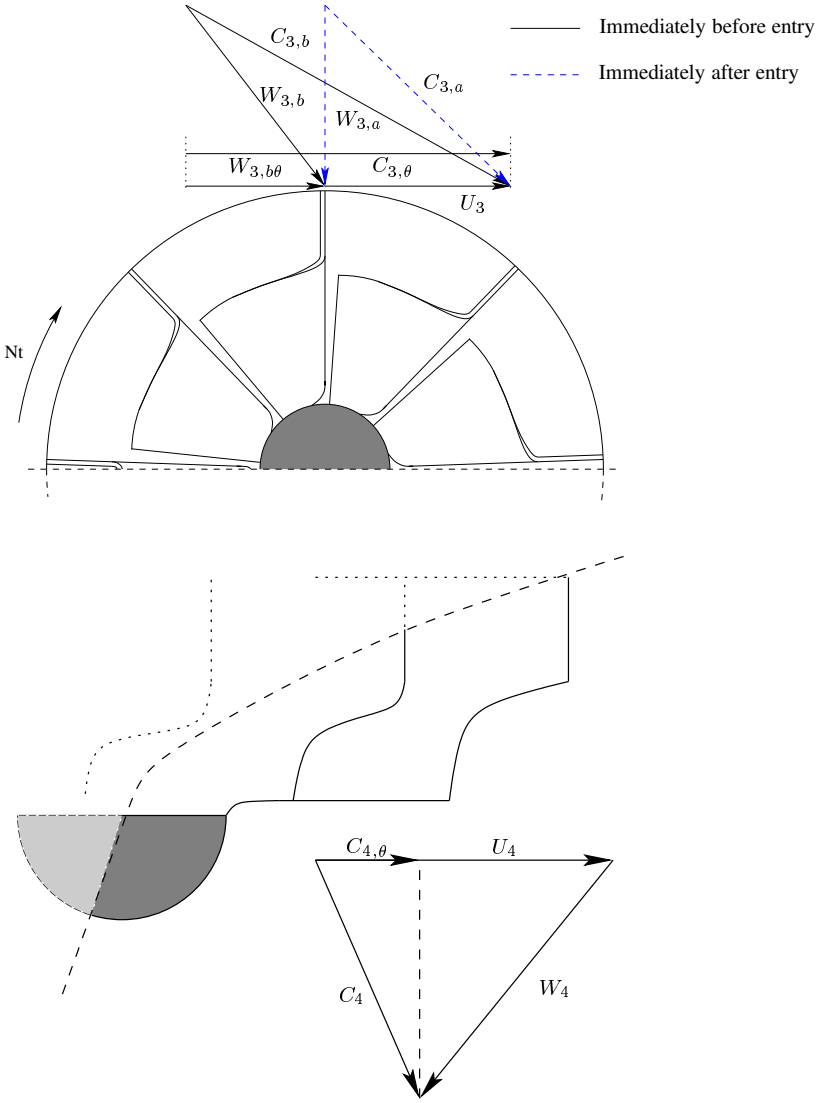

Figure 2.32: Rotor entry and exit velocity triangles.

Hence the total-to-total turbine efficiency is found to

$$\eta_{t,TT} = \frac{\Delta h_{0,t}}{\Delta h_{0t,i}} \approx \frac{c_{p,T_{01}} T_{01} - c_{p,T_{04}} T_{04}}{c_{p,T_{01}} T_{01} \left(1 - \left(\frac{p_{01}}{p_{04}}\right)^{\frac{1-\gamma}{\gamma}}\right)} \approx \frac{T_{01} - T_{04}}{T_{01} \left(1 - p_{r,TT}^{\frac{1-\gamma}{\gamma}}\right)} \tag{2.92}$$

However, the kinetic energy of the fluid leaving the exducer will always be lost. Therefore, a more natural choice of stage efficiency description is to relate inlet stagnation conditions to static outlet conditions, i.e.

$$\eta_{t,TS} = \frac{\Delta h_{0,t}}{\Delta h_{0t,i}} \approx \frac{c_{p,T_{01}} T_{01} - c_{p,T_{04}} T_{04}}{c_{p,T_{01}} T_{01} \left(1 - \left(\frac{p_{01}}{p_4}\right)^{\frac{1-\gamma}{\gamma}}\right)} \approx \frac{T_{01} - T_{04}}{T_{01} \left(1 - p_r^{\frac{1-\gamma}{\gamma}}\right)} \tag{2.93}$$

and

$$\Delta h_{0t,i} = c_p T_{01} \left(1 - \left(\frac{p_{01}}{p_4}\right)^{\frac{1-\gamma}{\gamma}}\right) \tag{2.94}$$

Finally, the total-to-static enthalpy loss is defined by,

$$\Delta h_{t,loss} = \Delta h_{0t,i} - \Delta h_{0t} = (1 - \eta_{t,TS})\, \Delta h_{0t,i} \tag{2.95}$$

In an effort to generalize specifications of turbines, manufactures also often use terms like aspect ratio, trim, and U/C characteristics.

The aspect ratio or abbreviated A/R (Area/Radius Ratio) of a turbine is defined as the ratio between volute inlet area and effective volute inlet radius (see e.g. [87]). This ratio gives a rough measure of the fluid's entry angle into the rotor in the case of a vaneless nozzle or into the vaned nozzle ring, respectively,and is thus a tool in the engine-turbine matching procedure. The setting of A/R is however most critical in the case with a vaneless nozzle ring.

The trim setting specifies the ratio between rotor inlet diameter and exducer diameter, and is already described in the compressor section (see 2.3.3.4 on page 75).

It is customary in the classification of turbine efficiency to plot the efficiency against the so called U/C (Turbocharger wheel velocity/maximum fluid velocity Ratio) number. The U/C term is a dimensionless number relating rotor tip velocity, U_3, to the gas velocity, C_s, achieved if the fluid had followed an isentropic expansion from inlet stagnation conditions to static outlet conditions, i.e.

$$\frac{U}{C} = \frac{U_3}{C_s} = \frac{U_r}{\sqrt{2 c_p T_{01} \left(1 - p_r^{\frac{1-\gamma}{\gamma}}\right)}} \tag{2.96}$$

Although the use of U/C ratio analogy is only valid for pure impulse turbine designs[13], it provides a non-dimensional form of the turbine speed, thus providing valuable information when matching turbines and compressors.

[13]The static rotor inlet enthalpy Δh_3 equals the outlet stagnation enthalpy Δh_{04} following an isentropic expansion line.

2.3.4.3 Literature

The literature on VGT modelling for MVEM or control purposes is sparse. Most models rely on table interpolation when computing the mass flow, $\dot{m}_t$ and the turbine efficiency η_t. However, as stated in the previous section, the turbines are often mapped very sparsely, and most often the map only covers the mid to high revolution areas of the turbine operating range. This of course hampers successful calculation of $\dot{m}_t$ and η_t.

In [91] two fitting techniques for VGT mass flow modelling purposes are presented: one based on the isentropic nozzle flow equation and one based on neural networks. However, the first fitting technique cannot capture the effect of the centrifugal field around the rotor, and large mass flow errors can be expected in the low pressure region of the turbine map. The neural network does not improve the prediction quality noticeably, and is further hampered by the need for artificial data points for realistic predictions in the low pressure range of the turbine map.

The turbine efficiency was modelled in [91] by a second order polynomial in U/C with the coefficients linearly dependent on turbine speed. Due to the relatively high amount of "fiddling" required getting the models proposed in [91] to work these models will not be considered further here.

Reverting to modelling of automotive turbines with a fixed geometry nozzle ring in the quest for a general VGT model, the three sources [63, 61, 83] are of interest. Addressing mass flow modelling the initial step in all three sources is an investigation of the possibilities in applying the isentropic nozzle flow equation repeated below

$$\dot{m}_{noz} = \begin{cases} C_D A_{noz} \frac{p_{01}}{\sqrt{RT_{01}}} p_r^{\frac{-1}{\gamma}} \sqrt{\frac{2\gamma}{\gamma-1}\left(1 - p_r^{\frac{1-\gamma}{\gamma}}\right)} & , \quad p_r \leq \left(\frac{\gamma+1}{2}\right)^{\frac{\gamma}{\gamma-1}} \quad \text{(subsonic)} \\ C_D A_{noz} \frac{p_{01}}{\sqrt{RT_{01}}} \sqrt{\gamma}\left(\frac{2}{\gamma+1}\right)^{\frac{\gamma+1}{2(\gamma-1)}} & , \quad p_r > \left(\frac{\gamma+1}{2}\right)^{\frac{\gamma}{\gamma-1}} \quad \text{(sonic)} \end{cases} \tag{2.97}$$

where $p_r = \frac{p_{01}}{p_4}$, C_D is the discharge coefficient, and A_{noz} the minimum effective open area of the nozzle.

The application of the isentropic nozzle equation is justifiable since the turbine, fundamentally speaking, may be viewed as two nozzles in series; the nozzle ring and the rotor, respectively.

Converting equation 2.97 into corrected mass flow, and collecting the upstream conditions together with C_D and A_{noz} an equivalence "area" factor, A_{eq}, may be found as

$$A_{eq} = C_D A_{noz} \frac{p_{01}}{\sqrt{RT_{01}}} \frac{\sqrt{\frac{T_{01}}{T_{01,ref}}}}{\frac{p_{01}}{p_{01,ref}}} = C_D A_{noz} \frac{p_{01,ref}}{\sqrt{RT_{01,ref}}} \tag{2.98}$$

This factor was in [61, 83] found to decrease with turbine speed increase and pressure ratio decrease, respectively. This is however to be expected due to the variation in the centrifugal field around the rotor wheel as it turns.

The variable A_{eq}'s variation was in [63, 61] found to be mainly a linear function for either fixed pressure ratio, p_r, or turbine speed, N_t. Hence, the equivalence area was approximated by

$$\begin{aligned} A_{eq} &\approx k_{t1} p_r + k_{t2} \\ \text{with} \\ k_{ti} &= k_{1,i} \frac{N_t}{\sqrt{T_{01}}} + k_{2,i}, \quad \text{for } i = 1, 2 \end{aligned} \tag{2.99}$$

where the constants, $k_{t,i}$, are determined subsequently by regression.

The turbine efficiency η_t was in [63, 61] modelled using a third order polynomial in U/C and speed dependent coefficients, i.e.

$$\begin{aligned} \eta_t = \eta_{t,TS} &= b_3 \Psi^3 + b_2 \Psi^2 + b_1 \Psi + b_0 \\ \text{with} \\ b_i &= \tfrac{k_{1,i} + k_{2,i} N_t}{k_3 - N_t} \text{ for } i = 0 \ldots 3, \quad \Psi = \tfrac{U_3}{C_s} \end{aligned} \tag{2.100}$$

However, this model was in [83] found being to inaccurate when applied to the map data for the KKK turbine investigated. Hence, the model structure was changed and a more suitable efficiency description was found to be

$$\begin{aligned} \eta_t &= t_2 \left(\Psi - \Psi_{ref}\right)^2 + t_1 \left(\Psi - \Psi_{ref}\right) + C \\ \text{where} \\ C &= t_3 - \eta_{T,ref} \\ \Psi_{ref} &= t_4 \eta_t + t_5 \\ \eta_{t,ref} &= t_6 N_t^3 + t_7 N_t^2 + t_8 N_t + t_9 \end{aligned} \tag{2.101}$$

necessitating a subsequent identification of the coefficients $t_1, \ldots, t_9$.

The turbine models presented above are split in two parts: a mass flow model and an efficiency model. The mass flow models are based on soft semi-physical considerations whereas the efficiency models are all pure fitting functions. Use of the models proposed in [63, 61, 83] to model VGT mass flow and efficiency would necessitate an augmentation of the models. An obvious augmentation would be to first identify the individual coefficients for a given fixed position of the nozzles vanes (fixed VGT position) and later model the coefficient's variation by polynomials of the VGT position, θ_{vgt}. However, this would clearly require identification of a relatively large number of coefficients. Moreover, the models only provide a quite ambiguous picture of the VGT behavior. This, together with the expected poor extrapolation accuracy, calls for a reinvestigation of turbine modelling, and is the task for the rest of this section.

2.3.4.4 VGT data set

The validation of the turbine identification procedures and theories established in the following section is based on a data set for an Allied Signal VGT. The data set

was selected because of its exceptionally large size (252 points). A normal data set may consist of as few as 35 point to cover the whole operating range of a VGT.

The dimensional specifications for the VGT are listed table 2.8, and the design basically speaking reassembles that of the VGT shown in figure 2.29.

Type definition	GT15V NS111(39)
Trim	76
A/R, [in]	0.42
No. of nozzles, N_{noz}	9
Rotor diameter, D_r, [mm]	39
Rotor inlet width, b_r^*, [mm]	6.2
Inner nozzle ring diameter, $D_{r,i}^*$, [mm]	41.3
Outer nozzle ring diameter, $D_{r,o}^*$, [mm]	77.5
Nozzle ring axel diameter, $D_{r,a}^*$, [mm]	60.0
Nozzle blade length, l_n^*, [mm]	17.0
Nozzle blade tip length, $l_{n,tip}^*$, [mm]	7.0
Maximum corrected mass flow, $\dot{m}_{t,c,max}$, $\left[\frac{\text{kg}}{\text{s}}\right]$	0.08

Table 2.8: Dimensional specifications for GT15V NS111(39) VGT (see also figure 2.30). The data marked with '*' is found by mechanical disassembling of the VGT and should thus be treated as more descriptive than accurate.

Figure 2.33 shows the flow characteristics of the turbine. The effect of the nozzle position variation on the mass flow characteristic is evident; an increase of the VGT position for a given pressure ratio, p_r, leads to higher a mass flow.

Creation of a comprehensive picture of the turbine efficiency is complicated due to the added degree of freedom. However, a general design rule, within the boundaries of the supplier map, is to peak the efficiency around a normalized VGT position of 0.5. This is also the case for the VGT investigated here and is unmistakably clear in figure 2.34. The figure also shows, that despite the uncommonly large amount of data, only the descending part of the U/C characteristic has been charted. This is of course unfortunate considering a subsequent efficiency identification investigation.

However, due to the large amount of data available for different θ_{vgt} settings, generalized conclusions concerning turbine modelling may nevertheless be extracted from the data.

2.3.4.5 LWLS (Locally Weighted Least Square) regression

Modelling of turbines, especially when employed in highly fluctuating flows, is as often stated a cumbersome affair. However, a model of the mass flow through the turbine is mandatory in the creation of an exhaust filling–emptying model which can predict the dynamic behavior of the exhaust temperature and pressure. This

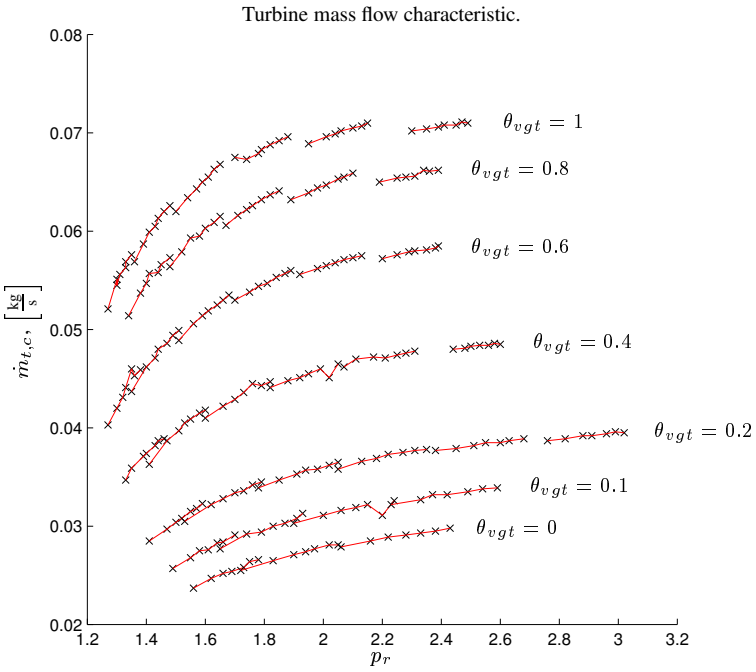

Figure 2.33: Mass flow characteristics for the GT15V NS111(39).

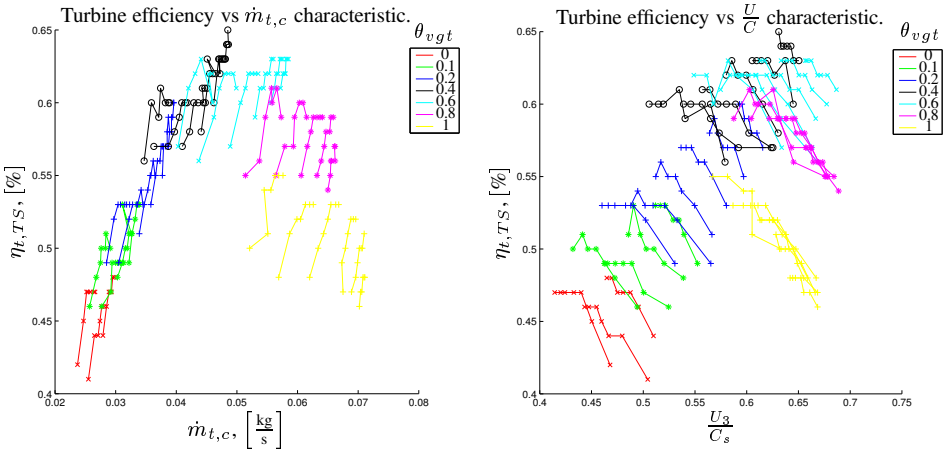

Figure 2.34: Efficiency characteristics for for GT15V NS111(39).

would commonly necessitate models of the exhaust port mass flow and temperature, EGR mass flow and turbine mass flow.

The insertion of variable vanes in the turbine nozzle evidently does not ease the modelling task. Therefore, the most customary used control oriented VGT's mass flow models found in the literature rely on table interpolation, regression analysis, or linear model approximation (see e.g. [16, 39, 104, 87, 91, 108, 84, 63]), where the two first methods of modelling are the most commonly found. That analysis and modelling based on map interpolation or regression are natural choices when modelling complex structures like the VGT is evident due to their reasonably simple employment in dynamical models. However, regression analysis should not be done without a initial analysis (physical investigation) for these obvious statements:

- The model quality is proportional to data quality.
- The data set must cover as the complete region of interest for simulation - and as dense as possible.
- Extrapolation accuracy is often very questionable.

The words of caution or prerequisites above are however quite often neglected, and the regression models derived are employed without question (see e.g. [83, 91, 108]).

However, since regression analysis has proven to be a very versatile tool in the analysis of complex phenomenons, e.g. combustion processes, internal engine friction forces etc. [49, 62], it is worth investigating the possibility of constructing a generalized regression tool for automotive analysis. This is the topic for rest of this section.

The most often encountered generalized modelling concepts in the literature are neural network or polynomial structures. Neural networks are certainly useful tools when addressing automotive modelling. However, successful application of neural networks requires a great deal of insight and use of sophisticated optimization algorithms. Hence, the emphasis here is on the application of polynomial structures in the search for a descriptive correlation between inputs and outputs.

The most often encountered multi variable polynomial structure for regression in the literature is based on the application of one high order multi variable polynomial to model the behavior of a given phenomenon e.g. VGT mass flow and efficiency (see e.g. [83, 108]). However, this method has several disadvantages:

- Undesirable extraneous curvature between data points.
- A large number of polynomial coefficients needs to be identified.
- Steep gradients outside the identification region due to high order polynomial terms.
- The cost function might not be convex.

- Large identification regions often necessitate high order polynomial structures to achieve an acceptable level of modelling accuracy.
- Sophisticated minimization algorithms are often needed.

Clearly, one of the biggest problems stated above is the need of higher order polynomials to achieve the desire level of modelling accuracy. This spawns of another requirement also listed above – identification of a large number of polynomial coefficients is mandatory. However, if the space spanned by the selected correlation function inputs is split into numerous subspaces, when a local multi variable polynomial structure, often of a much lower order, may be found. This paradigm is here referred to as **local regression**, and the details of establishing such a regression analysis are outlined below.

The signal of interest is assumed in the algebraic case described by

$$y = \mathrm{f}(i) + \epsilon \tag{2.102}$$

or in the dynamic case by the difference function

$$\begin{aligned} y_k &= \mathrm{f}(i_k) + \epsilon_k \\ \text{with} & \\ i_k &= (x_{k-1}, x_{k-2}, \ldots, x_{k-n}, u_k, u_{k-1}, \ldots, u_{k-m}) \end{aligned} \tag{2.103}$$

where ϵ is independent normally distributed noise, i.e. $\epsilon \in \mathrm{N}(0, \sigma^2)$.

In order for a viable solution to exist the following is required,

- The solution to the function $\mathrm{f}(\ldots)$ is unique with respect to i.
- The function f is continuously differentiable.

Proof: Follows directly from the definition of Taylor series.

The conditions above can most often not be checked prior to the regression analysis, however, a subsequent application of a statistical tool like the Anderson–Darling test may tell whether or not the functional description found can capture the essential features of y's behavior within the boundaries of the data set (see e.g. section 2.3.3.12).

Assuming that the function f fulfills the necessary requirements, f may be described by,

$$\mathrm{f}(\theta) = \sum_{i=0}^{\infty} \frac{1}{i!} \left(\delta \cdot \nabla\right)^i \mathrm{f}(\theta)_{|\theta=\theta_0} \tag{2.104}$$

The equation above uses a parallel space of θ i.e. $\theta = \theta_0 + \delta \Leftrightarrow \mathrm{f}(\theta) = \mathrm{f}(\theta_0, \delta)$. Introducing the error O this function is rewritten as

$$\mathrm{f}(\theta) = \mathrm{P}(\delta + \theta_0) + \mathrm{O}\left(\left(\delta + \theta_0\right)^{n+1}\right) \tag{2.105}$$

where P is a multi variable polynomial of order n and O is an error function.

Assuming that the error function is small in some neighborhood of θ_0 such that it can be represented by the noise process ϵ, then an estimate of y in the neighborhood of θ_0 is given by,

$$\begin{aligned} \hat{y} &= \mathrm{E}\,(y|\theta) = \mathrm{f}(\theta) \approx P(\theta;\Lambda) \\ \Lambda &= [c_n, c_{n-1}, \ldots, c_1, c_0] \end{aligned} \tag{2.106}$$

where Λ is the coefficient vector of the polynomial P.

Having established a feasible regression structure the next thing missing is the definition of *local data* – the data *belonging* to the local subspace defined earlier. Local data is here defined as a predetermined fraction, ζ, of the total data set laying within a hypersphere with Euclidian radius r and center θ_0. The radius r of the sphere may be found by a NN (Nearest Neighbor) criterion. The NN criterion follows: given N data points, a fraction factor ζ, and grid point θ_0, then NN data points are the $Q = \mathrm{round}(\zeta N)$ data points in the closest Euclidian proximity of the grid point θ_0.

A suitable cost function in the computation of Λ_k belonging to grid point k is the quadratic function given below

$$J_k = \sum_{i=1}^{Q} \omega\left(\frac{\rho_i}{r}\right)\left(y_i - P(\delta_i + \theta_{0,k};\Lambda_k)\right)^2 \tag{2.107}$$

Hence the coefficient vector, Λ_k, belonging to the polynomial $P_k(\cdot\,;\Lambda_k)$ is derived by computing

$$\Lambda_k = \arg\min_{\Lambda_k}\left(J_k\right) \tag{2.108}$$

The solution to the LS (Least Square) criterion in equation 2.108 is linear in the coefficients space. Hence the solution to Λ_k is found in a straightforward manner by applying the pseudo inverse,

$$\Lambda_k = \left(\phi^{\mathrm{T}}\Omega\phi\right)^{-1}\phi^{\mathrm{T}}\Omega Z \tag{2.109}$$

where ϕ is the regressor matrix containing the Q inputs to the system, Ω is a diagonal $Q \times Q$ weight matrix with the diagonal $\left[\omega_1^k, \ldots, \omega_Q^k\right]$[14], and Z is the measurement vector containing the Q measurements of y. Thus, the solution to Λ_k is global and optimal for a given polynomial structure.

Before proceeding to application of the theory outlined above on turbine estimation, a few words of caution should be mentioned about the influence of noise. It is thought that this is best illustrated with an example.

First equation 2.103 is generalized to

$$\begin{aligned} x_k &= \mathrm{f}\,(z_k) + \epsilon_k^p \\ y_k &= x_k + \epsilon_k^m \end{aligned} \tag{2.110}$$

[14] Another often applied data weighting structure is the Epanechnikov structure (see e.g. [72]).

where ϵ^p is white process noise, and ϵ^m is white measurement noise. An example of such a process given below

$$\begin{aligned} x_k &= -0.24999 x_{k-1}^2 + \epsilon_k^p \\ y_k &= x_k + \epsilon_k^m \end{aligned} \qquad \text{where} \quad \begin{cases} x_0 = 4 \\ \epsilon_k^p \in \mathrm{N}(0, \sigma_p^2) \\ \epsilon_k^m \in \mathrm{N}(0, \sigma_m^2) \end{cases} \tag{2.111}$$

This function was simulated in the MATLAB® environment and 100 data points were generated with different noise settings. The simulation results are given in figure 2.35.

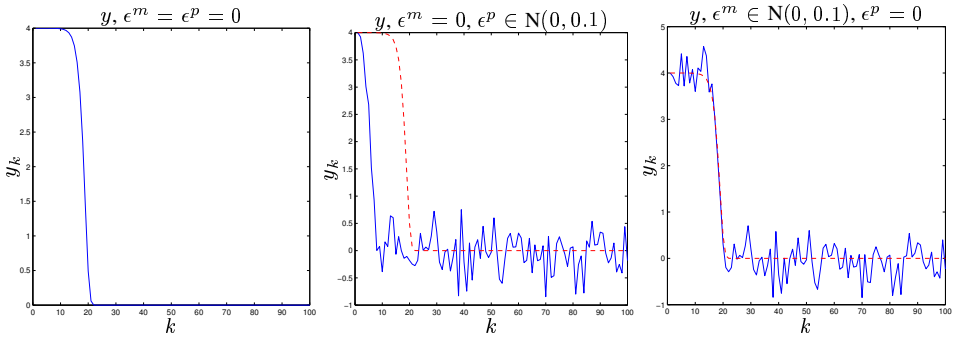

Figure 2.35: Illustration of the y_k noise penetration. Note, the realized noise time ϵ is same for the two plots on right.

The parameters identified listed in table 2.9 clearly show the noise effect on the estimation quality.

	c_2	c_1	c_0
$\sigma_p^2 = \sigma_m^2 = 0$	0.24999	0	0
$\sigma_p^2 = 0.1, \sigma_m^2 = 0$	0.2316	0.0565	-0.0502
$\sigma_p^2 = 0, \sigma_m^2 = 0.1$	0.1744	0.2796	-0.0625

Table 2.9: Identified parameters for P with different noise settings.

The table states a general problem in nonlinear system identification, noise spectrum wrapping (see e.g. [72]). In the case of process noise the noise spectrum is unchanged i.e.

$$\begin{aligned} \mathrm{E}\left(\hat{y} \,\middle|\, \hat{\theta} = \theta\right) &= \mathrm{f}(\cdot)\big|_{\hat{\theta}=\theta} \\ \mathrm{V}\left(\hat{y} \,\middle|\, \hat{\theta} = \theta\right) &= \sigma_p^2 \end{aligned} \tag{2.112}$$

However, in the case of measurement noise the chances of successful parameter estimation is ill conditioned for the following reason. The stationary white noise

to step k, ϵ_k^m, will enter the regressor ϕ_k in entry k of the identification data i.e. a wrapping of the noise spectrum will occur(see e.g. [17]). Thus the non-recursive estimates, $\hat{\theta}$, will be biased. The above explanation is sought illustrated by a small example:

Let W be stationary white noise such that $W \in \mathrm{N}(0, \sigma^2)$, and let $y = w^2$. The question is now what is the distribution of Y. The distribution may be found by investigating the cumulative distribution of w

$$F(w) = P(W \leq w) = \frac{1}{\sqrt{2\pi}\sigma} \int_{-\infty}^{w} e^{\frac{-\tau^2}{2\sigma^2}} d\tau \tag{2.113}$$

$$F(y) = \begin{cases} 0, & y < 0 \\ P(-\sqrt{y} \leq W \leq \sqrt{y}), & y \geq 0 \end{cases} \tag{2.114}$$

Hence, $F(y)$ may be written as,

$$F(y) = \begin{cases} \frac{1}{\sqrt{2\pi}\sigma} \int_{-\sqrt{y}}^{\sqrt{y}} e^{\frac{-\tau^2}{2\sigma^2}} d\tau, & y \geq 0 \\ 0, & y < 0 \end{cases} \tag{2.115}$$

A change of the noise mean value is clear from the equations above, hence the data vector, Z, will be biased. In the simple case above the bias is found to be

$$\begin{aligned} E(y) &= \int_0^{\infty} y f(y) dy \\ &\text{where} \\ f(y) &= \frac{1}{\sqrt{y}} e^{\frac{-y}{2\sigma^2}} \end{aligned} \tag{2.116}$$

The conclusion is, although the function order of the system to be identified is correct the estimation quality[15] might deteriorate when measurement noise is present.

$\dot{m}_t$ and η_t LWLS estimation Despite the warnings given above LWLS may be utilized to estimate the hypersphere of $\dot{m}_{t,c}$ and $\eta_{t,TS}$, since the turbine maps provide are made using state-of-the-art measurement equipment. Hence, the measurement noise level is assumed negligible.

The $\dot{m}_{t,c}$ and $\eta_{t,TS}$ hyperspheres are assumed affine in $N_{t,c}$, p_r and θ_{vgt}, i.e. a unique description is

$$\begin{aligned} \dot{m}_{t,c} &= \dot{m}_{t,c}\left(N_{t,c}, p_r, \theta_{vgt}\right) \\ \eta_{t,TS} &= \eta_{t,TS}\left(N_{t,c}, p_r, \theta_{vgt}\right) \end{aligned} \tag{2.117}$$

[15] Identification structure dependent.

The input variables are scaled prior to the identification procedure

$$\tilde{X} = \frac{2X - (\max(X) - \min(X))}{\max(X) - \min(X)} \tag{2.118}$$

where X is either one of $N_{t,c}$, p_r and θ_{vgt}, and $\tilde{X} \in [-1; 1]$. This step is taken to prevent numerical problems.

The second order Taylor series belonging to equation 2.117 with scaled dimensionless inputs has the structure

$$\begin{aligned} P(\tilde{N}_{t,c}, \tilde{p}_r, \tilde{\theta}_{vgt}) = \theta_0 &+ \theta_1 \left(\tilde{N}_{t,c} - \tilde{N}_{t,c,0}\right) + \theta_2 \left(\tilde{p}_r - \tilde{p}_{r,0}\right) + \theta_3 \left(\tilde{\theta}_{vgt} - \tilde{\theta}_{vgt,0}\right) \\ &+ \theta_{11} \left(\tilde{N}_{t,c} - \tilde{N}_{t,c,0}\right)^2 + \theta_{22} \left(\tilde{p}_r - \tilde{p}_{r,0}\right)^2 + \theta_{33} \left(\tilde{\theta}_{vgt} - \tilde{\theta}_{vgt,0}\right)^2 \\ &+ \theta_{12} \left(\tilde{N}_{t,c} - \tilde{N}_{t,c,0}\right) \left(\tilde{p}_r - \tilde{p}_{r,0}\right) \\ &+ \theta_{13} \left(\tilde{N}_{t,c} - \tilde{N}_{t,c,0}\right) \left(\tilde{\theta}_{vgt} - \tilde{\theta}_{vgt,0}\right) \\ &+ \theta_{23} \left(\tilde{p}_r - \tilde{p}_{r,0}\right) \left(\tilde{\theta}_{vgt} - \tilde{\theta}_{vgt,0}\right) \end{aligned} \tag{2.119}$$

The cubic space with the constraints $|\tilde{p}_r|, \left|\tilde{\theta}_{vgt}\right|, \left|\tilde{N}_{t,c}\right| \leq 1$ is divided into 1000 subspaces of equal size i.e. the side length of each individual subspace is 0.2. The origin of each Taylor expansion is now chosen as one of the $11^3 = 1331$ individual node points in the scaled input space, i.e.

$$\tilde{X}_0 \in \{-1, -0.8, -0.6, -0.4, -0.2, 0, 0.2, 0.4, 0.6, 0.8, 1\} \tag{2.120}$$

A reasonable data fraction, ζ, is here 0.3. This data fraction insures that inverse of $\phi^T \Omega \phi$ is well posed i.e. its eigenvalues are significantly different from 0. However, choosing ζ too high might limit the ability to capture local curvature. Hence, the local neighbor data fraction number is $0.3 \cdot 252 = 76$.

A cubic weighting function is selected here to shape the data kernel number g,

$$\omega_k^g = \begin{cases} \left(1 - \left(\frac{\rho_k}{r_g}\right)^3\right)^3 & , \quad \text{for } 0 \leq \frac{\rho_k}{r_g} \leq 1 \\ 0 & , \quad \text{else} \end{cases} \tag{2.121}$$

where the bandwidth r_g is set to be the euclidian distance between grid point $\theta_{0,g}$ and the closest measurement point outside the data kernel hypersphere i.e $r_g = \|y_{Q+1} - \theta_{0,g}\|_2$.

The setup is complete and the only thing missing is the computation of the coefficient vector Λ for of each the 1331 individual polynomials. This is done according to equation 2.109.

The LWLS estimates of $\dot{m}_{t,c}$ and $\eta_{t,TS}$, respectively, are compared to measurements in figure 2.36. The LWLS estimation technique are clearly able to resolve the curvature of the turbine mass flow and efficiency with reasonable smoothing.

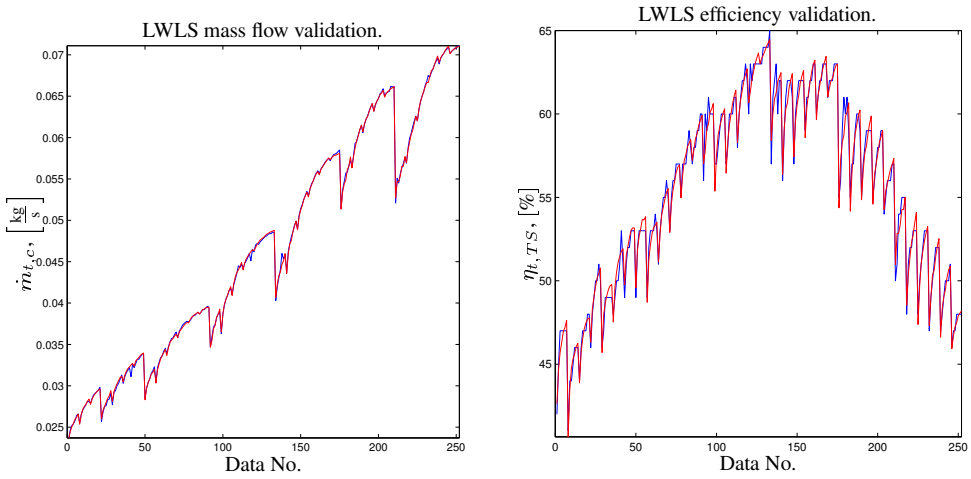

Figure 2.36: Comparison between $\dot{m}_{t,c}$, $\eta_{t,TS}$ (red curves) and the belonging LWLS estimates (blue curves), respectively.

The good quality of the fit within regression data boundaries is further confirmed by the small relative errors obtained. The relative estimation errors are plotted in figure 2.37.

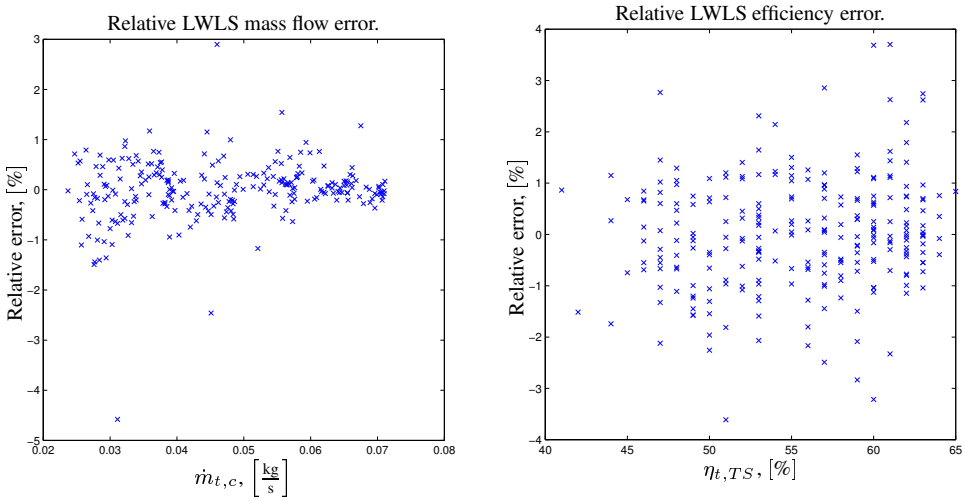

Figure 2.37: Relative LWLS estimation error.

However, despite the good estimation quality within kernel boundary the extrapolation accuracy deteriorates rapidly with increased kernel sphere distance. This is illustrated in figure 2.38.

The plot to the right shows the estimated $\dot{m}_{t,c}$ surface with θ_{vgt} fixed to 1. The surface shows the expected good performance within the kernel but a completely unrealistic curvature outside, especially for small U/C ratios. It should be noted that $\dot{m}_{t,c}$ has been limited to $0.08\frac{\text{kg}}{\text{s}}$ according to the specification in table 2.8.

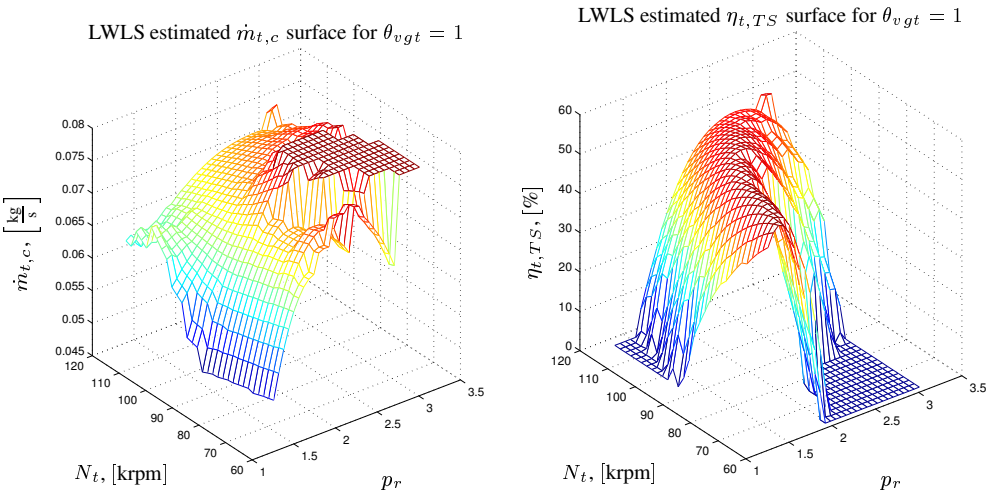

Figure 2.38: LWLS estimated surfaces for $\dot{m}_{t,c}$ respectively $\eta_{t,TS}$ with θ_{vgt} fixed to 1. The $\dot{m}_{t,c}$ surface is limited to $0.08\frac{\text{kg}}{\text{s}}$ according to specification in table 2.8, and the minimum efficiency is here set to 1 %.

The efficiency surface shows the same tendencies – good estimation within the kernel and a fast deteriorating performance outside the kernel, again especially in the case of small U/C ratios. However, this is to be expected since the kernel data generally only contains data points for the descending part of the U/C–$\eta_{t,TS}$ characteristic. Despite this unrealistic abrupt efficiency change as U/C approaches zero efficiency, surfaces of similar shape are used in the literature without question [108] possibly leading to completely erroneous control performance predictions. Instead the efficiency surface will tend towards zero asymptotically as U/C approaches 0. This may be proven as follows:

> *The pressure drop across the turbine stage is increased above choke limit meanwhile maintaining rotor speed fixed. Hence work is extracted. The isentropic enthalpy changes across the stage will approach c_pT_{01} asymptotically as $p_r \to \infty$. However, the Reynolds number, $Re = \frac{\rho c D}{\mu}$, will increases linearly with p_r since c, D and μ are fixed and the frictional losses will grow rapidly. A reasonable model of the frictional enthalpy loss is $\Delta h_{loss,fric} = aRe^b$ with $a, b \in \mathbb{R}_+$. Whence the frictional loss will approach the level of $\Delta h_{0t,s}$, and η_t will tend towards 0 asymptotically.*

LWLS (Locally Weighted Least Square) estimation has, despite its problems with measurement noise and extrapolation difficulties, proven itself as a versatile tool due to its realistic curvature reproduction within the kernel data limits, and because of its easy implementation. If engine simulation can be guarantied to stay within the data map provided, LWLS models are good model candidates.

2.3.4.6 Physical based VGT modelling

The modelling approach taken to model VGT characteristics is of a more pragmatic nature than the one taken in the compressor modelling section. This has been done mainly because of the reported relatively good accuracy within the data boundaries achieved utilizing the isentropic nozzle equation (see equation 2.97 on page 112). Whence, the mass flow, $\dot{m}_t$, and efficiency, η_t, aspects are here separated.

VGT mass flow modelling The theory to developed here is based on using the isentropic nozzle equation repeated below.

$$\dot{m}_{noz} = \begin{cases} C_D A_{noz,x} \frac{p_{up}}{\sqrt{RT_{up}}} p_{r,x}^{\frac{-1}{\gamma}} \sqrt{\frac{2\gamma}{\gamma-1}\left(1 - p_{r,x}^{\frac{1-\gamma}{\gamma}}\right)} & , \quad p_{r,x} \leq \left(\frac{\gamma+1}{2}\right)^{\frac{\gamma}{\gamma-1}} \quad \text{(subsonic)} \\ C_D A_{noz,x} \frac{p_{up}}{\sqrt{RT_{up}}} \sqrt{\gamma} \left(\frac{2}{\gamma+1}\right)^{\frac{\gamma+1}{2(\gamma-1)}} & , \quad p_{r,x} > \left(\frac{\gamma+1}{2}\right)^{\frac{\gamma}{\gamma-1}} \quad \text{(sonic)} \end{cases} \tag{2.122}$$

where p_{up} and T_{up} are the upstream pressure and temperature, respectively.

Due to the rotor rotation accompanied by a centrifugal pressure field buildup around the rotor a certain pressure ratio must exist for the mass flow to be positive. If the pressure ratio is smaller than this minimum pressure ratio, $p_{r,min}$, the characteristic will be inverted and the turbine will function as a bad compressor. Thus, it is assumed here that

$$p_{r,min} = p_{r,min}\left(N_t, p_r\right) \tag{2.123}$$

The flow through first the nozzle ring and later the rotor is considered equivalent to a flow through two nozzles in series. The flow through each nozzle is thus modelled as in equation 2.122. Whence the flow is,

$$\dot{m}_{noz/rot} = \dot{m}_{noz/rot}\left(A_{noz/rot}, C_{D,noz/rot}, p_{up,noz/rot}, T_{up,noz/rot}, p_{r,noz/rot}\right) \tag{2.124}$$

Since the volume of the turbine stage is expected to be of negligible size the gas dynamics may be neglected, i.e.

$$\dot{m}_{noz} = \dot{m}_{rot} = \dot{m}_t \tag{2.125}$$

The effective pressure ratio across the stage can naturally be split in two parts: the effective pressure ratio across the nozzle ring and the effective pressure ratio across the rotor, i.e $p_{r,eff} = p_{r,noz} p_{r,rot}$.

Based on the statement above the theory to be tested here is:

> *A certain pressure ratio across the turbine stage is required for a positive flow to exist. Therefore, the effective pressure ratio across the stage may be found as,*
>
> $$p_{r,eff} = \frac{p_r}{p_{r,min}}$$

This pressure ratio may subsequently be divided in two parts: a nozzle pressure ratio, $p_{r,noz}$ and a rotor pressure ratio, $p_{r,rot}$, i.e.

$$p_r = p_{r,min} p_{r,noz} p_{r,rot}$$

The pressure ratios, $p_{r,noz}$ and $p_{r,rot}$, derived may be found as

$$\begin{aligned} p_{r,rot} &= \alpha\left(p_{r,eff}, \theta_{vgt}\right) p_{r,eff} \\ p_{r,noz} &= \frac{1}{\alpha\left(p_{r,eff}, \theta_{vgt}\right)} \end{aligned}$$

Utilizing the pressure ratios found (provided C_D and A have been determined) the flow through the nozzle ring and rotor can be computed, respectively. However, neglecting the dynamics of the connecting volume only one of the pressure ratios is needed. Therefore, one turbine mass flow model candidate is

$$\dot{m}_t = \dot{m}_t\left(C_D, A_{rot}, p_{up}, T_{up}, p_{r,rot}\right)$$

In order to validate the theorem above the model given in the following three equations are implemented in the MATLAB® environment.

$$\begin{aligned} \left(\frac{U_3}{C_s}\right)_{|\dot{m}_{t,c}=0} &= \varsigma \\ \Updownarrow & \\ p_{r,min} &= \left(1 - \frac{\left(\frac{\pi}{60\varsigma} D_r N_{t,c}\right)^2}{2 c_p T_{01,ref}}\right)^{\frac{\gamma}{1-\gamma}} \end{aligned} \tag{2.126}$$

$$\begin{aligned} p_{r,eff} &= \frac{p_r}{p_{r,min}} \\ p_{r,rot} &= \frac{1 + \chi p_{r,eff}}{1 + \chi} \\ A_{eq} &= C_D A_{rot} \end{aligned} \tag{2.127}$$

$$\dot{m}_{t,c} = \begin{cases} A_{eq} \frac{p_{01,ref}}{\sqrt{R T_{01,ref}}} p_{r,rot}^{\frac{-1}{\gamma}} \sqrt{\frac{2\gamma}{\gamma-1}\left(1 - p_{r,rot}^{\frac{1-\gamma}{\gamma}}\right)} & , \quad p_{r,rot} \le \left(\frac{\gamma+1}{2}\right)^{\frac{\gamma}{\gamma-1}} \quad \text{(subsonic)} \\ A_{eq} \frac{p_{01,ref}}{\sqrt{R T_{01,ref}}} \sqrt{\gamma}\left(\frac{2}{\gamma+1}\right)^{\frac{\gamma+1}{2(\gamma-1)}} & , \quad p_{r,rot} > \left(\frac{\gamma+1}{2}\right)^{\frac{\gamma}{\gamma-1}} \quad \text{(sonic)} \end{cases} \tag{2.128}$$

The three parameters A_{eq}, ς and χ are found as the arguments that minimize the LS criterion for each of the seven different settings of the VGT position, θ_{vgt}, i.e.

$$\Theta = \arg \min_{\Theta=[A_{eq},\varsigma,\chi]} \sum_{n=1}^{N} \left(\dot{m}_{t,c,n} - \hat{\dot{m}}_{t,c,n}\right)^2 \tag{2.129}$$

	$A_{eq}\frac{p_{01,ref}}{\sqrt{RT_{01,ref}}}\left[\frac{\mathbf{kg}}{\mathbf{s}}\right]$	ς	χ
θ_{vgt} =**0**	0.0459	1.2019	0.7328
0.1	0.0513	1.2892	0.7557
0.2	0.0587	1.2131	0.9219
0.4	0.0722	1.3232	1.4536
0.6	0.0867	1.4976	1.9548
0.8	0.0976	1.4483	3.7628
1	0.1048	1.4839	4.4928

Table 2.10: Identified mass flow model parameters with variable ς.

The identified parameters are listed in table 2.10. As expected A_{eq} and $p_{r,rot}$ (χ) increase with θ_{vgt}, whereas ς exhibits only a slight tendency to increase with θ_{vgt} opening.

Inspired by [87] ς is fixed to the mean value of the column data in table 2.10, and a rerun of the identification procedure is made. Table 2.11 lists the identified values for A_{eq} and χ with ς fixed to 1.351. This value is reasonably close to the value of 1.2 given in [87].

	$A_{eq}\frac{p_{01,ref}}{\sqrt{RT_{01,ref}}}\left[\frac{\mathbf{kg}}{\mathbf{s}}\right]$	χ
θ_{vgt} =**0**	0.0457	0.6999
0.1	0.0512	0.7420
0.2	0.0584	0.8669
0.4	0.0722	1.4265
0.6	0.0870	2.2377
0.8	0.0976	4.6719
1	0.1049	5.9881

Table 2.11: Identified mass flow model parameters with $\varsigma = 1.3510$.

Another interesting phenomenon found by comparing table 2.10 and 2.11 is how fixing ς affects the two other parameters: A_{eq} is completely unaffected on any significance level, and only χ is noticeably altered. Comparing the A_{eq} and χ level against θ_{vgt} graphically the following very interesting plots in figure 2.39 are obtained.

The figure clearly shows that the first and second order approximation of A_{eq} and χ, respectively, are reasonable. The representative polynomials are identified as

$$\begin{aligned} A_{eq}\left(\theta_{vgt}\right) &= \left(1.7584\theta_{vgt} + 1.3174\right) \cdot 10^{-4}\mathrm{m}^2 \\ \chi\left(\theta_{vgt}\right) &= 5.9366\theta_{vgt}^2 - 0.4315\theta_{vgt} + 0.6930 \end{aligned} \tag{2.130}$$

These two functions provide the missing link between the position of the VGT vanes and the mass flow through the turbine.

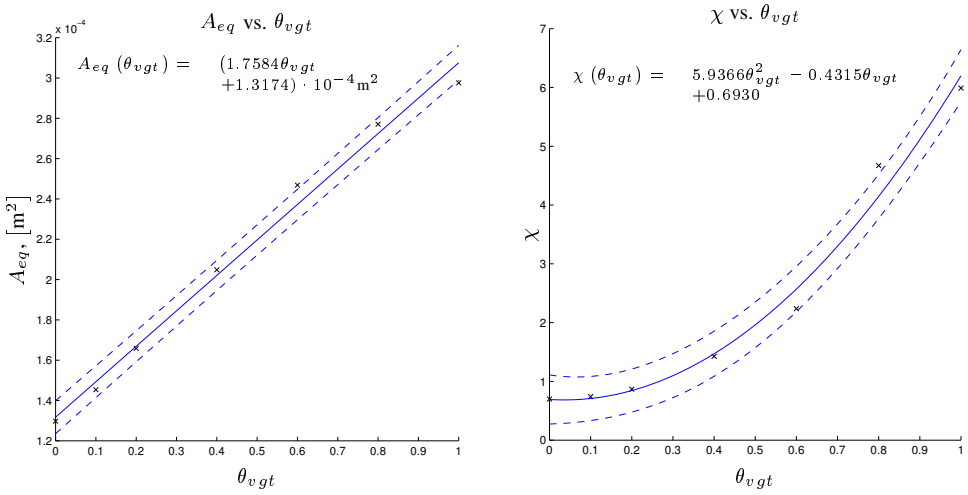

Figure 2.39: Equivalence area, A_{eq}, and fraction coefficient, χ, as function of the normalized VGT position. The dashed lines illustrate the 95% confidence intervals around the lines identified.

The final model is thus found by collecting equation 2.126, 2.127, 2.128 and 2.130.

Figure 2.40 compares the mass flow model with measurement, and indeed, the performance of the model is very good.

This good performance is confirmed further by investigating the relative error between model and measurement. The relative error is depicted to the left in figure 2.41.

As seen from the figure, the error stays between $\pm 1\%$ except for a few of outliers. Assuming the error is normally distributed the model error within the turbine map will with 99.7% certainty stay between $\pm$ 1.7%.

In addition to a good mass flow estimation the model also makes possible investigation of how the pressure drop across the stage is distributed between nozzle and rotor. This is illustrated to the right in figure 2.41. The plot shows as expected a decrease in nozzle pressure ratio and hence increase in rotor pressure ratio as the VGT is opened.

The turbine characteristics provided by manufactures notoriously lack low pressure ratio/low speed data points, thus hampering the modelling process. This is very unfortunate since the speedline characteristic for low p_r and N_t values is of paramount importance when evaluating engine model performance in the idle to mid load operating range. This problem is made worse when a pulse exhaust manifold is used. The problem is illustrated in figure 2.42. The figure shows the importance of including the pressure fluctuation in the calculation of $\dot{m}_{t,c}$ before the mean value computation. The idealized pressure ratio signal used here for illustrative purpose contains the mean and first harmonic (event frequency) of a imagined exhaust pressure trace for a four cylinder engine. However, the knowledge obtained using this imaginary and simple exhaust manifold pressure trace may be classified

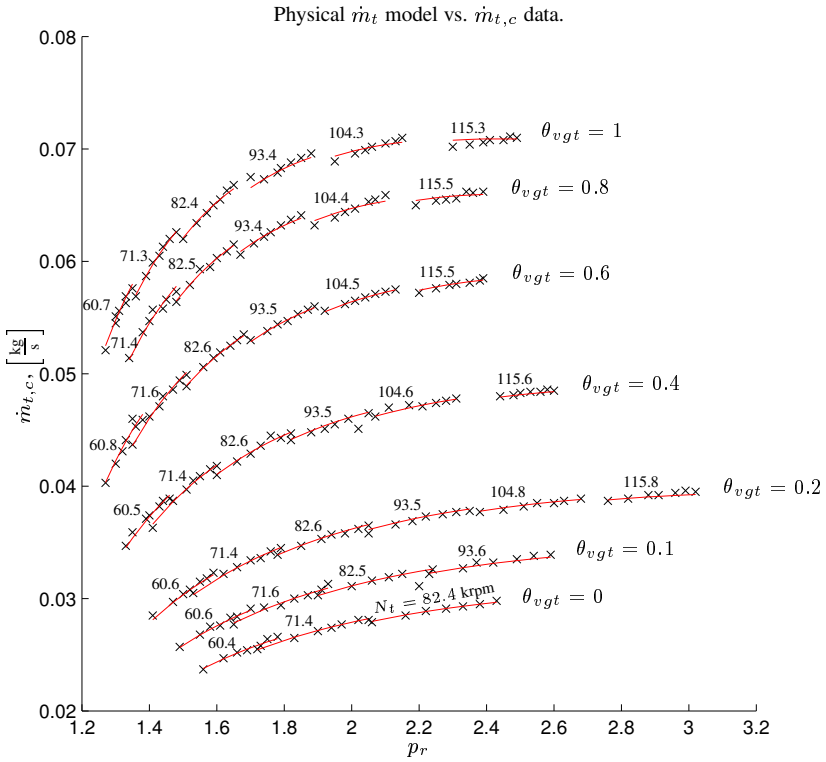

Figure 2.40: Comparison between the physical deducted VGT model and measurements. The measurements are marked with $\times$.

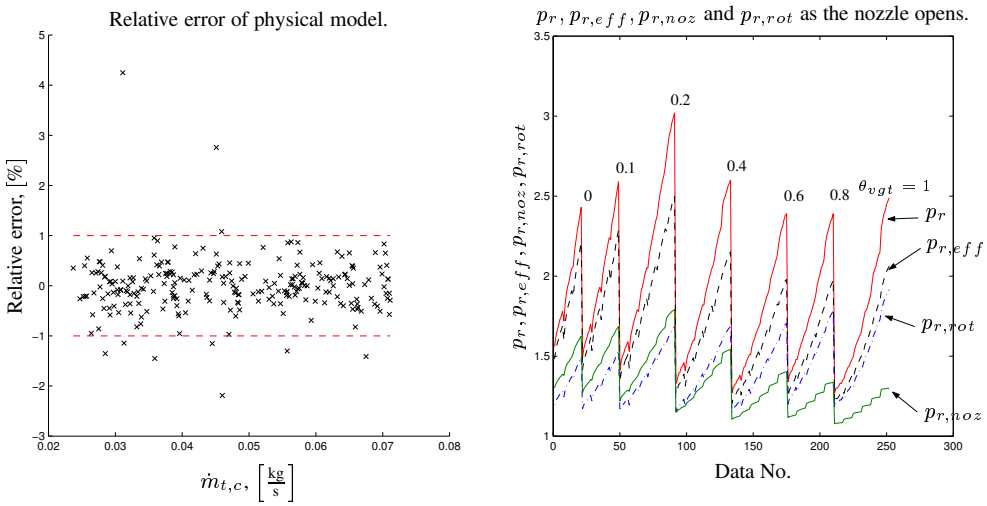

Figure 2.41: The relative error of the mass flow model predictions and measurements. The mean and variance of the relative error in % are computed to -0.002% and 0.305%^{2}, respectively. The plot to the right shows the distribution of the different important pressures as the nozzle opens.

as general for the for following reason. The pressure ratio across the turbine stage may stay close to zero flow conditions much of the time[16] i.e. (the pressure ratio across the turbine stage is close to ι, see e.g. [60]). This close to non-flow condition is followed by a hot, narrow and high pressure burst (see e.g [60]) which utilizes a great extend of the turbine p_r–$\dot{m}_{t,c}$ characteristic. Hence, the real turbine mass flow trace will be similar in appearance to the mass flow traces presented in presented in figure 2.42 .

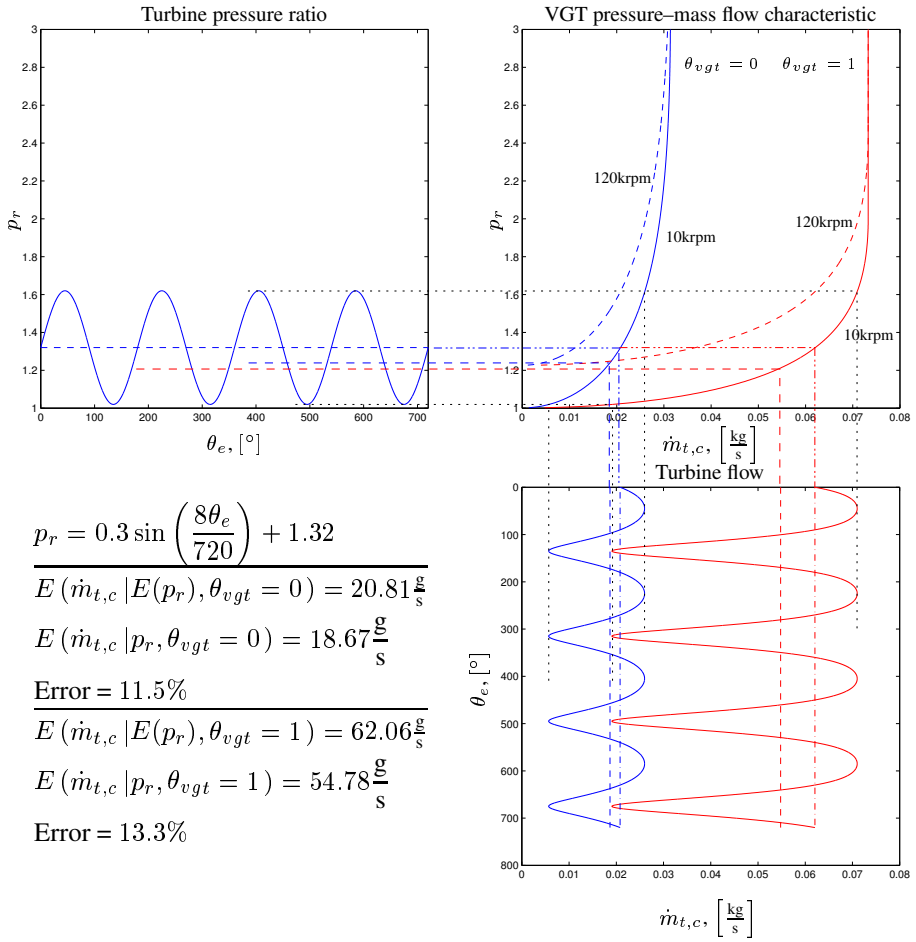

Figure 2.42: Fluctuation scenario in exhaust manifold and its influence on the effective Turbine mass flow. The figure also illustrates how the p_r–$\dot{m}_{t,c}$ characteristic alters with turbine speed due to the pressure gradient field created around the rotor.

This conclusion is analogous to the research presented in [10] where the intake manifold pressure fluctuation's influence on correct throttle mass flow estimation was investigated.

[16] Exhaust manifold design dependent.

VGT efficiency modelling The loss model to be present here is analogous to the compressor loss model and is primarily based on fluid velocity investigations. However, the availability of a mass flow model makes some of the turbine loss estimation steps easier when compared to their dual in the compressor loss model, since some of the important fluid velocities can be readily computer prior to the loss calculation.

The nozzle inlet conditions are sketched in figure 2.43, where the notation will be defined in which follows.

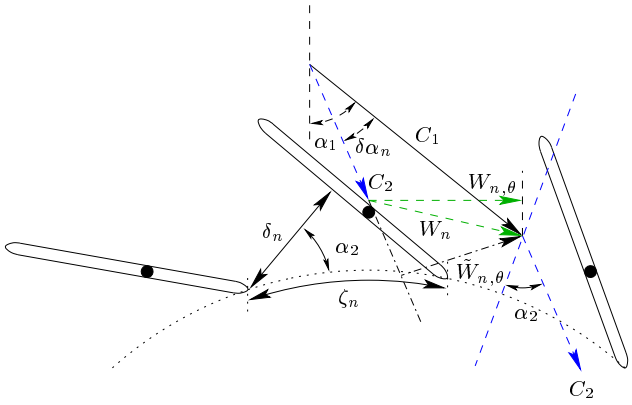

Figure 2.43: Diagrammatic illustration of the nozzle inlet conditions.

The first task is establish the size and direction of the absolute nozzle inlet velocity, C_1. Assuming the scroll inlet process is ideal the angular momentum of the gas is conserved, i.e.

$$R_s C_{s,\theta} = R_{n,o} C_{1,\theta} \tag{2.131}$$

where R_s is the distance from turbine center to the centroid of the scroll inlet where mass distribution is initiated. $R_{n,o}$ is the radius of the circle connecting the nozzle inlet tips, and is of course θ_{vgt} dependent.

The scroll volume of an automotive turbine is small, hence neglecting filling–emptying dynamics of the turbine stage is justifiable. Thus, due to mass conservation the mass flow in and out of the scroll are equal, i.e.

$$\dot{m}_t = \rho_s A_s C_{s,\theta} = 2\pi R_{n,o} b_r \rho_1 C_{1,r} \tag{2.132}$$

where A_s is the area of scroll inlet centroid mentioned above.

The inlet angle, α_1, is defined as

$$\cot(\alpha_1) \triangleq \frac{C_{1,r}}{C_{1,\theta}} \tag{2.133}$$

Collecting equation 2.131, 2.132 and 2.133 the cotangent of the inlet angle, α_1, can be rewritten as

$$\cot(\alpha_1) = \frac{A_s \rho_s}{2\pi b_r R_s \rho_1} \tag{2.134}$$

The acceleration of the flow from turbine inlet to nozzle is small. Hence, the static gas density change is small, i.e. $\rho_1 \approx \rho_s$, allowing a further reduction of equation 2.134 to

$$\cot(\alpha_1) = \frac{A_s}{2\pi b_r R_s} \tag{2.135}$$

Thus, the gas inlet angle, α_1 is only a function of the A/R setting of the turbine. Using the equation above, the inlet angle of the experimental turbine is found to be 75°.

The relation above is of course very idealized especially in the case of pulse turbocharging. However, the problem is most pronounced in the case with vaneless nozzle ring turbines due to the harsher accelerations (higher local friction) and the larger control volume, and less important in inlet nozzles with guide vanes. Due to its simplicity the inlet angle of the gas will thus be computed according to equation 2.135.

The inlet angle for turbine with vaneless nozzle ring has been studied in greater detail in [34] (see also [87]).

The next step in turbine loss modelling is the construction of a model of the nozzle friction and incidence losses, along with a discussion of the assumptions made in the pursuit of this goal.

Applying the theory above for the direction of the inlet flow velocity together with the law of continuity, C_1 may be written as

$$C_1 = \frac{C_{1,r}}{\cos(\alpha_1)} = \frac{\dot{m}_t}{2\pi R_{n,o} b_r \rho_1 \cos(\alpha_1)} \tag{2.136}$$

Due to the collision between gas and the vaned nozzle ring a loss will be present. Analog to the NASA incidence loss model presented in the compressor section this energy loss is modelled by

$$\Delta h_{inc,noz} = \frac{W_{n,\theta}^2}{2} \tag{2.137}$$

Whence, the change in the tangential velocity is dissipated as heat. However, the size and direction of the nozzle outlet velocity is not readily available.

According to [38] the outlet angle of the gas, α_2, may from common steam turbine practice be found as

$$\cos(\alpha_2) = \frac{\delta_n}{\zeta_n} \tag{2.138}$$

where ζ_n is the radial distance between the nozzle tips, and δ_n is the minimum distance between neighboring nozzle blades. Although the relation above is a rough approximation the error introduced is small according to [87]. However, it should not be forgotten how sensitive rotor operation is with respect to the incoming flow angle; an issue dual to the compressor impeller incidence losses discussed in the compressor section. It is therefore likely that a certain level of modelling error

may be expected when using this expression. However, it is decided here to proceed with the turbine loss modelling using this relation due to its simplicity

The radial distance, ζ_n, is found as (see evt. figure 2.32)

$$\zeta_n = \frac{2\pi \left(R_{r,a} - l_{n,tip} \cos\left(\alpha_n\right)\right)}{Z_n} \tag{2.139}$$

The minimum distance between blades, δ_n, may from geometrical considerations be found as the vector going through the nozzle outlet tip perpendicular to the direction vector of the neighboring nozzle blade.

Figure 2.44 shows ζ_n, δ_n and α_2 as a function of the nozzle blade angle α_n for the experimental VGT. It is noticed that α_2 is close being a linear function of the blade angle.

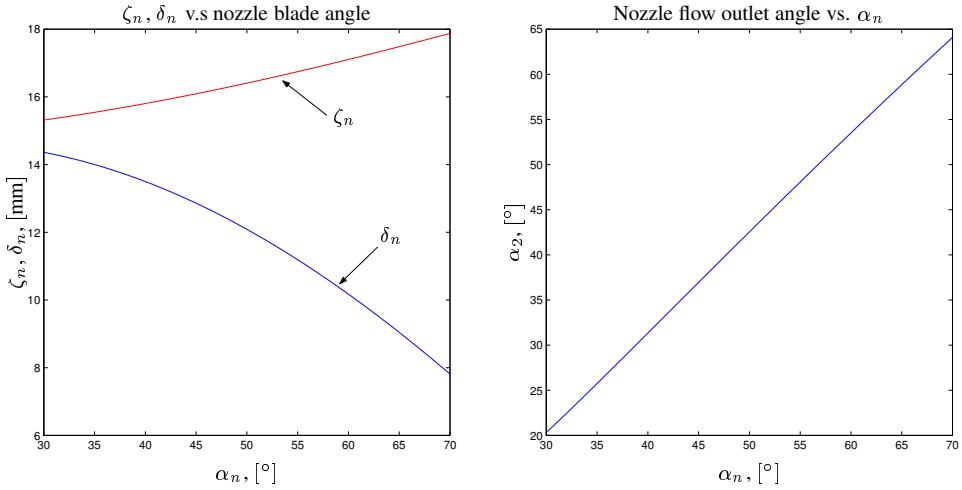

Figure 2.44: The nozzle flow

The size of the absolute outlet velocity C_2 is more difficult to characterize even before the strong influence of the frictional forces along nozzle passage, since it itself is a function of the energy loss $\Delta h_{inc,noz}$ i.e the relation is implicit. Instead it is assumed that the gas attains an angle of α_2 after nozzle entry, and the point of no loss is achieved when $\alpha_1 = \alpha_2$. A energy loss model fulfilling these conditions is

$$\begin{aligned} \Delta h_{inc,noz} &= \frac{\tilde{W}_{n,\theta}^2}{2} \\ &\text{with} \\ \tilde{W}_{n,\theta} &= C_1 \sin\left(\alpha_1 - \alpha_2\right) = C_1 \sin\left(\delta\alpha_n\right) \end{aligned} \tag{2.140}$$

The nozzle incidence loss will be modelled according to the definition above in the following.

The static pressure and temperature at the nozzle inlet after the nozzle collision process is found as

$$\begin{aligned} T_{1,a} &= T_{1,b} + \frac{\Delta h_{inc,noz}}{c_p} \\ p_{1,a} &= p_{1,b} \end{aligned} \tag{2.141}$$

assuming an isobaric loss profile is followed. The subscripts a and b denote after incidence and before incidence conditions, respectively.

The stagnation inlet conditions are from considerations of continuity derived as

$$\begin{aligned} T_{01,a} &= T_{1,a} + \frac{C_{1,a}^2}{2c_p} \\ p_{01,a} &= p_{1,a}\left(\frac{T_{1,a}}{T_{01,a}}\right)^{\frac{\gamma}{1-\gamma}} \end{aligned} \tag{2.142}$$

where

$$C_{1,a} = \frac{\dot{m}_t}{2\pi R_{n,o} b_r \rho_{1,a} \cos\alpha_2}$$

The inlet conditions and geometry, respectively, are now known and may together with the mass flow model form the basis for computation of the nozzle discharge coefficient.

$$\dot{m}_t = \begin{cases} C_D A_{noz} \frac{p_{01,a}}{\sqrt{RT_{01,a}}} p_{r,noz}^{\frac{-1}{\gamma}} \sqrt{\frac{2\gamma}{\gamma-1}\left(1 - p_{r,noz}^{\frac{1-\gamma}{\gamma}}\right)} & , \quad p_{r,noz} \leq \left(\frac{\gamma+1}{2}\right)^{\frac{\gamma}{\gamma-1}} \\ C_D A_{noz} \frac{p_{01,a}}{\sqrt{RT_{01,a}}} \sqrt{\gamma}\left(\frac{2}{\gamma+1}\right)^{\frac{\gamma+1}{2(\gamma-1)}} & , \quad p_{r,noz} > \left(\frac{\gamma+1}{2}\right)^{\frac{\gamma}{\gamma-1}} \end{cases}$$

where

$$\begin{aligned} A_{noz} &= b_r \delta_n Z_n \\ p_{r,noz} &= \frac{p_r}{p_{r,min} p_{r,rot}} \end{aligned} \tag{2.143}$$

The discharge coefficient for each of the seven θ_{vgt} positions is found as the argument minimizing the cumulative quadratic error between $\dot{m}_t$ and $\hat{\dot{m}}_t$, i.e.

$$C_D = \arg \min_{C_D \in]0;1]} \sum_{k=1}^{N} \left(\dot{m}_{t,k} - \hat{\dot{m}}_{t,k}\right)^2 \tag{2.144}$$

where $\hat{\dot{m}}_t$ is computed according to equation 2.143.

The results of the C_D computations are graphically illustrated in figure 2.45.

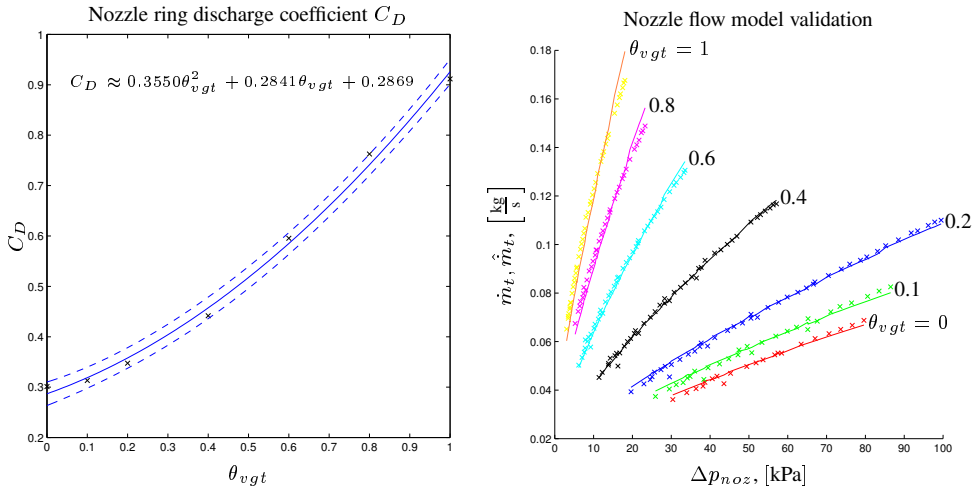

Figure 2.45: Computed discharge coefficient and nozzle flow model validation.

The plot to the left shows the computed discharge coefficients for the seven VGT positions. The discharge coefficient may be approximated with good accuracy by a second order polynomial in θ_{vgt}. The polynomial together with it's 95% confidence interval are seen as a solid and dashed blue lines, respectively.

The discharge coefficient, as expected, is found to increase as the VGT opens. Hence, frictional forces become more and more dominant with VGT closure.

The plot to the right in figure 2.45 shows a comparison between flow measurements and estimates obtained utilizing equation 2.143 with the discharge description just mentioned. The agreement is good and adds to the confidence in the pressure distribution model developed as a part of the turbine mass flow model. Only at large VGT positions and relatively large pressure drops is a small disagreement noticed. This disagreement can possibly be traced back to the nozzle incidence loss approximation made earlier in this section. However, since the disagreement is so small this has not been investigated.

The next problem is the development of suitable models for the nozzle passage friction loss, rotor incidence loss and rotor friction loss. This is, however, an extremely difficult task since the individual loss process are hard to separate. An identification procedure must thus estimate the individual loss process parameters simultaneously in order to be successful.

The friction loss in the nozzle passages is Reynolds number dependent, and is commonly approximated as a power function of this number, i.e

$$\Delta h_{fric} \approx aRe^b, \qquad \text{for } a, b \in \mathbb{R}_+ \tag{2.145}$$

A loss model with the structure given above was implemented however in vain. The structure was found to give unrealistic low friction losses at small VGT openings and at high inlet temperatures, respectively. Instead, the Reynolds number

definition was changed from $\frac{\rho_{1,a} C_{1,a} \delta_n}{\mu}$ to

$$Re = \sqrt{\frac{T_{01}}{T_{01,ref}}} \frac{C_{1,a} \rho_{1,a} \delta_n}{C_D^2 \mu} \tag{2.146}$$

and the nozzle enthalpy loss due friction computed as

$$\Delta h_{fric,noz} = a \sqrt{\frac{T_{01}}{T_{01,ref}}} Re^b \tag{2.147}$$

Using this analogy the Reynolds number loss correlation is made almost independent of the nozzle position and the upstream temperature conditions i.e geometric and thermodynamic conditions are lumped into the correlation.

Before the rotor inlet conditions can be computed the nozzle outlet conditions must be determined.

The pressure ratio across the nozzle ring, $p_{r,noz}$, is readily available from the mass flow model, and the nozzle outlet temperature following an isentropic expansion process may be found as

$$T_{2,i} = T_{01,a} p_{r,noz}^{\frac{1-\gamma}{\gamma}} \tag{2.148}$$

However, due to the friction loss the real static outlet temperature is

$$T_2 = T_{2,i} + \frac{\Delta h_{fric,noz}}{c_p} \tag{2.149}$$

The static outlet pressure is readily found to be

$$p_2 = \frac{p_{01,a}}{p_{r,noz}} \tag{2.150}$$

Hence, the absolute velocity of the gas leaving the nozzles is

$$C_2 = \frac{\dot{m}_t R T_2}{Z_n b_r \delta_n p_2} \tag{2.151}$$

After nozzle exit the flow is accelerated further due to area decrease. This flow acceleration may with good approximation be assumed lossless since the flow distance from nozzle exit to rotor inlet is small. Furthermore, it is assumed that the flow retains the flow angle α_2. Thus, the tangential velocity increase is derived to

$$C_{3,\theta,b} = \frac{R_{n,e}}{R_r} C_2 \sin \alpha_2 \tag{2.152}$$

and the radial velocity component of C_3 before rotor entry to

$$C_{3,r,b} = \frac{R_{n,e}}{R_r} C_2 \cos \alpha_2 \tag{2.153}$$

The rotor inlet conditions are shown schematically in figure 2.32 on page 110.

The collision loss is found analogous to the compressor impeller incidence loss assuming that the complete tangential component of the relative kinetic energy is destroyed. This model is in the literature referred to as the *NACA model* (see e.g. [98, 87]). The loss in specific energy is thus found as

$$\Delta h_{inc,rot} = \frac{W_{3,\theta,a}^2}{2} = \frac{\left(C_{3,\theta,b} - U_3\right)^2}{2} \tag{2.154}$$

The pressure and temperature before rotor entry are

$$\begin{aligned} T_{3,b} &= T_2 - \frac{C_{3,b}^2 - C_2^2}{2} \\ p_{3,b} &= p_2 \left(\frac{T_2}{T_{3,b}}\right)^{\frac{\gamma}{1-\gamma}} \end{aligned} \tag{2.155}$$

Assuming an isobaric loss profile the inlet conditions immediately after rotor entry are (see evt. figure 2.32 on page 110)

$$\begin{aligned} T_{3,a} &= T_{3,b} + \frac{\Delta h_{inc,rot}}{c_p} \\ p_{3,a} &= p_{3,b} \\ W_{3,a} &= C_{3,r,a} = \frac{\dot{m}_t R T_{3,a}}{2\pi R_r b_r p_{3,a}} \qquad \text{(radial rotor design)} \end{aligned} \tag{2.156}$$

In the computation of the relative velocity it is assumed, that the flow follows the rotor blade angle immediately after the collision.

The friction model structure developed in the compressor section is here reused to model the rotor friction loss, i.e.

$$\Delta h_{fric,rot} = \frac{T_{3,a}}{T_{01,ref}} \left(\varrho_1 U_3^2 + \varrho_2 W_{3,a} U_3 + \varrho_3 W_{3,a}^2\right) \tag{2.157}$$

The scaling coefficient $\frac{T_{3,a}}{T_{01,ref}}$ is introduced since the rotor friction loss was found to scale badly with temperature increase.

The total specific enthalpy loss is found as the sum of the four contribution just modelled

$$\Delta h_{t,loss} = \Delta h_{inc,rot} + \Delta h_{fric,rot} + \Delta h_{inc,noz} + \Delta h_{fric,noz} \tag{2.158}$$

The coefficients of the frictional loss model are found by minimizing the criterion in equation 2.159, and are listed in table 2.12.

$$J_{loss} = \sum_{k=1}^{N} \left(\Delta h_{t,loss,k} - \Delta \hat{h}_{t,loss,k}\right)^2 \tag{2.159}$$

a	b	ϱ_1	ϱ_2	ϱ_3
0.0984	0.9416	0	0.0028	0.6413

Table 2.12: Turbine friction coefficients identified.

Interestingly, the rotor friction is found independent of the rotational speed. Moreover, the cross term product, $W_{3,a}U_3$, is not significantly different from zero, and the rotor channel friction loss is found to be mainly dependent on $W_{3,a}$. This is opposite the impeller friction conclusions made earlier in the compressor section, and may have to do with the much higher turbine trim setting.

The VGT efficiency model implemented may, according to the total-to-static efficiency definition, be expressed as

$$\boxed{\eta_{t,TS} = \frac{\Delta h_{0t}}{\Delta h_{0t,i}} = \frac{c_p T_{01}\left(1 - p_r^{\frac{1-\gamma}{\gamma}}\right) - \Delta h_{t,loss}}{c_p T_{01}\left(1 - p_r^{\frac{1-\gamma}{\gamma}}\right)}} \tag{2.160}$$

The performance of the model is graphically evaluated in the three upper plots of figure 2.46. The relative error of the model within map boundaries is found to be slightly biased and varying between -12 and 21%. The error is largest for $\theta_{vgt} = 0.2$ and $\theta_{vgt} = 0.4$ where the high rotational speed losses are clearly overestimated. This is seen in the center plot where the measured and estimated enthalpy loss levels computed are depicted. However, the general picture of the turbine performance provided is physically correct. This may be appreciated by comparing the change in the $\Delta h_{t,loss}$ level as the VGT opens. In vicinity of the closed position the curvature of both estimate and measurement is smooth (nozzle friction is dominant) changing to a step like structure for both curves near as the VGT approaches its fully open VGT position (rotor incidence is dominant).

In order to remove the error bias the following pure fitting function is proposed

$$\Pi = \Pi(N_t, p_r, \theta_{vgt}) \tag{2.161}$$

and computed by finding the loss function minimum below

$$J_{min} = \min_{\theta} \left(\eta_{t,TS} - \Pi\left(\cdot;\theta\right)\hat{\eta}_{t,TS}\right)^2 \tag{2.162}$$

where θ is a parameter vector. The correct turbine efficiency is finally realized as

$$\hat{\eta}_{t,TS,c} = \Pi(\cdot;\theta_{min})\hat{\eta}_{t,TS} \tag{2.163}$$

Since it is desirable, as mentioned in the beginning of this section, that the fitting function works within regression data limits only to avoid extrapolation the multiplicative correction function, Π, is realized as a function of θ_{vgt} only. The final

fitting function minimizing the LS criterion is realized as a second order polynomial in θ_{vgt}

$$\Pi_{vgt} = -0.7315\theta_{vgt}^2 + 0.7375\theta_{vgt} + 0.9622 \tag{2.164}$$

The corrected turbine efficiency, $\hat{\eta}_{t,TS,c}$, is graphically evaluated in the two lowermost plots in figure 2.46. It is clearly seen here that the fitting function is able to remove the bias from the relative error, and reduces the relative error to be within a window of $\pm 10\%$. However, since the function only works on $\hat{\eta}_{t,TS}$ it does not provide any information on where the enthalpy losses are falsely distributed. Hence, the correction will not be used in the evaluation of the enthalpy loss distribution of the turbine stage.

The efficiency model makes a better understanding possible of how the enthalpy loss is distributed between the nozzle ring and rotor as the VGT opens. This loss distribution is graphically illustrated in figure 2.47. The figure clearly shows, as expected from figure 2.46, that the two most dominant loss sources are the nozzle ring friction loss for small VGT settings and rotor incidence loss for larger VGT settings, respectively. Another interesting observation made is the rather low magnitude of the computed rotor friction. However, the trim size of 76 (see table 2.8) for the rotor is a lot larger than those for the compressors examined in the compressor modelling section i.e. the flow path basically speaking only changes its direction but not its dimensions. Hence, the rotor loss computations presented above are not unrealistic.

The physical loss model is now complete making a loss surface estimation from θ_{vgt}, $N_{t,c}$ and p_r alone possible. Such surfaces are for $\theta_{vgt} = 0$, 0.5 and 1 depicted in figure 2.48. The surfaces show the skewed nature of the turbine efficiency. Unfortunately, as mentioned in discussion of the pressure fluctuations and effective turbine mass flow, a great deal of the turbine operation takes place in the vicinity of $p_r = \iota$ (no flow). Hence, following a typical pressure cycle in the exhaust manifold, an efficiency trajectory may be drawn on these surfaces exactly where they are strongly skewed. Therefore, the effective efficiency mean value may be considerably smaller than in the case with constant pressure turbocharging.

Although the low-speed/high pressure efficiencies look a bit too high, they are not unrealistic. The measurements, however, do not cover this region, but the general U/C line shows a growing tendency with a U/C decrease (see figure 2.33 on page 115). Thus none of the U/C-$\eta_{t,TS}$ lines have reached their maximum level.

Increasing the pressure ratio (not shown graphically here) the surfaces are found tending towards zero efficiency asymptotically. This is a property desired from the theory outlined in the beginning of this section.

The following natural question to the just presented radial turbine efficiency model now arises: "Is a relative error window of approximately $\pm 10\%$ acceptable?". The answer is: "It depends on the application". If the model should be used in an high fidelity application requiring a level of accuracy within a few percent the only natural step further would be to model the complete exhaust system by wave action models (see e.g [118]). These model structures generally tend to have

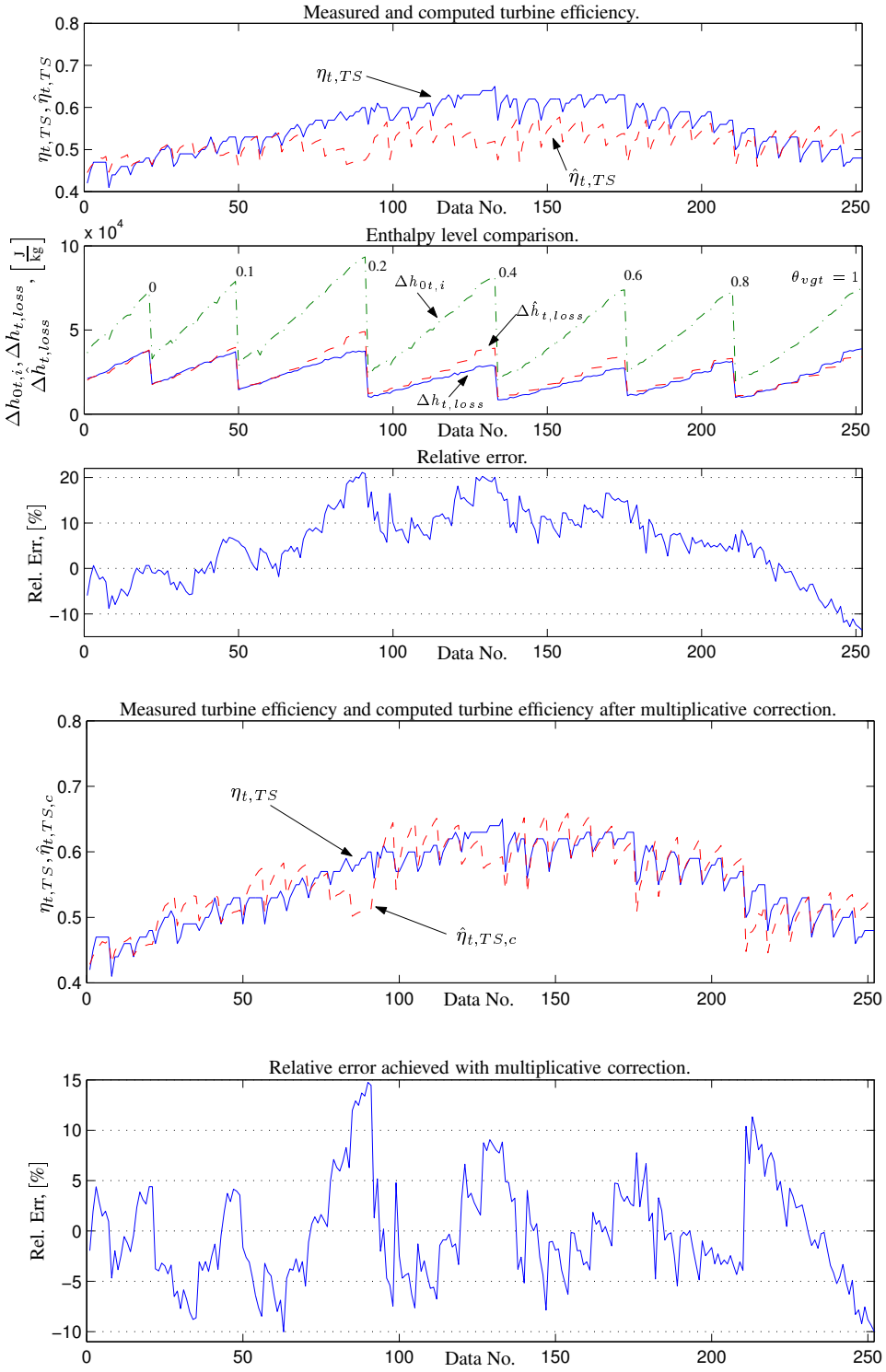

Figure 2.46: $\eta_{t,TS}$ model performance. The first three plot show the performance of the turbine efficiency model before multiplicative correction, and the last two plots depict the turbine model performance after the correction.

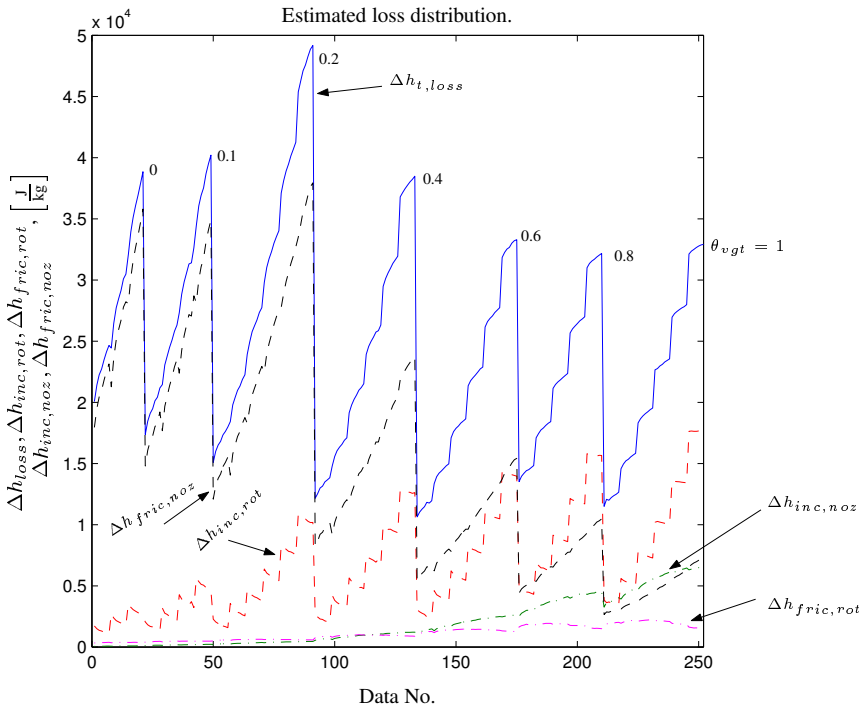

Figure 2.47: Enthalpy loss distribution.

a higher number of tuneable parameters compared to the radial turbine model just presented. Thus, a higher level of accuracy can more easily be achieved. However, such models are not suited as modelling background for engine control designs. If however a MVEM framework is considered, in which the exhaust fluctuations are neglected, the accuracy level of the VGT efficiency model presented is sufficient for the following intuitive reasons. Efficiency degradation levels up to 30% in pulse-turbocharging application are to be expected (see [60]) if the turbine efficiency estimate is computed utilizing the mean values of the exhaust pressure and the temperature. If an on-engine turbine efficiency modelling accuracy level should be achieved within a few percent the thermodynamic states in front of the turbine inlet must be known within high precision. It is shown in [118] that a reasonable detail level of the inlet state frequency spectrum must contain at least information about the third harmonic of the exhaust pulsation (this corresponds to three times the event frequency of a four cylinder engine). This required spectrum bandwidth is much larger than the bandwidth obtainable with MVEM realized engine models. According to e.g. [43] the bandwidth of MVEM type models are bit below the engine cycle frequency. Hence, the spectrum provided by a MVEM type engine model is at least one decade below that required by a successful physical based computation of the turbine efficiency. Thus, if a high fidelity MVEM type engine model is required a substantial amount of work used on massaging model parameters to fit the data is to be expected.

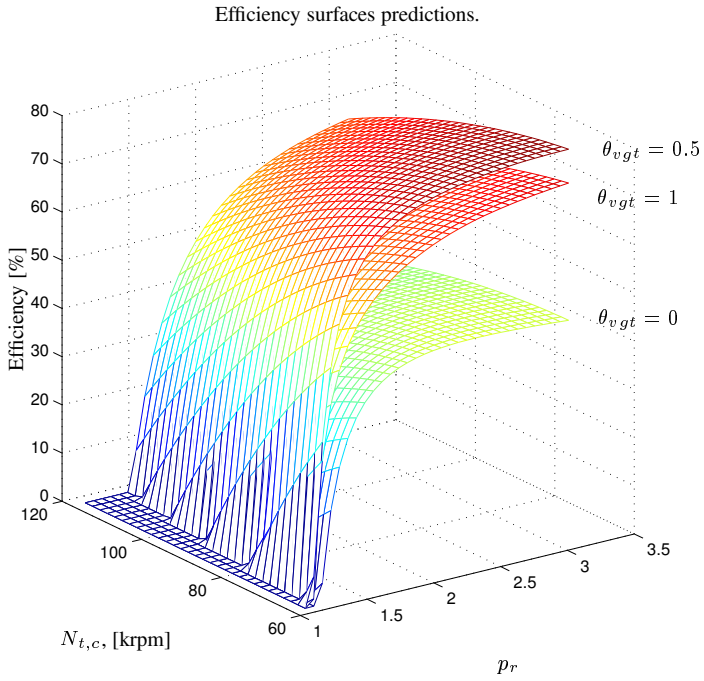

Figure 2.48: Extrapolated turbine efficiency surfaces for $\theta_{vgt} = 0$, 0.5 and 1. Remark: in the region with compressor like behavior of the turbine, the efficiency has been fixed at 1%.

A non-dimensional approach to encompass the effect of exhaust pulsations on the turbine efficiency is provided in [60]. However, this approach requires a mapping of the instantaneous static pressure in front of the turbine; a job almost impossible to complete on an engine equipped with an EGR system and a VGT. This would require an mapping of the engine in the minimum four following dimensions: engine speed, engine torque, VGT position and EGR valve position.

2.3.4.7 Summary

The modelling of the turbine mass flow and efficiency are divided in this section in contrast to the compressor model, since it is found that separate mass flow modelling could give remarkably good mass flow estimation (within 1.7% relative accuracy). This model provides the mass flow input to the efficiency model.

The mass flow model is new in its concept, since it can predict the pressure distribution across the nozzle ring and rotor, respectively. Along with this pressure ratio distribution, the pressure ratio needed to overcome the pressure gradient developed by rotor rotation is also computed. Hence, the model can also predict when the turbine characteristic is inverted (compressor like operation is observed). All these estimation possibilities are made available by the model from the VGT setting θ_{vgt}, the turbine speed N_t, and the pressure ratio across the stage p_r data alone.

The three sub models making up the mass flow model are repeated below.

$$\begin{aligned} \left(\frac{U_3}{C_s}\right)_{|\dot{m}_{t,c}=0} &= \varsigma \\ \Updownarrow & \\ p_{r,min} &= \left(1 - \frac{\left(\frac{\pi}{60\varsigma} D_r N_{t,c}\right)^2}{2c_p T_{01,ref}}\right)^{\frac{\gamma}{1-\gamma}} \end{aligned} \tag{2.165}$$

$$\begin{aligned} p_{r,eff} &= \frac{p_r}{p_{r,min}} \\ p_{r,rot} &= \frac{1+\chi p_{r,eff}}{1+\chi} \\ A_{eq} &= C_D A_{rot} \end{aligned} \tag{2.166}$$

$$\dot{m}_{t,c} = \begin{cases} A_{eq}\frac{p_{01,ref}}{\sqrt{RT_{01,ref}}} p_{r,rot}^{\frac{-1}{\gamma}} \sqrt{\frac{2\gamma}{\gamma-1}\left(1 - p_{r,rot}^{\frac{1-\gamma}{\gamma}}\right)} & , \quad p_{r,rot} \leq \left(\frac{\gamma+1}{2}\right)^{\frac{\gamma}{\gamma-1}} \quad \text{(subsonic)} \\ A_{eq}\frac{p_{01,ref}}{\sqrt{RT_{01,ref}}} \sqrt{\gamma}\left(\frac{2}{\gamma+1}\right)^{\frac{\gamma+1}{2(\gamma-1)}} & , \quad p_{r,rot} > \left(\frac{\gamma+1}{2}\right)^{\frac{\gamma}{\gamma-1}} \quad \text{(sonic)} \end{cases} \tag{2.167}$$

The equivalence rotor area, A_{eq}, and fraction coefficient, χ, are found to be accurately described by a first order and second order polynomial in θ_{vgt}, respec-

tively.

$$\begin{aligned} A_{eq}\left(\theta_{vgt}\right) =& \upsilon_1 \theta_{vgt} + \upsilon_2 \\ \chi\left(\theta_{vgt}\right) =& \chi_2 \theta_{vgt}^2 + \chi_1 \theta_{vgt} + \chi_0 \end{aligned} \tag{2.168}$$

The turbine efficiency does not require extra auxiliary inputs other than those described above. The model accuracy within the map limits is found to be between -12% and 21% relative accuracy, and slightly biased. Introducing a pure polynomial fitting function of second order, $\Pi(\theta_{vgt})$, with the independent variable being the VGT position, θ_{vgt}, the bias on the relative turbine efficiency modelling error can be removed. The span of relative modelling error is thereby also reduced, and tend to stay within a limit of $\pm 10\%$ in general. This level of modelling accuracy is of a level generally acceptable for the MVEM framework.

Since the model is built up by sub-models of the collision and friction enthalpy losses appearing in the nozzle ring and rotor, respectively, it allows an inspection of the total enthalpy loss distribution.

2.3.5 Turbocharger speed modelling

The rotational speed of the turbocharger, as is evident from the compressor and turbine model investigations, is of paramount importance in the description of the compressor's and the turbine's characteristics. A good model of the turbocharger shaft dynamics must thus exist if off line turbocharger simulations are to be accurate.

Since the impeller wheel and rotor wheel are connected through a shaft i.e.

$$N_T \equiv N_c \equiv N_t \tag{2.169}$$

only one state equation is needed to describe the shaft dynamics.

The power delivered to the shaft is computed by the VGT model as

$$P_t = \dot{m}_t \eta_{t,TS} c_p T_{01,exh} \left(1 - p_{r,exh}^{\frac{1-\gamma}{\gamma}}\right) \tag{2.170}$$

and the power extracted by the compressor to

$$P_c = \dot{m}_c \Delta h_{0c} \tag{2.171}$$

Hence a good model candidate is given by Newton's second law,

$$\dot{N}_t = \left(\frac{\pi}{30}\right)^2 \frac{1}{J_T N_T} \left(P_t - P_c\right) \tag{2.172}$$

where J_T is the moment of inertia of the shaft, impeller and rotor combination.

However, depending on design it might be necessary to include viscous forces in the bearing, and/or the viscous drag force between the turbocharger housing and

impeller and rotor backside, respectively. An alternative form of equation 2.172 is thus

$$\dot{N}_t = \left(\frac{\pi}{30}\right)^2 \frac{1}{J_T N_T}\left(P_t - P_c\right) - \frac{\pi}{30}\frac{\tau_{aux}}{J_T} \tag{2.173}$$

with

$$\tau_{aux} = a_{s,1} N_t^{a_{s,2}} + C_{D,t}\frac{\rho_t \pi^2 N_T^2}{1800}\left(R_r^5 - R_s^5\right) + C_{D,c}\frac{\rho_c \pi^2 N_T^2}{1800}\left(R_I^5 - R_s^5\right) \tag{2.174}$$

where the the coefficients $a_{s,1}$, $a_{s,2}$ and $C_{D,t}/C_{D,c}$ need to be estimated from experimental data. $a_{s,2}$ is most likely found in the interval between 1 and 2, whereas $C_{D,x}$ decreases from 0.1 to 0.002 as the Reynolds number, $\frac{\omega_T R_I}{\nu}$ or $\frac{\omega_T R_r}{\nu}$, is increased from 10^3 to 10^7 (see e.g. [87, 65]).

Another more pragmatic approach is to include the viscous effects on the shaft dynamics by introducing a mechanical efficiency scalar, $\eta_{T,m}$ in equation 2.172. Hence, the effects of the auxiliary viscous forces, τ_{aux}, are included in $\eta_{T,m}$, and the turbo shaft state equation is rewritten as

$$\dot{N}_t = \left(\frac{\pi}{30}\right)^2 \frac{1}{J_T N_T}\left(\eta_{T,m} P_t - P_c\right) \tag{2.175}$$

2.4 Filling and Emptying models

Filling and Emptying modelling has proven its quality in engine state estimation (see e.g. [19, 50, 53, 103, 112]), as a modelling foundation for engine state predictors (see e.g. [10, 22]), and OBD (Onboard Diagnostics) systems (see e.g. [76]).

An illustration of a FE (Filling and Emptying) volume is depicted in figure 2.49, and such a volume may be described by the laws of energy conservation and mass conservation, i.e.

$$\begin{aligned}
\dot{U} &= \dot{(mu)} = \dot{m}u + m\dot{u} \\
&= \dot{m}c_v T + mc_v\dot{T} \\
&= \sum_{k=1}^{N_f}\dot{m}_{f,k}h_k + \sum_{k=1}^{N_P} P_k + \sum_{k=1}^{N_Q}\dot{Q}_k \\
\dot{m} &= \sum_{k=1}^{N_f}\dot{m}_{f,k}
\end{aligned} \tag{2.176}$$

assuming that the volume properties are spatially constant. Since auxiliary power inputs (e.g. actuator actions) may safely be neglected, except for the combustion process, P is assumed equal to zero in the following.

Differentiating the ideal gas law with respect to time, assuming constant volume, the following ODE (Ordinary Differential Equation) is found

$$\dot{m} = \frac{V}{RT}\dot{p} - \frac{pV}{RT^2}\dot{T}, \qquad \left(\dot{V} \equiv 0\right) \tag{2.177}$$

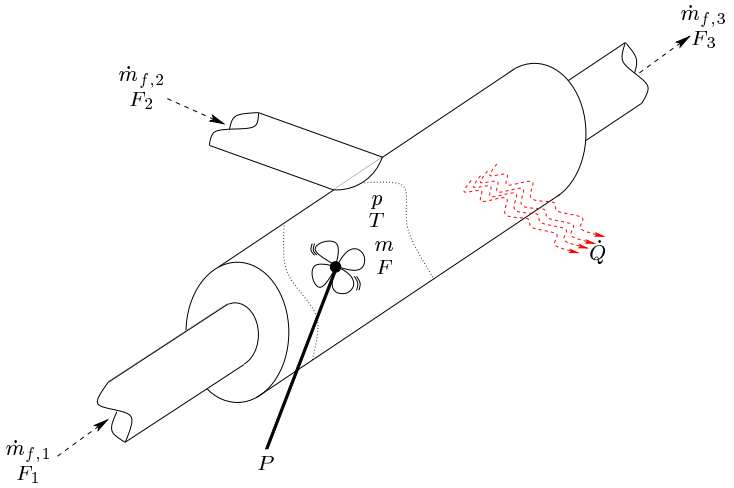

Figure 2.49: Filling and Emptying modelling approach illustration. The propeller illustrates the auxiliary power input, P, and Q is the heat transfer.

Utilizing the equations above the pressure in the volume may be derived to be

$$\dot{p} = \frac{\gamma RT}{V}\left(\sum_{k=1}^{N_f}\left(\left(\dot{m}_{f,k} \geq 0\right)\frac{T_k}{T}\dot{m}_{f,k} + \left(\dot{m}_{f,k} < 0\right)\dot{m}_{f,k}\right) + \sum_{k=1}^{N_Q}\frac{\dot{Q}_k}{c_p T}\right) \tag{2.178}$$

The introduction of EGR necessitates a description of the concentration of the exhaust gas content in the individual FE volumes. A way to model the dynamic behavior of the exhaust gas concentration, is by describing the mass fraction burnt, F, of the total control volume mass[17], m, i.e.

$$F \triangleq \frac{m_{burnt}}{m} \tag{2.179}$$

A dynamic description of F in a control volume may be derived as

$$\dot{F} = \frac{1}{m}\sum_{k=1}^{N_f}\left(\dot{m}_{f,k} \geq 0\right)\left(F_k - F\right)\dot{m}_{f,k} \tag{2.180}$$

Hence, the dynamic behavior of a control volume in the engine's air path may

[17]The spatially variation of F is neglected, i.e. instantaneous perfect mixing is assumed as soon as the burnt mass has entered the control volume

be describe by three ODEs and one algebraic equation

$$\boxed{\begin{aligned}
\dot{p} &= \frac{\gamma R T}{V}\left(\sum_{k=1}^{N_f}\left(\left(\dot{m}_{f,k} \geq 0\right)\frac{T_k}{T}\dot{m}_{f,k} + \left(\dot{m}_{f,k} < 0\right)\dot{m}_{f,k}\right) + \sum_{k=1}^{N_Q}\frac{\dot{Q}_k}{c_p T}\right) \\
\dot{m} &= \sum_{k=1}^{N_f}\dot{m}_{f,k} \\
\dot{F} &= \frac{1}{m}\sum_{k=1}^{N_f}\left(\dot{m}_{f,k} \geq 0\right)\left(F_k - F\right)\dot{m}_{f,k} \\
T &= \frac{pV}{mR}
\end{aligned}} \tag{2.181}$$

The dynamics of individual control volumes are implemented according to equation 2.181 in the VES C library.

2.5 Pipe flow model

One desired VES property is the ability to describe the temperature distribution in an engine's air path. Hence, models of the different flows in the air path, e.g fresh air flow and EGR flow, must be present. However, a general descriptive zero dimensional flow model to describe the individual internal flows in the engines air path is difficult to construct due to phenomena such as pumping fluctuation/wave effects and geometric design differences. For many years, experimentalists have tried to relate surface roughness, Reynolds number, pressure drop and various friction factors to find a mathematical description of the mass flow through pipes. So far they have only found empirical relationships (for example the Moody diagram [96]).

The gas velocities experienced in an engine's intake system are generally low in order to minimize friction losses. However, except for high viscosity fluid flows in narrow pipes, the individual intake manifold flows are generally of turbulent nature due to the low viscosity of the intake air. To serve as an example, disregarding the fluctuation effects, the flow in the inlet manifold throat for the British Leyland engine at idle speed has a Reynolds number close to 8000[18]; A value significantly larger than the general value of 2300 where the flow undergoes a transition from laminar to turbulent.

Although the general flow behavior may be characterized as turbulent the author chose here to couple a laminar flow- and turbulent flow description. Hence, very small flow velocities will also be treated properly.

[18]This value is computed with the following assumed setting of the relevant engine parameters and states: An intake manifold pressure of 0.4 bar, an intake temperature of 300 K, a steady throttle mass flow of 4.53 $\frac{\text{kg}}{\text{s}}$, an engine speed of 1000 rpm, and the intake throat diameter is 40 mm.

In [40] the pipe mass flow after the compressor is described as a linear function of the pressure drop across the pipe only, i.e. the following must have been assumed,

- The flow is laminar and steady
- Potential energy changes are neglected, i.e. the pipe is assumed horizontally mounted.
- The flow is incompressible.
- The pipe form is simple, i.e the pipe can be described with one diameter and length specification alone.

According to [96] a laminar mass flow through a pipe with diameter D and length L may be computed as

$$\begin{aligned} p_{up} - p_{down} &= \frac{32\mu\overline{v}_p L}{D^2}, \qquad \text{(Hagen-Poiseuille expr.)} \\ &\Updownarrow \\ \dot{V}_p &= \frac{\pi D^4 \left(p_{up} - p_{down}\right)}{128\mu L}, \qquad \text{(Volume flow)} \\ &\Updownarrow \\ \dot{m}_p = \rho\dot{V}_p &= \begin{cases} \frac{p_{up}}{RT_{up}} \frac{\pi D^4 (p_{up} - p_{down})}{128\mu L} & , \quad p_{up} \geq p_{down} \\ \frac{p_{down}}{RT_{down}} \frac{\pi D^4 (p_{up} - p_{down})}{128\mu L} & , \quad p_{up} < p_{down} \end{cases} \end{aligned} \tag{2.182}$$

However, the model given in equation 2.182 is naturally only valid for small pipe pressure drops when working with air. Hence, unrealistically large pipe mass flows may be encountered during simulation when the engine model is being excited e.g. throttle actuation. Whence, for higher pressure drops the mass flow behavior is described by the following model (see [97]).

$$\begin{aligned} v_p &= \begin{cases} \sqrt{\frac{2D(p_{up} - p_{down})}{fL\rho_{up}}} & , \quad p_{up} \geq p_{down} \\ -\sqrt{\frac{2D(p_{down} - p_{up})}{fL\rho_{down}}} & , \quad p_{up} < p_{down} \end{cases} \\ \dot{m}_p &= \begin{cases} \frac{p_{up}}{RT_{up}} \frac{\pi D^2}{4} v_p & , \quad p_{up} \geq p_{down} \\ \frac{p_{down}}{RT_{down}} \frac{\pi D^2}{4} v_p & , \quad p_{up} < p_{down} \end{cases} \\ f &\approx bRe^a \end{aligned} \tag{2.183}$$

Imposing a straight line on the Moody diagram[19] under the assumptions that the relative roughness factor, $\frac{\Delta}{D}$, and Reynolds number stay below 10^{-3} and 10^6, respectively, a representative value of the friction factor is

$$f \approx 0.15Re^{-0.16} \tag{2.184}$$

[19]Diagram relating relative roughness, $\frac{\Delta}{D}$, friction factor, f, and Reynolds number, Re, to each other.

The roughness value for the intake manifold material is normally found to be between $1.62{\cdot}10^{-3}$mm (plastic) and 0.02mm (steel) (see [29]) and the hydraulic pipe diameter is normally above 10mm. The roughness value is assumed to be in the neighborhood of 0.001 (conservative estimate). Reynolds numbers in the neighborhood of 10^6 would require flow velocities close to the speed of sound for all normal intake manifold designs i.e. a maximum upper limit of Re to 10^6 is valid.

Combining the laminar and turbulent pipe flow models presented above the final model is derived as,

$$\begin{aligned}
\overline{c} &= \sqrt{\frac{1}{2} R\gamma \left(T_{up} + T_{down}\right)} \\
\overline{\tilde{v}}_p &= \frac{D^2 \left(p_{up} - p_{down}\right)}{32\mu L} \\
\overline{v}_p &= \begin{cases} \left(\frac{(p_{up}-p_{down})D^{1.16}}{0.075\rho_{up}^{0.84}\mu^{0.16}L}\right)^{\frac{1}{1.84}} & , \quad p_{up} \geq p_{down} \\ \left(\frac{(p_{down}-p_{up})D^{1.16}}{0.075\rho_{down}^{0.84}\mu^{0.16}L}\right)^{\frac{1}{1.84}} & , \quad p_{up} < p_{down} \end{cases} \\
\overline{w} &= \begin{cases} \tanh\left(\frac{\overline{v}_p}{\overline{c}}\right)\overline{c} & , \quad \frac{\rho D\overline{\tilde{v}}_p}{\mu} \geq Re_t \\ \tanh\left(\frac{\overline{v}_p}{\overline{c}}\right)\overline{c} & , \quad \frac{\rho D\overline{\tilde{v}}_p}{\mu} < Re_t \end{cases} \\
\dot{m}_p &= \begin{cases} \frac{p_{up}}{RT_{up}}\frac{\pi D^2}{4}\overline{w} & , \quad p_{up} \geq p_{down} \\ \frac{p_{down}}{RT_{down}}\frac{\pi D^2}{4}\overline{w} & , \quad p_{up} < p_{down} \end{cases}
\end{aligned} \tag{2.185}$$

The Reynolds number, Re_t, where the transition from laminar to turbulent flow occurs is found as the point of intersection between the two friction lines $f = \frac{64}{Re}$ (laminar) flow and $f = 0.15Re^{-0.16}$ in the Moody diagram. Hence the point of transition is here selected to be

$$Re_t = \left(\frac{64}{0.15}\right)^{\frac{1}{1.84}} \approx 1350 \tag{2.186}$$

The value of Re_t is a bit lower than the normal value of 2300. However, the general value of 2300 is for steady flows and not unsteady flows. The general velocity profile of the flow will hence reassemble a turbulent profile rather than a laminar profile i.e. the lower Re_t value is reasonable.

The post-processing of the computed gas velocities, $\overline{v}_p$ and $\overline{\tilde{v}}_p$, with a hyperbolic tangent function insures that the flow velocity, $\overline{w}$, never exceeds the speed of sound.

Figure 2.50 shows the mass flow characteristic of 1m long pipe with a varying diameter between 1cm and 5cm under normal atmospheric conditions.

It should be be noted that extreme accuracy of the pipe mass flow model is not mandatory since the bandwidth limiting components are normally not the pipes but

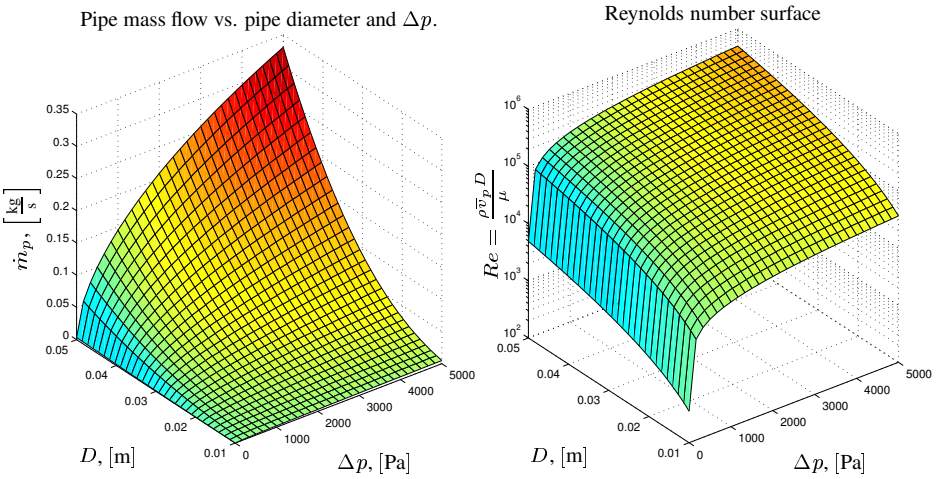

Figure 2.50: Pipe mass flow and Reynolds number surfaces for a 1m long pipe evaluated with normal atmospheric dry air properties, i.e. $\mu = 1.781 \cdot 10^{-5}$Pa·s, $T = 298$K, and $p =$101.3207kPa

rather *input components* like throttles or compressors, and *output components* like the intake port mass flow (speed-density equation). Furthermore, the pressure gradient between the individual volumes comprising the intake system are normally very small for both transient and steady state pipe flows. However, the mass flow computations must still be descriptive i.e. mass flows which are too small will give an unrealistically slow response of the pressure and temperature states to excitation, and mass flows which are too large will give an unrealistically fast pressure rise time and unrealistically large temperature spikes due to expansion/compression.

The pipe mass flow model implemented in VES follows the structure given in equation 2.185.

2.6 Throttle model

The mass flow to a SI engine, without VVT/VVL, is normally controlled by a throttle, hence the name throttle body for the intake system upstream of the throttle plate position. However, throttles are nowadays also encountered in Diesel engines as a means to increase the EGR rate and/or to increase pumping losses and reduce fresh air flow, thereby increasing the exhaust temperature, to promote DPF regeneration. Furthermore, a throttle is also normally used to damped out engine shaking during shut down (closing the throttle completely introduces a large vacuum in the intake manifold and the engine comes rapidly to a standstill).

The mass flow passing the throttle is normally modelled by the isentropic flow equation for a converging–diverging nozzle. The nozzle equation is repeated below

for the sake of convenience.

$$\dot{m}_{noz} = \begin{cases} C_D A_{noz}(\alpha) \frac{p_{up}}{\sqrt{RT_{up}}} p_r^{\frac{1}{\gamma}} \sqrt{\frac{2\gamma}{\gamma-1}\left(1 - p_r^{\frac{\gamma-1}{\gamma}}\right)} & , \quad p_r \geq \left(\frac{\gamma+1}{2}\right)^{\frac{\gamma}{1-\gamma}} \\ C_D A_{noz}(\alpha) \frac{p_{up}}{\sqrt{RT_{up}}} \sqrt{\gamma}\left(\frac{2}{\gamma+1}\right)^{\frac{\gamma+1}{2(\gamma-1)}} & , \quad p_r < \left(\frac{\gamma+1}{2}\right)^{\frac{\gamma}{1-\gamma}} \end{cases}$$
$$p_r \leq 1 \tag{2.187}$$

with p_r being the ratio between upstream stagnation pressure and static throat pressure, and α the throttle angle. However, it is evident that a direct measurement of the throat pressure is impossible, since first the flow is divided around the throttle plate, and second the position of the throat varies with the throttle angle. Hence, the kinetic energy of the flow is commonly assumed lost following an isobaric line (converging–sudden expansion nozzle). Thus, it is customary to approximate the throat pressure with the downstream pipe or plenum pressure. However, just as there is no such thing as a perfect isentropic process, there is no such thing as a perfect loss either, i.e. some of the of kinetic energy will be recovered as pressure.

The complexity of the throttle mass flow is sought illustrated in figure 2.51. The figure illustrates how the flow is divided in a primary- and secondary flow around the throttle plate. Immediately after the throttle plate vortices will be generated due to local pressure differences and internal flow friction. This phenomenon is illustrated by the two large scale vortices generated behind the throttle plate. Streamline photographs made of an experimental setup analogous to a series coupling of a venturi, throttle and manifold plenum is presented in [54].

The minimum geometrical area for flow passage of an elliptical throttle plate capable of complete passage closure is

$$A_{noz}(\alpha) = \pi r^2 \left(1 - \frac{r}{r_1}\cos(\alpha)\right) \tag{2.188}$$

where the plate- and stem thickness are assumed negligible, r is the pipe radius, and r_1 is maximum plate radius. The detailed calculations behind equation 2.188 may be found in [103].

The idea of dividing the throttle flow in a primary mass flow, $\dot{m}_P$, and a secondary mass flow, $\dot{m}_S$, was first presented in [47] under the term *two flow path throttle model*. Furthermore, the main functional effects of the throttle angle and pressure ratio on the throttle flow were here separated into two functions, $\beta_1(\alpha)$ and $\beta_2(p_r)$, i.e.

$$\dot{m}_{at}(\alpha, p_{0,up}, p_{man}, T_{0,up}) = \frac{p_{0,up}}{\sqrt{T_{0,up}}} \beta_1(\alpha)\beta_2(p_r) \tag{2.189}$$

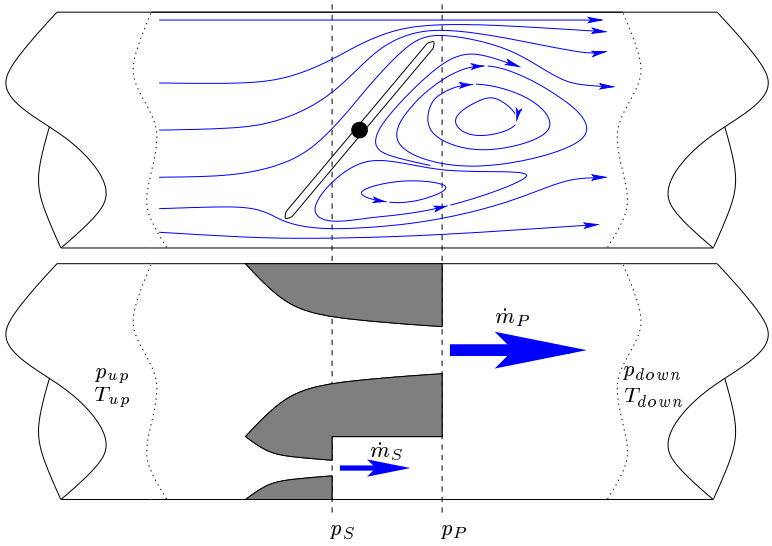

Figure 2.51: The upper part of the figure shows an illustration of the throttle flow conditions. The lower part of the figure illustrate the simplifications, presented in [47], made from geometrically considerations. The throttle mass flow model derived from this simplified flow scenario is known as the *two flow path throttle model*.

The structure of equation 2.189 is in [21] further expanded/refined. The general structure of this model is repeated below for the sake of convenience.

$$\dot{m}_{at}(\theta) = \begin{cases} \frac{p_{up}}{\sqrt{T_{up}}}\beta_1(\alpha)\beta_2^*(p_r) & , \quad p_{up} \geq p_{down} \\ -\frac{p_{down}}{\sqrt{T_{down}}}\beta_1(\alpha)\beta_2^*(p_r) & , \quad p_{up} < p_{down} \end{cases} \tag{2.190}$$

$$\theta = [\alpha, p_{up}, p_{down}, T_{up}, T_{down}]$$

$$\beta_1(\alpha) = b_{10} + b_{11}\cos(\alpha) + b_{12}\cos^2(\alpha) + b_{13}\cos^3(\alpha) \tag{2.191}$$

$$p_r = \begin{cases} \frac{p_{man}}{p_{up}} & , \quad p_{up} \geq p_{down} \\ \frac{p_{up}}{p_{man}} & , \quad p_{up} < p_{down} \end{cases}$$

$$\beta_2^*(p_r) = \underbrace{\frac{1}{1+\nu}\beta_2(p_r)}_{\text{Primary flow}} + \underbrace{\frac{\nu}{1+\nu}\beta_2(1-\delta(1-p_r))}_{\text{Secondary flow}} \tag{2.192}$$

$$\beta_2(x) = \sqrt{\frac{\max(x,p_c)^{\frac{1}{\gamma}} - \max(x,p_c)^{\frac{1+\gamma}{\gamma}}}{p_c^{\frac{1}{\gamma}} - p_c^{\frac{1+\gamma}{\gamma}}}} \tag{2.193}$$

$$p_c = \left(\frac{2}{\gamma+1}\right)^{\frac{\gamma}{\gamma-1}} \approx 0.53 \text{ (Dry air)}$$

The parameters ν and δ represent the secondary–primary mass flow ratio and secondary pressure drop fraction of the total pressure drop $p_{up} - p_{down}$, respectively.

The parameters ν, δ and b_{1x} must be identified numerically from throttle flow measurements. It can be argued that ν and δ must be functions of the throttle position, i.e. $\nu = \nu(\alpha)$ and $\delta = \delta(\alpha)$. However, through discussion with one of the co-authors of [47, 21], *A. Chevalier*, it was clarified that the parameters exhibited only very moderate α dependency. Hence the parameters ν and δ are assumed constant in [21]. The explanation behind this might be found in the concept behind the two-channel converging–sudden expansion model. The geometrical effects is apparently not as important as stated in [47].

Despite the high level of model accuracy achieved, $< \pm 10\%$ for pressure ratios below 0.95 with real engine data, the two flow path model fails to capture the effects for pressure ratios above 0.95. In this region the relative error is close to -60% and $\pm 15\%$ when mean pressure and real pressure conditions are utilized in the mass flow calculation, respectively. Thus, the mass flow estimate error has clearly increased in this part of the throttle characteristics i.e. the throttle friction level is estimated wrongly. This is understandable since the model exhibits an extreme pressure ratio sensitivity in this region, since

$$\frac{\partial \dot{m}_{at}}{\partial p_r} \to -\infty \text{ for } p_r \to 1 \tag{2.194}$$

Instead it is here suggested that the throttle airflow to computed according to either one of the throttle models presented above, and the equivalent pipe mass flow using the pipe mass flow model presented in section 2.5 on page 146 in parallel. The pipe length L is set to the horizontal distance between the throttle tips, and the equivalent pipe diameter is computed such that $\frac{D^2\pi}{4} = A_{noz}(\alpha)$. The actual pipe mass flow is sequently found as

$$|\dot{m}_{at}| = \min\left(|\dot{m}_{at,n}|, |\dot{m}_{at,p}|\right) \tag{2.195}$$

where $\dot{m}_{at,n}$ and $\dot{m}_{at,p}$ are the mass flow solution to the isentropic nozzle equation and the pipe equation, respectively. This is the model implemented in VES.

As a final word of caution it should be mentioned that correct estimation of the throttle mass flow close to $p_r = 1$ is extremely problematic based on pressure measurements alone. Even if such a thing as a perfect physical model of a butterfly valve existed, it would be "useless" with the current automotive pressure sensors available (¿1% absolute measurement accuracy). This is here exemplified by a small example: A throttle plate for a 2.0 liter NA SI engine normally has a diameter close to 50mm, [103]. The throttle geometry is here approximated by a pipe with an inner diameter of 50mm and a length of 55mm. A pressure drop of 1kPa across such a pipe would, using the pipe model, attain a value of approximately 600 $\frac{g}{s}$ under normal atmospheric upstream conditions. The pressure drop of 1kPa is exactly the absolute deterministic measurement error for the commonly used 0–1 atm intake manifold piezo-resistive pressure transducer [103, 22, 10]. Hence, if this setup is to be used for online throttle flow estimation with $p_r > 0.95$, sensor fusion is needed. An obvious choice for automotive application would of course be to

fuse the estimation of the throttle mass flow with an eventual hotwire/hotfilm MAF measurement. However, when the throttle is close to WOT (Wide Open Throttle) the waves will propagate more easily through the intake system. This might course serious problems obtaining the correct measurement if a hotwire/hotfilm sensor is used, since such sensor's measurement quality deteriorates rapidly when exposed to pumping fluctuations. This phenomenon has been investigated thoroughly in the ECG at DTU and is still under investigation (see e.g. [44])

2.7 Intake ports

A good knowledge of the intake port mass flow is of paramount importance if acceptable performance of several control strategies is to be achieved. Two such control problems are the AFR control problem of MPI equipped SI engines and the EGR rate control in Diesel engines. The first simply because this is the flow for which the AFR is sought kept constant (see [112, 22]) and the latter since no direct measurement method of the EGR mass flow is currently available, i.e. $\dot{m}_{egr}$ is approximated as $\dot{m}_{ap} -$ MAF. However, commercial sensors for series production applications, capable of measuring the port mass flow directly, are currently not available[20]. Instead, the air mass is often estimated from other engine measurements. The most common open loop estimation strategy used to derive a measure of the cycle averaged port air mass flow is the well known speed-density equation. Dependent upon which engine sensor signals are available this equation may have several different structures, where two most common equation forms encountered are repeated below

$$\begin{aligned} \overline{\dot{m}}_{ap} &= \eta_{vol}^{amb} \frac{NV_d}{120} \rho_{amb} \\ \overline{\dot{m}}_{ap} &= \eta_{vol}^{man} \frac{NV_d}{120} \overline{\rho}_{man} \end{aligned} \tag{2.196}$$

where $\overline{\ }$ indicates that the corresponding variable has averaged over an engine cycle. The non-dimensional variable η_{vol}, referred to as the volumetric engine efficiency, is an empiric attempt to describe the breathing performance of the engine. The parameters η_{vol}^{amb} and η_{vol}^{man} are normally found from steady state engine measurements, i.e.

$$\begin{aligned} \eta_{vol}^{amb} &= \frac{120RT_{amb}}{NV_d p_{amb}} \overline{\text{MAF}} \\ \eta_{vol}^{man} &= \frac{120R\overline{T}_{man}}{NV_d \overline{p}_{man}} \overline{\text{MAF}} \end{aligned} \tag{2.197}$$

[20] A prototype port air mass flow sensor has been developed by the ECG at DTU (see [37]). However, the measurement principal is not completely non-intrusive, and might thus change the breathing performance of the engine. Furthermore, the method is not directly applicable on DI engines with EGR

and sequently stored in a 2D engine map with N and $\overline{p}_{man}$ as indices. For a acceptable performance it might however be necessary to readjust the level of η_{vol} by an intake temperature correction factor. A commonly used correction factor is $\sqrt{\frac{\overline{T}_{man}}{T_{man,ref}}}$, [54].

It is shown in [47, 75], referred to as the "$e_v \cdot p_i$" methodology, that $\eta_{vol}^{man}\overline{p}_{man}$ exhibits a strong linear $\overline{p}_{man}$ dependency and only a weak engine speed dependency for pressure ratios, $p_r = \frac{\overline{p}_{man}}{p_{amb}}$ smaller than 0.95. Hence, using this methodology when storing the volumetric efficiency, i.e. $\eta_{vol}^{man}\overline{p}_{man}$ is stored instead of η_{vol}^{man}, the interpolation accuracy may be improved.

Since no direct measurement method, as mentioned, is available the static η_{vol} map is also used to derived the port air mass flow during transients. It is thus likely that this might introduce significantly errors due to ramming effect. However, the magnitude and characteristic of this likely error is investigated thoroughly in [21] by 1D modelling. It is found that the static speed density equation, for a plenum type manifold, is able to describe the event mean value of the port mass flow with a remarkably accuracy. Hence for MVEM based modelling and control the speed density equation is a good choice.

In the cases where a greater model detail level is desired (e.g. wave modelling) the intake and exhaust valve's flow restriction need separate modelling. The intake and exhaust are customarily of the poppet valve type except for a few exotic engine designs. One modelling approach (as with other common valve types) is to utilize the isentropic nozzle equation together with a geometrically derived model of the minimum flow area, and a discharge coefficient, C_D, to account for the unavoidable modelling errors introduced by the isentropic assumption. Models of the minimum valve area are readily available in literature, and it is in VES selected to implemented a poppet valve model structure according to model proposed in [54]. The size and character of the discharge coefficient are also addressed in [54]. Since poppet valves are utilized to control other flows than just the engine port mass flow e.g. EGR mass flow and idle speed by-pass mass flow, the model is also used in larger VES engine sub-models like the EGR cooling system described in section 2.8.1.

2.8 Heat exchangers

Two heat exchangers are commonly found in a modern turbocharged engine's air path namely the intercooler and the EGR cooler. Depending on the engine configuration the added air path volume due to the heat exchangers may need dynamic modelling in the description of the three main air path characteristics: pressure, gaseous mass contained and burnt mass fraction. Hence, this section is devoted to the investigation of possible model structures for convenient 0-D heat exchanger models.

2.8.1 EGR cooler

Assuming that the EGR mass may be characterized as a heat sink alone[21] (a more thorough treatment may be found in [64]) the absorbed combustion energy during steady state engine operation may be approximated by

$$Q = \dot{m}_{egr}\, c_p \Delta T = \dot{m}_{egr}\, c_p \left(T_{exh} - T_{man}\right) \tag{2.198}$$

Hence, the overall combustion temperature will decrease due to the energy absorbtion of the inert gas. Clearly, a intake manifold temperature decrease, evident from the above equation, will promote the combustion temperature reduction desired even further. Hence, it is common on modern DI Diesel engines to cool the EGR mass flow down before intake manifold entry. Due to packaging and response time issues these coolers are normally of the air-to-water type using the engine coolant water as coolant medium. An EGR cooler is schematically depicted in figure 2.52.

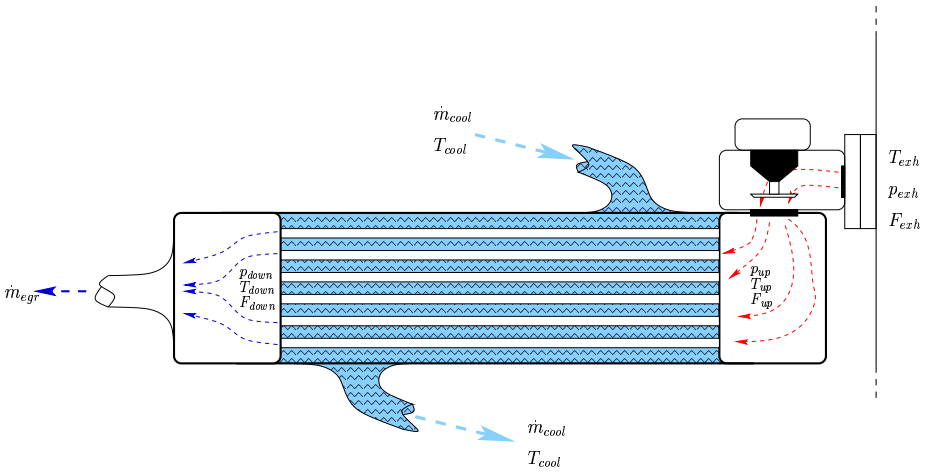

Figure 2.52: 1-pass water jacket EGR cooler with exhaust side mount EGR valve.

Commercially available EGR coolers normally feature 1, 2 or 3 flow paths through the coolant medium before exit. A greater number of flow paths will clearly increase cooler effectiveness due to linear velocity increase (the intern area-volume ratio increases but the overall size of the cooler is fixed) and heat transfer coefficient increase (Reynolds number increase leads to heat transfer coefficient increase). However, this better cooler effectiveness is normally paid for in terms of added pressure loss across the cooler. Since the pressure difference between exhaust and the intake manifold is moderate on CI engines (after-treatment system back pressure issues are not taken into account) the introduction of extra friction in the EGR flow path may hamper the flow too much, such that the desired EGR levels at idle/part load operation cannot be achieved. Table 2.13 shows general values for

[21] The combustion kinetics are neglected

the effectiveness and maximum pressure drop across the EGR cooler at maximum rated EGR mass flow. Although the table values should only be seen as descriptive

	Effectiveness, [%]	Δp_{max}**, [kPa]**
1-Pass	57	0.85
2-Pass	67	1.69
3-Pass	89	8.47

Table 2.13: General values for effectiveness and maximum pressure drop for 1-, 2- and 3-pass EGR coolers after completed soot fouling [26].

values, they give a picture of what cooler effectiveness and pressure losses that can be expected. Only three-pass EGR coolers provide a high enough effectiveness that the exhaust gas temperature influences on the intake manifold properties may be regarded as constant (the EGR inlet temperature is fixed to the coolant temperature). One- and two-pass EGR coolers will need modelling to understand the influence of the exhaust gas on other engine dynamics properly.

As stated previously the application of FE modelling technique poses problems when applied to heat exchangers, since the cooler is best described by PDE (Partial Differential Equation). However, convenient control oriented models should be comprised of ODEs only if they are to be applied in a later controller synthesis. Therefore the model concept utilized here will be zero dimensional.

In the search for a model of the water jacket EGR cooler the following is assumed

- The coolant flow is large enough such that coolant temperature increase from inlet to outlet may be neglected. Furthermore, the cooler is well designed such that each region is properly flushed. Hence, the coolant temperature inside the cooler is spatially constant.

- The wall thickness of the individual pipe is normally very thin ($\approx$0.25mm). Furthermore, the heat conductivity between the liquid coolant is much better than the conductivity between the EGR and the wall. Hence, the wall temperature will be assumed equivalent to the coolant temperature.

- The heat transfer coefficient, k, is assumed globally constant.

- Condensing effects are neglected, i.e. the water contained in the EGR mass flow as steam is not thought to change phase during the passage through the cooler.

- Steady flow conditions, i.e. $\ddot{m}_{egr} \equiv 0$.

- The pressure drop across the cooler is negligible in the outlet temperature computation.

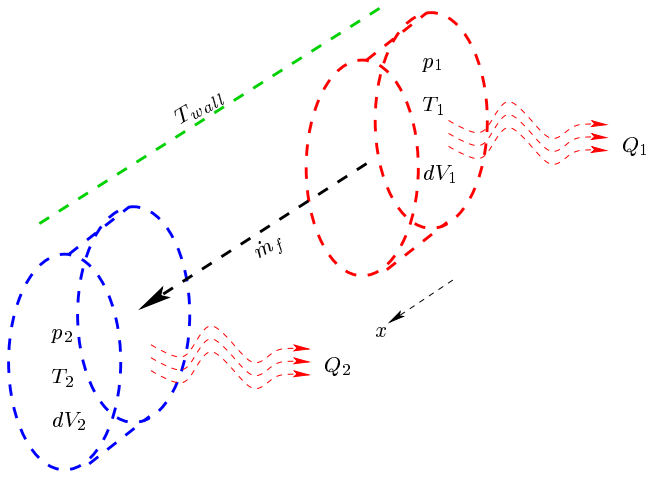

Figure 2.53: Illustration of EGR mass packet on its way through one of the N_p EGR cooler pipes.

- The mass flow through the individual pipe is position independent, i.e. $\dot{m}_{egr,1} = \dot{m}_{egr,N_p} = \frac{\dot{m}_{egr}}{N_p}$, where N_p is the number of cooling pipes in the cooler.

Of the above assumptions the largest error is most likely introduced by the steady flow assumption. EGR cooler are normally closely coupled to the exhaust manifold with the EGR valve mounted up or downstream of the cooler. Hence, rather large flow fluctuations may be expected. Treatment of the fluctuations mentioned will be addressed in section 2.8.5.

The outlet temperature model proposed here will be derived from a lagrangian point of view.

Figure 2.53 illustrates the passage conditions for package of constant mass on its way through one of the EGR cooler pipes.
This mass package may be described by the following four equations.

The volume rate change of the package is given by

$$\begin{array}{c} \overset{(\equiv 0)}{\cancel{\dot{p}V} + p\dot{V}} = \overset{(\equiv 0)}{\cancel{\dot{m}}RT + mR\dot{T}} \\ \Updownarrow \\ \dot{V} = \frac{V}{T}\dot{T} \end{array} \tag{2.199}$$

The local velocity of the package, $\dot{x}$, is found as

$$\dot{x} = \frac{4RT}{\pi D_p^2 p}\frac{\dot{m}_{egr}}{N_p} \tag{2.200}$$

The change in the internal energy of the package is found as

$$\begin{aligned}\dot{U} = \frac{d\left(mu\right)}{dt} &= \cancelto{(\equiv 0)}{\dot{m}u} + m\dot{u} = \frac{pV}{RT}c_v\dot{T} \\ &= Q + P = Q - p\dot{V}\end{aligned} \tag{2.201}$$

The heat transfer, Q, from the mass package to the pipe wall is thought to be pure convective. The convective heat transfer is here modelled by

$$Q = k\left(T_{wall} - T\right)dA = k\pi D_p\left(T_{wall} - T\right)dx = k\frac{4V}{D_p}\left(T_{wall} - T\right) \tag{2.202}$$

The package temperature, T, as function of time, t, may now be found by combining equation 2.199, 2.201 and 2.202 to obtain

$$\begin{aligned}&\dot{T} = k\frac{RT}{pD_pc_p}\left(T_{wall} - T\right) \\ &\Updownarrow \\ &t = \frac{pD_pc_p}{4Rk}\int_{\tau=T_{exh}}^{T}\frac{1}{T\left(T_{wall} - T\right)}d\tau \\ &\Updownarrow \\ &T(t) = \frac{T_{exh}T_{wall}e^{\alpha t}}{T_{exh}\left(e^{\alpha t} - 1\right) + T_{wall}}\end{aligned} \tag{2.203}$$

with

$$\alpha = \frac{4RT_{wall}k}{pD_pc_p}$$

The position, x, at time t is now found by combining equation 2.200 and 2.203 to

$$\begin{aligned}x(t) &= \frac{4\dot{m}_{egr}RT_{exh}T_{wall}}{\pi D_ppN_p}\int_{\tau=0}^{t}\frac{e^{\alpha t}}{T_{exh}\left(e^{\alpha t} - 1\right) + T_{wall}}d\tau \\ &= \frac{4\dot{m}_{egr}RT_{wall}}{\pi D_p^2pN_p\alpha}\ln\left(\frac{T_{exh}\left(e^{\alpha t} - 1\right) + T_{wall}}{T_{wall}}\right) \quad \text{for } 0 \le x \le L_p\end{aligned} \tag{2.204}$$

Finally, the solution to equation 2.204 for which $x(t) = L_p$ is found and inserted in equation 2.203, thereby deriving the following expression for the cooler outlet temperature, T_out.

$$\boxed{\begin{gathered}T_{out}\left(\dot{m}_{egr}, T_{wall}, T_{exh}\right) = \frac{T_{wall}\left(e^{\left(\frac{\pi D_pN_pL_pk}{\dot{m}_{egr}c_p}\right)} - 1\right) + T_{exh}}{e^{\left(\frac{\pi D_pN_pL_pk}{\dot{m}_{egr}c_p}\right)}} \\ \text{for } \dot{m}_{egr} > 0\end{gathered}} \tag{2.205}$$

2.8.2 Intercooler

The principal motivation behind turbocharging an IC engine is naturally to increase its specific power and brake torque. However, since not only the pressure after the compressor is raised but also the temperature the benefits of the turbocharger are partly offset. To minimize the negative effects of the increased inlet temperature the charged air is nowadays commonly sent through a heat exchanger, the intercooler, to increase the density of the boosted air charge before its entry into the intake manifold. The insertion of an intercooler in the air path will, however, degrade the transient response of the engine due to the added intake volume. Thus, selecting an appropriate intercooler is often a compromise between desired effectiveness at a rated mass flow, restriction concerns and transient performance expectations. Fortunately, the air-to-air coolers, customarily used nowadays, have normally a very high level of effectiveness. The cooler effectiveness is defined as

$$\epsilon_{ic} \triangleq \frac{\Delta h_{actual}}{\Delta h_{ideal}} \approx \frac{T_{in} - T_{out}}{T_{in} - T_{amb}} \tag{2.206}$$

The effectiveness of a properly sized intercooler is in [83] found between 0.82 and 0.99, i.e. the output flow temperature will be close to the ambient temperature[22]. Due to the high effectiveness expected the focus here will be on adequate cooler temperature description for a later inclusion in the heat exchanger pressure dynamics description. In this quest the following will be assumed

- The ambient temperature is well known.
- The cooling flow through the air cooler is large compared to the intercooler flow, i.e. the coolant temperature changes across the cooling element are negligible.
- The pressure drop across the intercooler is negligible in the computation of the total gaseous mass contained in the intercooler.
- Intercooler fouling due to e.g. evaporated turbocharger oil is neglected.
- Steady flow conditions prevail.
- The intercooler effectiveness is constant.
- The intercooler temperature only varies along the flow direction and is flow path independent.
- The convection parameter k is assumed globally constant for fixed values of $\dot{m}_{ic}$, T_{in} and T_{amb}.

[22]The intercooler is often dimensioned such that the maximum difference between the intake plenum temperature and the ambient temperature is close to 35K at maximum rated boost pressure [2].

The first goal is to derive the mean intercooler temperature, $T_{ic,m}$, fulfilling

$$\frac{p_{ic}V_{ic}}{RT_{ic,m}} = m_{ic} \tag{2.207}$$

Hence, first the total gaseous mass contained in the intercooler must be computed. Assuming the outlet profile along the flow path may be described by equation 2.205 the heat transfer coefficient required to obtain intercooler effectiveness $\overline{\epsilon_{ic}}$ is

$$k\left(\overline{\epsilon}_{ic}, \dot{m}_{ic}\right) = \ln\left(\frac{1}{1-\overline{\epsilon}_{ic}}\right)\frac{\dot{m}_{ic}c_p}{\pi D_p L_p N_p} \tag{2.208}$$

Inserting this in equation 2.205 where L_p has been exchanged with the relative position x, the temperature profile along the flow path is found to

$$\begin{aligned} T(x) &= \frac{T_{amb}\left(\left(\frac{1}{1-\overline{\epsilon}_{ic}}\right)^{\frac{x}{L_p}} - 1\right) + T_{in}}{\left(\frac{1}{1-\overline{\epsilon}_{ic}}\right)^{\frac{x}{L_p}}} \\ &\text{for } \begin{cases} x \in [0; L_p] \\ \overline{\epsilon}_{ic} \in]0; 1[\end{cases} \end{aligned} \tag{2.209}$$

The gaseous mass contained in the intercooler is found by

$$\begin{aligned} m_{ic} &= \int_0^{V_{ic}} \rho(V)dV = \int_{x=0}^{L_p} \frac{p_{ic}L_{ic,y}L_{ic,z}}{R} \frac{\left(\frac{1}{1-\overline{\epsilon}_{ic}}\right)^{\frac{x}{L_p}}}{T_{amb}\left(\left(\frac{1}{1-\overline{\epsilon}_{ic}}\right)^{\frac{x}{L_p}} - 1\right) + T_{in}} dx \\ &= \frac{pV_{ic}}{RT_{amb}} \frac{\ln\left(\frac{T_{in}}{T_{amb}}\right) - \ln\left(\frac{T_{in}}{T_{amb}} + \frac{\overline{\epsilon}_{ic}}{1-\overline{\epsilon}_{ic}}\right)}{\ln\left(1-\overline{\epsilon}_{ic}\right)} \end{aligned} \tag{2.210}$$

Finally is the mean temperature of the intercooler is found by a combination of equation 2.207 and 2.210:

$$\boxed{T_{ic,m} = \frac{\ln(1-\overline{\epsilon}_{ic})}{\ln\left(\frac{T_{in}}{T_{amb}}\right) + \ln\left(\frac{T_{amb}(1-\overline{\epsilon}_{ic})}{T_{in}(1-\overline{\epsilon}_{ic})+\overline{\epsilon}T_{amb}}\right)} T_{amb}} \tag{2.211}$$

It is customary in the assessment of the gaseous mass contained in the intercooler to use the ideal gas law with the mean temperature set to $T_{ic,m} = \frac{1}{2}(T_{in} + T_{out})$ (see e.g [83]). Hence, it is interesting to investigate the behavior of the difference between this assumption and the averaged cooler temperature model developed above. The mean cooler temperature model derived above is the reference model in the following. Figure 2.54 shows the relative computational error for the mean cooler temperature and mass, respectively. As expected the error is seen to

increase with temperature difference and cooler effectiveness, and might be as high 19% on the temperature calculation and -16% in the contained mass computation. However, since the cooler effectiveness drops with mass flow increases the relative error is for all normal steady flow operating conditions[23] most likely to be within 8% and -7% for the temperature and mass computation, respectively.

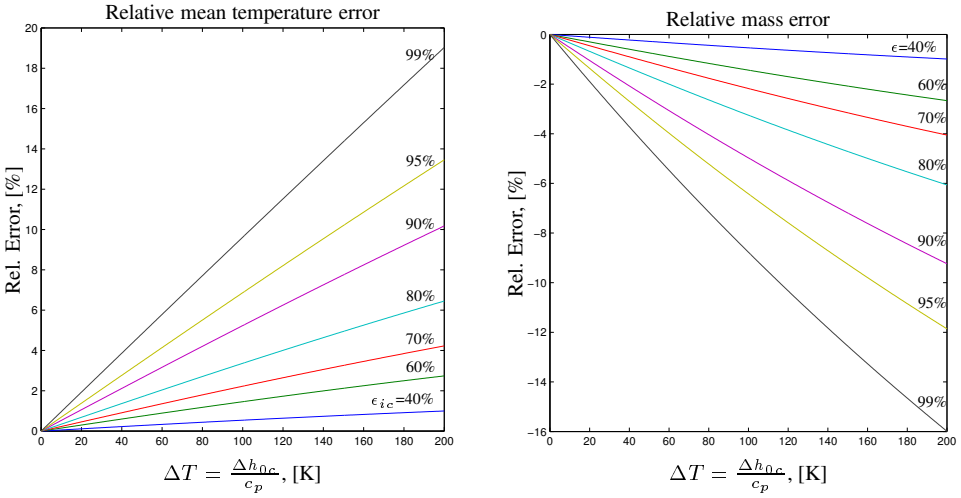

Figure 2.54: Relative error made when using the assumption $T_{ic,m} = \frac{1}{2}(T_{in} + T_{out})$. The plot to the left shows the relative temperature error for different levels of cooler effectiveness. The plot to the right shows the accompanying mass assessment error.

2.8.3 MVEM approach to intake system modelling

Since the introduction of turbochargers, heat exchangers and exhaust recirculation equipment in the automotive engine's air induction path the one state, p_{man}, equation approximation (also known as the IMVEM, see e.g [47, 49]) commonly used fails to describe the dynamic and steady state behavior of the complete intake system adequately. The two state, $p_{man}$and T_{man}, intake system model, also known as the AMVEM (Adiabatic Mean Value Engine Model) (see the SAE-paper number 1999-01-0909 included on page 200) was therefore introduced, which should be able to estimate the impact of the high temperature EGR inlet flow on the intake manifold conditions. This model was later experimentally tested by one of the co-authors, *Professor E. Hendricks*, on an engine dynamometer test bench at DTU. The experimental results obtained, of which some are included in the SAE-paper number 1999-01-0909, clearly showed a high consistency between the simulation results and the experiments, and the good modelling properties of the AMVEM

[23] For a properly fitted turbocharger the compressor outlet temperature increase is in the vicinity of 0 K close to engine idling. As the engine speed increases the pressure ratio across the compressor is increased; and thereby are also the temperature difference and the compressor mass flow increased. Hence, the temperature difference will generally increase with engine fresh air mass flow increases.

were confirmed. However, the intake manifold of the experimental NA SI test engine can with good approximation be classified as one large plenum with the EGR entry point located just downstream of the throttle plate (see e.g. the pictures in [37]). Furthermore, the EGR valve is mounted close to the EGR entry point, thus, the (small) volume of the EGR pipe[24] is separated from the intake system. Hence, the layout of the intake system will, generally speaking, fulfill the assumptions made with a two state FE modelling approach. However, considering the normal design of the intake system for a modern intercooled and turbocharged DI Diesel engine equipped with an EGR system (see e.g. the engine illustration in figure 4.3 on page 235), the AMVEM will most likely fail to predict the dynamic and steady state behavior of the intake manifold states, since it does not take into account the geometric location of the individual mass flow entry- or exit points. The reasoning for this will be explained in the following.

Normally, the total volume of a modern turbocharged DI Diesel engine's intake air system is distributed in the following manner [2]:

- The intake plenum volume downstream of the EGR inlet point is approximately 50% to 60% of the engine displacement.
- The intake system volume including the intercooler volume (throttle body volume) is about 200% to 250% of that of the engine displacement.
- The volume of the EGR system is about 25% the engine displacement.

With this distribution of the intake air path the intake plenum volume will only comprise 22% to 27% of the total volume of the intake system. However, it is the temperature of this volume which determine the accuracy of the total mass flow estimation (speed-density equation). Thus, a good estimation of this temperature is highly desirable.

In order to be a bit more specific the intake system layout for a modern 2.0 liter turbocharged Diesel engine will roughly follow the specifications in figure 2.55 [3]. The distribution of the gaseous mass between the seven intake sections depicted in figure 2.55, when evaluated on the corresponding steady state engine map of a 2.0 liter engine[25], is shown in figure 2.56. The total mass, m, in the system is computed as the sum of the masses contained in the seven volumes. The mass entrapped in the heat exchangers is computed by equation 2.210 and not by the ideal gas law as it is done for the remaining five volumes. The mass contained, when following the one volume approach, is calculated as

$$\hat{m} = \frac{p_{man} \sum_{i=1}^{7} V_i}{RT_{man}} \tag{2.212}$$

[24] No EGR cooler was used during the experimental work.

[25] Dipl. Ing. Daniel Röttger is gratefully acknowledged for providing the steady state engine map.

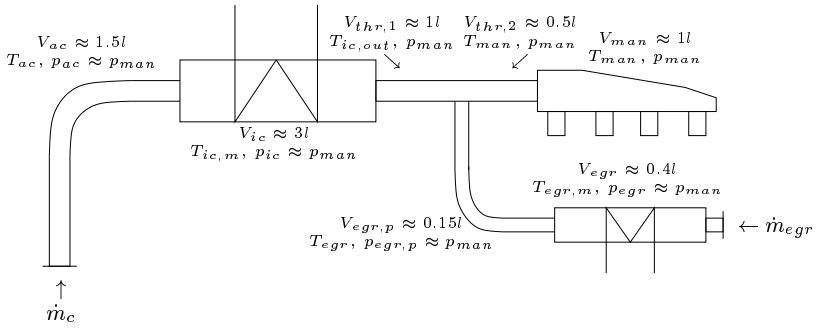

Figure 2.55: Illustration of a typical intake system for a modern 2.0 liter turbocharged Diesel engine. The figure also depicts the approximate values of the volume and states for the individual sections.

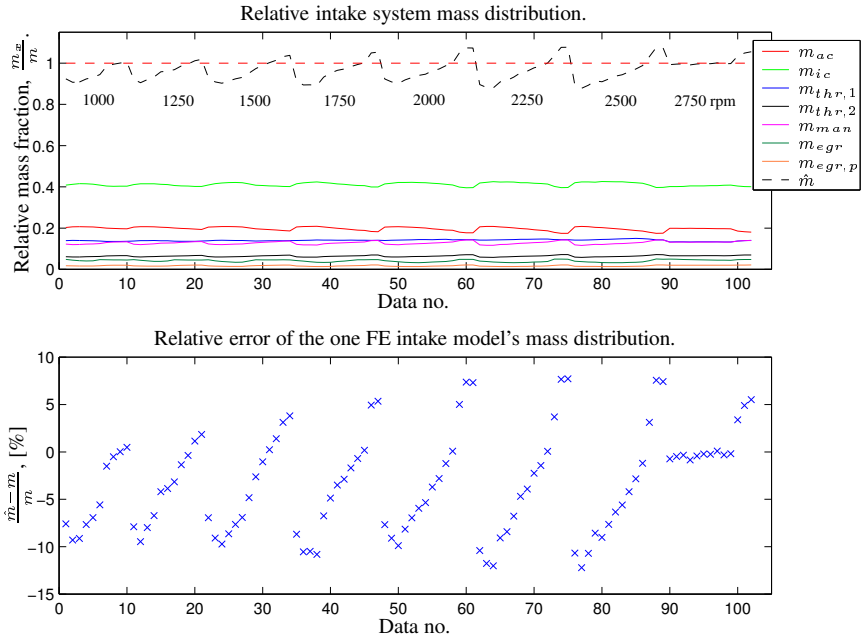

Figure 2.56: Typical distribution picture of the intake system mass for a 2.0 liter turbocharged Diesel engine generated from experimental data. The dashed black line shows the ratio between the estimated mass by the one volume model, $\hat{m}$, and the total intake mass obtained using a sectioned volume approach. The subscripts indicate the geometric location of the different masses (see figure 2.55). **Remark:** The mass contained in the heat exchangers is computer by equation 2.210.

The ratio between $\hat{m}$ and m is plotted as a dashed black line in the upper plot in figure 2.56. The regions where the $\hat{m}$ is smaller than m indicates low/part load operation points with the EGR system being active. In these cases the estimate computed by the one volume approximation is too small since the temperature of the intake manifold is in general higher than the rest of the intake system. This can be traced back to the influence of the high temperature EGR inlet flow. When $\hat{m}$ is too large the engine is operated in a high load with no EGR key point of the engine map. Here, the boost pressure is high and the temperature upstream of the intercooler is significantly above that of the ambient temperature but also that of the intake manifold temperature. Hence, the one volume approximation will produce a too large estimate of the mass contained. However, the relative error of the one volume approximation is reasonably small. This is confirmed by the lower plot in figure 2.56 showing that the relative error between $\hat{m}$ and m stays between -15% and 10% within the supplied engine map. Hence, although the volume of intake manifold only constitute about 20% of the total intake system volume, the total steady state mass contained in the system can be estimated fairly well from the pressure and the temperature measurements obtained in the intake plenum alone. This is fortunate since it speaks in favor for the approximation of the intake system by one FE volume alone.

Adequate modelling accuracy of the intake system's dynamic response will, however, most likely not be obtainable with the AMVEM model proposed in SAE-paper number 1999-01-0909 (see [75]), when this model is utilized on a intercooled turbocharged Diesel engine equipped with an EGR system. The differential equations of the AMVEM are repeated below for the sake of convenience.

$$\begin{aligned}\dot{p}_{man} &= \frac{\gamma R}{V_i}\left(\dot{m}_{at}T_{amb} + \dot{m}_{egr}T_{egr} - \dot{m}_{ap}T_{man}\right)\\ \dot{T}_{man} &= \frac{RT_{man}}{p_{man}V_i}\left((\gamma T_{amb} - T_{man})\dot{m}_{at} + (\gamma T_{egr} - T_{man})\dot{m}_{egr} - (\gamma - 1)T_{man}\dot{m}_{ap}\right)\end{aligned} \tag{2.213}$$

where V_i is the volume of the intake system downstream of the throttle plate. This model in [75] is developed for NA SI engines which have a simpler intake system than those of modern Diesel engines. Furthermore, the AMVEM does not respect geometrically how the EGR enters the intake system. Inspecting the generic intake system for a Diesel engine depicted in figure 2.55 a reasonable approximation of the volume split would more likely be

V_{ac}: The volume of the pipe connection between the compressor and the intercooler. This volume has a reasonable low area-to-volume ratio, and the relevant FE model is therefore adiabatic.

V_{ic}: Intercooler volume. This volume has a very high area-to-volume ratio. Hence, a reasonable simple FE model is isothermal. The corresponding mean temperature of the cooler is found by equation 2.211 on page 160.

$V_{thr,1}$: This volume separates the intercooler exit and the EGR inlet point. This volume has a low area-to-volume ratio, and the relevant FE model is therefore adiabatic.

$V_{thr,2} + V_{man}$: The volume comprising the intake system downstream of EGR point and upstream of the engine's intake ports. This volume has reasonably low area-to-volume ratio. Hence, the adequate FE model for this volume is of an adiabatic nature.

$V_p + V_{egr}$: The total volume of the EGR system. This volume is in general small compared to the volume of the complete intake system. Hence, the volume can with a reasonable good approximation be neglected in the dynamic mean value description of the intake system pressure.

The system order of the complete intake system volume is thus seven, four pressure ODEs and three temperature ODEs, if the temperatures and pressures of intake system are approximated according to the philosophy above. However, the general level of the flow friction between individual volumes is low (normally the pressure loss is within a few kPa). Hence, the following assumption for the general intake system pressure level, p_i, is reasonable.

$$p_i \equiv p_{ac} \equiv p_{ic} \equiv p_{thr,1} \equiv p_{thr,2} \equiv p_{man} \tag{2.214}$$

The total order of the intake model is thereby reduced by three state equations to a total of four state equations.

The next challenge is to examine the relative importance of the three temperature state equations $\dot{T}_{ac}$, $\dot{T}_{thr,1}$ and $\dot{\tilde{T}}_{man}$, where the temperature $\tilde{T}_{man}$ is the spatially averaged temperature of the volume downstream of the EGR inlet point, $V_{thr,2} + V_{man}$. First, the relative importance of the dynamic response of T_{ac} will be discussed. The volume V_{ac} is in general smaller than the engine displacement volume. Hence, the mass contained in this volume is exchanged at a rate between a half and one engine cycle. Hence, the mean value response[26] of the temperature will rapidly follow the exit temperature of the compressor during quasi-steady engine operation. The only expansion or compression phenomena experienced in this volume are due to either turbocharger excitation, EGR valve actuation, or engine speed changes. The frequency spectrum of these excitations is in general small compared to the bandwidth of the T_{ac} state equation. Hence, the time response of V_{ac}'s temperature may be approximated by T_c and thus be considered as an algebraic equation i.e. $\dot{T}_{ac} \equiv 0$. In addition to this the intercooler would dampen (filter) the effects of possible neglected compression/expansion spikes in T_{ac} on T_{man}. In analogy with this approach the time response of $V_{thr,1}$'s temperature will primarily follow the exit temperature of the intercooler. The dynamic behavior of $T_{thr,1}$ may in correspondence with the T_{ac} model also be neglected, since the assumptions

[26]The individual compressions and expansions due to engine pumping is neglected in accordance with the MVEM philosophy.

made previously for V_{ac} are in general also valid here. However, this volume does directly interact with the intake plenum, and modelling errors in its temperature description will by nature have a more severe effect than T_{ac} model errors. The volume is, however, typically small and the flow restriction to the intake plenum and intercooler, respectively, is negligible. Hence, rapid compression or expansion spikes in the time response of $T_{thr,1}$ are highly unlikely to be encountered independently of how the Diesel engine is excited.

The intake temperature, however, is controlled by three mass flows or better energy flows, namely $\dot{m}_{thr,1}c_pT_{ic} \approx \dot{m}_c c_p T_{ic}$, $\dot{m}_{egr}c_pT_{egr}$ and $\dot{m}_{ap}c_p\tilde{T}_{man}$. The dynamic behavior of $\tilde{T}_{man}$ can in contrast to T_{ac} and $T_{thr,1}$, respectively, not be neglected due to the possible large temperature difference between T_{ic} and T_{egr}. Hence, T_{man} cannot adequately be approximated by any of the upstream temperatures, and a dynamic model is needed to reproduce its time response.

The AMVEM in its current structure does not provide a means to estimate the amount fresh air entering the intake ports during transient engine operation when the EGR system is activated. A convenient way to overcome this problem is to estimate the time response of the burnt mass fraction in the intake throat and plenum, $\tilde{F}_{man}$. The fresh air mass flow at the intake ports, $\dot{m}_{ap,f}$, during steady state as well transient engine operation, may then later be obtain by the speed-density equation as

$$\dot{m}_{ap,f} = (1 - F_{man})\frac{\eta_{vol}p_i N V_d}{120R\tilde{T}_{man}} \tag{2.215}$$

A good knowledge of this flow is of evident importance when addressing the problem of transient control of a Diesel engine's AFR. The dynamic equation for $\tilde{F}_{man}$ may directly be derived from the material in section 2.4 as

$$\dot{\tilde{F}}_{man} = \frac{p_i\tilde{V}_{man}}{\tilde{T}_{man}R}\left((F_{egr} - \tilde{F}_{man})\dot{m}_{egr} - \tilde{F}_{man}\dot{m}_{thr,1}\right) \tag{2.216}$$

Collecting the assumptions and simplifications made above the dynamic behavior of the intake system for a modern turbocharged diesel equipped with EGR may be described by the following equations (the equations are derived in appendix D).

$$\begin{aligned}
\dot{p}_i &= k_p\left(T_{egr}\dot{m}_{egr} + T_{ic}\dot{m}_c - \tilde{T}_{man}\dot{m}_{ap}\right)\\
k_p &= \frac{R\gamma T_c T_{ic,m} T_{ic}}{V_{ac}T_{ic}T_{ic,m}\tilde{T}_{man} + V_{ic}T_cT_{ic}\tilde{T}_{man} + V_{thr,1}T_cT_{ic,m}\tilde{T}_{man} + \tilde{V}_{man}T_cT_{ic,m}T_{ic}}\\
\dot{\tilde{T}}_{man} &= \frac{R\tilde{T}_{man}}{p_i\tilde{V}_{man}}\left((\gamma T_{egr} - \tilde{T}_{man})\dot{m}_{egr} + (\gamma T_{ic} - \tilde{T}_{man})\dot{m}_c - (\gamma - 1)\tilde{T}_{man}\dot{m}_{ap}\right)\\
\dot{\tilde{F}}_{man} &= \frac{p_i\tilde{V}_{man}}{\tilde{T}_{man}R}\left((F_{egr} - \tilde{F}_{man})\dot{m}_{egr} - \tilde{F}_{man}\dot{m}_c\right)
\end{aligned}$$

Assumptions:

$$\dot{m}_{thr,1} \equiv \dot{m}_c,\ \dot{m}_{egr}, \dot{m}_c, \dot{m}_{ap} \geq 0$$

(2.217)

This third order system will be referred to as the TDMVEM (Turbo Diesel Mean Value Engine Model). The close relationship between the TDMVEM and the

AMVEM revisited in equation 2.213 is easily appreciated when $T_c = T_{ic,m} = T_{ic} = \tilde{T}_{man}$. In this case the pressure state equation is equivalent to the AMVEM pressure state equation.

This close relationship is further confirmed by comparing the k_p factor in the TDMVEM pressure ODE with the corresponding k_p factor ($\frac{\gamma R}{V_i}$) in the AMVEM. This comparison is graphically evaluated in figure 2.57 at the operating points from the steady state engine map utilized earlier in this section. The figure clearly shows

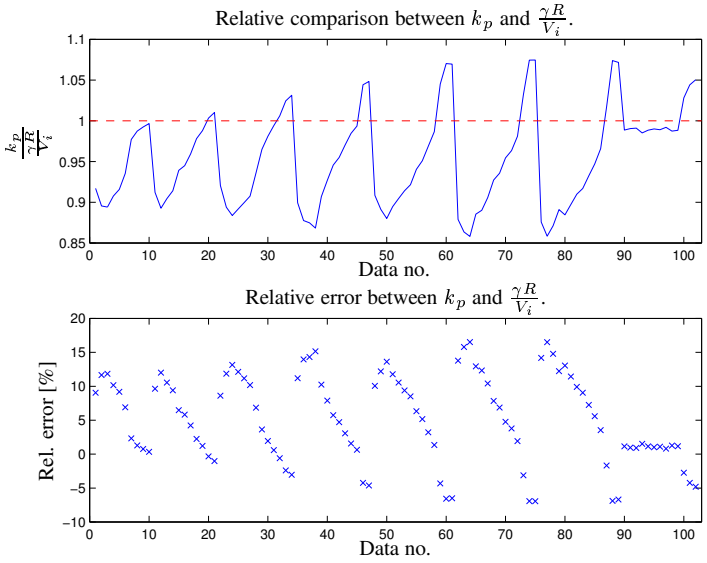

Figure 2.57: Relative comparison between k_p from the TDMVEM and $\frac{\gamma R}{V_i}$ from the AMVEM.

that the k_p factor in the TDMVEM is reasonably close to the normal value of $\frac{\gamma R}{V_i}$, and the relative error between the to factors stays between -10% and 20% within the limits of the engine map. However, the k_p factor is in general less than $\frac{\gamma R}{V_i}$ in the map key points where the EGR system is active. The reason for this may be traced back to the fact that the plenum temperature is higher than the overall temperature of the intake system for such map key points. Hence, the time response of the TDMVEM pressure state equation will be slower than the corresponding pressure equation in the AMVEM. When the EGR system is inactive and the boost pressure is high the overall intake temperature is higher than the intake plenum temperature. In such scenarios the response time of the TDMVEM pressure state equation will be somewhat smaller than AMVEM pressure's response time.

The importance of respecting how the EGR flow enters the system, however, is clear from the temperature state equation. The volume of interest is here the volume downstream of the EGR inlet point, $\tilde{V}_{man}$, and not the total system volume, V_i. Thus, the temperature state equation would for a normal intake system design be a factor of approximately five times faster than the state equation in the AMVEM. This is very important for the accuracy of the transient AFR control.

In this respect the AMVEM has been augmented further by a third state equation; The burnt mass fraction state equation. This estimate of the burnt mass content in the intake plenum may later be applied together with the commonly used speed-density equation to provide an estimate of the fresh air mass flow at the intake ports during transient as well as steady state engine operation.

2.8.4 Sectioned dynamic heat exchanger modelling

The local temperature differences observed in the intake system may in some cases be of vital importance in the estimation of how the individual sections of the intake system interact with each other. Thus, it may be convenient to divide the intake system up in several subsystems such that a more coherent picture of the temperature distribution can be established. In such a modelling concept it is natural to separate the cooler volume from the piping- and plenum volumes since the largest temperature changes are to be expected here.

A picture of the cooler's temperature distribution is here established by dividing this component into three separate volumes: inlet volume, cooling element and outlet volume. The dynamic description of the inlet and outlet volume follows the general FE modelling concept outlined in section 2.4, whereas the dynamic behavior of the cooler element pressure is modelled assuming isothermal conditions; An assumption justifiable due to the large area-volume ratio of the cooler. The separate control volumes are in the following referred to as nodes.

The mass flow or rather energy flow between the individual nodes are computed using the pipe flow model described in section 2.5. The pipe model requires the geometrical distance between the individual nodes as input for the flow computation. This is achieved in the following manner. It is here decided to locate the inlet and outlet node in the geometrically defined center of the assumed cylindrical profile of the these volumes. The geometric location of the cooling element node is chosen to follow the mean temperature location. The relative node location under steady flow conditions is depicted in figure 2.58. Finally, the geometric distance between neighboring nodes is used as input to the pipe mass flow model.

2.8.5 Unsteady flow conditions

Since the flow conditions normally experienced in automotive coolers are far from being steady, some special care in the cooler temperature distribution modelling must be taken, such that the physic effects experienced during throttle tip-ins and tip-outs, or simply with the unavoidable pumping fluctuations, can be included. This is, however, a challenging task due to the limitations imposed by the 0-D modelling concept. Fortunately, the wavelength of the pumping fluctuations is large in comparison with the longitudinal length of the cooling element under all normal engine operation and engine design conditions . Hence, the phasing error between the mass flow estimation provide by the pipe mass flow model and the actual mass flow conditions are negligible. Therefore, the mass flow estimation of

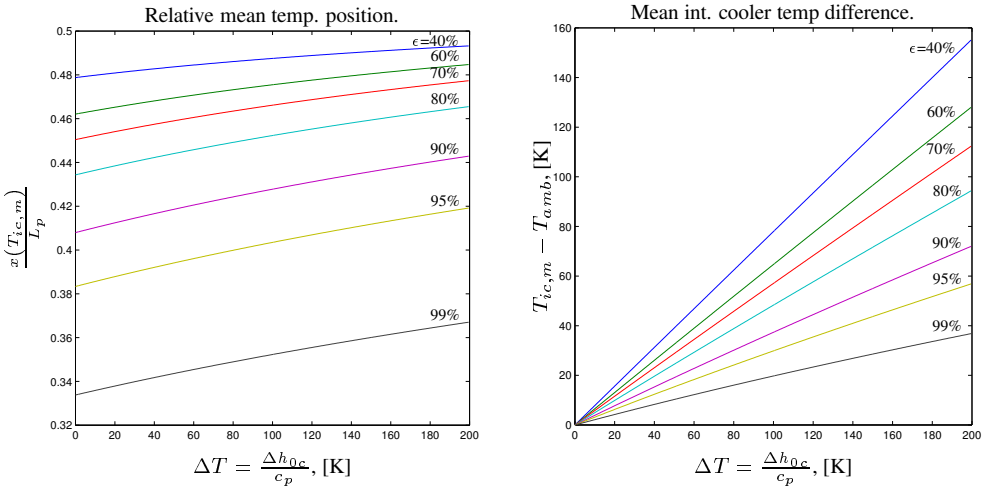

Figure 2.58: Relative longitudinal position of the mean cooler temperature together with the mean temperature gradient for different cooler effectiveness levels. In the computations the ambient temperature is assumed to be 298 K.

the inlet and outlet flow of the cooler may be used as a toggle in the estimation of the inlet and outlet temperature of the cooling element along with mean cooler temperature estimation. Furthermore, the temperature is assumed to follow the flow i.e. no energy dissipation will take place in the longitudinal direction of the element. Hence, a suitable model for the dynamic response of the inlet cooler temperature is

$$\begin{aligned} \dot{T}_{he,in} &= \begin{cases} 0, & \dot{m}_{in} > 0 \\ \frac{1}{\tau_{he,in}} \left(\tilde{T} - T_{he,in} \right), & \dot{m}_{in} < 0 \end{cases} \\ T_{he,in} &= T_{he,1}, \quad \dot{m}_{in} > 0 \end{aligned} \tag{2.218}$$

and the dynamic response of the of outlet temperature is found to

$$\begin{aligned} \dot{T}_{he,out} &= \begin{cases} 0, & \dot{m}_{out} < 0 \\ \frac{1}{\tau_{he,out}} \left(\tilde{T} - T_{he,out} \right), & \dot{m}_{out} > 0 \end{cases} \\ T_{he,out} &= T_{he,3}, \quad \dot{m}_{out} < 0 \end{aligned} \tag{2.219}$$

where $\tilde{T}$ is the flow direction dependent cooler inlet/outlet temperature. The flow direction dependent temperature may be computed by equation 2.206 using a fixed setting of the effectiveness or a effectiveness map. If the effectiveness level, ϵ, is unknown the inlet/outlet temperature can be derived by applying equation 2.205. The individual time constants, τ, in the two first order ODEs is set to a third[27] of

[27]The factor $\frac{1}{3}$ insures that the ODE has reached approximately 95% of its steady state value within the pipe transportation time.

the travel time of a plug flow between the inlet node and outlet node i.e.

$$\tau = \frac{L\rho A}{3\,|\dot{m}|} \tag{2.220}$$

The mean temperature dynamic is treated in the same manner as the inlet and outlet temperature except for the velocity calculation, which is taken as the mean value of the inlet and outlet mass flow.

In the case where the mass flow through the cooling element approaches zero the dynamics described by the above temperature distribution model will be too slow. A situation where this happens is for instance when the EGR valve is closed, and the EGR cooler volume is acting as a resonance volume. Instead, the gaseous matter inside the cooler is treated as a stationary gas dissipating energy to the coolant medium, i.e. the three temperatures describing the temperature distribution along the element follow

$$\dot{T} = \frac{kA}{c_v m}\left(T_{cool} - T\right) \tag{2.221}$$

2.8.6 EGR cooler simulation study and engine measurements.

This section presents and discusses the simulation results obtained with the heat exchanger model presented above. The purpose with this simulation study is to investigate the behavior of cooler's temperature distribution and flow characteristic when the EGR system is exposed to upstream pressure pulsations.

The cooler type selected for simulation is a water jacket cooled EGR heat exchanger normally fitted on a 2.0 liter 4 cylinder turbocharged DI Diesel engine. The cooler model, augmented with an extra node to described the local thermodynamic conditions in the pipe connection between the EGR cooler and intake plenum, is graphically summarized in figure 2.59. The notation for the individual

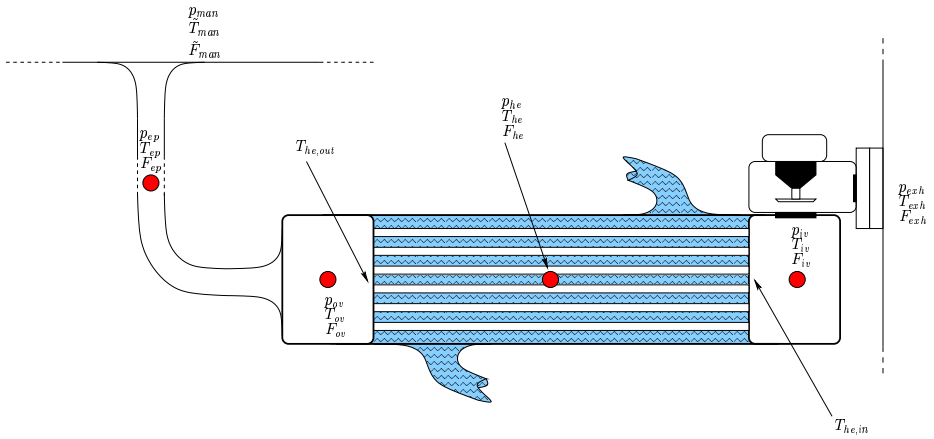

Figure 2.59: Selected EGR cooler node location.

thermodynamic conditions belonging to the corresponding node is also depicted in figure 2.59.

The geometrical design specifications of the cooler, EGR valve and the pipe connecting the cooler to the intake manifold, are listed in table 2.14, and the physical constants and parameters used for simulation are listed in table 2.15. The

Cooling Element	
Number of cooling pipes	27
Cooling pipes length, [mm]	300
Cooling pipe diameter, [mm]	6
Inlet volume*, [ml]	40
Outlet volume*, [ml]	40
EGR Valve (Poppet valve type)	
Port diameter*, [mm]	20
Seat diameter*, [mm]	24
Seat angle*, [°]	45
Connecting Pipe	
Pipe length*, [mm]	300
Pipe diameter*, [mm]	20

Table 2.14: EGR cooler system specifications. **NOTE:** Specifications marked with '*' are found by local dismantling of the EGR system.

Parameters		Constants	
Coolant water temperature, [K]	350	R, $\left[\frac{\mathrm{J}}{\mathrm{kg\,K}}\right]$	287.15
Intake manifold temperature, [K]	300	γ	1.4
Intake manifold pressure, [kPa]	130	k, $\left[\frac{\mathrm{W}}{\mathrm{m}^2\,K}\right]$	25
Intake manifold burnt mass fraction	0.1	μ, [Pa·s]	$1.781{\cdot}10^{-5}$
Exhaust manifold pressure (mean), [kPa]	150	EGR Valve C_D	0.6
Exhaust pressure fluctuation (peak-to-peak), [kPa]	40		
Exhaust temp.[K]	700		
Exhaust burnt mass fraction	0.8		
Engine Speed, [rpm]	2000		
Ambient temperature around cooler [K]	350		

Table 2.15: Physical constants and engine parameters used in the VES EGR cooler simulation study.

pressure level in the exhaust pipe is approximated by a biased sine wave. The bias or mean exhaust pressure level is selected to a constant level of 150 kPa, and the sine wave frequency will follow the frequency of the first harmonic of the exhaust pressure (≈67Hz). The peak-to-peak amplitude of the exhaust pulsation is fixed at 40 kPa. This fixed portrait of the exhaust pressure conditions upstream of the

turbine is of course a very simplified. The peak-to-peak amplitude of the pulsation will change with engine load changes and/or actuation of the VGT's position of the vanes. However, despite this simple picture the pulsation model does reflect the pressure level conditions fairly well when compared to the experimental pressure traces presented in [60] and [59]. The pressure pulsation level in the exhaust manifold is in [59] experimentally found to vary as much as 65 kPa peak-to-peak despite a moderate level of engine load (25% of maximum rated torque). Furthermore, due to this rather excessive level of pulsation the absolute exhaust pressure is below that of the intake system pressure for a significant fraction of the event period. The EGR mass flow is therefore negative for a considerable fraction of the engine event period. The EGR mass flow's behavior is also examined by a wave action model based simulation study in the research presented in [59]. Using this model based approach it is determined that EGR backflow may exist for as much as 50% of the engine's event period. Hence, the selected pulsation model is reasonable since it covers such scenarios.

The exhaust temperature is kept constant at 700 K in the following simulation study. This is obviously not representative for the stagnated temperature conditions normally experienced in a turbocharged DI engine. However, this step is made such that the effect of the exhaust pressure pulsations can be isolated. This is also reason for keeping the intake manifold's temperature and pressure fixed at 300 K and 130 kPa, respectively.

Figure 2.60 and 2.61 show the simulation results obtained with the isolated VES implemented EGR system. The first column of plots depicts in both figures the raw signals whereas the the second columns show the cycle averaged signals. To aid the interpretation of the individual curve plots the tables 2.16 and 2.17 are included to support the notation used in mentioned figures.

The first row in figure 2.60 illustrate the slowly opening–instantaneous closing of the EGR valve. The slowly opening of the valve insures a quasi steady state behavior of the system throughout the duration of the valve opening process.

The second row shows the individual node temperatures, which can be seen as a discrete EGR cooler temperature distribution. The different nodes, i.e. inlet volume, cooling element volume, outlet volume and pipe connection volume, are plotted with red, blue, magenta and orange, respectively. The green and black curves are the inlet temperature and outlet temperature of the cooling element, respectively. It is interesting to observe at low flow rates (the first 4 sec.) that although the mean flow through the cooling system is positive, the temperature in the pipe connection drops below the coolant and ambient surrounding's temperature of 350 Kelvin. This is due to the moderate fluctuation level in the system. Hence, if the cooler effectiveness is computed utilizing pipe connection temperature measurements, effectiveness levels larger than 100% may be expected. At higher flow rates the outlet temperature of the cooling system increases and cooler effectiveness drops. Here, it is interesting to notice how the inlet volume- and mean cooler temperatures begin to drop (after 4 and 7 sec, respectively) due to an increasingly severeness of the pumping fluctuations in the system i.e. the back flow between

the exhaust pipe and the cooler are no longer of a negligible level. After 80% of the opening period the flow through the system saturates i.e. the flow through the EGR valve is now restricted by the valve throat diameter and not the poppet valve itself, and the outlet temperature reaches a final level of approximately 480 K corresponding to a cooler effectiveness level of 37%.

The third row in figure 2.60 depicts the raw- and cycle averaged pressure levels at the different node locations, respectively. The red curve is the exhaust pressure, green the cooler entry volume pressure, blue the cooler element pressure level, black the cooler outlet volume pressure, magenta the pipe connection pressure level, and finally the orange curve is the intake manifold pressure level which is held constant. The pressure distribution clearly shows that inclusion of the pipe friction is important at higher flow rates for a correct estimation of the overall mass flow through the EGR system. If the pipe friction is neglected, however, this could lead to significant errors in the EGR valve mass computation. The reason is for this is simple. The pressure in the inlet volume downstream of the EGR valve will at relative high flow rates be significantly offset from the intake pressure. This will of course offset the prediction of the pressure ratio across EGR valve if the inlet volume pressure is approximated by the intake plenum pressure. The first row in figure 2.61 depicts the distribution of burnt mass in the EGR cooler system, and the corresponding curve color notation is given in the first row of table 2.17. It should here be noted that the burnt mass fraction, F, is a volume averaged measure and not a position dependent measure. The burnt mass level in the pipe connection decreases in the beginning away from its initial value of 0.5, again, due to engine pumping. The effect of the fluctuations is here, however, even more pronounced than in the case with the EGR system temperature distribution. First the mean pipe connection fraction reaches a peak value of approximately 0.55 after which the burnt mass level decreases and finally attains a level of approx 0.47 as the flow rate through the system saturates. This behavior would of course not be encountered with steady mass flows where all node burnt mass fraction would attain the same level of 0.8 as in the exhaust system. After the first initial 10 sec. the EGR valve is instantaneously closed. This is followed by a rapid decrease of the burnt mass fraction especially in the pipe connection node due to the gas contraction initiated by the heat transfer between the EGR system and the coolant water/surroundings.

The second row in figure 2.61 illustrates the raw- and cycle averaged mass flow between the individual nodes and the boundary systems, where orange is the EGR valve mass flow, magenta is the inlet mass flow to the cooler, black is the flow out of the cooling element, the blue curve is the mass exchange between the outlet volume and the pipe connection, and finally the red curve depicts the mass flow out of the EGR pipe connection. As expected the flow through the system increases as the EGR valve is opened reaching a final mean value of approximately $17\frac{g}{s}$.

The characteristic of the individual node burnt mass fraction might of course lead to the question: is the law of mass conservation violated? Hence, in order to prove that the burnt mass flow into the EGR system equals the burnt mass flow out of the system during steady state operation, the instant burnt mass exchange

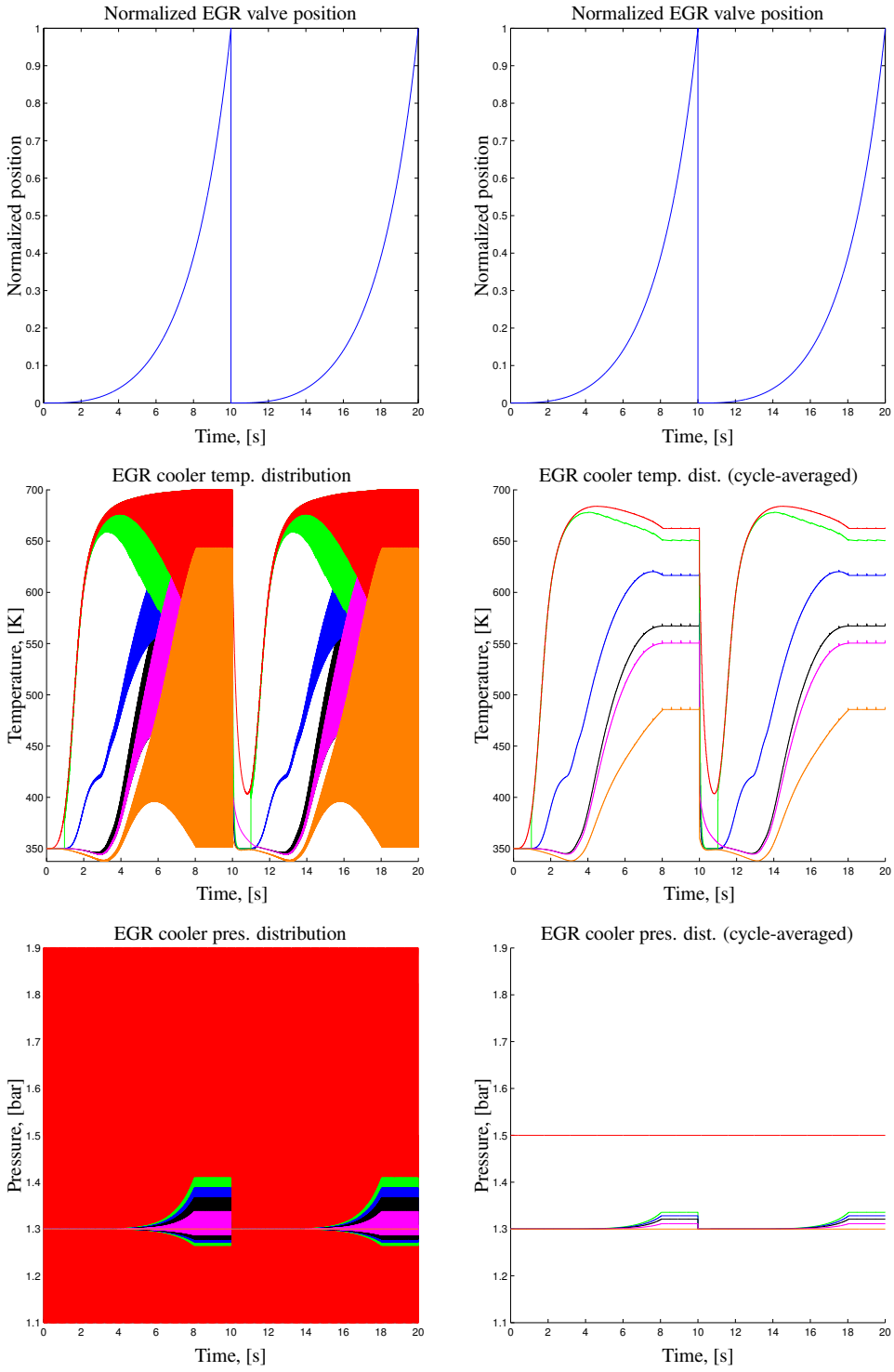

Figure 2.60: Isolated EGR cooler system simulation study. The individual plot portray the raw and cycle-averaged normalized EGR position, temperature distribution and pressure distribution, respectively. The curve color notation utilized is given in table 2.16

Temperature distribution – second row of figure 2.60							
T_{exh}	T_{iv}	$T_{he,in}$	T_{he}	$T_{he,out}$	T_{ov}	T_{ep}	$\tilde{T}_{man}$
-	red	green	blue	black	magenta	orange	-
Pressure distribution – third row of figure 2.60							
p_{exh}	p_{iv}	-	p_{he}	-	p_{ov}	p_{ep}	p_{man}
red	green	-	blue	-	black	magenta	orange

Table 2.16: Notation support to figure 2.60

between the EGR system and its surrounding is computed i.e

$$\dot{m}_b = F\dot{m} \tag{2.222}$$

This instant burnt mass exchange is depicted in the lowest left plot in figure 2.61, where the blue curve is the burnt mass flow at the EGR valve and the green curve is the burnt mass flow out the EGR system into the intake manifold. The lowest righthand plot depicts cycle averaged burnt mass flows, which lay on top of each other reaching the expected maximum value of $14\frac{\text{g}}{\text{s}}$ ($\approx 0.8 \cdot 17\frac{\text{g}}{\text{s}}$). Hence, the law of mass conservation is not violated when computing the burnt mass flow in and out of the EGR system despite the mixing assumption made. In order to further stress the importance of a correct knowledge of the fluctuation level and structure when evaluating EGR system performance the same series of simulations is carried out again, however in a steady flow scenario where the mean mass flow through the system is kept around the cycle averaged values presented in figure 2.61. The simulation results obtained in this steady flow scenario are presented in figure 2.62. Again, the red curve is the inlet node temperature, the green the inlet temperature of the cooling element, the blue curve is the mean temperature of the cooling pipe section, the black is the element outlet temperature, magenta is outlet volume node temperature, and finally the pipe connection temperature is graphically illustrated by the orange curve. Comparing the plots it is easily concluded, as expected, that the presence of pumping fluctuations promotes the effectiveness of the EGR cooler system due to the reprocessing of the gaseous matter during flow reversal. Hence, the minimum EGR system effectiveness encountered at maximum mass flow through the system is reduced to approximately 16% instead of the 37% obtained in the unsteady flow case. Furthermore, the initial temperature drop in the pipe connection is now absent due to the missing mixing process between the intake manifold and the gaseous matter in the pipe.

Figure 2.63 shows experimental data from a 2.0 liter four cylinder turbocharged DI Diesel engine obtained at different engine speeds. The EGR rate, or mass flow, is computed from CO_2 measurements in the intake manifold. Furthermore, the water cooled EGR heat exchanger's effectiveness is derived utilizing the mean value of the coolant inlet- and outlet temperature, the temperature upstream of the tur-

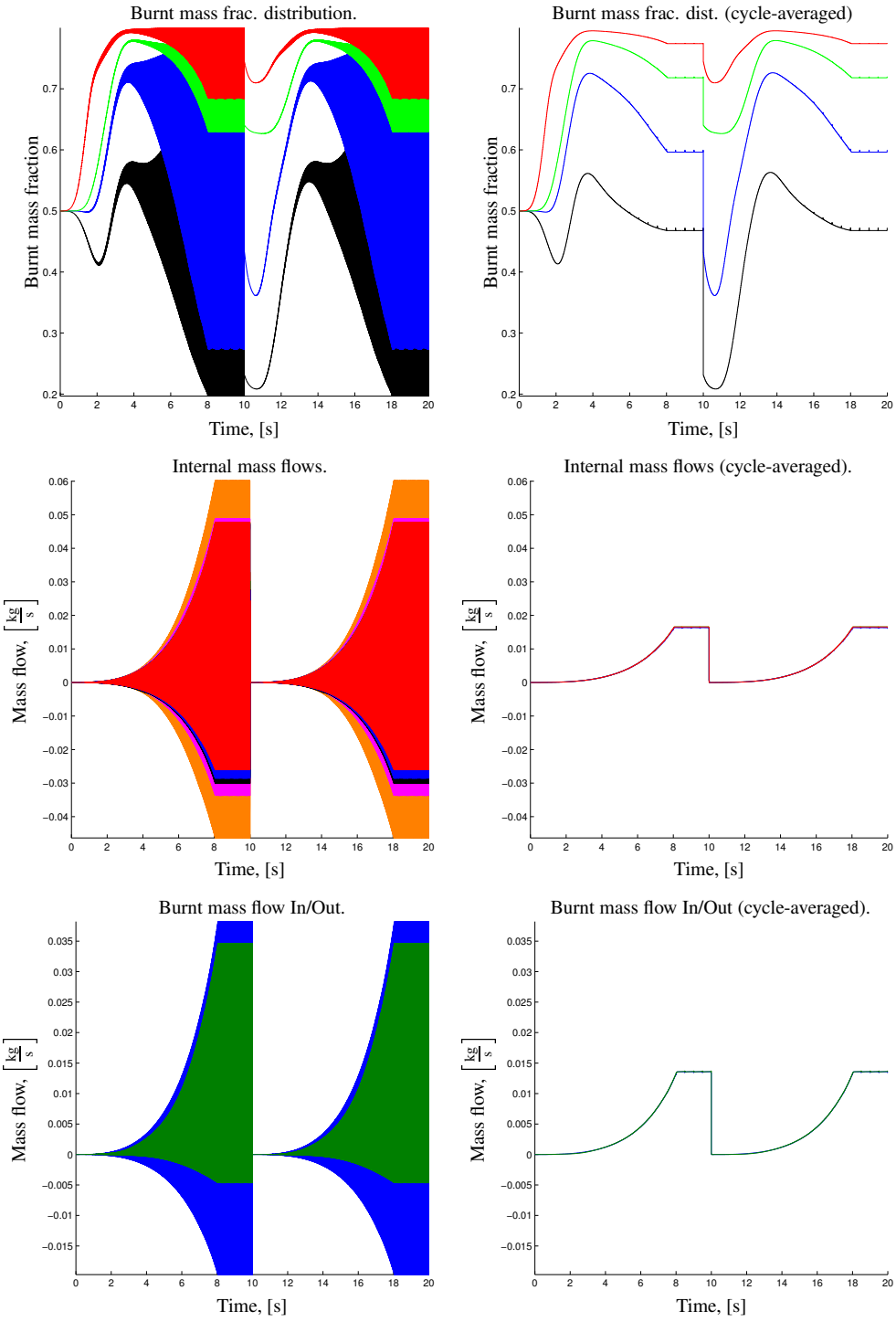

Figure 2.61: Isolated EGR cooler system simulation study. The individual plots portray the raw and cycle-averaged burnt mass fraction distribution, control volume flows and burnt mass boundary flows, respectively. The curve color notation used is given in table 2.17

Burnt mass distribution – first row of figure 2.61							
F_{exh}	F_{iv}	-	F_{he}	-	F_{ov}	F_{ep}	$\tilde{F}_{man}$
-	red	-	green	-	blue	black	-
Local mass flow – second row of figure 2.61							
$\dot{m}_{egr,v}$	-	$\dot{m}_{he,in}$	-	$\dot{m}_{he,out}$	-	$\dot{m}_{ep,in}$	$\dot{m}_{egr}$
orange	-	magenta	-	black	-	blue	red
In/out burnt mass exchange – third row of figure 2.61							
$\dot{m}_{egr,v,b}$	-	-	-	-	-	-	$\dot{m}_{egr,b}$
blue	-	-	-	-	-	-	green

Table 2.17: Notation support to figure 2.61

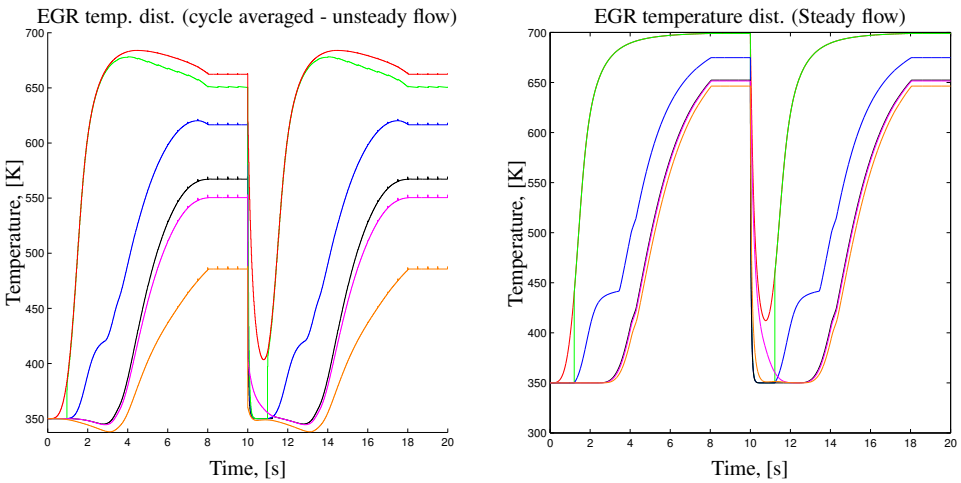

Figure 2.62: Temperature distribution in the EGR system with/without pumping fluctuation presence. The distribution from the unsteady flow simulation (see figure 2.61) is plotted to the left for the sake of convenience. The plot to the right depicts the temperature distribution obtained in the steady flow scenario.

bine, and the temperature in the pipe connecting the EGR cooler to the intake manifold i.e.

$$\epsilon_{egr} \approx \frac{\overline{T}_{exh} - \overline{T}_{pipe}}{\overline{T}_{exh} - \overline{T}_{cool}} \tag{2.223}$$

Since the mapping data set does not contain any complete cycle measurement traces but only steady state measurement points the level of the pumping fluctuation in the EGR system is unknown. However, a kind of fluctuation level indication must be provided to aid the investigation of the EGR cooler effectiveness' behavior. The following non-dimensional fluctuation level indicator is proposed here

$$I = \frac{\overline{p}_{exh} - \overline{p}_{man}}{\overline{p}_{exh}} \frac{\tau_b}{\tau_{b,max}} \frac{N}{N_{max}} \tag{2.224}$$

The first part expresses the pressure difference ratio across the complete EGR system, and hence a measure of what fluctuation amplitude may be expected across the system. The second part relates the measured engine brake torque to the maximum engine brake torque. Since the enthalpy level in the exhaust system generally increases with engine load this ratio is a good indicator of the fluctuation amplitude in the exhaust system. The third and final part relates the engine speed to a selected maximum speed level. Since the harmonics of the individual pulsations are locked to the engine cycle frequency, this last part will give an indication the pulsation frequency intensity. A similar approach is utilized in [60] to characterize the turbines' efficiency under pulsating flow conditions.

The data evaluation is further hampered by the fact that the temperature measurements obtained are something in between the local static and stagnation temperature. This problem may especially be important for the exhaust manifold temperature measurement due to the high kinetic energy pulsations present, and may as such offset the EGR cooler effectiveness computation.

The first plot in figure 2.63 illustrates the EGR effectiveness computed by equation 2.223 at engine speeds ranging from 1000 rpm to 2500 rpm. The pulsation indicator, used to assist the interpretation of effectiveness characteristic, is shown to the right in figure 2.63. That the indicator indeed provides useful information is clear from the fact that where the mass flow data points are in the vicinity of each other, the effectiveness speed-line curvature follows the indicator speed-line curvature, except for a couple of low mass flow measurement points.

The effectiveness figure clearly shows the mixing phenomenon experienced with pulsating flows as the effectiveness level for low mass flows are found to exceed 100%. This effectiveness behavior is already found and discussed in the simulation study presented earlier. The low speed effectiveness speedlines (1000 rpm–1500 rpm) exhibit an interesting behavior at higher mass flows where the effectiveness level is seen to increase within a reasonable narrow mass flow window. The indicator I is for these point, however, found to be almost constant, hence the changes in engine load and pressure gradient across the heat exchanger system can be assumed constant for these operating points. Furthermore, the exhaust temperature is found to change less than 40K, where the effectiveness level increases

more than 20%. It will be argued that since the upstream and downstream conditions of the cooler are unchanged these upward characteristic bends are linked to an excessively opening of the EGR valve. An excessively opening of the EGR valve will in these operating ranges of the engine only lead to a moderate EGR mass flow increase due to the small pressure gradient across the valve, however the pulsation level will noticeably increase. Hence, just as it was experienced in the simulation study, the increase in the fluctuation level will enhance EGR cooler effectiveness. However, to draw general conclusions the effectiveness may be said to increase with pulsation amplitude and frequency and decrease with EGR mass flow, the general trends also predicted by the VES implemented EGR model.

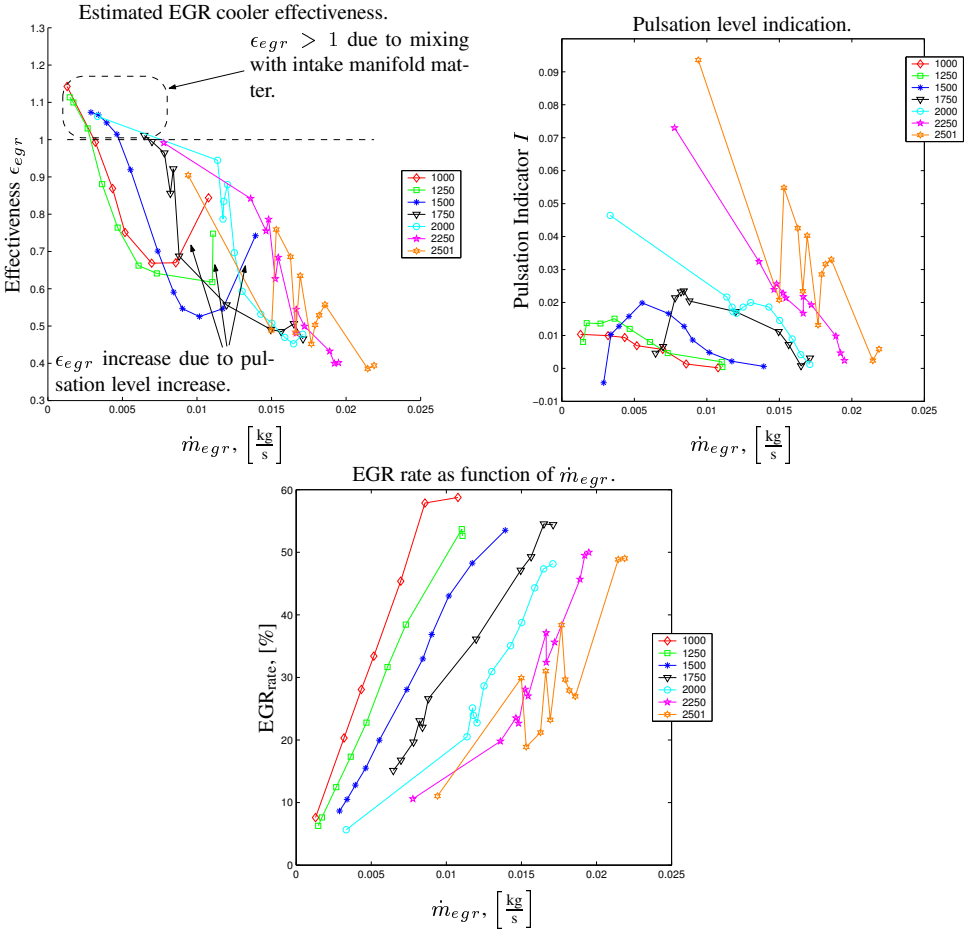

Figure 2.63: Water jacket cooled EGR heat exchanger performance derived from a steady state mapping data set of a 2.0 liter turbocharged DI Diesel engine.

The lower plot in figure 2.63, illustrating the EGR_{rate} as function of $\dot{m}_{egr}$, clearly shows that the engine map presented span the complete range of the EGR rate levels in normal modern Diesel engine. The findings and statements derived from the simulation study and the measurement data inspection may thus be regarded to be of general nature.

The simulation study, supported by steady state engine measurements, unfortunately shows that effectiveness level of the EGR cooler is very dependent upon a good knowledge of the pulsation level and frequency in the assessment of this property. This will of course make an EGR cooler model inclusion in the MVEM structure for either observer or modelling purposes difficult.

2.8.7 Summary

This section is devoted completely to the investigation of how the two most commonly encountered heat exchangers in the engine air path, the intercooler and EGR cooler, may be included in a non-iterative engine model design. The problem of modelling the pressure and temperature dynamics for zero dimensional engine model inclusion are essentially made difficult due to the large entropy gradient across this control volume. However, the air-to-air cross flow intercooler normally has a high level of effectiveness such that this parameter can be regarded as constant. This way it is possible to derive a mean temperature model, which is valid for quasi-stationary modelling purposes, and makes possible a better assessment of the gaseous mass contained in the heat-exchanger volume. Furthermore, it is argued that the dynamic heat exchanger temperature and pressure modelling may be separated i.e. the heat exchanger may be regarded as an isothermal control volume. Next, a new non-iterative EGR cooler model capable of predicting the essential effects encountered with pulsating flows is also presented. The trends found by simulation are supported by steady state engine measurements and the model thus provides a fast non-iterative heat exchanger modelling approach. However, due to the model complexity, the model cannot readily be included in an observer design but is rather intended to be used in off-line 0D and 1D engine simulation studies.

2.9 Phenomenological combustion modelling

The combustion process, regardless of whether it is the SI or CI case, is probably the least understood part of the physical phenomena taking place in an engine, and hence the part providing the greatest difficulties to explain within the confines of current physical- and chemical understanding.

2.9.1 DI Diesel engines

Modern DI engines equipped with common rail technology are capable of multiple diesel fuel injections before and after TDC (Top Dead Center). Normally, two injections take place before TDC. These injections are classified as the pilot- and main injections. The pilot injection is used to reduce the steep cylinder pressure gradient occurring shortly after the main injection. Post injection is used as means

to accelerate the warmup process of after treatment component e.g. the oxidation catalyst.

The modelling of the ignition and combustion phenomena following the individual injections is extremely complex. Each injection combustion process is governed by effects such as fuel jet penetration, break-up and evaporation, the geometrical distribution of fuel in the chamber, ignition delay, combustion chemistry, and the swirl and tumble inside the chamber [33]. Highly complex three dimensional models describing the chemical interactions between liquid and gaseous matter, and the internal chemical processes taking place in the different combustion phases have become available in the last decade (see e.g [8, 7]). Recently, these models have been further extended with NO_X and soot formation sub-models [18] such that studies of diesel emissions may be undertaken. However, despite the huge effort invested, these models still need a high level of empiricism for a successful description of properties like the heat release rate among others. In other words the predictive capabilities of the models are still rather limited, and the models should as such only serve as trend descriptors and not as models capable of accurate quantitative estimations of different combustion properties.

Due to the high amount of skill, insight and not to forget computer power required by the 3D combustion models, and when the level of detail requirements are low to moderate, combustion controlling aspects like the heat release rate are often sought described by empiricism alone. One such empiric approach is the use of zonal models, where the combustion chamber is split into one or more zones. The interchange of fuel and air between the zones is described by a set of algebraic or differential relations. The functional form of these equations is subsequently shaped from experimental data. Each zone is treated as a zero dimensional volume governed by energy- and mass conservation.

The simplest zonal model is the single zone model. Here, it is assumed that the combustion chamber contents are adequately mixed, such that the chamber may be described by one set of averaged state equations alone. One such single volume model proposal is given in [86]. Here the heat release is attributed to a premixed part, described by M_p, and a diffusion part modelled by the function M_d . The distribution between the premixed and diffusion heat release is described by the weighting factor β. Hence, the mass fraction of the fuel burnt can be described as

$$\begin{aligned} \frac{m_{f,b}(\tilde{\theta})}{m_f} &= \beta M_p(\tilde{\theta}) + (1-\beta) M_d(\tilde{\theta}) \\ &\text{with} \\ 0 \leq \beta &\leq 0 \end{aligned} \tag{2.225}$$

where $m_{f,b}$ is fuel mass burnt, m_f is the total amount of fuel injected per power stroke, and $\Delta\theta_{comb}$ is the nominal combustion duration. The non dimensional crank angle, $\tilde{\theta}$, is given by

$$\tilde{\theta_e} = \frac{\theta_e - \theta_{ign}}{\Delta\theta_{comb}} \tag{2.226}$$

where θ_e is the crank angle domain of interest, and θ_{ign} is the crank angle where the ignition is initiated. The premixed combustion phase is described by

$$M_p(\tilde{\theta}) = 1 - \left(1 - \tilde{\theta}^{C_{p1}}\right)^{C_{p2}} \tag{2.227}$$

and the diffusion governed combustion is model by

$$M_d(\tilde{\theta}) = 1 - e^{-C_{d1}\tilde{\theta}^{C_{d2}}} \tag{2.228}$$

where the later is recognized as a normal Wiebe function. The empirical coefficients C_{p1}, C_{p2}, C_{d1} and C_{d2} are modelled by,

$$\begin{aligned} C_{p1} &= 2 + 1.25 \cdot 10^{-8} \left(\tau_{ign} N\right)^{2.4} \\ C_{p2} &= 5000 \\ C_{d1} &= \frac{14.2}{\phi^{0.644}} \\ C_{d2} &= 0.79 C_{d1}^{0.25} \end{aligned} \tag{2.229}$$

where N is the engine speed, τ_{ign} is the ignition delay in milliseconds, and ϕ is the fuel-air ratio of the matter trapped in the combustion chamber. The distribution between premixed- and combustion may be modelled as

$$\beta = 1 - \frac{\alpha \phi^b}{\tau_{ign}^c} \tag{2.230}$$

where suitable ranges for the three empirical constants are given as

$$0.8 < \alpha < 0.95 \qquad 0.25 < b < 0.45 \qquad 0.25 < c < 0.5 \tag{2.231}$$

Finally may the heat release rate be found from

$$Q_{comb} = \frac{dm_{f,b}}{d\theta} E_{HV} = \left(\beta \frac{dM_p}{d\theta} + (1 - \beta) \frac{dM_d}{d\theta}\right) m_f E_{HV} \tag{2.232}$$

where E_{HV} is the heating value of the fuel. The single zone, or Watson model, has been applied with success in global diesel engine performance studies [27], and is thus a good model candidate when only a moderately detailed model of the combustion system is required.

In the two zone model the combustion chamber is split in two zones, where one contains bulk air and the other the volume of combustion. The heat release in the combustion zone may, analogous to the single zone model, be described by a phenomenological heat release model like the one presented above. Since the model is capable of distinguishing between bulk air temperature and the combustion zone temperature more realistic inputs to emission models can be provided. This more realistic picture of the emission formation has triggered off the development of multi zone combustion models. The multi zone models have shown

improved emission prediction capabilities (see eg. [25]) compared to the simpler single- and two zone models. However, the introduction of a large number of coefficients and parameters that need to be identified prior to model application often makes the problem mathematically as well as physically undefined i.e. the identification problem is not affine in the parameter space. Hence, for the most part it cannot be concluded whether or not the same level of model accuracy could not be achieved with a completely different setting of the parameters.

In the case where only a MVEM modelling level is needed the actual combustion processes may be disregarded completely, and the crank angle dynamics may be described from energy conservation alone. The distribution of the energy released by combustion between heat losses, shaft work, friction losses among others can thus be described by efficiencies and/or MEP (Mean Effective Pressure) alone (see e.g. [63, 54]). The different efficiencies/MEPs are of course dependent on several engine design- and operating point parameters and variables. These dependencies are often extremely complex and not well understood. Hence, the different efficiencies and MEPs are sought modelled from empiricism alone.

It is in this research found that the LWLS estimation scheme presented in section 2.3.4.5 on page 114, with a following appropriate validation of the correlations obtained, provides a fast and easy tool for MVEM based combustion modelling. However, it cannot be stated strongly enough, that the input variables to the correlation routine must not only span the steady operating range but also the transient range. If this evident, but hardly practically met, condition is neglected, unfortunate regions of the correlation sphere without data support may be entered and lead to erroneous simulation results. The LWLS method will verified on steady state map data for a 2.0 l VGT equipped DI Diesel engine[28]. The engine was mapped at selected key points in the speed-torque map of the engine up to 2750 rpm and was controlled by the standard ECU (Engine Control Unit). Hence, the engine map utilized will completely cover the region of speed-torque engine map where the EGR system is active.

In the analysis of the engine data it is found convenient to describe the combustion behavior by the three following phenomenological properties:

- η_i: Indicated engine efficiency.
- FMEP: Friction mean effective pressure.
- ζ_{exh}: Exhaust energy fraction.

The indicated engine efficiency is defined as the fraction of the released fuel energy extracted as useful piston work during the compression–expansion part of the cycle, i.e.

$$\eta_i \triangleq \frac{\oint_{\text{cycle}} p_{cyl} dV}{m_{f,cycle} E_{HV}} = \frac{P_{cyl,gross}}{\dot{m}_f E_{HV}} \tag{2.233}$$

[28]Dipl. Ing. Daniel Röttger is gratefully acknowledged for providing the steady state engine map.

The efficiency is dependent on the point of combustion, AFR, initial inert gas content ($\approx F_{man}$), and entrained mass in the combustion chamber among others. However, η_i is found to have a strong λ dependency, and a weaker F_{man} dependency[29]. These observed properties were utilized in a successful second order LWLS identification of η_i as function of F_{man} and λ. The successfully identified η_i surface spanned by λ and F_{man} is shown in figure 2.64. The surface covers a rather large

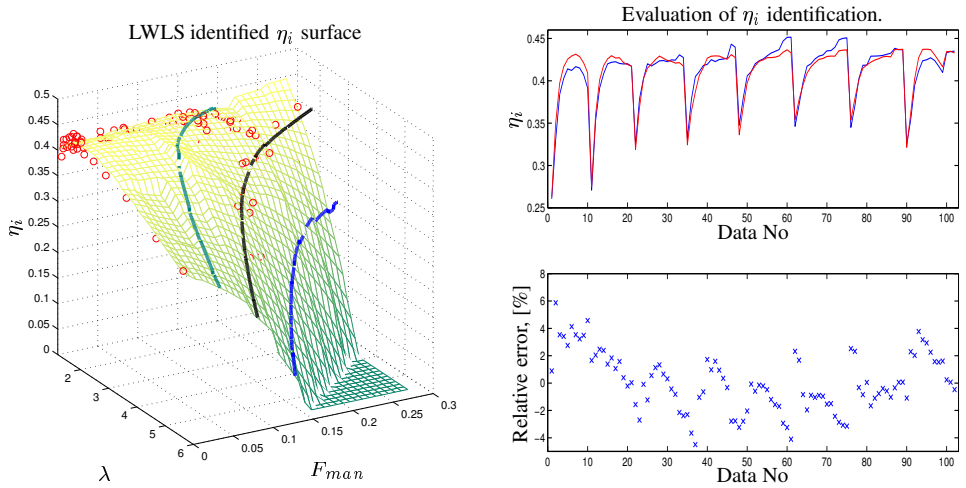

Figure 2.64: η_i LWLS identification. The green surface to the left shows the η_i surface identified by a second order LWLS polynomial in F_{man} and λ with 25 grid points. The map data points are marked with o, and as an addition the 25% (green line), 50% (black line) and 75% (blue line) steady state EGR rate lines are imposed on the surface. The plots to the right depicts the LWLS estimated η_i (solid red curve) together measurement data points and the belonging relative error. The individual "bows" in this upper righthand plot indicate data points belonging to the same engine speed set point.

region necessitating extrapolation. However, this region is located primarily outside the 50% EGR rate line, and thus is only reachable during large engine speed decelerations. During such scenarios the magnitude of the engine efficiency is of minor importance compared to friction and load factors for a correct estimation of the crankshaft speed dynamics. The good identification quality of the 25 grid point LWLS is supported by a relative low relative error, which is basically kept within $\pm 5\%$.

Viscous friction and pumping losses cannot be avoided and play an important role in characterization of the crank shaft dynamics close to idle speed or part load engine operation. However, it is difficult to divide the total loss in either pumping work, which is mainly a function of intake, exhaust and ambient pressure, and the inevitably viscous friction loss between cylinder liners and walls, and bearings.

[29] No injection point data is provided with the data set. Hence, it is assumed here that the injection timing is optimized for maximum engine efficiency.

Hence it is here decided only to address phenomenological modelling of the total work i.e. the pumping work is lumped into the frictional mean effective pressure, FMEP (Friction Mean Effective Pressure), definition. The frictional mean effective pressure is from the data derived as

$$\text{FMEP} = \frac{2P_{fric,pump}}{V_d N} = \frac{2\left(\eta_i \dot{m}_f E_{HV} - \tau_b N\right)}{V_d N} \tag{2.234}$$

since the indicated efficiency is known. In the case where η_i is unknown FMEP is often identified from the so called *Willans line* [54]. However, this method was tested for the sake of completeness but found very inaccurate. The size of the experimental DI engine's FMEP is found to be strongly rotational speed dependent, as expected, and to a minor degree intake manifold density dependent. This observation was utilized in a successful LWLS identification with 25 grid points. The performance of the LWLS FMEP algorithm is graphically illustrated in figure 2.65. The FMEP level is clearly overestimated in the low speed–high intake density re-

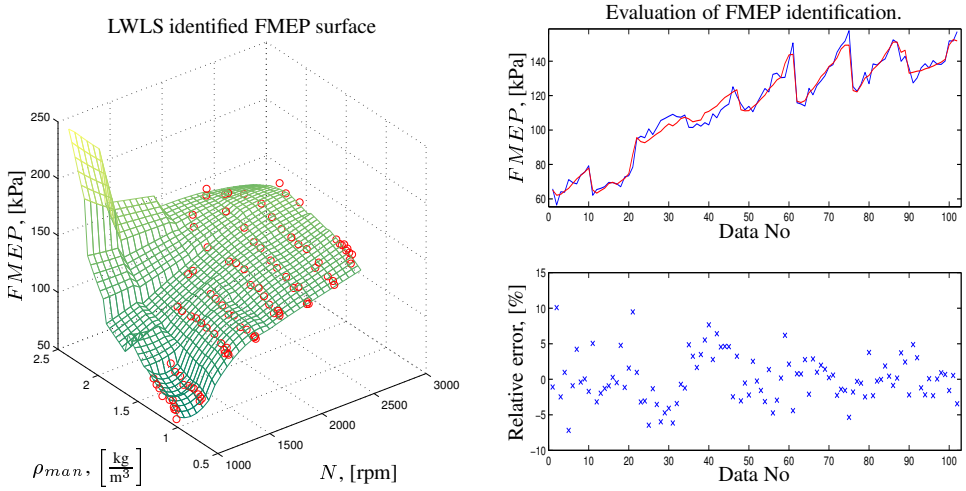

Figure 2.65: LWLS identified FMEP for the experimental 2.0l Diesel engine. The FMEP surface identified (green mesh surface) together with measurements is seen to the left. The identification routine (solid red line) compared to measurements as a function of operating point is illustrated to the right. The relative modelling error can with the LWLS algorithm selected be kept within $\pm$ 10%.

gion of the surface. However, since the intake dynamics is a lot faster compared to the crankshaft dynamics this region will never be entered during either steady state or transient operating conditions. Hence, the FMEP surface spanned by N and ρ_{man} may be accepted to be globally valid.

The two quantities η_i and FMEP are in principle together with engine speed and fuel flow the only variables needed in a MVEM modelling of the crankshaft dynamics. However, due to the AFR and ρ_{man} dependencies the crank shaft dynamics will also be indirectly dependent upon the turbocharger performance. Since

the turbocharger estimation quality is very dependent upon a good knowledge of the thermodynamic conditions upstream of the turbine, it is of vital importance to know the level of thermal combustion energy purged into the exhaust manifold. It is here found convenient, due to the good indicate engine efficiency estimation quality, to describe the exhaust enthalpy increase by the non dimensional fraction ζ_{exh}. ζ_{exh} is defined as the fraction of released thermal fuel energy leading to an enthalpy rise in the exhaust manifold. Hence, the energy distribution between coolant loss fraction, ζ_{cool}, and exhaust energy fraction, ζ_{exh}, are readily found as

$$\begin{aligned} \zeta_{exh} &= \frac{c_p^{exh}\left(T_{0,exh}\right) T_{0,exh} - c_p^{man}\left(T_{0,man}\right) T_{0,man}}{\dot{m}_f E_{HV}} \\ \zeta_{cool} &= 1 - \eta_i - \zeta_{exh} \end{aligned} \tag{2.235}$$

The coolant loss fraction ζ_{cool} is very dependent upon how long the entrained gaseous combustion chamber matter is exposed to the surrounding cylinder walls, hence ζ_{cool} must have an inverse speed dependence. The heat transfer coefficient between the combustion matter and the enclosing walls is function of the Nusselt number. The Nusselt number may be derived from Reynolds and Prandtl numbers, which in turn are indirect functions of the enclosed mass level and engine speed. Hence, ζ_{exh} will be functionally dependent upon engine speed, N, and indirectly upon the intake manifold density, ρ_{man}. These observations are utilized in a successfully identification of ζ_{exh} by the LWLS method. The ζ_{exh} identification is graphically evaluated in figure 2.66 It is clear from the ζ_{exh} surface in figure 2.66,

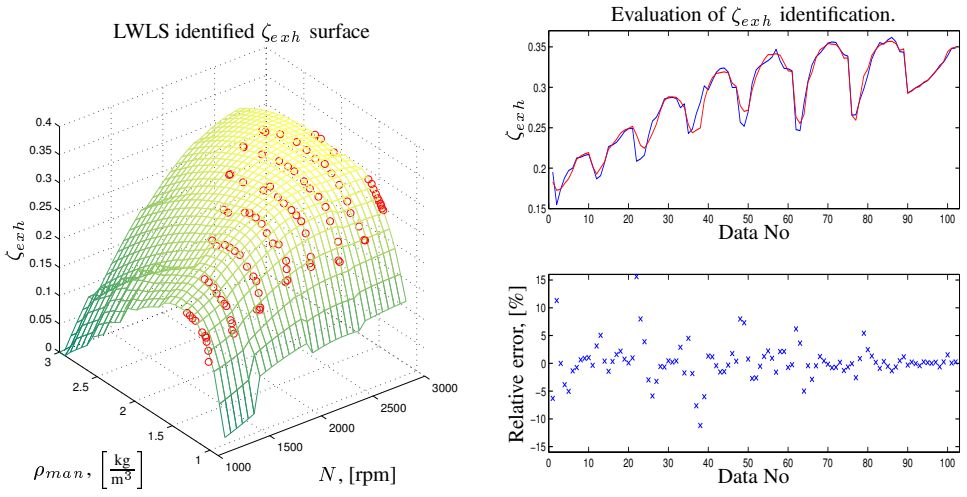

Figure 2.66: Graphical evaluation of the ζ_{exh} identification.

that ζ_{exh}'s gradient in the extrapolation region (in the vicinity of $\rho_{man} = \rho_{amb}$) is too steep. However, this region is not reachable unless engine throttling is used (e.g. DPF regeneration or EGR rate increase purposes). The ζ_{exh} level is also unrealistic low in the low speed–high density region of the surface necessitating

extrapolation. These area is however not reachable independent of transient- or steady state operation of the engine due to the low level of thermodynamic energy available in the exhaust manifold. Hence, the ζ_{exh} surface identified may be used in both transient and steady state simulation studies of un-throttled DI Diesel engines. If data points are available in this region of the map, it is believed that a successfully identification of ζ_{exh} as a function of N and ρ_{man} alone will still be possible.

Finally, the estimation quality of the exhaust port temperature after exhaust port coolant loss, T_{ep}, is evaluated for the sake of completeness. This temperature may readily be found found from the definition of ζ_{exh} to

$$T_{ep} = \zeta_{exh} \frac{\dot{m}_f}{\dot{m}_{ap} + \dot{m}_f} \frac{E_{HV}}{c_p^{exh}} + \frac{c_p^{man}}{c_p^{exh}} T_{man} \tag{2.236}$$

This equation is implicit due to c_p^{exh}'s exhaust temperature dependence. Instead, a descriptive mean value of c_p^{exh} is used i.e.

$$\overline{T}_{ep} = \zeta_{exh} \frac{\dot{m}_f}{\dot{m}_{ap} + \dot{m}_f} \frac{E_{HV}}{\overline{c}_p^{exh}} + \frac{c_p^{man}}{\overline{c}_p^{exh}} T_{man} \tag{2.237}$$

Both equations are graphically evaluated in figure 2.67. The implicit estimation

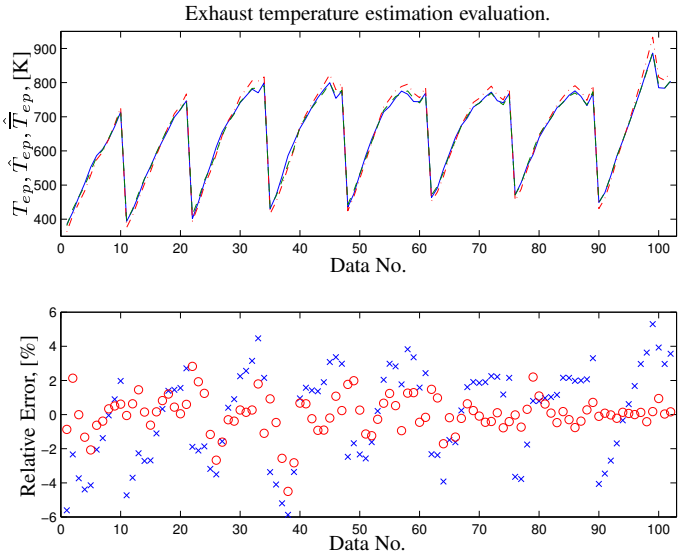

Figure 2.67: Exhaust port temperature estimation. The measurements as function of operating point are seen as a solid blue curve in the upper plot. The green dashed line is the implicit estimation of T_{ep}, and red dash-dot line illustrates the explicit solution to T_{ep} utilizing $\overline{c}_p^{exh}$. The relative error of the implicit estimation and explicit estimation algorithm are marked by 'o' and 'x', respectively, in the lowest plot.

algorithm is better than the explicit solution, as expected. However, the difference is small, and the T_{ep} can in an explicit manner be estimated within $\pm$ 5% relative accuracy – an accuracy level generally acceptable for the MVEM framework.

2.9.2 Gasoline engines with port fuel injection

Since the combustion mixture can be assumed mixed homogeneously with good accuracy before combustion is initiated, SI combustion appears much simpler in terms of the physics involved than the heterogeneous DI Diesel combustion process. Hence, it is in the literature customary (see e.g. [37]) to model the SI combustion for cycle simulation purposes by two zones, a burned and unburned mixture zone, separated by a thin reaction sheet referred to as the flame. Despite the chaotic geometrical structure of this reaction sheet, evolving from the spark plug and eventually sweeping the complete combustion chamber, the volume occupied is negligible, [33]. Hence, the two zone model seems ideal for cycle simulation studies. However, a description of the flame speed is still not well understood, and physical modelling is therefore complicated. Instead, the volume fraction, x_b, captured by burned combustion products are modelled by correlation functions alone like the Wiebe function i.e.

$$x_b = 1 - e^{-\alpha\left(\frac{\theta-\theta_0}{\Delta\theta_{comb}}\right)^{m+1}} \tag{2.238}$$

or in terms of heat release by

$$\frac{dE}{d\theta} = m_{f,cyl} E_{HV} \frac{\alpha}{\Delta\theta_{comb}^{m+1}} e^{-\alpha\left(\frac{\theta-\theta_0}{\Delta\theta_{comb}}\right)^{m+1}} (\theta - \theta_0)^m \tag{2.239}$$

where $m_{f,cyl}$ is fuel mass per stroke, θ_0 is the point of combustion start, and α and m are correlation constants. Good agreement between experimental results and predictions utilizing equation 2.238 with $\alpha = 5$ and $m = 2$ is reported in [55].

In case of MVEM modelling of the crank shaft dynamics the necessary input information can be expressed by mean value properties like indicated engine efficiency, friction and pumping mean effective pressures, fuel mass flow supplied and exhaust energy fraction as discussed in the previous section. This type of phenomenological combustion modelling has often been applied in the literature with a reported good performance for either control, estimation or simulation purposes (see e.g. [49, 83]).

2.9.3 Combustion chamber heat transfer.

The heat loss due to forced convection and radiation between combustion matter and chamber is not negligible and may waste as much as 26% of the supplied thermal fuel energy in SI engines, [54], or 40% in DI Diesel engines. Hence, a good description of the heat transfer between combustion matter and combustion chamber during the compression and stroke is paramount for proper cyclic simulation of

the combustion process. Furthermore, the exhaust enthalpy loss, primarily due to the high turbulence level in the vicinity of the exhaust valve during cylinder purging, is also important in the description of the exhaust pipe enthalpy level. Exhaust gas temperature drops exceeding more than 400 K across the exhaust port for some SI engine scenarios with bad port insulation have been reported in the literature [83, 57]

In the calculation of the cylinder wall heat transfer it is customary in 0D/1D simulation studies to rely on spatially averaged (the temperature of the gaseous matter and surrounding wall of the given zone/chamber are assumed constant) empirical relationships. One commonly encountered model in the literature is the *Annand model* [83, 33] which utilizes Newton's law of cooling in description of the convective heat transfer and grey body modelling in the description of the heat transfer due to radiation. Hence, the Annand expression in its final form becomes

$$Q = A_{comb}\left(Nu\frac{k_{cond}}{x}\left(T_{gas} - T_{wall}\right) + \varepsilon\sigma\left(T_{gas}^4 - T_{wall}^4\right)\right) \tag{2.240}$$

where A_{comb} is the wetted surface area of the combustion chamber and thus a function of the piston position, x is a characteristic length normally chosen as the cylinder bore width, k_{cond} the conductivity of the combustion chamber material, and ε is the radiative emissivity. Normally the corresponding Nusselt number is computed as,

$$Nu = aRe^b = a\left(\frac{\rho u x}{\mu}\right)^b \tag{2.241}$$

with the characteristic velocity, u, often set to the mean piston velocity i.e.

$$u = \frac{L_{stroke}N}{30} \tag{2.242}$$

Although the above correlation does not take flow characteristics like swirl and tumble into consideration, good agreement with measurements using values of b between 0.7 and 0.85 is reported in the literature [33], while the parameters a and ε have to be identified from existing experimental data.

In the computation of the enthalpy loss in the exhaust port the same analogy, just presented, is used except for the Reynolds number computation [83]. Here one of the following Reynolds numbers is used.

$$Re = \frac{4\dot{m}}{\mu\pi D_v} \qquad \text{or} \qquad Re = \frac{\dot{m}D_{port}}{\mu A_{port}} \tag{2.243}$$

where D_v is the valve head diameter, D_{port} is the minimum port diameter, and A_{port} is the exit cross sectional area of the port.

2.10 Crank shaft

The crank shaft or engine speed N is an important variable in computation of the algebraic and differential equations comprising the different engine sub-models.

However, the level of detail or signal spectrum needed for appropriate transient modelling of the crank shaft's rotational speed is very task dependent.

In cycle based simulation studies a mechanical model of the drive line is necessary for a dynamical description of different powertrain components e.g. the individual combustion's influence on the crank dynamics. Such models of different detail level ranging for pure stiff mechanical analysis [109] to models incorporating the dynamical performance of the individual intake and exhaust valves [113] are readily available in the literature.

In MVEM based simulation and control studies the dynamic detailing level requirement is often much smaller. Hence, the crank shaft state equation is based on conservation of rotational energy using cycle mean values of the individual energy inputs and outputs of the system. Hence, the rate of change of the engine speed utilizing the definition outlined in section 2.9.1 is found as

$$\dot{N} = \left(\frac{30}{\pi}\right)^2 \frac{\dot{m}_f E_{HV} \eta_i - \frac{V_d N}{120}\text{FMEP} - P_{load}}{J_{eng} N} \tag{2.244}$$

where J_{eng} is the engine's moment of inertia. However simple, this type of model has shown good agreement with experimental data both during harsh transient and steady state engine operation (see e.g. [63, 49]).

2.11 VES and a simulation example

The main motivation behind the VES (Virtual Engine Simulation) C library for SIMULINK® is the development of a package containing different IC engine submodels for the automotive control engineer. The advantages of this over a direct implementation in SIMULINK® are the shorter simulation time and the improved flow control offered by S-functions. The first is obvious since a direct hard coded implementation in C generally has a lower number of required CPU operations than SIMULINK® only models. The latter since the structure of the model implementation is directly controllable within C; this is not generally the case with SIMULINK®. The downside of the coin is the lost graphical interpretation of the system; the model is no longer in block diagrammatic form.

The model background for VES is so far simply the C implemented version of the material previously presented in this chapter[30]. The idea, however, is that the library should be expandable with new user defined functions similar to libraries behind the KIVA CFD environment[31].

[30] Remark: Some of the models exist at the point of writing only in the SIMULINK® environment.

[31] The KIVA framework, a transient, three-dimensional, multi-phase, multi-component code for the analysis of chemically reacting flows with sprays has been developed at the Los Alamos National Laboratory. This CFD code provides a way to analyze the combustion quality of e.g. Diesel. More information may be obtained online at http://gnarly.lanl.gov/Kiva/Kiva.html

2.11.1 A simulation example

This section will give an example of the possibilities with the simplified engine submodels offered by VES. A simulation study using VES has already been conducted earlier in section 2.8.6 where the exhaust fluctuations' effect on the effectiveness level of EGR-cooler was investigated. However, the focus of the simulation to be presented will not be on the *instantaneous* behavior of an isolated engine component or subsystem but the *mean value* behavior of a full implementation of a DI Diesel engine according to the MVEM framework.

The model utilized in the engine simulation was originally the model of a prototype Ford V6 Diesel engine which has been used to study different control and estimation designs and drive-cycle performance at FFA (Ford Forschungszentrum, Aachen). A more detailed list of applications cannot be included for proprietary reasons.

The twin turbocharged V (Diesel) engine design has always been appealing for packaging reasons, and with the advances made in the turbocharging technology area in the recent years, this engine design is becoming more and more common in the engine selection for the upper middle class car to the luxury car. Examples of the commercially available passenger cars featuring this engine design are the 4.0 liter V8 BMW engine, the Mercedes 4.0 liter Diesel V8 in the S400 CDI, and the V6 and V10 Diesel engines manufactured by Volkswagen. All these engines use twin turbocharging to reached their individual performance targets. Hence, with the recent boom in the Diesel market and the reasonably large market for upper medium class and luxury cars, the turbocharged V engine will most likely become very popular in the near future. Modelling, estimation and control research in such engine designs is therefore naturally of interest.

The specifications for the V6 engine simulation model are briefly outlined in table 2.18.

It has earlier been shown that the mass flow through the EGR cooler, fitted on a DI Diesel engine, and its effectiveness cannot be well described (see section 2.8.6) by the MVEM framework; a description of the pumping fluctuations is required since the system is operated in an area with strong nonlinearities. However, to be able to describe the dynamic and steady state trends introduced by the EGR system a model of the EGR mass flow and the EGR temperature must be present. Thus, a fairly simple model is constructed by describing the EGR mass flow through the system by the isentropic nozzle equation utilizing the mean exhaust and the mean intake manifold pressure, and by fixing effectiveness level of the cooler to a reasonable value of 50% (see e.g. table 2.13).

The scope of the simulation study presented will be limited to a study of the V6 engine's response to a part of the EUDC (EUropean Drive Cycle). The reason for this is natural when considering that the V6 has seven inputs (brake load, two EGR valve positions, two VGT rack positions and two bank fuel injection inputs) and numerous outputs; The system space of interest is enormous. Thus, the workload required by a complete graphical documentation of possible excitation of the

Engine type	Diesel
Engine design	Bi-turbo equipped V6
Displacement	3.0 liter
Injection system	Direct Injection, Common Rail
Turbocharging	Twin VGT equipped turbo
Intercooled	Yes
Number of intercoolers	One
EGR-cooler	Yes
Number of EGR coolers	Two
Intake layout	Single plenum
Intake volume total	10 liter
Exhaust volume total	3 liter
Intercooler efficiency	70%
EGR-cooler efficiency	50%

Table 2.18: Specifications for the V6 engine. **Remark:** Some of the design parameters have been changed compared to the original model for propriety reasons.

system is immense and outside the scope for this dissertation.

The input commands to the engine are acquired from a data logging of the outputs of a 2.0 liter Puma Diesel engine ECU running a EUDC (e.g. see [108]). Hence, active control of the VGTs and EGR valves will not be investigated here. This would require an implementation and calibration of an ECU simulation model for the prototype engine and thus out of the scope for this dissertation. Needless to say, these command signals will not likely correspond to the control signals from the final calibrated ECU for the V6 engine, however, they do give a realistic picture of future control trajectories[32].

The drive cycle engine speed reference and the load torque have been scaled by a factor of 1.5 and 2, respectively, to insure a reasonable excitation of the engine. These inputs are also acquired from the experimental EUDC study conducted for the 2.0 liter Puma engine. The scaled speed reference and load torque trajectories are depicted in figure 2.68. The actual engine speed is during the simulation controlled by a simple anti-windup PI strategy.

The figures 2.69, 2.70 and 2.71 present some of the simulation results obtained. In the graphical presentation of the simulation results the following color–abscise notation has been utilized:

Abscise variable number	Color
1'st	Blue
2'nd	Green
3'rd	Red
4'th	Cyan

[32]Slight modifications of the trajectories were necessary to insure that the turbochargers did not overspeed at high engine speeds.

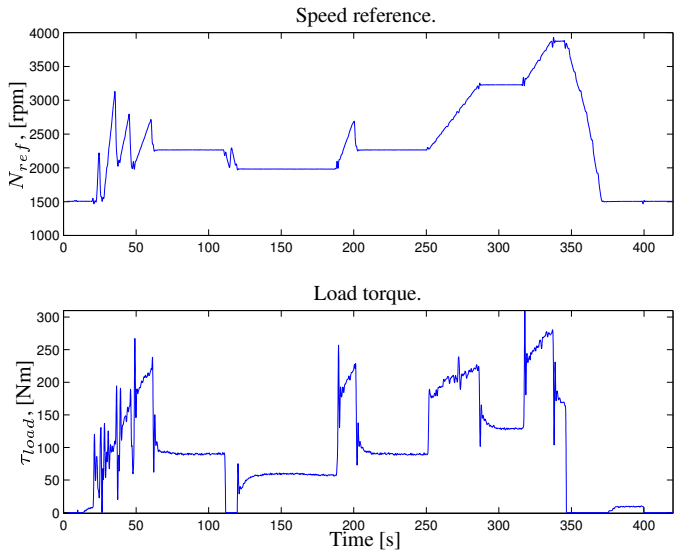

Figure 2.68: Speed reference and load torque trajectories utilized in the simulation study.

The variable notation has been defined earlier, however, an explanation of the all variables to be presented may also be found in the glossary starting at page 259. The figures clearly show that a large portion of the engine's speed-load map has been excited with the model exhibiting a reasonable behavior i.e.:

- The closing and opening of the VGTs lead to an increase and a decrease in the intake pressure, respectively.
- The closing and opening of the VGTs lead to an increase and a decrease in the exhaust pressure, respectively.
- The closing and opening of the EGR valves lead to an increase and decrease in the EGR rate, respectively.
- The closing and opening of the EGR valves lead to an increase and decrease in the exhaust pressure, respectively.
- The exhaust temperature goes up with load increases and λ decreases. The exhaust temperature goes down with load decreases and λ increases.
- The intake temperature is a weighted sum of the EGR temperature and the exit temperature of the intercooler.

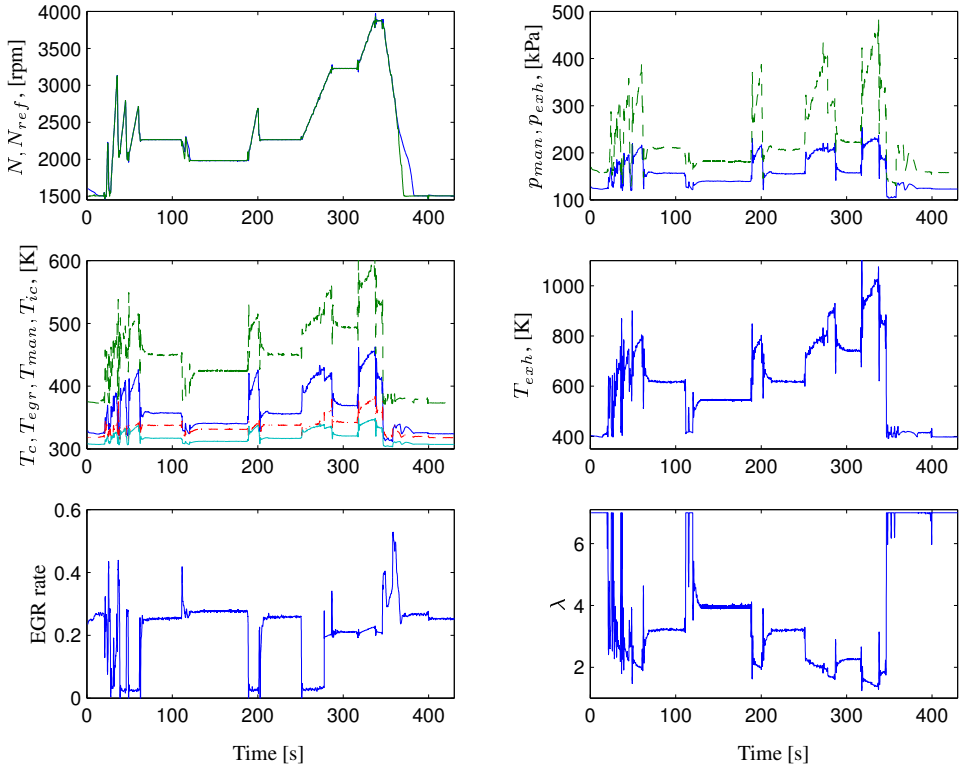

Figure 2.69: Simulation study of a twin turbocharged V6 Diesel engine. The upper left plot shows the relative fast accelerator tip-ins and tip-outs during the first 60 seconds of simulation. The corresponding fast responses of the intake- and exhaust temperatures and pressures are clear in the three surrounding plots. The displacement of the simulated V6 engine is larger than the original specification for the prototype. The compressors will therefore operate closer to the choke limit, the so called the stonewall, and the pressure drop across turbines increases due to the possible larger mass flow. The pressure difference between the exhaust- and the intake system is due to this turbocharger–engine mismatch thus larger than the pressure difference normally experienced with modern turbocharged Diesel engines. The λ level depicted in the lower right plot is in the high load part of the simulation (250 sec. to 340 sec.) lower than normally required due to the high amount of EGR applied. Normally, EGR is only utilized up to approximately 2500 rpm on a normal Diesel engine for light duty applications. The θ_{egr} control trajectory used (see figure 2.71) would most likely lead to immense soot emissions in reality.

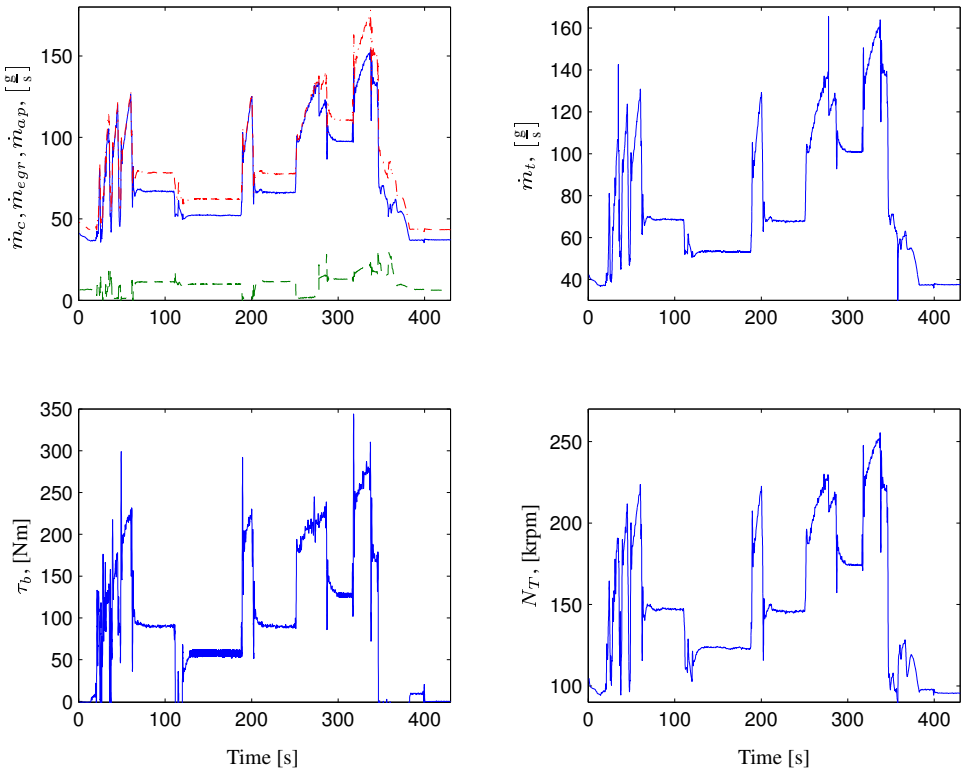

Figure 2.70: Simulation study of a twin turbocharged V6 Diesel engine – continued. **Remark:** The flows $\dot{m}_c$, $\dot{m}_{egr}$, $\dot{m}_{ap}$ and $\dot{m}_t$ are the flows through the individual components and not the total mass flows. The upper left plot shows that the compressor mass flow (blue line) responds very promptly to changes in the accelerator, the VGT and the EGR position. The mass flow through the individual turbines ($\dot{m}_t \approx \dot{m}_{ap} + \dot{m}_f - \dot{m}_{egr}$) is even more sensitive to fast EGR valve VGT vane position actuation due to the much smaller exhaust manifold volume. This is especially noticed between 270 to 300 seconds of simulation where the VGT- and the EGR position are changed fast one and two times, respectively. This fast excitation of the actuators leads to relatively large excursions in $\dot{m}_t$. Furthermore, the turbocharger speed responds faster to changes than the engine speed. This is clear from the steps in the N_T curve followed a slope nearly matching the engine speed slope. Finally, the produced engine brake torque is depicted in the lowest left plot.

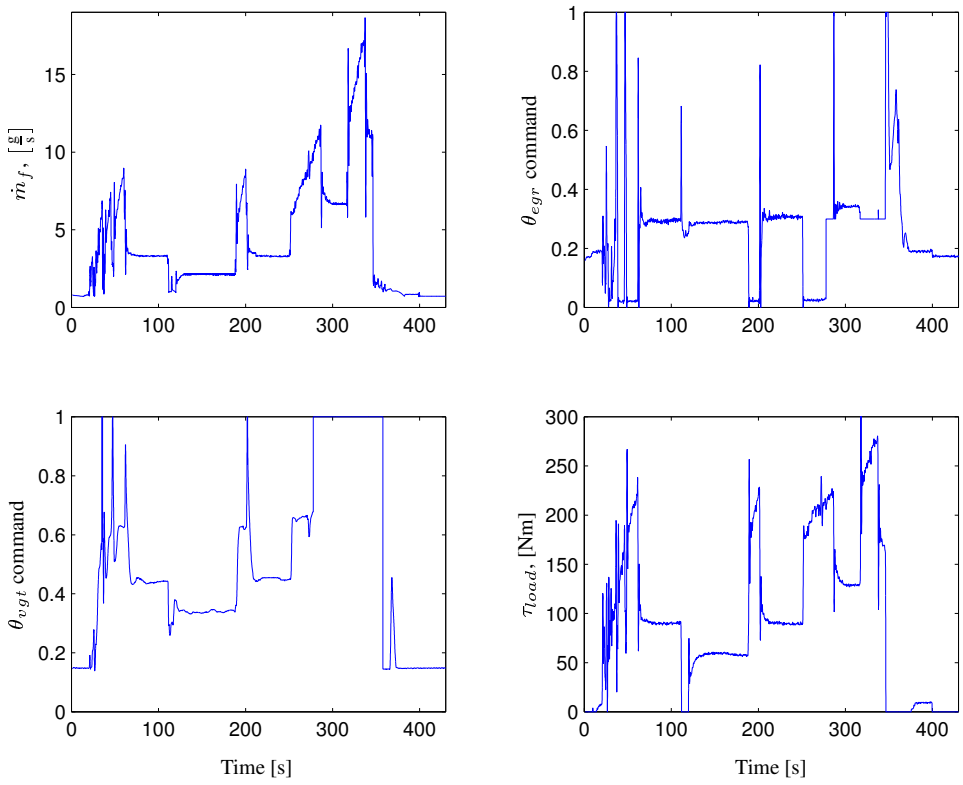

Figure 2.71: Simulation study of a twin turbocharged V6 Diesel engine – continued 2. The upper left plot shows the fuel command generated by the fuel controller. The modification of the original EGR and VGT control trajectories is noticed between 280 and 350 seconds of simulation. Here, the VGTs were required to be opened fully and the minimum EGR valve position was set to 0.3 to avoid turbochargers from over-speeding.

The simulation results presented confirm the driving philosophy behind the MVEM framework: The ability to describe the response trends of IC engines by an interconnection of compact physically based engine sub-models. Although the V6 MVEM has been augmented by several new sub-models or revised sub-models compared to earlier work published by the ECG to capture the picture of the fundamental dynamics governing the V6 engine, it is still in a very compact form and is thus suitable for engine estimation and control design. Hence, the simulation results presented here support the statements made earlier by *E. Hendricks and S. C. Sorenson* in [49] and *J. P. Jensen et al* in [63] that MVEM modelling is a valuable tool in the development of engine control strategies.

2.12 Summary, remarks and conclusions

The chapter has dealt with the development or presentation of simple comprehensive engine sub-models. First, the commonly found radial turbocharger has been divided in three separate models; an algebraic compressor model, an algebraic variable geometry turbine model and a first order dynamic model of the turbocharger wheel velocity. In the compressor model the mass flow and enthalpy losses are treated simultaneously, whereas the VGT mass flow and efficiency are separated into two independent models. All models show a reasonably good modelling accuracy even in regions necessitating extrapolation from mapped data.

Next, a dynamic model of heat exchangers capable of describing the trends in unsteady flow scenarios is presented. Based on this model, it is concluded that accurate estimation of the burnt mass flow or energy flow into the intake manifold is badly posed when EGR back flow exists due to the mixing with intake manifold matter because of the pressure fluctuations.

Furthermore, the TDMVEM (Turbo Diesel Mean Value Engine Model), an extension to the MVEM framework, has also been presented in the section. This model is derived by utilizing a simplified model of the gaseous mass contained in the intercooler and a soft assumption on the intake throat mass flow. Hence, the heat exchanger is included in the normal filling-emptying picture of the intake dynamics earlier utilized in other MVEM applications (e.g. see [63, 49]).

Phenomenological combustion models are presented together with the introduction of a new way of creating different maps for zero dimensional energy conservation based combustion models utilizing the LWLS algorithm. Selected combustion process related maps have been identified for a 2.0 liter turbocharged DI Diesel engine. These maps are presented together with steady state dynamometer data.

The three models described above are implemented in an object oriented C library, VES, together with templates of FE volume models, butterfly and poppet valve models and crankshaft models. This makes it possible to rapidly create SIMULINK® models of SI or CI engines independently of the engine air path design.

The modelling framework presented is at the present time implemented in stand alone engine simulation tools, which have aided in control, estimation and emission strategies, and power-train performance research and development studies at FFA. A more detailed presentation of such applications and the corresponding results obtained cannot be given in this dissertation for confidentiality reasons.

Comments to the fuel film dynamics.
The careful reader has probably noticed a missing modelling section: fuel film dynamics modelling for MPI equipped SI engines, a step deliberately taken after many hours of work unsuccessfully trying to describe engine measurement traces by the simple X-τ models (e.g. see [10]). Although the simplified X-τ models presented in the literature by Hendricks (see e.g [52]) and Aquino (see e.g [12]) clearly could provide some compensation of the fuel film dynamics experienced in CFI (Central Fuel Injection) equipped SI engines, due to the large manifold wall area exposed to the fuel film, they are clearly giving problems when used with MPI systems. It will here be argued that the fuel rail pressure regulation system's dynamics is of higher or at least just as high importance as the fuel film dynamics.

The fuel mass flow leaving the MPI injectors may within good accuracy be modelled by a simple Bernoulli relation (this assumption is even reasonably valid for modern Diesel injectors where a pressure more than hundred times larger than the rail pressure in a typical MPI system is utilized; see e.g. [8]) .i.e.

$$\dot{m}_{f,inj} = A_{noz}\sqrt{2\rho_f \Delta p} = A_{noz}\sqrt{2\rho_f \left(p_{rail} - p_{man}\right)} \tag{2.245}$$

where A_{noz} is the sectional area of the injector outlet, and p_{rail} is the rail pressure. Since the rail pressure in MPI systems is relative low ($\approx 2.5 - 3.5$ bar, absolute) the injected fuel mass is greatly influenced by variations in the average intake manifold pressure. Normally, the pressure drop across the injectors, Δp, is maintained constant by controlling the rail pressure. This is customarily accomplished by a mechanically controlled pressure regulator fitted to the fuel rail system. The mechanically controlled system is basically two control volumes separated by a diaphragm. The pressure of one control volume is controlled by the intake manifold pressure, whereas the pressure on the other side is developed by the fuel supply system. A small mass-spring-damper system (a combination of a control ball and a retainer) is fitted to the diaphragm controlling the pressure loss across the fuel exit valve. A schematic diagram of a sectioned pressure regulator for MPI systems may be found in [67].

Hence, the valve system is basically a coupling of two mass-spring-damper systems and is of fourth order. However, since the control ball–retainer system is significantly smaller than the diaphragm system its bandwidth is likely to be noticeable larger than the diaphragm system's bandwidth. For this reason, a reasonable approximation is to assume that the pressure drop across the injectors is controlled by the diaphragm system and the fuel pressure pulsations are attenuated by the control valve–retainer system. Thus, the system of interest in the modelling of the

signal transfer between the intake manifold pressure and the fuel rail pressure is the diaphragm system with the control ball attaining a fixed position (working like a normal needle valve). Hence, the dynamics of the control ball–retainer will be neglected and referred to as a needle in the following.

A change in the averaged intake manifold pressure leads to a movement of the diaphragm. The diaphragm is physically connected to a spring and the valve needle itself, thus the equilibrium position of the diaphragm or needle is

$$\Delta p A_{mem} = k\left(x - x_0\right) \tag{2.246}$$

where k is the spring constant of the diaphragm-spring combination, x the needle position, A_{mem} the diaphragm area, and x_0 is the needle position for $\Delta p = 0$. The diaphragm and spring system can at best be classified as a mass-spring-damper system i.e. a dynamic system of second order. Now suppose the bandwidth of this system is comparable to the frequency of the engine pumping. In such a scenario the needle position would basically follow a sine curve with a frequency dictated by the engine speed, thus leading to very poor control of the fuel mass flow. If, on the other hand, the bandwidth of the pressure regulator is well below the engine pumping frequency a good control of the steady state fuel mass flow can be achieved. However, the response time of the intake manifold pressure, during engine idling or part load operation scenarios, is generally in the vicinity of the first engine pumping harmonic's period. Hence during harsh throttle tip-ins or tip-outs large deviations in the desired pressure drop across the injectors may be expected, thus lead to significant deviations away from the desired fuel mass flow. This problem is not present with the CFI system due to the injector's location upstream of the throttle plate. Finally, it should be stated here that this scenario is only speculation and not confirmed yet by experiments made by the author. However, *R. P. Izydorek and G. C. Oberheide* have in [93] included experimental results showing that the settling time of the rail pressure is more than **12 times** longer than the settling time of the intake manifold pressure after a step in the throttle plate position leading to an increase of 50 kPa in the intake pressure. In addition to this, fuel rail pressure variations up to 91 kPa still exist in the fuel rail after the intake pressure has settled. Using the Bernoulli flow model mentioned earlier and a settled rail pressure of 380 kPa this is equivalent to a relative error in the mass flow injection between -7% and 9%, and an absolute error in λ of 7% to -8%! Furthermore, the time response of the fuel rail pressure resembles that of a second order system to a high degree, thus supporting the second order (linear) system approximation of the intake pressure–fuel rail pressure signal path discussed earlier.

The use of the X-τ model with MPI systems, in either of its two forms (see [52] and [12]), itself is heavily attacked in [31]. The fuel film fraction, X, is according to [31] very close to 1, and almost all of the injected fuel enters the combustion chamber in liquid form. Hence, in accordance with the pressure rail dynamic issues presented previously, a fuel film compensator implemented according to either [52] and [12] will most likely rather compensate for some of the fuel rail dynamics than the fuel film dynamics itself.

2.13 Appendix

The use of EGR as a means to lower the NO_X production of the IC engine is today a well establish technology with more than 30 years of reported experimental and theoretical results in the literature. During this time areas like promoted engine wear due to EGR, engine efficiency influences due to EGR, NO_X emissions reduction capabilities with EGR on CI and SI engines etc. have been and are still investigated. However, dynamic model based control of the EGR is today still in its infancy which is interestingly enough since tight control of EGR is of paramount importance in modern DI engines if the emissions legislation is to be met.

The problem of including EGR in the MVEM framework has been attacked earlier in section 2.8.3 leading to the formulation of the TDMVEM. However, the development of the this model is heavily inspired by the work already existing in the literature. The first MVEM based attempt to describe the dynamic behavior of a NA SI engine equipped with an EGR system reported to the SAE community is to the author's knowledge presented by *Weeks, R. W. et al* in [95]. The pressure state equation presented in this work does include a derivative temperature dependency. The final SIMULINK® model presented does, however, not respect the difference in the internal energy between the EGR flow and the intake air flow, and the intake temperature is fixed to a constant value. This temperature difference may however be significantly and thereby offset the intake manifold temperature considerably compared to the ambient temperature. Hence, in order to improve the transient and steady state estimation capabilities of the MVEM when the EGR system is activated the MVEM was first reworked in [83] and later in [37]. The research carried out in [83] and [37] was in 1999 presented at the annual SAE conference in Detroit in the SAE-paper number 1999-01-0909. The paper was entitled *Mean Value Engine Modeling of an SI engine with EGR*. This article presents the theoretical work behind the new MVEM extension – the AMVEM. The good estimation (observer) properties of this simplified engine model were later confirmed by *Professor E. Hendricks* through an experimental study conducted on a NA SI engine retrofitted with an EGR system. The experimental study was conducted at DTU and some of the experimental results made during this study are included in the SAE-paper number 1999-01-0909, [75]. Furthermore, the article provides a good introduction to and a preliminary study of the EGR estimation and/or control problem. Hence, the paper is included here for the sake of completeness.

1999-01-0909

Mean Value Engine Modelling of an SI Engine with EGR

Michael Fons
Maersk Oil and Gas A/S

Martin Muller
Delphi Automotive Systems

Alain Chevalier
Ford Motor Co.

Christian Vigild, Elbert Hendricks and Spencer C. Sorenson
Technical University of Denmark

ABSTRACT

Mean Value Engine Models (MVEMs) are simplified, dynamic engine models which are physically based. Such models are useful for control studies, for engine control system analysis and for model based engine control systems. Very few published MVEMs have included the effects of Exhaust Gas Recirculation (EGR). The purpose of this paper is to present a modified MVEM which includes EGR in a physical way. It has been tested using newly developed, very fast manifold pressure, manifold temperature, port and EGR mass flow sensors. Reasonable agreement has been obtained on an experiemental engine, mounted on a dynamometer.

1. INTRODUCTION

It is clear that Exhaust Gas Recirculation (EGR) is a vital component of modern engine control systems. It is only with the use of this technology that it is possible to reduce the NO_x component of SI engine exhausts to acceptable levels given current legislation. EGR also provides a method to reduce exhaust temperature and thus prevent Three Way Catalyst (TWC) damage.

At the current time the only EGR control strategy which has been described in detail in the literature is based on static relationships depending on stationary engine mapping [1]. It is however by now well known that in order to do accurate air/fuel ratio control, dynamic engine models are necessary for the design of engine control systems, for model and/or observer based control [2], [3]. Thus a dynamic engine model has to be constructed which includes EGR and which is of the Mean Value Engine Model (MVEM) type. Currently only such models have a simplicity and accuracy which allows them to be coded into engine control microprocessors.

This paper is a preliminary study of the possibility of constructing such a model using conventional physical principles. Unfortunately EGR systems are somewhat more complex than purely naturally aspirated Spark Ignition (SI) engines because of the heat of the exhaust gases. It is however the essence of modelling on the MVEM level to isolate the dominant physical effect or effects in any engine subsystem, not to describe all of the details of engine operation. This paper is aimed at this goal.

2. ISOTHERMAL MVEM DEVELOPED EARLIER

In work which has been published earlier, a model for the intake manifold filling dynamics has been derived and validated in a number of different experiments [2] and applications [3], including some production ones: [4], [5], [6]. This model is obtained by differentiating the ideal gas law applied to the mass of air in the intake manifold:

$$p_i = \frac{R\,T_i}{V_i}\; m_i \quad . \tag{1}$$

Assuming that

$$\dot{m}_i = -\dot{m}_{ap}(n, p_i) + \dot{m}_{at}(\alpha, p_i) \quad , \tag{2}$$

this yields with the differentiation of equation (1) the most simple manifold pressure state equation

$$\dot{p}_i = \frac{R}{V_i}\left(\dot{m}_i T_i + m_i \dot{T}_i\right) = \frac{R T_i}{V_i}\left(-\dot{m}_{at} + \dot{m}_{ap}\right) \quad , \tag{3}$$

where the last equation on the right is obtained by assuming that the intake manifold temperature is constant. This is thus an isothermal MVEM. The port and throttle air mass flows are given by the expressions

$$\dot{m}_{ap}(n,\ p_i\ ) = \frac{V_d}{120\ R\ T_i}\ (\ e_v \cdot\ p_i\ )\ n, \qquad (4)$$

and

$$\dot{m}_{at}(\alpha,\ p_i\ ) = m_{at}1\ \frac{p_a}{\sqrt{T_a}}\ \beta_1(\alpha)\ \beta_2(p_r\ ) + m_{at0}\ ,$$

where

$$\beta_1(\alpha) = 1 - \alpha_1\cos(\alpha) + \alpha_2\cos^2(\alpha)$$

$$p_r = \frac{p_i}{p_a} \qquad (5)$$

$$\beta_2(p_r) = \begin{cases} \frac{1}{p_n}\sqrt{p_r^{p_1} - p_r^{p_2}}, & \text{if } p_r \geq p_c \\ 1, & \text{if } p_r < p_c \end{cases}$$

and m_{at0}, m_{at1}, α_1, α_2, p_1, p_2, p_n, p_c are constants.

3. ADIABATIC MVEM INCLUDING EGR

In an SI engine which is not equipped with EGR it has been shown that the simple state equation on the right in equation (3) is sufficiently accurate to describe the dynamics of the intake manifold. This however cannot obtain in an engine which has EGR because then the intake manifold temperature cannot even approximately be assumed to be constant. The presence of EGR thus makes it imperative to consider the energy balance in the intake manifold. Neglecting heat exchange, this leads to the next higher order MVEM model of the intake manifold filling dynamnics: an adiabatic model.

When EGR is taken into account mass conservation requires that

$$\dot{m}_i = \dot{m}_{at} + \dot{m}_{EGR} - \dot{m}_{ap}\ . \qquad (6)$$

Using energy conservation this leads to the equation

$$\dot{m}_{at} \cdot\ h_a + \dot{m}_{EGR} \cdot\ h_{EGR} - \dot{m}_{ap} \cdot\ h_i$$

$$= \frac{d(m \cdot\ u)}{dt} = \dot{m}_i\ c_v\ T_i + m_i\ c_v\ \dot{T}_i \qquad (7)$$

As the enthalpy can be expressed as $h_x = T_x\ R\kappa\ /\ (\kappa - 1)$, equation (7) can be written as the differential equation

$$\dot{T}_i = \frac{\dot{m}_a T_a R\kappa}{(\kappa-1)\, m_i c_v} + \frac{\dot{m}_{EGR} T_{EGR} R\kappa}{(\kappa-1)\, m_i c_v}$$

$$- \frac{\dot{m}_{ap}\ T_i\ R\kappa}{(\kappa\ -\ 1)\ m_i\ c_v} - \frac{\dot{m}_i\ T_i}{m_i} \qquad (8)$$

where $\kappa = c_p\ /c_v$. Using the ideal gas law, equation (1) for m_i and the fact that $c_v = R\ /\ (\kappa\ -\ 1)$, this equation can be further reduced to

$$\dot{T}_i = \frac{\dot{m}_{at}\ T_a\ R\kappa\ T_i}{p_i\ V_i} + \frac{\dot{m}_{EGR}\ T_{EGR}\ R\kappa\ T_i}{p_i\ V_i}$$

$$- \frac{\dot{m}_{ap}\ T_i^2\ R\kappa}{p_i V_i} - \frac{\dot{m}_i\ T_i^2\ R}{p_i\ V_i} \qquad (9)$$

Applying mass conservation from equation (6) finally leads to the expression:

$$\dot{T}_i = \frac{RT_i}{p_i V_i}\Big[- \dot{m}_{ap}(\kappa - 1) T_i$$

$$- \dot{m}_{at}\left(\kappa T_a - T_i\right) + \dot{m}_{EGR}\left(\kappa T_{EGR} - T_i\right)\Big] \qquad (10)$$

Using equation (3) this means that the manifold pressure state equation becomes

$$\dot{p}_i = \frac{R}{V_i}\left(\dot{m}_i T_i + m_i \dot{T}_i\right)$$

$$= \frac{\kappa R}{V_i}\left(-\dot{m}_{ap} T_i + \dot{m}_{at} T_a + \dot{m}_{EGR} T_{EGR}\right) \qquad (11)$$

Together equations (10) and (11) are the adiabatic MVEM which includes EGR. An assumption which is implicit in their use is that there is perfect mixing of the fresh air flow and the EGR flow.

In the limit when the EGR flow is zero, equations (3) and (10) and (11) give exactly the same solution as should be expected. However during rapid transients, equation (10) gives a differentiating effect, leading to a temperature spike in its response. This is due to adiabatic compression or expansion, depending on whether the throttle is being opened or closed. This leads in turn to an increase or decrease of the air density in the intake manifold, resulting in different port air mass flows than those predicted by equation (3) during transitions. The error involved can be significant during such transients [3], [7].

In order to use the adiabatic MVEM it is necessary to specify the EGR mass flow and temperature. To find these quantities without using direct measurements is not straight forward and does require the use of some empirism because of the wide range of the physical effects which determine them. Using one of the devices currently available for EGR mass flow control it is possible to solve the EGR mass flow determination problem using feedforward and calibration techniques. Finding the EGR temperature is somewhat more difficult and will not be treated here.

3.1 EGR MASS FLOW DETERMINATION – A device which is currently available of EGR control is the Delphi Linear Exhaust Recirculation Valve [8]. In use, this valve

is driven with a Pulse Width Modulated (PWM) signal, the duty cycle or mark/space ratio (MSR) of which determines the valve mass flow. In reality this flow also depends on the pressure difference across the sensor as well as the duty cycle of the impressed PWM signal. However calibration curves are provided for the valve which give the mass flow as a function of PWM duty cycle with the impressed pressure difference as a parameter. The valve is also provided with a potentiometer which makes it possible to sense the intantaneous valve position. Using a feedback loop and microprocessor control the nonlinear valve flow characteristics can be linearized so that the valve flow can be made a linear function of the PWM duty cycle.

For the work to be related here, the EGR flow control was established in a different way than recommend by the manufacturer. This was necessary because it was desired to verify equations (10) and (11) as written and the EGR temperature could be measured directly. Study of the EGR valve flow characteristics in [8] revealed that they could be fitted with good accuracy by the expression

$$\dot{m}_{EGR}(D_c\ ,\ \Delta p) \;=\; a(\Delta p)\,\frac{1}{2}\left[\;\tanh\left(\frac{D_c\ -\ D_{cm}}{\tau_{dc}}\right)+\ 1\right], \qquad (12a)$$

where

$$a(\Delta p) \;=\; \dot{m}_{EGR}(max)\left(\ 1\ -\ e^{-\frac{\Delta p}{\tau_{\Delta p}}}\ \right),$$

D_c is the mark/space ratio (MSR) of the PWM drive signal, Δp (bar) is the pressure drop across the EGR valve (effectively across the engine from the exhaust to the intake manifold), D_{cm} is the common PWM MSR center value for all pressure ratios (0.6), τ_{dc} is the effective relaxation MSR of the PWM control signal (0.273), $\dot{m}_{EGR}(max)$ is the maximum amplitude of the

EGR mass flow at a given pressure differential (11 g/sec) and $\tau_{\Delta p}$ is the effective relaxation pressure for the valve (0.12 bar). The values of the constants given in the parentheses above are for the Delphi LEGR valve type 10 G/S. Equation (12a) was found to represent the valve characteristics accurately for MSR of between 0.1 and 0.9 and pressure differences of 0.15 to 0.7 bar.

Equation (12a) has the fortunate property that it can be inverted analytically to obtain

$$D_c \;=\; \frac{1}{\tau_{dc}}\ \tanh^{-1}\left(\ 2\,\frac{\dot{m}_{EGR}}{a(\Delta p)}\ -\ 1\ \right)\ +\ D_{cm}\,. \qquad (12)$$

Thus when the desired EGR mass flow is given, and Δp is known, equation (12) gives the required PWM drive signal duty cycle which must be applied to the EGR valve. This simplifies EGR control significantly as the EGR mass flow can be controlled directly with good accuracy at any given operating point.

In order for equation (12) to be valid the EGR valve must be driven with a PWM signal with an amplitude of 13.5 V at the recommended carrier frequency of 128 Hz at an ambient temperature of 25 C. While there is some leakage as indicated in equation (12), it can be taken into account as required. In spite of its specified time constant (< 1.25 sec), the actual response time of the LEGR valve is on the order of 25 msec (opening) and 50 msec (closing) for the recommended PWM carrier frequency of 128 Hz. This is sufficently fast for all practical applications.

To determine the pressure difference across the valve, some theoretical results can be derived from earlier published work. In the paper [2] it was shown that the normalized air charge/stroke of an SI engine can be written as

$$\begin{aligned} m_i' \;&=\; e_v\cdot p_i \;=\; s_i(n)\,p_i\ -\ y_i(n) \\ &=\; s_i(n)\,p_i\ -\ \sigma(\Delta T)\,\frac{p_e}{\kappa(r-1)}\quad , \end{aligned} \qquad (13)$$

where $s_i(n)$, $y_i(n)$ and $\sigma(\Delta T\ )$ are approximately constant. This expression was derived theoretically and shown to be valid for a number of engines. It has also been used by other workers in production engine control strategies [5].

In order to find the pressure drop across and engine, equation (13) can be solved for p_i and the result subtracted from p_e:

$$\begin{aligned} \Delta p \;&=\; p_e\ -\ p_i \\ &=\; -\,\frac{1}{s_i(n)}\,m_i'\ +\ p_e\left(1\ -\ \frac{\sigma(\Delta T)}{s_i(n)\,\kappa(r-1)}\right)\,. \\ &=\; -\,s_e(n)\,m_i'\ +\ y_e(n) \end{aligned} \qquad (14)$$

This expression shows that the pressure drop across an engine is proportional to the normalized air charge per stroke $m_{i'} = e_v \cdot p_i$. As the normalized air charge per stroke is proportional to the actual air charge per stroke (equation (4)), equation (14) provides a simple way to determine Δp in an engine controller. The accuracy of this determination will be of the same order as that which is possible for the air charge calculation itself. That is the standard deviation of error in calculating Δp for the data is on the order of 1 - 2% over the operating range of the engine.

The simple general form of equation (14) is what makes it useful. In general, the y intercept of the curve is a little greater than 1 and is basically constant for all crank shaft speeds since κ = 1.4 and r $\geq$ 9 for most modern engines. The slope of the curves at constant crank shaft speeds is the reciprocal of the slope of the curve in (13).

Using the same numbers which were used in [2], $\Delta T = 15C$, $T_i = 300C$, $r = 10$, $\kappa = 1.4$, $p_e = 1.05$ bar and $\iota = 0.9$, it is possible to find the approximate numbers $s_e = 1.050$ and $y_e = 0.952$. Thus for this "standard" engine example one finds equation (14) to be

$$\Delta p = p_e - p_i = -1.050 \cdot m_{i'} + 0.952 . \quad (15)$$

That engines do display the dependence predicted by equation (14) can be shown using data from the five engines considered in [2]. Figures 1a - 1c are plots of the differential engine pressure vs the normalized air charge for three of the engines from this paper. The basic validity of the functional form of equation (14) is thus confirmed.

Mean values for the parameters of the engines in [2] are given in table 1 below. This table shows that the predicted slopes and y intercepts agree fairly well with those of the actual engines. Obviously some of the inaccuracy in the table is due to the approximate way in which the parameters have been determined. Only the mean slopes are given, the crank shaft speed dependence being ignored, as it is weak.

Table I. Approximate mean values of the parameters in equation (14) for the set of engines treated in [2]. Notice that the values displayed have been obtained in part graphically from figures 1a - 1c.

parameters	s_e	y_e
1.1 L Ford (1.)	1.026	0.925
1.1 L Ford (2.)	1.000	0.910
1.8 L 4v/cyl (< 4000 rpm)	1.080	0.920
4.9 L Ford	0.880	0.905
1275 cc BL	1.000	0.900

It has to be remembered that equation (14) is generally valid for engines but because of details intake and exhaust manifold configuration, it will in most cases require some detailed engine mapping. Equation (14) suggests however that this mapping will not be very difficult because of the simple form of the equation, except at very low and very high air mass flows. At these extremes the curve will bend upwards due to heating.

On the other hand that the engine output power is dependent on the actual fresh air charge per stroke and not on the EGR air mass flow. This means that the actual fresh air mass flow,

$$\dot{m}_{apf} = \dot{m}_{ap} - \dot{m}_{EGR} , \quad (16)$$

(where f refers to the fresh charge) is what determines the fuel which is injected into the engine while Δp is found from

$$\Delta p(n, m_{ap}') = -s_e(n)\, m_{ap}' + y_e(n) , \quad (17)$$

and

$$m_{ap}' = \frac{120 R T_i}{V_d n} \dot{m}_{ap} . \quad (18)$$

The port air mass flow, $\dot{m}_{ap}$, has to be measured or estimated. If estimation is to be used then this can take several different forms, depending on the air mass flow related sensor type used [2], [4], [5], [6], [9].

Once the differential pressure is known, it is possible to use this information together with the documentation for the Delphi EGR valve to determine the EGR mass flow. If other valves are to be used a similar approach can be taken.

4. EXPERIMENTAL RESULTS

In order to test the adiabatic MVEM above experiments were conducted with a modified 1275 cc British Leyland engine. This engine was equipped with a specially designed 7 port head [10] which made it into a crossflow engine. The intake and exhaust valves were of Cooper S dimensions. It was provided with port fuel injectors and could work either in an EFI or SEFI mode, requiring only software changes. The intake manifold volume was about 3 times the engine displacement volume. Very fast pressure, port air mass flow and temperature sensors were installed in the intake manifold and the throttle air mass flow was measured with a laminar flow meter. These sensors are all significantly fast to resolve all of the transients which might be applied to the engine down to an event level (see Appendix).

To control the engine, log data and carry out simulations a specially developed Engine Control Development System (ECDS) was used together with 12 bit A/D and D/A cards in a Pentium PC. This software was also used to linearize the Delphi 18 g/s LEGP Valve which was installed for EGR control. The ECDS system is very fast and allows sampling times down to 0.25 msec. Sampling times used for the experiments to be reviewed were 0.25 - 1 msec.

Tests were carried out over the entire operating range of the engine but only a few of these will be reviewed here. The main question is if the model of equations (10) and (11) show the correct behavior for common EGR feed levels. Figure 2 shows a sample of results obtained at a typical operating point, both with and without EGR.

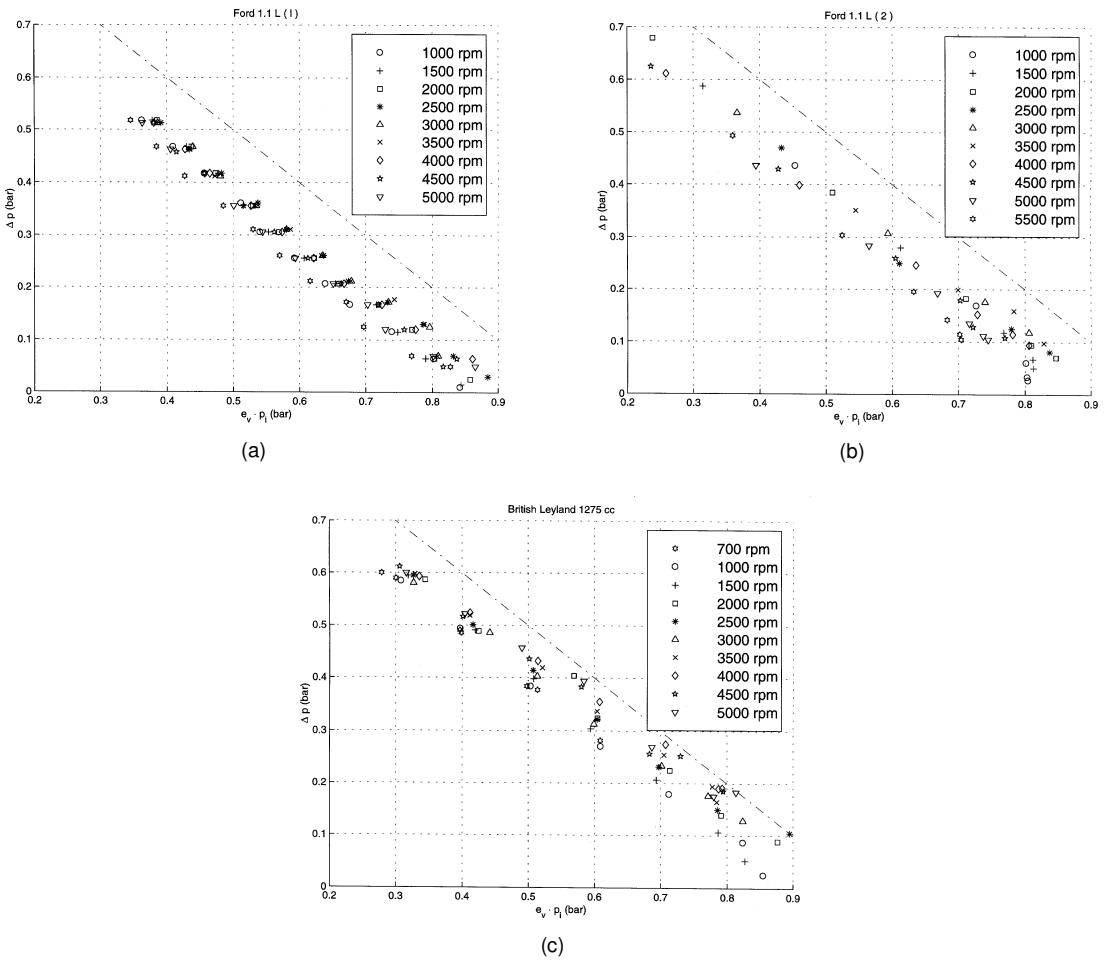

Figure 1. Figures 1a - 1c. Above and to the right. These figures show the differential engine pressure plotted as a function of the normalized air charge per stroke for three engines treated earlier in [2]. The two Ford 1.1 L engines are different engines ((1) and (2)) and were measured at different times by different groups. The 1275 cc BL (British Leyland) engine is the experimental engine used in this paper.

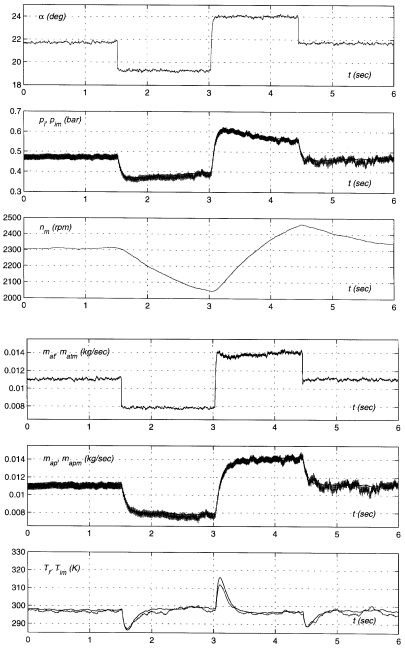

(a)

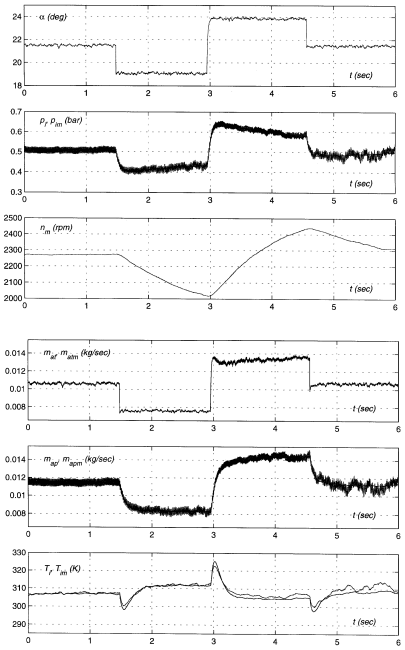

(b)

Figure 2. Figure 2a (without EGR: left and above) and figure 2b (with EGR: left and below) at approximately the same operating point. The EGR mass flow is about 10% of the fresh mixture flow and the EGR gas temperature is about 448 K. Measurements are shaded and model simulations are solid black lines.

Figures 2a and 2b show the response of the engine with and without EGR at a low part load operating point. In figure 2a there is no EGR and in figure 2b the EGR mass flow is about 10% of the fresh air mass flow: the EGR temperature is about 448 K. Measurements are shown shaded while parallel simulations with the model of equations (10) and (11) are single lines. Engine pumping fluctuations are apparent in the intake manifold pressure and the fast throttle transients are somewhat smoothed by manifold filling. The throttle air mass flow shows the expected filling spike and the total port air mass flow shows the effect of engine pumping. The port air mass flow is obtained by event averaging and summing the 4 intake port air mass flow measurements. At the rapid throttle transitions the manifold temperature increases or decreases significantly: this is an effect of the new MVEM temperature equation. It can be seen that the intake manifold temperature measurements do not quite come up to the model predictions. It is thought that this is the result of heat transfer in the intake manifold to the surroundings in the engine.

Figure 2b shows what happens when the EGR is applied to the engine at nearly the same operating point as in figure 2a. The manifold pressure increases but at the same time the crank shaft speed decreases significantly. Air mass flow to the engine via the throttle body decreases at the same time, while the port air mass flow increases. The intake manifold temperature increases due to the effect of the EGR gas heat and the same rapid temperature spikes as before occur but this time with a somewhat larger amplitude.

The overall accuracy displayed in figure 2 is reasonably good but the temperature predicitons are in all cases a little too low. This suggests that there is some heat transfer which takes place which is not in the model.

5. CONCLUSIONS

A dynamic adiabatic model has been constructed for the intake manifold with EGR using physical considerations. It has been found that this model is closely related to the isothermal MVEM investigated earlier and is a natural extention of it. The main difference between the isothermal and adiabatic models is the presence of a large temperature spike during rapid throttle plate movements. The accuracy displayed by the model is sufficient for most practical control purposes.

As a secondary result, a useful expression for the pressure difference between the intake manifold has been derived which is simple and relatively accurate. This expression makes it possible to predict the performance of the EGR valve without extra measurements.

Clearly the results which have been presented are preliminary but the overall accuracy displayed is encouraging and suggests that it may soon be possible to include EGR in model based control systems in a convenient and simple manner. This is currently a subject for continuing research.

6. ACKNOWLEDGEMENTS

The authors wish to acknowledge the professional assistance of Joe Asik, Dave Trumpy and Mike O'Sullivan of Ford Motor Co. in early stages of this work. They also wish to thank Jim Waters of Delphi Automotive Systems for his help in obtaining the Delphi EGR valves used in this paper.

7. REFERENCES

1. Azzoni, P., Minelli, G., Moro, D., and Serra, G., "A Model for EGR Mass Flow Rate Estimation", SAE Technical Paper No. 970030, 1997.
2. Hendricks, E., Chevalier, A., Jensen, M., Sorenson, S. C., Trumpy, D., and Asik, J., "Modelling of the Intake Manifold Filling Dynamics", SAE Technical Paper No. 960037, 1996.
3. Müller, M., Hendricks, E., and Sorenson, S. C., "Mean Value Modelling of Turbocharged Spark Ignition Engines", SAE Technical Paper No. 980784, 1998.
4. Hendricks, E., Vesterholm, and Sorenson, S. C., "Nonlinear Closed Loop, SI Engine Control Observers", SAE Technical Paper No. 920237, 1992.
5. Gerhardt, J., Benninger, N., and Hess, W., "Torque-Based System Structure of an Electronic Engine Management System as a New Base for Drive Train Systems (Bosch ME7 System)", 6. Aachener Kolloqium, Fahrzeug- und Motorentechnik, Aachen, Germany, 20.-22. October, 1997.
6. Maloney, P., and Olin, P., "Pneumatic and Thermal State Estimators for Production Engine Control and Diagnostics", SAE Technical Paper No. 980517, 1998.
7. Føns, M., Indførelse af Recirkulering af Udstødningsgas (EGR) i SI-Motorer (Implementation of EGR on an SI Engine, In Danish), Masters Thesis, Institute for Automation, Laboratory for Energetics, Report No. IAU97E09, Technical University of Denmark, September, 1998.
8. Lyko, B. M., Application Manual for the Linear Exhaust Gas Recirculation Valve, Delphi Energy and Engine Management Systems, Rochester, New York, 1995.
9. Jensen, P. B., Olsen, M. B., Poulsen, J., Fons, M., and Hendricks, E., "A New Family of Nonlinear Observers for SI Engine Air/Fuel Ratio Control", SAE Technical Paper No. 970615, 1997.
10. The specially prepared 7 port head for the 1275cc British Leyland engine was provided by Georg Mikkelsen, ÅKM Racing, Lerpyttervej 31, 7700 Thisted, Denmark, +45 97 92 01 82.

8. NOMENCLATURE

The following symbols are used in this paper:

t	time (sec)
α	throttle plate angle (degrees)
n	engine speed (rpm/1000 or krpm)
p_a	ambient pressure (bar)
T_a	ambient temperature (degrees Kelvin)
p_i	absolute manifold pressure (bar)
T_i	intake manifold temperature (degrees Kelvin)
T_{EGR}	EGR temperature (degrees Kelvin)
p_e	exhaust manifold pressure (bar)
Δp	p_e - p_i (bar)
$\dot{m}_{at}$	air mass flow past throttle plate (kg/sec)
$\dot{m}_{ap}$	air mass flow into intake port (kg/sec)
$\dot{m}_{EGR}$	EGR mass flow (kg/sec)
$m_{i'}$	$(e_v \cdot p_i)$ normalized air charge per stroke
m_i	air mass in the intake manifold (kg)
x_m	measured value of the variable x3
e_v	volumetric efficiency based on manifold conditions
V_d	engine displacement (liters)
V_i	manifold + port passage volume (m^3)
R	gas constant (here 287 X 10^{-5})
κ	ratio of the specfic heats = 1.4 for air
L_{th}	stoichiometeric air/fuel ratio (14.67)
$s_e(n)$	slope of pressure difference curve, with normalized air charge, see [2]
$y_e(n)$	intercept of pressure difference curve, with normalized air charge, see [2]
r	compression ratio
$\sigma(\Delta T)$	$1 / (1 + \Delta T / T_i)$
ΔT	mean temperature rise during intake stroke

APPENDIX

The basic characteristics of the prototype port air mass flow and EGR flow sensors used in this paper are summarized below.

Port Mass Air Flow (MAFp) and EGR Flow Sensor Characteristics:

a. basic accuracy: +/- 1 %, error standard deviation.
b. linearity (steady state): +/- 0.5 %, physical linearization.
c. linearity (dynamic): +/- 1.0 %.
d. response direction: bi-directional, symmetric.
e. response time: < 1 msec.
f. vibration sensitivity: small.
g. temperature error: +/- 2.0 %, -5/+50°C (approx.).
h. light off time: < 10 msec.
i. size: 38 mm (MAFp) and 22 mm (EGR).

The basic characteristics of the prototype fast temperature sensors used in this paper are summarized below.

Temperature Sensor Characteristics:

a. basic accuracy: +/- 1 %, error standard deviation.
b. linearity (steady state): +/- 0.5 %, physical linearization.
c. linearity (dynamic): as above.
d. response direction: bi-directional, symmetric.
e. response time: < 1 msec.
f. vibration sensitivity: small.
g. temperature range: 0 - 350 C.
h. light off time: < 5 msec.
i. size: small.
j. mounting sensitivity:non-critical.

Chapter 3

Estimation & Identification

EGR mass flow estimation is a critical point in modern engine control strategies if current emissions legislation is to be met. Since most estimation strategies utilize MAF, exhaust gas composition or temperature measurements in the computation of the EGR mass it is vital to know what level of estimation accuracy can be expected using these inputs. Hence, the first topic of this chapter is the investigation of different EGR estimation strategies and how deterministic measurement errors will influence estimation accuracy. Secondly, anti-aliasing filters, developed for event-based strategies, capable of providing optimal measurement bandwidth without the danger of aliasing are presented. High measurement bandwidth without the danger of signal aliasing is of great importance for a correct estimation of several engine states.

3.1 EGR Rate estimation

Tight control of the exhaust gas recirculation (EGR) is of paramount importance when targeting the minimization of NO_X and PM emissions from DI engines. Hence, in the light of the future requirement for stringent control of the EGR rate, or rather the burnt mass fraction level in the intake manifold, this section is dedicated to the investigation of what accuracy level can be obtained with production type engine sensors.

Direct measurement of the EGR volume flow is possible by measuring the pressure drop across a restriction. However, due to the relative high exhaust PM level in DI engines, this method is not viable due to restriction clogging issues. Hence, the EGR mass flow must be estimated from other engine state measurements and state estimates.

The MAF measurement, normally obtained with a hot-wire/film sensor downstream of the intake air filter box, is without doubt the single most important measurements in a conventional EGR estimation strategy. However, new exhaust O_2/λ sensors suited for application with lean burn engines are emerging on the automo-

tive market. Combined with the exhaust gas composition information provided by these new exhaust sensors and with other selected engine measurement/estimates, new EGR estimation strategies are made possible.

Dependent upon operating point and AFR the EGR rate may maximally vary $\pm 5\%$ relatively to the EGR rate set point, or otherwise excessive Diesel engine emissions [5] can be expected. This maximum setting of $\pm 5\%$ for the relative tolerance on the EGR rate will be used throughout this section.

First the EGR rate estimation strategy based solely on the MAF measurement will be evaluated and later compared to the corresponding results expected using a linear O_2/λ exhaust sensor.

Since direct measurement of the EGR mass flow is complicated due to the high EGR particulate level, this section will also evaluate estimation strategies based upon thermal information from temperature measurements obtained in the engine intake system, thereby avoiding the use of the speed-density equation.

3.1.1 MAF sensor performance

The EGR rate is commonly computed by subtracting the MAF signal from the intake port mass flow normally estimated by the speed-density equation. Hence, it is of natural interest to determine what level of steady state accuracy that can be achieved with production type MAF sensors.

The best MAF sensors currently available from Bosch, based on hot film technology, have a relative error on the mass flow measurement in the range of $\pm 3\%$ (see [6])[1]. Although this error seems negligible it has a major impact on the estimation of the EGR rate even when the total mass flow to the engine is known exactly. This significant influence on the EGR estimation will be shown below.

The ratio between the intake air mass flow and the EGR flow is by definition,

$$\frac{\dot{m}_{thr,1}}{\dot{m}_{egr}} = \frac{1 - \text{EGR}_{\text{rate}}}{\text{EGR}_{\text{rate}}} = X_{egr} = \frac{\dot{m}_{ap} - \dot{m}_{egr}}{\dot{m}_{egr}} \tag{3.1}$$

and

$$\text{EGR}_{\text{rate}} \triangleq \frac{\dot{m}_{egr}}{\dot{m}_{ap}} \tag{3.2}$$

The intake throat mass flow, $\dot{m}_{thr,1}$, is in steady state related to the measure intake mass flow, MAF, in the following manner

$$\begin{aligned} &\dot{m}_{thr,1} \equiv \text{MAF}(1-\delta) \\ &\Downarrow \\ &\hat{\dot{m}}_{egr} = \dot{m}_{egr} + \delta\text{MAF} \end{aligned} \tag{3.3}$$

[1]The setting of $\pm 3\%$ is for a new sensor. However, the absolute value of the relative sensor error is known to increase to approximately 25% (see [94]) over time depending on the local pollution level.

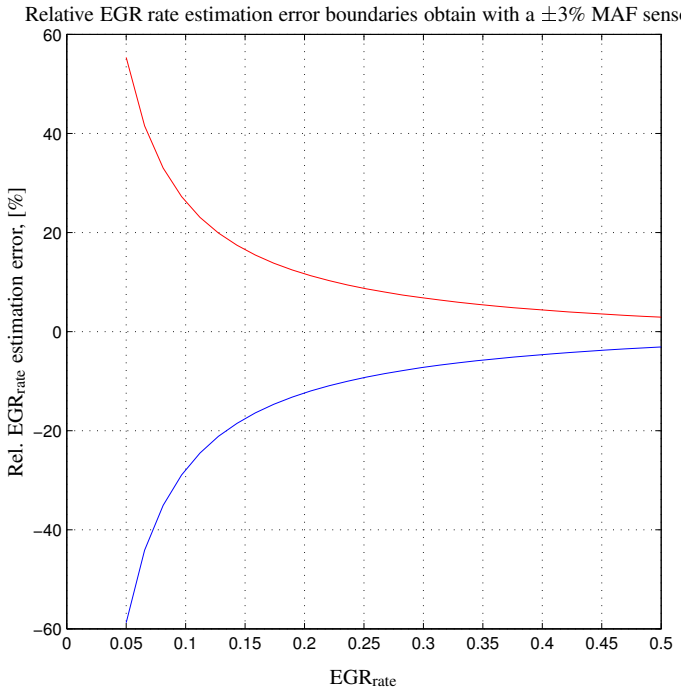

Figure 3.1: Relative EGR rate error boundaries with ±3% MAF sensor.

since the $\dot{m}_{ap} \equiv \dot{m}_{thr,1} + \dot{m}_{egr} = \text{MAF} + \hat{\dot{m}}_{egr}$ under the assumption that the port mass flow can be estimated correctly. The parameter δ is in the last equation the relative fractional error on the MAF measurement. The relative steady state error on the EGR rate estimation may now independently of the engine characteristics be derived from the last two equations as

$$\begin{aligned} \text{EGR}_{\text{rate,est}} &= \frac{\hat{\dot{m}}_{egr}}{\dot{m}_{ap}} = \frac{1+\delta X_{egr}}{1+X_{egr}} \\ &\Downarrow \\ \text{Error,}[\%] &= 100\frac{\text{EGR}_{\text{rate,est}} - \text{EGR}_{\text{rate}}}{\text{EGR}_{\text{rate}}} \\ &= 100\delta X_{egr} = 100\delta\frac{1-\text{EGR}_{\text{rate}}}{\text{EGR}_{\text{rate}}} \end{aligned} \tag{3.4}$$

Figure 3.1 shows the error boundaries on the EGR rate estimation expected with a ±3% MAF sensor. It is clear from the figure that even if the total mass flow inducted by the engine is known precisely, the slightest error in the MAF measurement will have a serious impact on the EGR rate estimation/control accuracy. Only at higher EGR rates will the error approach the acceptable level of ±5%. Inaccuracies in the fuelling rate (error between demanded and actual fuelling) are not considered in this analysis, but will further exacerbate the EGR/AFR control accuracy.

3.1.2 Exhaust Sensor Performance

The effect of the relative error on the O_2 measurements in the engine's exhaust pipe on the estimation of the EGR rate is examined in this section.

3.1.2.1 Differential Equations for the relevant dynamics

The burnt mass fraction in the intake manifold, F_{man}, can be described by the ODE (see e.g. appendix C on page 255 where the burnt mass fraction of a arbitrary control volume fulfilling the assumption made with the filling and emptying approach is derived),

$$\dot{F}_{man} = \frac{RT_{man}}{p_{man}V_{man}}\left((F_{egr} - F_{man})\dot{m}_{egr} - F_{man}\dot{m}_{thr,1}\right) \tag{3.5}$$

where R is the gas constant for air, T_{man} is the gas temperature in the intake manifold. p_{man} and V_{man} are the manifold pressure and the manifold volume, respectively. F_{egr} is the burnt mass fraction content in the EGR mass flow, $\dot{m}_{egr}$. Finally, $\dot{m}_{thr,1}$ is the air mass flow in the intake throat just upstream of the EGR inlet point.

The change of mass in the intake manifold is given by mass conservation,

$$\dot{m}_{man} = \dot{m}_{egr} + \dot{m}_{thr,1} - \dot{m}_{ap} \tag{3.6}$$

where $\dot{m}_{ap}$ is the mass flow at the intake ports.

Scaled exhaust O_2 equations The scaled O_2 concentration[2] in the cylinder of a DI engine can be described as,

$$O_{2,cyl}(t) = \frac{\overbrace{(1 - F_{man}(t-\tau_i))\dot{m}_{ap}(t-\tau_i)}^{\text{Fresh air mass flow available for combustion}} - \overbrace{\lambda_{ref}\dot{m}_f}^{\text{Fresh air mass flow required by stoichiometric combustion}}}{\underbrace{\dot{m}_{ap}(t-\tau_i) + \dot{m}_f}_{\text{Total mass flow through the system}}} \tag{3.7}$$

where τ_i is the time delay between the closing of the intake valve and fuel injection. The numerator is simply the difference between the fresh air mass flow available before combustion and air mass consumed by combustion ($\lambda_{ref}\dot{m}_f$). The scaled oxygen concentration in the exhaust is just a time delayed version of the oxygen concentration in the cylinder. Hence, the following expression for $O_{2,exh}$ is obtained.

$$\begin{aligned} O_{2,exh}(t) &= \frac{\dot{m}_{air,exh}}{\dot{m}_{air,exh} + \dot{m}_{burned,exh}} \\ &= \frac{(1 - F_{man}(t-\tau_i-\tau_c))\dot{m}_{ap}(t-\tau_i-\tau_c) - \lambda_{ref}\dot{m}_f(t-\tau_c)}{\dot{m}_{ap}(t-\tau_i-\tau_c) + \dot{m}_f(t-\tau_c)} \end{aligned} \tag{3.8}$$

[2]The O_2 is here scaled such that O_2=1 and O_2=0 refer to fresh air flow and completely burned flow respectively

where the time delay τ_c is the time between fuel injection and the opening of the exhaust valve. The equation is schematically depicted in figure 3.2.

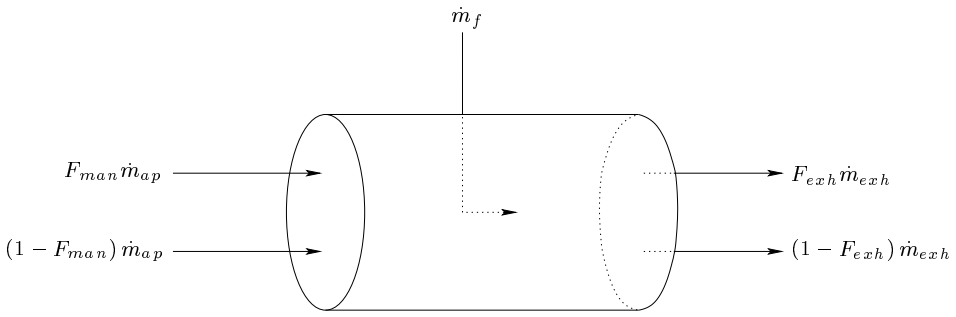

Figure 3.2: Schematic diagram of the combustion process in a diesel engine.

Scaled λ equations The description of the scaled air-to-fuel ratio[3], λ, is directly available from O_2 expressions derived previously. However, special care must be taken in the definition of the fresh air mass flow and the fuel mass flow going to engine or else the the computed λ level exhaust will be biased compared to measurements. The total air flow intake, fresh as well as burnt, is computed as

$$\dot{m}_{air} = \dot{m}_{ap}\left(1 - \frac{1}{\lambda_{ref}+1}F_{man}\right) \tag{3.9}$$

Thus, the total intake air flow is the difference between the total intake flow, $\dot{m}_{ap}$ and intake flow which was formerly fuel. The total fuel flow is found analogous to the previous equation as

$$\dot{m}_{fuel} = \dot{m}_f + \frac{1}{1+\lambda_{ref}}F_{man}\dot{m}_{ap} \tag{3.10}$$

The scaled λ in the cylinder can be described as,

$$\boxed{\begin{aligned}\lambda_{cyl}(t) &= \frac{\dot{m}_{air}}{\lambda_{ref}\dot{m}_{fuel}} \\ &= \frac{1 - \frac{1}{\lambda_{ref}+1}F_{man}(t-\tau_i)}{\lambda_{ref}\left(\frac{\dot{m}_f}{\dot{m}_{ap}(t-\tau_i)} + \frac{1}{\lambda_{ref}+1}F_{man}(t-\tau_i)\right)}\end{aligned}} \tag{3.11}$$

After combustion the cylinder mass is purged into the exhaust pipe during the exhaust stroke, hence the λ level in the exhaust pipe will be the total cylinder λ time delayed. Therefore the λ level in the exhaust pipe, λ_{exh}, is,

$$\lambda_{exh}(t) = \lambda_{cyl}(t - \tau_c) \tag{3.12}$$

[3] λ is scaled with the stoichiometric ratio, λ_{ref}, between diesel and fresh air, which in this work is fixed to a value of14.7.

where the delay τ_c is the time between the fuel injection and the corresponding opening of the exhaust valves.

3.1.2.2 Steady State Operation

The burnt mass fraction in the intake manifold will in steady state be,

$$\begin{aligned} \dot{F}_{man} &= 0 \\ \Updownarrow & \\ F_{man} &= \frac{\dot{m}_{egr}}{\dot{m}_{egr} + MAF} F_{egr} \\ &= \text{EGR}_{\text{rate}}(1 - \text{O}_{2,exh}) \end{aligned} \tag{3.13}$$

since

$$\begin{aligned} \dot{m}_{thr,1} &= MAF \\ \text{EGR}_{\text{rate}} &= \frac{\dot{m}_{egr}}{\dot{m}_{egr} + MAF} \\ F_{egr} &= 1 - \text{O}_{2,exh} \end{aligned} \tag{3.14}$$

Exhaust O_2 in steady state Inserting the above equations in equation 3.8, the following expression for the steady state EGR rate is obtained,

$$\text{EGR}_{\text{rate}} = \left(1 - \text{O}_{2,exh}\left(1 + \frac{\dot{m}_f}{\dot{m}_{ap}}\right) - \lambda_{ref}\frac{\dot{m}_f}{\dot{m}_{ap}}\right)\frac{1}{1 - \text{O}_{2,exh}} \tag{3.15}$$

The fresh air mass flow to the engine, MAF, is related to the EGR rate in the following way,

$$\text{MAF} = \dot{m}_{ap}\,(1 - \text{EGR}_{\text{rate}}) \tag{3.16}$$

Inserting this information into equation 3.15 the scaled $\text{O}_{2,exh}$ can be found as,

$$\begin{aligned} \text{EGR}_{\text{rate}}(1 - \text{O}_{2,exh}) &= 1 - \text{O}_{2,exh}\left(1 + (1 - \text{EGR}_{\text{rate}})\frac{\dot{m}_f}{\text{MAF}}\right) \\ &\quad - \lambda_{ref}(1 - \text{EGR}_{\text{rate}})\frac{\dot{m}_f}{\text{MAF}} \\ \Updownarrow & \\ (1 - \text{EGR}_{\text{rate}})(\text{O}_{2,exh} - 1) &= -\text{O}_{2,exh}(1 - \text{EGR}_{\text{rate}})\frac{\dot{m}_f}{\text{MAF}} \\ &\quad - \lambda_{ref}(1 - \text{EGR}_{\text{rate}})\frac{\dot{m}_f}{\text{MAF}} \\ \Updownarrow & \\ \text{O}_{2,exh} &= \frac{1 - \lambda_{ref}\frac{\dot{m}_f}{\text{MAF}}}{1 + \frac{\dot{m}_f}{\text{MAF}}} \end{aligned} \tag{3.17}$$

Equation 3.17 shows that the oxygen level in the exhaust during steady state engine operation does not explicitly depend on the EGR rate and the burnt mass fraction in the intake manifold. There will be an implicit EGR dependency however, since introduction of EGR lowers the MAF to the engine.

Exhaust λ in steady state In order to simplify the structure of the equations the fuel-to-port mass flow ratio, Φ, is introduced, defined as

$$\Phi = \frac{\dot{m}_f}{\dot{m}_{ap}} \tag{3.18}$$

The burnt mass level in the exhaust pipe, F_{exh}, will in steady state be equal to F_{cyl}, and F_{egr} will be equal to F_{exh}. This makes

$$F_{egr} = \frac{F_{man} + (1 + \lambda_{ref})\Phi}{1 + \Phi} \tag{3.19}$$

and similarly, the burnt mass fraction, F_{man} is,

$$F_{man} = F_{egr}\frac{\dot{m}_{egr}}{\dot{m}_{ap}} = F_{egr}\text{EGR}_{\text{rate}} \tag{3.20}$$

Now inserting equation 3.19 into equation 3.20, the following equation for F_{man} can be derived,

$$F_{man} = \frac{(1 + \lambda_{ref})\Phi\text{EGR}_{\text{rate}}}{1 + \Phi - \text{EGR}_{\text{rate}}} \tag{3.21}$$

The scaled air-to-fuel ratio, λ, is defined as the ratio between air and fuel in a system normalized by the stoichiometric ratio between the two reactants. Thus, when the burnt mass fraction equals one, $F = 1$, λ will by definition be equal to 1. Suppose the fuel content in the flow mentioned has not been burnt, and the total mass flow entering the intake ports is known, the flow may be divided into an air flow and a fuel flow going to the cylinder,

$$\begin{aligned} \lambda_b = 1 &= \frac{\dot{m}_{air,b}}{\lambda_{ref}\dot{m}_{f,b}} \\ &= \frac{XF_{man}\dot{m}_{ap}}{\lambda_{ref}(1-X)XF_{man}\dot{m}_{ap}} \\ &= \frac{X}{\lambda_{ref}(1-X)} \\ \Updownarrow & \\ X &= \frac{\lambda_{ref}}{1+\lambda_{ref}} \end{aligned} \tag{3.22}$$

where the constant X is the fraction of the total burnt mass flow, $F_{man}\dot{m}_{ap}$, which was formerly fresh air. With the help of equation 3.22 the steady state λ level in the exhaust pipe can be derived as,

$$\boxed{\lambda_{exh} = \frac{1 + F_{man}(X-1)}{\lambda_{ref}\left(\Phi + (1-X)F_{man}\right)}} \tag{3.23}$$

3.1.2.3 Relative Error Bounds for the Exhaust Sensors

The effect of measurement errors on the O_2/λ level in the exhaust will be studied in this section. A MATLAB® program was constructed in order to analyze the sensor error's effect on the accurate estimation of the EGR_{rate}. This program is capable of calculating the maximum allowed relative sensor error for various error bounds on the EGR_{rate}. The following are assumed in the simulations,

- The port mass flow $\dot{m}_{ap}$ can be determined exactly from the speed-density equation. The speed-density equation is given as,

$$\dot{m}_{ap} = \frac{\eta_{vol} N V_d p_{man}}{120 R T_{man}} \tag{3.24}$$

  where η_{vol} is the engine's volumetric efficiency. N and V_d are the engine's speed and displacement respectively. Perfect knowledge of the intake manifold conditions will also be assumed.

- The fuel system provides a precise measurement of the injected fuel mass flow, $\dot{m}_f$.

- The maximum allowed relative error on the EGR_{rate} is here, to serve as an example, set to $\pm 5\%$.

- The relative sensor error is assumed to be the same as for the MAF sensor ($\pm 3\%$).

Figure 3.3 shows the burnt mass fraction, F_{man}, in steady state as a function of the O_2 concentration in the exhaust pipe, exhaust λ and EGR rate. In order to

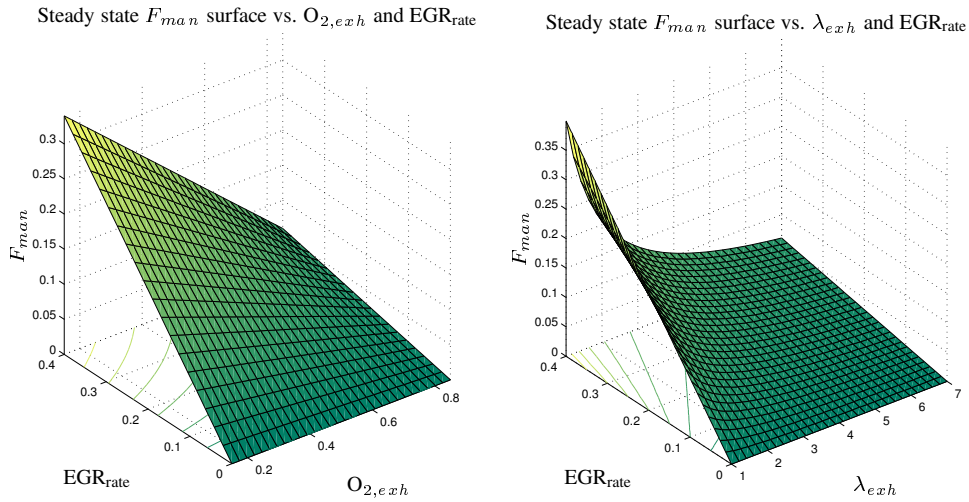

Figure 3.3: Steady state burnt mass fraction in the intake manifold, F_{man}, as a function of $O_{2,exh}$, λ and EGR_{rate}

compute F_{man}, the program must first determine the surface of the fuel-port mass flow ratio, Φ, at the equilibrium levels defined in section 3.1.2.2. Figure 3.4 shows the surface computed for Φ. These surfaces define the fuelling strategy used in

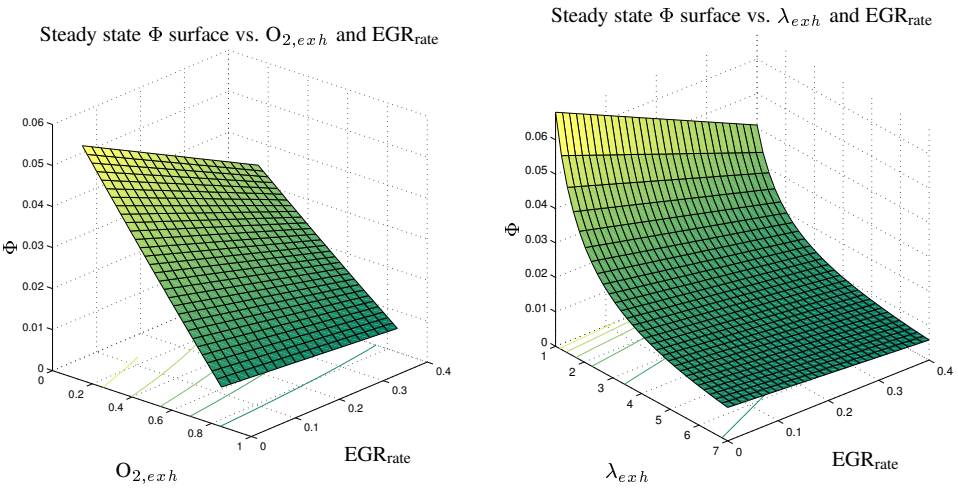

Figure 3.4: Fuel–port mass flow, Φ, surface as a function of O_2, λ in the exhaust pipe and EGR_{rate} during steady state engine operation

the simulations. The corresponding error surfaces are shown in figure 3.5, and the contour of the upper surfaces are plotted in figure 3.6. The figures clearly show the difficult requirements of the O_2/λ sensor's performance, if the relative error on the EGR_{rate} is to be kept below the specified limits everywhere in the plane. As one might expect, the sensor requirements are more relaxed as the EGR_{rate} is increased. Figure 3.7 shows the relative error on EGR_{rate} for fixed relative sensor error readings at $\pm 3\%$. The figure shows, as expected, that the EGR_{rate} error goes up as the EGR_{rate} decreases and that a large region of the surface is outside the window $\pm 5\%$.

This section has clearly shown the importance of the ability to obtain accurate measurements of the oxygen/λ level in the exhaust if the EGR rate is to be controlled accurately without the use of a MAF sensor. The bottom line is that an estimation of the EGR rate based solely on the O_2/λ sensor information will **not** be able to determine the EGR rate within a $\pm 5\%$ relative error bound everywhere in the O_2/λ–EGR_{rate} plane.

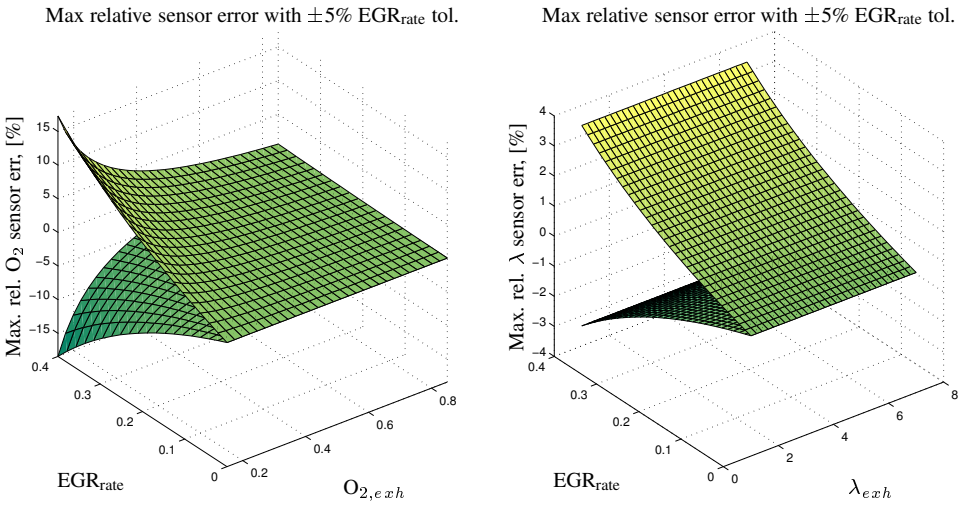

Figure 3.5: Requirements to the exhaust sensors' performance if a relative error of $\pm 5\%$ on the EGR_{rate} is desired. The plots show the error surfaces on which the performance requirements are just met.

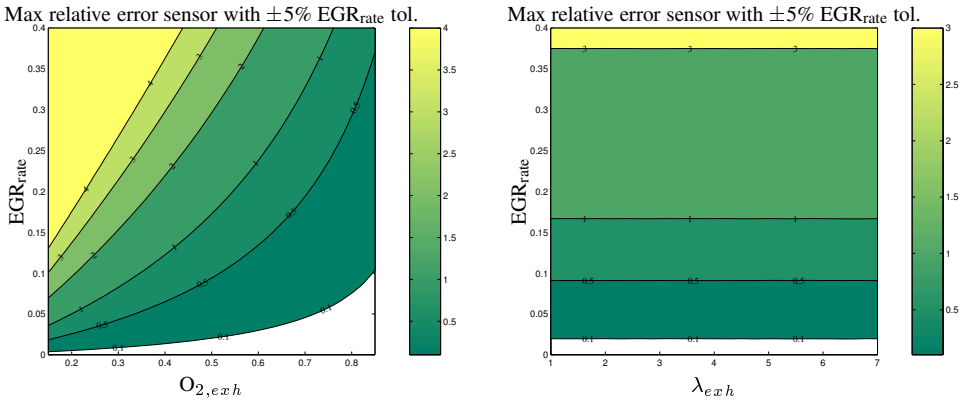

Figure 3.6: Contour plot of the upper error surfaces shown in figure 3.5.

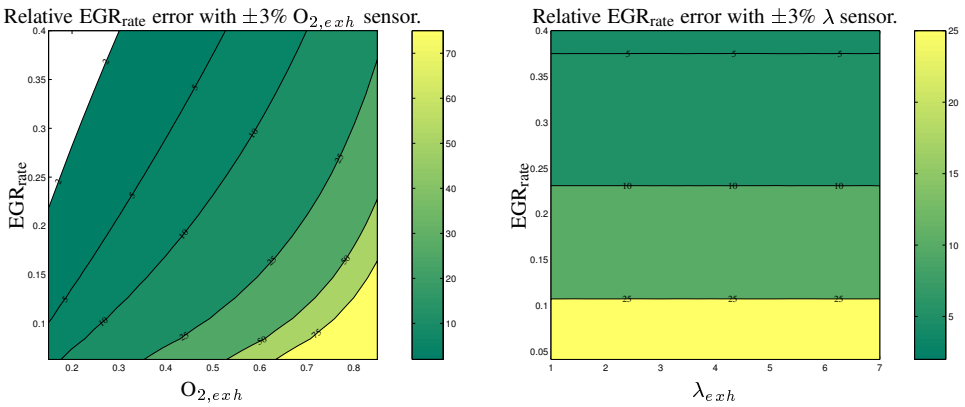

Figure 3.7: Relative EGR_{rate} error contours achieved with a $\pm 3\%$ O_2/λ sensor.

3.1.3 Thermal ratio EGR estimation

The temperature difference between the intake air and the recirculated exhaust mass flow is often of a considerable magnitude. Hence, if just one of the inlet mass flows to the intake manifold is known/measured the energy exchange between the intake manifold, engine, throttle body and EGR system may be computed and such provide innovation information for an EGR mass flow observer design (see e.g. [75, 85]). Since the time constant of the automotive series production thermocouples/thermistors is between 5 sec. and 44 sec. (see e.g. [6]), the use of a dynamic model of the intake system together with dynamic sensor models to boost the response of the EGR estimation loop is mandatory (e.g in Extended Kalman Filter Observer Design). However, due to the unavoidable pulsations in the intake system inherently accompanied by a mixing process, the determination of the actual temperature during positive and negative flow conditions around individual temperature measurement locations is difficult. Hence, the thermistors will only provide some spatially–time averaged measurement of the local thermal conditions in the intake manifold, and a correct determination of the instantaneous enthalpy level up- and down-stream of the thermistor is difficult. Furthermore, due to the physical non-linearities the cycle averaged energy exchange between the EGR system and intake manifold is not necessarily equivalent to the product of cycle averaged mass flow and the cycle averaged enthalpy level , i.e $\frac{1}{T_{\text{cycle}}} \int\limits_{\text{cycle}} \dot{m}(t)h(t)dt$ will not necessarily equal $\overline{\dot{m}}\overline{h}$. This problem will especially be pronounced at locations where the spatial temperature gradient is large. The possible presence of this problem, which was already introduced in section 2.8.1, may lead to large estimation errors even at steady engine operating points. The size and behavior of this possible error will be investigated in the following.

In the steady state the energy flow into the intake system must equal the energy flow out of the intake plenum. Neglecting heat transfer between the intake plenum and the ambient surroundings the energy balance may readily be written as,

$$\dot{m}_{ap} c_p T_{man} = \dot{m}_{egr} c_p T_{egr} + \dot{m}_{thr,1} c_p T_{ic} \tag{3.25}$$

where $\dot{m}_{thr,1}$ and T_{ic} are the mass flow out of the intercooler and the intercooler exit temperature, respectively. Hence, if either the EGR outlet temperature T_{egr} or mass flow $\dot{m}_{egr}$ are measured $\dot{m}_{egr}$, or vice versa, T_{egr} may be estimated i.e.

$$\begin{aligned} \hat{\dot{m}}_{egr} &= \frac{T_{man} - T_{ic}}{T_{egr} - T_{man}} \dot{m}_{ic} \\ \hat{T}_{egr} &= \frac{\left(\dot{m}_{egr} + \dot{m}_{ic}\right) T_{man} + \dot{m}_{ic} T_{ic}}{\dot{m}_{egr}} \end{aligned} \tag{3.26}$$

These last two equations formulate the basis for *thermal ratio based EGR estimation*, where the estimate of interest can be either the EGR mass flow, $\dot{m}_{egr}$, or EGR temperature T_{egr}.

The two thermal ratio estimation algorithms are evaluated on a steady state engine map[4]. The engine is a 2.0 liter turbocharged DI common rail Diesel engine. The measurements are obtained with state-of-the-art measurement equipment insuring the best possible accuracy available with commercial engine test-beds. The experimental results obtained are graphically illustrated in figure 3.8. The plots to the left, evaluating the performance of the $\dot{m}_{egr}$ estimation algorithm, clearly shows the inferior estimation quality obtainable with thermal EGR$_{rate}$ estimation. Relative errors on the order of 1000% were encountered when using thermal information for EGR estimation purposes. The thermal based EGR estimation strategies can thus clearly not cope with the temperature deviations caused by pumping fluctuations.

The performance of the T_{egr} steady state estimation algorithm is graphically seen to the right in figure 3.8. The plots clearly show the mixing problem discussed in section 2.8.1, and the EGR temperature is generally, as expected, estimated to be too high.

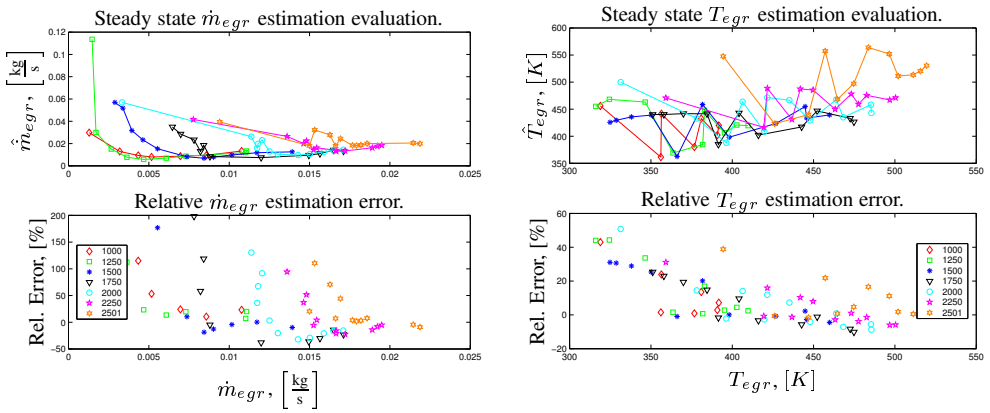

Figure 3.8: Evaluation of the steady state $\dot{m}_{egr}$ and T_{egr} estimation algorithms on engine map data for a 2.0 liter turbocharged Diesel engine with engine speeds ranging from 1000 rpm to 2500rpm. Note: $\dot{m}_{egr}$ errors larger than 200% are neglected for the sake of graphical clarity.

3.1.4 Summary

This section has dealt with EGR rate estimation accuracy issues related to MAF and O_2/λ measurement errors, and thermal estimation of the EGR mass flow or EGR system outlet temperature. The section initially described the necessary equations for a steady state analysis, and these equations were later analyzed in the MATLAB® environment. Based on this analysis it can be concluded that even the slightest relative error on either of the measurements will have a major impact on the EGR estimation accuracy at lower EGR flow rates. None of the sensors analyzed alone are able to keep the relative EGR rate error within $\pm 5\%$ everywhere

[4]Dipl. Ing. Daniel Röttger is gratefully acknowledged for providing the steady state engine map.

in the operating space. Even with sensor fusion it will be hard to improve the **low level EGR rate** estimation accuracy, since all the estimation algorithms exhibit the same large error sensitivity tendency at small EGR rates. When evaluating the data it can be concluded that the O_2/λ based EGR control algorithm exhibits the same error sensitivity as the one based on the MAF sensor. However, the use of an O_2/λ sensor will allow for better control at small air–fuel ratios, AFR, (i.e. close to the smoke limit) by nature of the feedback information it provides. Furthermore, it provides for robust control of the AFR across the operating range, irrespective of fuelling rate tolerances.

In the MAF/exhaust sensor analysis it is assumed that the gaseous mass flow entering the engine is known exactly, however, correct estimation of the mass flow is known to be troublesome since it depends on intake temperature and pressure, pressure difference across the engine, and the engine's breathing behavior among others. Along with this it is also assumed that the fuel injection system will be able to provide an exact estimate of the fuel mass flow injected. Errors in these two estimates, $\dot{m}_{ap}$ and $\dot{m}_f$, will of course have a detrimental effect on the EGR rate estimation and control schemes. Again, when using the O_2/λ sensor, the AFR control can be made robust with respect to the aforementioned estimation errors.

The section also concludes that EGR rate estimation based on temperature information obtained by thermistors mounted in the intake air path can only be expected to be of inferior quality, and are hence not applicable in high performance EGR estimation strategies.

3.2 Interfacing strategy and reality

The automotive engine is a machine governed by a mixture of differential equations in continuous time, event based equations linked to the crankshaft timing, and algebraic equations. Hence, which domain, time based or event based, should be selected for off-line engine simulations is often rather a matter of taste than actual science. However, the choice of domain for estimation and/or control strategy designs is more complicated. In [111] it is concluded that the speed control of DI Diesel engines should be implemented time based for reasons of stability, whereas control involving flows (e.g. EGR rate control) should be implemented event based to minimize the size of the gain scheduling maps.

A digital implementation of the individual control and estimation strategies in the ECU is today mandatory. The reason for this is evident due to the much broader window of functions (some of which are unique) and flexibility, and the better performance/cost ratio offered by digital systems compared to analog systems. The downside of the digital systems, however, is the required discretization of the underlying control/estimation dynamics and the sampling of the continuous exogenous input signals to the different algorithms. This necessitates an analog low pass filtering of the external signals mentioned prior to the sampling process. If this low pass filtering of the individual signals is ignored danger of data corrup-

tion exists since some of the higher frequencies ($> \frac{2}{T_s}$) of the input signal may be convoluted into a frequencies between 0 and half the sampling frequency, $\frac{2}{T_s}$. This phenomenon is known as signal aliasing. Thus, the signal frequencies above $\frac{2}{T_s}$ must be attenuated appropriately by low pass filters, the anti-aliasing filters, before the input signals are quantized by the analog-to-digital converter.

One of the implementation issues arising when designing anti-aliasing filters for engine strategies utilizing event sampled measurements is the selection of filter bandwidth. The filter bandwidth needs to be within half the sampling frequency at engine idling if signal aliasing is to be avoided. However, such a filter bandwidth would generally be five to nine times smaller than the bandwidth achievable at maximum rated engine speed. Hence, the bandwidth attainable for some selected event-based estimation and control strategies might reduced with such a conservative filter design. This problem was addressed in the SAE paper *"Avoiding Signal Aliasing in Event Based Engine Control"*, number 2000-01-0268 and a possible solution realized by a combination of time based sampling and separate digital filter design was provided. The paper is included in this research but was also presented at the 2000 SAE conference held in Detroit.

2000-01-0268

Avoiding Signal Aliasing in Event Based Engine Control

Christian Winge Vigild
Alain M. R. Chevalier
Ford Forschungszentrum Aachen

Elbert Hendricks
Technical University of Denmark

ABSTRACT

Many modern control strategies for engine control are based on event based sampling. Operating the control strategy in the event domain makes it possible to obtain samples at specific crank shaft angles in the engine cycle, which is often desirable for certain control strategies. One of the biggest disadvantages involved with event based strategies is signal aliasing at low engine speeds or a high computational burden at higher engine speeds.

This paper presents an easy solution to the aliasing problem above. If the data between the event based samples is stored using a time based strategy, it is shown here that a subsequent treatment of the sampled data as a time series together with a suitable low pass filter structure can avoid aliasing.

1 INTRODUCTION

During the last 20 years application of electronic control as a means to achieve certain control goals has gone from non-existant to complete sovereignty. One of the reasons for this change from mechanical control to electronic control is to keep up with the ever increasing harder emission legislation. An obvious example is Air/Fuel Ratio (AFR) control for SI engines. In order to achieve maximum Three Way Catalyst (TWC) efficiency the AFR has to be kept within a $\pm 3\%$ window around the stoichiometric AFR in the mean. Such accuracy was not possible with carburetor technology.

Electronic microprocessor control is inherently based on discrete sampling for many reasons of which two will be mentioned here. First, today's control strategies are of fairly complex nature (table lookup, nonlinear control strategies etc.) such that an electronic implementation with purely analog devices is not possible. Second, the wish to change strategies without changing hardware for time and cost reasons suggests that the strategy should be implemented as code.

During the development of today's engine control strategies one on going discussion has been whether the control strategy should be implemented event based (the sampling frequency is locked to engine speed) or time based (constant sampling frequency). The supporters of event based strategy, see [1], have claimed that the data sampling and control should be implemented event based since some of the major engine equations could be simplified. They also claim that it is more natural to do the sampling event based (**EB**) since the engine itself is an event driven machine. The supporters of time based (**TB**) strategy, see [2], [3] and [4], have claimed that sampling should been done using a constant sampling time, since many time-constants (e.g. sensor time constants) will stay constant in the engine operating range and the EB sampling frequency must be high at idle speed to describe the manifold dynamics during throttle tip-in and tip-out with sufficient bandwidth precision. Furthermore it is claimed that anti-aliasing filters will be difficult to design for the event based case, since the sampling frequency is not fixed in time. That the last problem can be solved if the data samples are acquired time based and subsequently treated digitally in a microprocessor is shown in this paper.

It is well known (Shannon's rule) that all frequencies above half the sampling frequency, if not suppressed, will be folded into a frequency window below half the sampling frequency. This effect will corrupt the measured data which eventually is to be translated by a controller or human operator such that appropriate control actions can be taken. Faulty aliased data will certainly lead to erroneous control actions. Aliasing is often avoided by filtering the signals before they are sampled. This method is well known for time based sampling and the actual implementation is easy since the bandwidth of the pre-filters is fixed. For event based sampling, however, a proper choice of pre-filter bandwidth is more delicate. If the bandwidth is too small, too much information will vanish at higher engine speeds and thus limit the achievable performance of the control feedback loops. If, on the other hand, the bandwidth is chosen too high, data will be aliased at lower

This paper is typeset in LaTeX 2_ε

engine speeds. Design of pre-filters is therefore normally a compromise between the desire to reconstruct the total frequency picture as accurately as possible at higher engine speeds and the desire to eliminate aliasing at lower engine speeds.

A solution to the aliasing problem in event based strategies will be given in this paper. Furthermore it should be stated that the goal of this paper is **not** to conclude whether or not data sampling and control should be done event or time based.

2 ALIASING

In most engine control systems the mean value of certain engine parameters like intake manifold pressure, p_{man} and/or air mass flow to the engine, $\dot{m}_{at}$, are necessary for the computation of important control signals like the fuel mass flow, $\dot{m}_{fi}$, to the engine, [5], [6] and [7].

An example of how aliasing can distort the mean value is shown in Figure 1. The figure shows two sample sequences

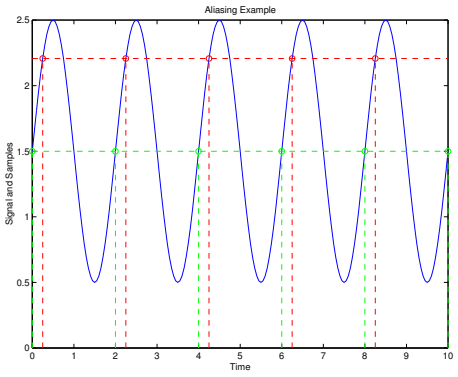

Figure 1: Mean value distortion by aliasing.

for the same continuous time signal. The first sequence is perfectly in phase with the continuous signal and the mean value is thus not affected. In the second case the continuous signal is shifted 45° compared to the sampling event, which clearly leads to a mean value bias.

A more general picture of aliasing is given in Figure 2. The top of the figure shows a given signal spectrum. This signal is now sampled with the sampling frequency f_s. The low sampling frequency forces all frequencies outside the $\left[\frac{-f_s}{2}; \frac{f_s}{2}\right]$ window, if not removed, to be down-sampled into this window. This effect is illustrated in the lower part of Figure 2. Instead of obtaining the desired signal spectrum (light gray spectrum) the acquired spectrum will be distorted as pictured by the upper spectrum (dark gray spectrum) in the figure.

The conclusion is that in order to achieved the desired spectrum for control or OBD (On Board Diagnostics) purposes, the frequencies above $\frac{f_s}{2}$ need to be removed. Since perfect filters do not exist (e.g. unit amplification up to

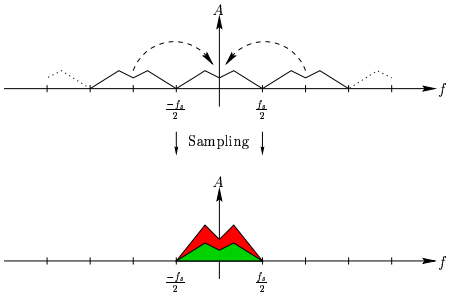

Figure 2: Distorted spectrum after sampling. f_s is the sampling frequency and A is the spectrum amplitude.

$\frac{f_s}{2}$ and zero amplification outside this region), it is normally necessary to choose the sampling frequency, f_s, at least 4 times higher than the bandwidth of the low pass filter (anti-aliasing filter) to provide enough high frequency attenuation.

3 FILTER STRUCTURES

Three different solutions to the aliasing problem related to the event based control strategies are given in the following.

The basic idea behind the filter design is outlined schematically in Figure 3. The figure shows how the analog inputs are first pre-filtered by appropriately designed analog anti-aliasing filters (bandwidth, $f_{3dB,A}$, 4 or more times smaller than the sampling frequency, f_{TB}) followed by time based sampling. The acquired samples are then fed to digital filters. The bandwidth of these filters are changed online as function of either engine speed, N, or received an EB interrupts, I_{EB_n}. The reader should note that the bandwidth of the digital filters does not necessarily have to be the same, but can be adjusted for each input signal. This makes it possible to adjust the bandwidth of each filter such that only the desired frequency spectrum for each input signal is acquired.

As explained previously, it is desirable that the cutoff frequency of the (digital) anti-aliasing filter be locked to the engine frequency,

$$f_{3dB} = \frac{f_{EB}}{r} \tag{1}$$

where r is the desired ratio between event based sampling frequency, f_{EB}, and the filter bandwidth, f_{3dB}. It is recommended that r is 4 or larger. The event frequency, f_{EB}, is given by,

$$f_{EB} = \frac{N n_r}{60} \tag{2}$$

where N is the engine speed in rpm, n_r is the number of event based samples per engine revolution (e.g. $n_r = 8$ for 45° sampling period).

In the following the term *Plug On Device* is used to refer to the fact that the aliasing filter is a hardware or software

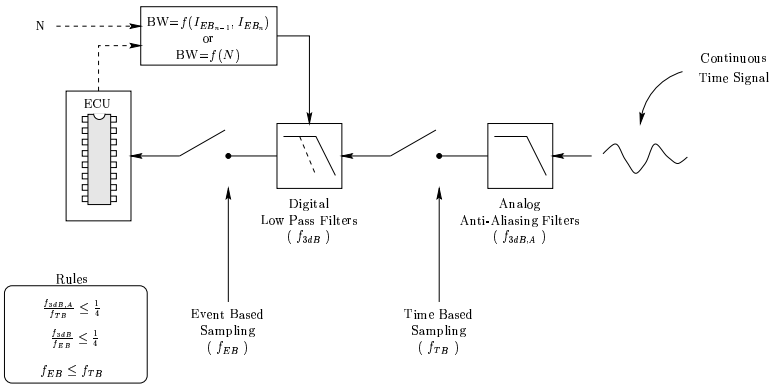

Figure 3: Modus Operadi of Analog/Digital Anti-Aliasing Filter.

implemented unit, inserted between the measured signals and the ECU.

Three proposed filter implementations will be described in the following.

3.1 Plug On Device with N as Input

If the engine speed N is continuously available (i.e. for each EB sample), the cutoff frequency, f_{3dB}, of the anti-aliasing filter can be updated at each EB event as a function of engine speed,

$$f_{3dB} = \frac{N n_r}{60} \frac{1}{r} = f_{EB} \frac{1}{r} \tag{3}$$

The filter bandwidth obtained, f_{3dB}, can be normalized with respect to the constant TB sampling frequency, f_{TB},

$$\begin{aligned} f_{3dB}^{norm} &= \frac{f_{3dB}}{f_{TB}} \\ &= \frac{N n_r}{60} \frac{1}{f_{TB}} \frac{1}{r} \end{aligned} \tag{4}$$

This way of describing the filter bandwidth is convenient since the filter parameters stay constant for a fixed $\frac{f_{3dB}}{f_{TB}}$ ratio.

3.2 Plug On Device with EB Interrupt as Input

In the case where the engine speed, N, is not directly (and continuously) available, it can be approximated by counting the number of TB events between two successive EB events,

$$N \approx \frac{60}{n_r \; n_{TB}\left(I_{EBn-1}, I_{EBn}\right) T_{TB}} \tag{5}$$

where $n_{TB}\left(I_{EBn-1}, I_{EBn}\right)$ is the number of time samples between the current and the previous EB samples, and T_{TB} is the constant sampling time. Combining equation (5) with equations (1) and (2) gives the bandwidth, f_{3dB}, of the digital filter, which in normalized form becomes,

$$f_{3dB}^{norm} = \frac{1}{n_{TB}\left(I_{EBn-1}, I_{EBn}\right) T_{TB}} \frac{1}{f_{TB}} \frac{1}{r} \tag{6}$$

The design of the digital filters is then comparable to that described in the previous section except for the bandwidth calculation (explained above) and the fact that it is not possible to update the filters from TB sample to TB sample (explained later in the section).

A schematic hardware diagram of this filter is shown in Figure 4. Here $n_{TB}\left(I_{EBn-1}, I_{EBn}\right)$ is provided by

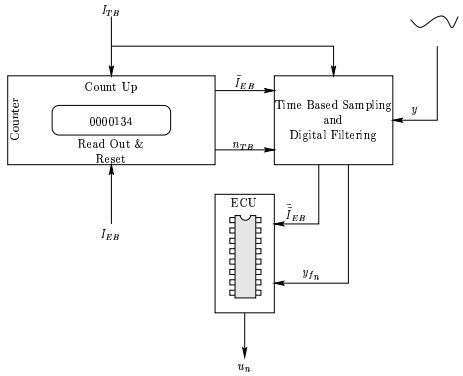

Figure 4: Schematic diagram of Interrupt Governed Filtering

a simple counter network. The purpose of the counter is to count the number of TB samples between EB samples. When an EB interrupt is received, the counter value is placed in an output register followed by a counter reset and re-arming. The individual bandwidth of the filters are then updated as in equation (6).

Because the f_{3dB} frequency can only be calculated at the end of each EB slice, the sampled data need to be stored in a buffer for batch processing at the end of each EB event. When the next EB interrupt occurs, the following happens (in a compact form).

- n_{TB} is read.

- The bandwidth for each filter (may be different from channel to channel) is computed as in equation (6).
- The individual filter parameters, a_x^q and b_x^q, are updated.
- The output of each filter is updated with the stored input data i.e.

$$y_n^q = \sum_{i=n-n_s}^{n} a_1^q y_{i-1}^q + a_2^q y_{i-2}^q + \ldots + a_k^q y_{i-k}^q + b_1^q u_i^q + b_2^q u_{i-1}^q + \ldots + b_l^q y_{i-l+1}^q$$

  where y_n^q is the output of the qth filter to sample n, a_x^q and b_x^q are the filter coefficients (see above), and u_n^q is the nth sample input to the filter.
- Update the output register with the newest filter outputs and send an interrupt to the ECU.
- The ECU reads the filtered signals and executes control and OBD tasks.

A proposal to the data buffer structure is shown schematically in Figure 5. The buffer design is cyclic

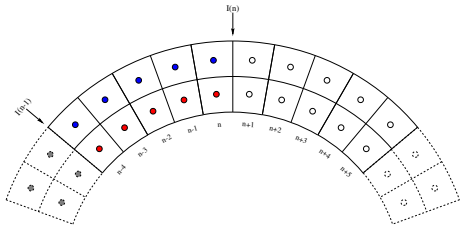

Figure 5: Structure of the data buffer. $I(x)$ is an EB interrupt at sample x. Each band in the pointer holds the acquired samples of the individual input signals.

with the outer rim containing just as many bands as there are input signals. The maximum length[1] is designed such that the structure can handle the worst situation. A worst case situation is when the engine is idling such that the difference between EB and TB sampling frequency is the largest. In this situation each band in the pointer must be capable of storing the individual TB samples in between EB interrupts.

The above filter can be simplified in two ways

- The EB sampling time is assumed constant, $T_{EB_n} \equiv T_{EB_{n-1}}$. This is highly justifiable since the engine speed, N, is a slowly varying variable under normal operating conditions. In this case the data buffer is not needed since the output of the individual filters can be updated at each TB sample. Another advantage of this approach is that the CPU load will be evened out over time, thus reducing the requirement of the microprocessor performance.

[1] Length means number of samples that can be stored in the individual band

- Upon receiving an EB interrupt a flag is stored in the memory. The EB sampling time can then be calculated by counting the number of TB samples between EB interrupts. This way the hardware counter can be eliminated.

3.3 Code Embedded Filter

In those cases where the ECU microprocessor is fast enough, the actual filtering can be implemented as a parallel task along with the control and OBD tasks. The actual implementation follows directly from the filter descriptions given in Sections 3.1 and 3.2.

4 EXAMPLE

The purpose of this example is to stress how seriously signal aliasing can affect data obtained in event based strategies. Readers not familiar with the aspects of EB and TB strategies are referred to [5] and [7]. The following is assumed:

- Two samples are taken per engine revolution. This gives a sampling time, T_{EB_s}, between 50 ms at 600 rpm down to 5 ms at 6000 rpm [8]. This means that the microprocessor must be able to compute the entire control strategy within 5 ms (worst case).
- The analog anti-aliasing filter has a 3dB bandwidth of 50 Hz which corresponds to one fourth of the maximum EB sampling frequency. In other words, the filter is constructed such that it is possible to reconstruct the frequency spectrum as well as possible at high engine speeds.
- The bandwidth adjustable digital filter is implemented as a fourth order butterworth low pass filter with a 3dB cutoff frequency at $\frac{1}{4}$ of the EB sampling frequency. In other words the bandwidth of the low pass filter can vary between 5 Hz at idle speed to 50 Hz at full speed.
- The digital filter is implemented according to the description in Section 3.1.

The signal used to examine the aliasing effect with and without bandwidth adjustable filters is a simulated pressure trajectory in an SI engine's intake manifold. It is shown in [2] and [7] that the pressure in the intake manifold can with good accuracy be described by the following Fourier series,

$$\begin{aligned} p_{man} =& a_1 + a_2 \sin(2\pi f_e t - \phi_1) \\ & a_3 \sin(4\pi f_e t - \phi_2) + a_4 \sin(6\pi f_e t - \phi_3) + \nu \end{aligned} \quad (7)$$

where a_x are the individual Fourier coefficients which can be found by FFT analysis, f_e is the event frequency, ϕ_x is the phase change caused by the transit time of the pressure pulse from the intake port to the measurement point. ν is a white noise process encompassing unmodelled dynamics and measurement noise. Equation (7) clearly shows that

the sampled data is bound to become aliased at lower engine speed, since the sampling frequency is equal to the event frequency. The frequencies above 10 Hz to approximately 50 Hz (filter cutoff freq.) will thus be folded into frequencies between 0 and 10 Hz. In this case the perturbation, δ_{err}, of the mean value, without considering noise and filtering effects, can be derived as,

$$\begin{aligned}\delta_{err} = & -a_1 \sin(2\pi f_e \tau_p) - a_2 \sin(4\pi f_e \tau_p) \\ & - a_3 \sin(6\pi f_e \tau_p) \\ & = a_1 \sin(-\phi_1) + a_1 \sin(-\phi_2) + a_1 \sin(-\phi_3)\end{aligned} \quad (8)$$

where

$$\tau_p = \frac{l}{\sqrt{\gamma R T}}$$

with τ_p the travel time of the pressure pulse from the intake valve to the measurement point, and l the distance between these two points.

Figure 6 shows a simulated intake manifold pressure trajectory for engine speeds from 1000 rpm to 6000 rpm and back again. The pressure trace has been simplified e.g. the manifold filling dynamics have been neglected and the coefficients in equation (7) are assumed to be independent of engine operating point. These simple physical assumptions are only made to illustrate clearly the effect of signal aliasing.

The figure clearly shows the aliasing problem at low engine speeds. This is as expected since the analog anti-aliasing filter is, as mentioned previously, adjusted such that the signal spectrum at high engine speeds are preserved as accurately as possible.

5 CONCLUSION

This paper has addressed the aliasing problem involved with EB sampling and has proposed three Analog/Digital Anti-Aliasing filters to solve this problem. All proposed filters sample the data at a constant sampling time. Then with a subsequent digital filtering process, the samples are processed (continuously or in a batch mode) such that the spectrum of each signal fulfills Shannon's sampling law, i.e., that the highest desired frequency is no more than half the event based sampling frequency.

6 NOMENCLATURE

Acronyms.

EB: Event Based.

ECU: Engine Control Unit.

OBD: On Board Diagnostic.

TB: Time Based.

TWC: Three Way Catalyst.

Variables, Parameters and Constants.

a_x^q: x'th denominator coeffient in the q'th digital anti-aliasing filter.

b_x^q: x'th nominator coeffient in the q'th digital anti-aliasing filter.

A: Amplitude

δ_{err}: DC error due to aliasing.

f_{3dB}: 3dB cutoff frequency of the digital anti-aliasing filter, $[Hz]$.

f_{3dB}^{norm}: Normalized 3dB cutoff frequency of the anti-aliasing filter.

$f_{3dB,A}$: 3dB cutoff frequency of the analog anti-aliasing filter

f_{EB}: Event based sampling frequency, $[Hz]$.

f_s: Sampling frequency, $[Hz]$.

f_{TB}: Constant sampling frequency, $[Hz]$

γ: Ratio between specific heat capacities at constant pressure and constant volume.

I_{EB_n}: Event based interrupt at sample n.

I_{EB_n}: Time based interrupt at sample n.

N: Crankshaft revolutions per minute, $[rpm]$.

n_r: Number of samples per engine revolution.

p_{man}: Intake manifold pressure, $[bar]$.

$p_{man_{NEB}}$: Intake manifold pressure, normal Analog Anti-Aliasing Filter.

$p_{man_{EBVBW}}$: Intake manifold pressure, Analog/Digital Anti-aliasing Filter.

R: Gas constant for dry air, $287.15 \frac{J}{kgK}$

r: Ratio between EB sampling frequency and filter bandwidth.

τ_p: Travel time of the pressure puls from the intake port to the measure point in the intake manifold, $[s]$.

T_{EB}: Event based sample time, $[s]$.

T_{man}: Temperature in the intake manifold, $[K]$.

T_{TB}: Constant sample time, $[s]$.

u_n^q: Input to filter q at sample n.

y_n^q: Output of filter q at sample n.

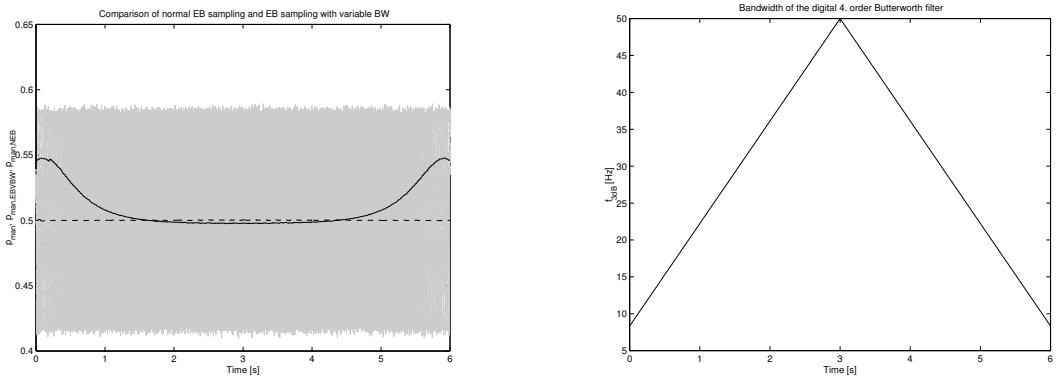

Figure 6: The left plot shows a simulated pressure trajectory in the intake manifold along with the normal EB sampling (solid line), $P_{man_{NEB}}$, and EB sampling with adjustable aliasing filter bandwidth (dashed line), $P_{man_{EBVBW}}$. The plot on the righthand shows how the bandwidth of the adjustable digital filter varies as the engine speed changes from 1000 rpm to 6000 rpm and back again.

References

[1] Chin, Y-K and Coats, F E., "Engine Dynamics: Time-Based Versus Crank-Angle Based," *SAE Technical Paper*, no. 860412, 1986.

[2] Hendricks, E., Jensen, M., Chevalier, A., Sorenson, S. C., Trumphy, D., and Asik, J., "Modelling of the intake manifold filling dynamics," *SAE Technical Paper*, no. 960037, 1996.

[3] Hendricks, E., Jensen, M., Chevalier, A., and Vesterholm, T., "Conventional Event Based Engine Control," *SAE Technical Paper*, no. 940377, 1994.

[4] Hendricks, E., Chevalier, A., and Jensen, M., "Event Based Engine Control: Practical Problems and Solutions," *SAE Technical Paper*, no. 950008, 1995.

[5] Chevalier, A. M. R., Vigild, C. W., and Hendricks. E., "Predicting the Port Air Mass Flow of Si Engines in A/F Ratio Control Applications," *SAE Technical Paper*, no. 2000-01-0260, 2000.

[6] Vigild, C. W., Andersen, K. P. H., Hendricks, E., and Struwe, M., "Towards Robust H-infinity Control of an SI Engine's Air/Fuel Ratio," *SAE Technical Paper*, no. 1999-01-0854, 1999.

[7] Chevalier, A. M. R., *Wide Bandwidth Control of the Air/Fuel Ratio of Spark Engines*. PhD thesis, The Technical University of Denmark, Institute for Automation, Aug. 1999.

[8] Trajkovski, L., "Computer Controlled Engine Management System, in danish," Master's thesis, The Technical University of Denmark, Institute for Automation, Sept. 1997.

Chapter 4

Control of sign-reversal systems

This chapter is devoted to the presentation of a newly developed estimation algorithm: the sign reversal estimator. The estimator developed is later applied in a control design for a V6 Diesel engine. The control problem involves the balancing of the intake mass flow between the compressors on a twin-turbocharger equipped V6-engine. The sign-reversal point in VGT-MAF characteristic, who's exact location is unknown, is found utilizing the estimation methodology developed.

4.1 Sign-reversal control

Most control strategies rely on a good a priori knowledge of the functional interface between the control inputs and state derivatives, or at least the sign of the transfer function should be known. The matter of sign determination can also be reformulated as; will a change in u lead to an increase or decrease of x? Assuming that the system may be described by

$$\dot{x} = f(x) + g(u) \tag{4.1}$$

this problem may be graphically illustrated as in figure 4.1.

Assuming the autonomous system, $\dot{x} = f(x)$, independent of x, is stable the functional behavior of $g(u)$ visualized in figure 4.1 is readily interpretable. First, an increase in u will increase x, which is followed by region where x decreases as u increases further. Finally, passing the local minima in a left to the right manner the slope, $\frac{dx}{du}$, is again positive. Following this trajectory the controllability of the dynamic system is lost twice when $\frac{dg(u)}{du} = 0$. Such points, where system controllability is lost followed by a slope inversion in the slope characteristic, will be referred to here as **sign reversal points**. If the transfer characteristics of $f(x)$ and $g(u)$ are assumed known with good accuracy or more generally the system

$$\begin{aligned} \dot{x} &= f(x, u) \\ y &= g(x, u) \end{aligned} \tag{4.2}$$

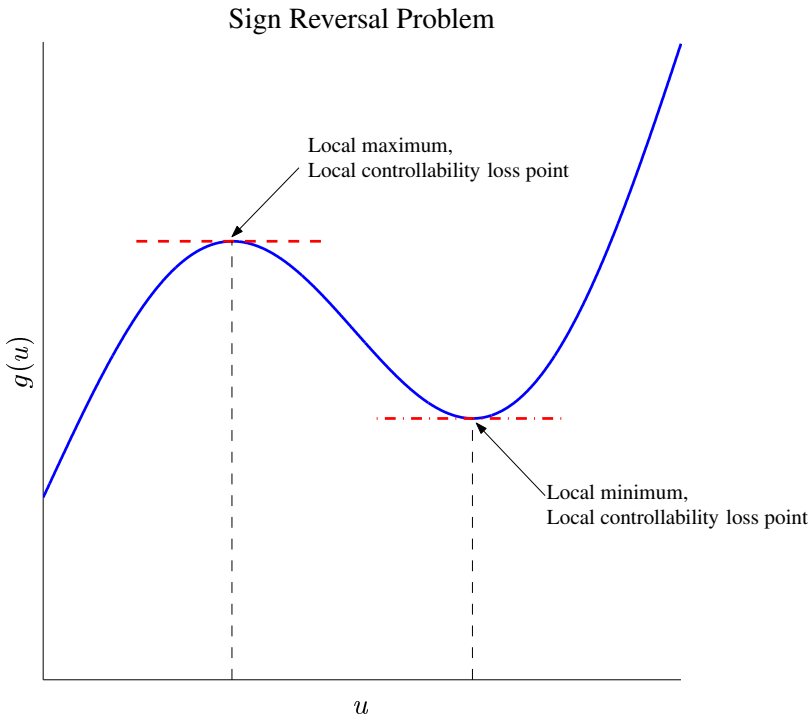

Figure 4.1: Sign reversal illustration.

is well defined, controllers based on a standard LQG (Linear Quadratic Gaussian) or $\mathcal{H}_\infty$ framework utilizing gain-scheduling techniques may readily be used, provided

$$f(x,u), g(x,u) \in C^1 \tag{4.3}$$

and

$$\begin{aligned} &\left(\left.\frac{\partial f(x,u)}{\partial x}\right|_{\substack{x=x_0\\u=u_0}}, \left.\frac{\partial f(x,u)}{\partial u}\right|_{\substack{x=x_0\\u=u_0}} \right) \text{ are stabilizable} \\ &\left(\left.\frac{\partial f(x,u)}{\partial x}\right|_{\substack{x=x_0\\u=u_0}}, \left.\frac{\partial g(x,u)}{\partial x}\right|_{\substack{x=x_0\\u=u_0}} \right) \text{ are detectable} \end{aligned} \tag{4.4}$$

Depending on the controller layout further system properties may be required (see e.g. [41, 99, 71, 24]).

In the vicinity of the sign reversal points special care must be taken to avoid chattering e.g. the controller output must be limited to u_0 when $\frac{\partial f(x,u)}{\partial u} = 0$ as long as the unlimited controller output, $K(v)$, stays within a predefined signal window[1].

[1]Controller integrator states need to be frozen when the control signal is within the predefined

It is clear from the above, that although realizable, the design of a linear controller utilizing gain scheduling to accomplish the control criteria set for systems with sign reversal points is not an easy task. Furthermore, the location of the sign reversal points in the system's transfer characteristic must be known exactly or else regions with system instability or marginal stability may be encountered. However, as shown in the modelling chapter, the accuracy of automotive models may not be high enough that such a gain-scheduled linear control design can be used.

This section will introduce a new and simple nonlinear estimation methodology - *the sign reversal estimator*. The basic idea behind this estimation was conceived while studying a well known radio broadcasting technology[2], namely the AM broadcasting system. The basic principle behind AM broadcasting lies in the well known cosine-sine relations repeated below

$$\begin{aligned} \cos(\alpha \pm \beta) &= \cos(\alpha)\cos(\beta) \mp \sin(\alpha)\sin(\beta) \\ \sin(\alpha \pm \beta) &= \cos(\alpha)\sin(\beta) \pm \sin(\alpha)\cos(\beta) \\ \cos^2 &+ \sin^2 = 1 \end{aligned}$$

Using the above relations the following is readily derived

$$\cos^2(\omega t) = \frac{1}{2} + \frac{1}{2}\cos(2\omega t) \tag{4.6}$$

and is exactly the property used in the AM broadcasting technique. The AM technique is graphically outlined in figure 4.2.

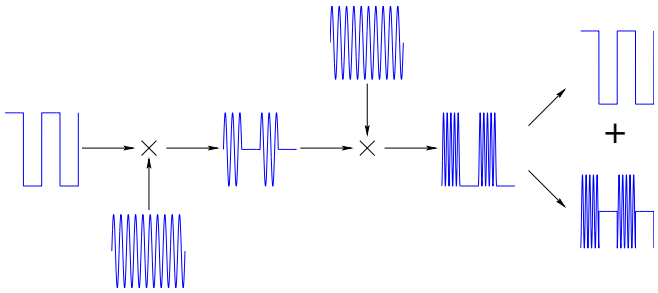

Figure 4.2: Amplitude Modulation illustration.

First the source signal, seen as an incoming square wave, is modulated with the carrier signal (the sine wave with frequency ω_c in the figure). Hence, the base signal frequency content is in the frequency spectrum moved up around the carrier frequency. This modulated signal is then transmitted through a medium, picked up by a receiver, and demodulated by a multiplication with a sine wave also with

signal window.

[2]The AM method was investigated as a possible technique to broadcast detection signals in a preliminary study of fluid temperature and velocity measurement techniques. This study was conducted by the ECG at DTU (see e.g. [110]).

frequency ω_c. The demodulated signal may now be low pass filtered, thereby removing the signal content around the frequency $2\omega_c$, amplified, and finally the source signal is recreated. This property may be exploited in a system identification process to acquire small signal amplitude and phase information for a dynamic system.

In order to apply the sign reversal estimator, only a few requirements need to be fulfilled. When the unknown system has a sine wave on one of its inputs the output of interest must fulfill the following:

- The system output may be represented by a Fourier series .i.e

$$\begin{aligned} y(t) = \Phi(t, u(t) = \sin(\omega_c t), \cdot) &= a_0 + \sum_{n=1}^{\infty} a_n \cos(n\omega_c t) + b_n \sin(n\omega_c t) \\ &= a_0 + \sum_{n=1}^{\infty} c_n \sin(n\omega_c t + \phi_n) \end{aligned} \tag{4.7}$$

- Signal energy at the carrier frequency must exist i.e.

$$(a_1 \neq 0 \quad \vee \quad b_1 \neq 0) \Leftrightarrow c_1 \neq 0 \tag{4.8}$$

- The transition function is continuous and at least one time differentiable i.e. $\Phi \in C^1$

The first two requirements insure existence of information energy at the carrier frequency ω_c, and the third requirement ensures that the slope of Φ is well defined.

Assuming the amplitude of the sine wave imposed is small enough such that small signal plant operation can be supposed, the small signal output may be approximated by

$$\delta y(t) \approx A \sin(\omega_c t + \phi) \tag{4.9}$$

where the amplitude A may be interpreted as the secant of the Φ region excited by $\delta u(t) = sin(\omega_c t)$.

The next problem is the isolation of $\delta y(t)$. This problem is solved using a tuned linear second order filter, referred to as a *pick-up* in the following, designed to attenuate frequencies around ω_c. The transfer function of this filter is

$$H_{\text{pick-up}}(s) = \frac{K}{s^2 + 2\zeta\omega_n s + \omega_n^2} \tag{4.10}$$

where ζ is the damping ratio, ω_n is the undamped filter frequency, and K is the filter amplification. The filter parameters K and ω_n are adjusted such a way that the requirements in equation 4.11 are fulfilled.

$$|H_{\text{pick-up}}(\jmath\omega_c)| = 1 \quad \wedge \quad \left.\frac{d\,|H_{\text{pick-up}}(\jmath\omega)|}{d\omega}\right|_{\omega\,=\,\omega_c} = 0 \tag{4.11}$$

However, the application of this filter will shift the phase of $\delta y(t)$ somewhat, which later on must be considered in the A and ϕ identification procedure. The filter will here be referred to as a pick-up filter due to its amplitude characteristic.

The pick-up filter output is subsequently multiplied by $\cos(\omega_c)$ and $\sin(\omega_c)$, respectively. Hence the following estimation signals are created

$$\begin{aligned}\hat{\tilde{y}}_1 &= A\sin(\omega_c t+\phi+\phi_{pu})\sin(\omega_c t)\\ &= \frac{1}{2}A\cos(\phi+\phi_{pu})-\frac{1}{2}A\cos(2\omega_c t+\phi+\phi_{pu})\\ \hat{\tilde{y}}_2 &= A\sin(\omega_c t+\phi+\phi_{pu})\cos(\omega_c t)\\ &= \frac{1}{2}A\sin(\phi+\phi_{pu})+\frac{1}{2}A\sin(2\omega_c t+\phi+\phi_{pu})\end{aligned} \tag{4.12}$$

where ϕ_{pu} is the pick-up filter phase shift mentioned at the carrier frequency ω_c. These signal are subsequently low-pass filtered, thus providing the two quasi steady state signals

$$\begin{aligned}\hat{y}_1 &= \frac{1}{2}A\cos(\phi+\phi_{pu})\\ \hat{y}_2 &= \frac{1}{2}A\sin(\phi+\phi_{pu})\end{aligned} \tag{4.13}$$

Finally, utilizing the equation above the small signal amplitude and phase shift are estimated as

$$\boxed{\begin{aligned}\hat{\phi} &= \begin{cases}\arctan\left(\frac{\hat{y}_2}{\hat{y}_1}\right)-\phi_{pu} & -2\pi \quad , \quad \hat{y}_1,\hat{y}_2\geq 0\\ \vdots & +0 \quad , \quad \hat{y}_1\geq 0,\hat{y}_2<0\\ \vdots & -\pi \quad , \quad \hat{y}_1<0\end{cases}\\ \hat{A} &= \begin{cases}2\frac{\hat{y}_1}{\cos(\hat{\phi}+\phi_{pu})} & , \quad \hat{\phi}+\phi_{pu}\in\left[\frac{-\pi}{4};0\right]\cup\left[\frac{-5\pi}{4};\frac{-3\pi}{4}\right]\cup\left]-2\pi;\frac{-7\pi}{4}\right]\\ 2\frac{\hat{y}_2}{\sin(\hat{\phi}+\phi_{pu})} & , \quad \hat{\phi}+\phi_{pu}\in\left]\frac{-3\pi}{4};\frac{-\pi}{4}\right[\cup\left]\frac{-7\pi}{4};\frac{-5\pi}{4}\right[\end{cases}\end{aligned}} \tag{4.14}$$

Due to the estimator's construction phase shifts can only estimated within a 360° window. However, most physical automotive subsystems can at best be described as low-pass filters with a falling phase shift characteristic, and the system's signal amplification is normally heavily attenuated after the first -180° of phase shift. Thus, it is decided to position the phase in a $[0;360°[$ window, since this is the phase window normally of interest for most normal control applications. However, for the sake of completeness, systems with a large time delay in the signal path should be mentioned. Here system amplitude characteristic may remain flat while the phase is undergoing large changes.

Since the sign reversal estimator does not contain any model, dynamic nor non-dynamic, providing innovation information in a broad frequency window, the estimator can only provide amplitude and phase information at one frequency only

- the carrier frequency ω_c. However, to put it a bit philosophically; too much information may equal entropy increase – it is not the amount of information that matters, it is the right information that matters. Increasing the number of necessary identification algorithmic procedure steps, prerequisites and assumptions etc. aiming to lower information entropy might instead unwillingly increase the entropy.

4.1.1 VGT-MAF sign reversal control

An example of a system where sign reversal may be encountered is in the translation of the VGT position, θ_{vgt}, to engine air mass flow. Normally, closure of the VGT will lead to a higher fresh air mass flow, MAF, to the engine. Assuming the EGR valve is closed, such that the EGR–VGT interaction can be neglected, a slight closure of the nozzle vanes around the turbine rotor will increase the pressure drop across the turbine implying a potential energy increase. Assuming that turbine efficiency changes may be neglected, the transformation of this extra potential energy into kinetic energy will speed up the turbine. The faster revolution of the turbo wheel leads to an increase of the intake manifold pressure and thereby increase the intake port air mass flow. Furthermore, since the compressor fundamentally speaking is a *mass flow follower* the fresh air mass flow to the engine, MAF, will also be increased. The extra exhaust mass flow will increase the speed of the turbocharger further until the equilibrium $\dot{m}_c \Delta h_{0,c} + \tau_{aux}\omega_t = \dot{m}_t \Delta h_{0,t} \eta_{t,TS}$ is reached. However, further closure of the VGT might at some point lead to a drop in MAF although the pressure drop across the turbine is increased. This is due to the steep slope of the nozzle ring friction. Hence, the thermodynamic power delivered to the turbine rotor will drop, followed by decreasing turbocharger speed, intake manifold pressure and MAF. The reader is referred to chapter 2 where the dynamic behavior of the individual subsystems are explained.

The phenomenon just explained is graphically illustrated in figure 4.3. The figure shows a ϕ-θ_{vgt} 1D WAVE® model[3] mapping of the θ_{vgt}–MAF characteristics for a V6 DI Diesel engine. The engine is equipped with two turbochargers fitted to a split intake manifold construction. The mapping was accomplished utilizing a MATLAB®/SIMULINK®–WAVE® maximum/minimum procedure interface developed by the author.

The left upper contour plot in figure 4.3 shows the anticipated behavior of VGT closure leading to a MAF gain can be expected independently of engine fuelling and VGT position at an engine speed of 1500rpm (revolutions per minute). This is as expected since the exhaust energy is relatively low at 1500rpm and lower. At an engine speed of 2000rpm the first signs of sign reversal begin to emerge. Closing the VGT below a point of approximately 0.15 will lead to a MAF decrease instead of the expected increase. The same behavior is also clear in the 2500rpm to 3500rpm contour plots. However, a model related problem was encountered here, related to the sparse turbocharger map density in the outer operating regions of

[3]Dr. Arnd Sommerhoff from FFA is gratefully acknowledged for the provision of the WAVE® engine model, and for the discussions during the interpretation of the simulation results obtained.

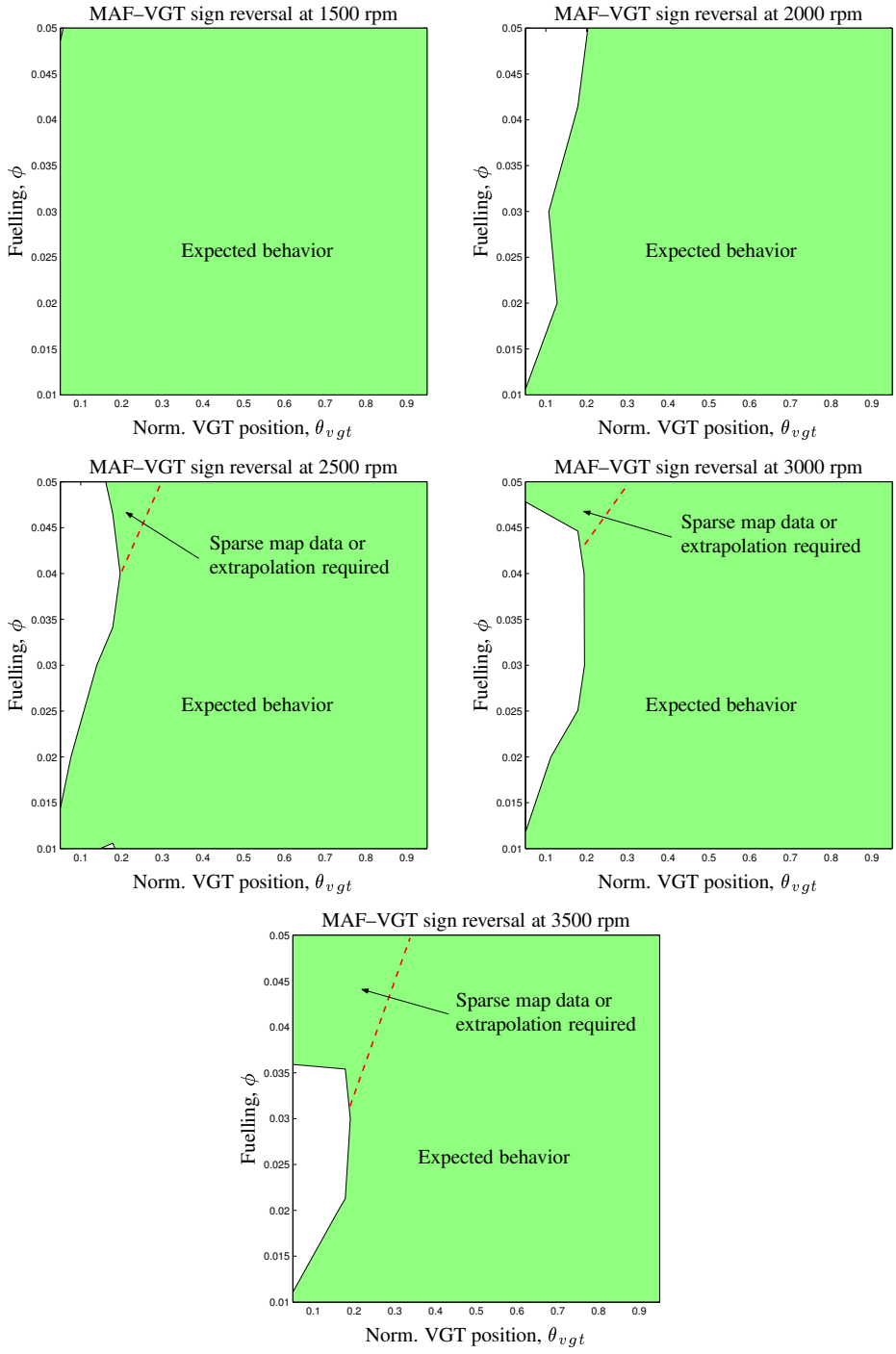

Figure 4.3: Sign reversal regions found by 1D WAVE® simulation. In the green regions the VGT equipped turbochargers behave as expected i.e. VGT closure leads to a higher mass flow through the compressor. The red dashed border line indicates regions where turbine/compressor map data density is low or where map extrapolation is required.

the turbocharger. This problem is already addressed in the turbocharger modelling section. Hence turbocharger operation in this area might lead to large modelling errors. This is mainly noticed in the 2500rpm–3500rpm contour plots as an overrated turbine efficiency. Instead, the boundary between normal and inverted VGT operation is believed to follow the red dashed line. The turbocharger maps used during the WAVE® simulation study could have been extended using the turbocharger modelling techniques developed in section 2.3, and thereby probably provide a better simulation performance. However, since the simulation study is very time consuming[4] and the existence of sign reversal has been proven, further WAVE® simulation studies have been omitted. Furthermore, the point of sign reversal is also dependent upon the ambient conditions, and an exact specification of where inverted VGT operation can be expected is thus difficult to predict or map.

Simulation studies at higher engine speeds have been omitted since the maximum rated turbocharger speed is reached before the point of sign reversal.

4.1.1.1 MAF Balancing

Having proven the existence of a sign reversal point in the θ_{vgt}–MAF characteristic this section will illustrate how control problems arising from sign reversal points can be avoided when balancing the MAF between two turbochargers on a Diesel V-engine.

The control problem to be presented is not only present with blue sky research projects but is already an issue with commercially available engines. Examples of commercially available passenger cars featuring a twin turbocharged engine design are the 4.0 liter V8 BMW engine, the Mercedes 4.0 liter Diesel V8 in the S400 CDI, and the V6 and V10[5] Diesel engines manufactured by Volkswagen. All these engines use twin turbochargers to reached their individual performance targets. The control problem to be presented is therefore of generic nature.

The V6 engine is fundamentally speaking designed like two three cylinder engines sharing a common crankshaft and intake manifold, and each engine bank has its own set of sensors and actuators. The location of the engine sensors and actuators are shown in the engine illustration in figure 4.4.

The V6 Diesel engine is modelled in the MATLAB®/SIMULINK® environment using the zero dimensional modelling methodologies explained in chapter 2, except for the turbochargers and EGR cooling system[6][7]. The turbocharger efficiency and mass flow rate of the compressor and turbine, respectively, are modelled by single polynomial regression equations. This turbocharger modelling concept caused

[4]The WAVE® simulation study presented used more than one week of effective simulation time on a HP work-station

[5]The V10 Diesel engine is part of the engine program for the new VW Phaeton to be introduced.

[6]The V6 Diesel MVEM was constructed from an existing model of an Diesel engine, see e.g. [108]

[7]Dr. Urs Christen is gratefully acknowledged for helpful discussions during the development of the first V6 model

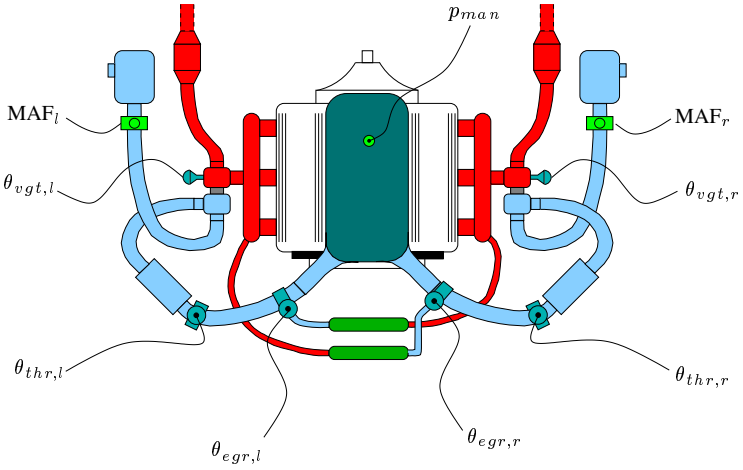

Figure 4.4: Schematically illustration of the V6 Diesel engine together with the location specification of selected sensors and actuators.

certain problems during the simulation study, which will be addressed later in this section[8]. Furthermore, the turbochargers used are approximately 60% too large[9] and high intake manifold pressures ($>$1.8 bar) in the mid-load engine operating range are inaccessible. However, despite the oversized turbochargers the sign reversal point is present in the characteristic, and the turbocharger model is thus good enough to prove the validity of the sign reversal control concept.

The EGR cooler's effectiveness level and the mass flow rate through the system are described by regression equations [108].

The V-engine design combined with the use of a bi-turbo–common manifold strategy might lead to certain imbalance problems between the engine banks for the following reasons:

- If the engine is mounted in an east–west manner in the engine compartment a difference in the ambient air temperature surrounding the two exhaust manifolds will inevitably exist. Furthermore, the convective heat transfer between the front side exhaust manifold will be forced more strongly than the heat transfer on the engine backside. Thus, depending on vehicle speed and ambient temperature the energy level in the two exhaust manifolds may be different, and front side turbocharger's speed will be lower than the backside turbocharger's speed. This speed difference may cause the turbocharger with the lower speed to go into surge operation, dependent on the intake manifold pressure.

[8]The problems encountered with regression based model were the motivation behind the physically derived turbocharger model presented in the modelling chapter.

[9]The layout of the V6 was not fixed at the time the simulation study was conducted. It was therefore decided to use the turbocharger model readily available from another Diesel engine model.

- Due to packaging restrictions the design of the individual throttle bodies may be significantly different in both volume and shape posing both transient and steady state balancing issues between the two engine banks. One issue could be a significant difference in the breathing behavior between the two engine banks.

- Since the intake manifold is shared a normal speed density strategy can only estimate the total mass flow to the engine. This may lead to an EGR imbalance between the banks, since the normal speed density-MAF based EGR estimation strategy can only provide an estimate of the total EGR mass flow to the engine and not how the EGR mass flow, $\dot{m}_{egr}$ is distributed between the two banks.

- In the case where a significant EGR imbalance between the banks exists, despite non-discriminating VGT control, danger of turbocharger surge is present due to the significant difference in the energy flow through the individual VGTs.

Two of the imbalance issues above concerns the danger of surge. One way (neglecting the relative small pressure drop difference between the throttle bodies and the possible difference between the compressors) to minimize the danger of one turbocharger pushing the other turbocharger into surge operation is to insure that the speed of the turbochargers are kept at the same value. However, a direct measurement of the turbocharger speed is normally not available. A way to overcome this problem is by controlling the air mass flow through each compressor, since, if the differences in the upstream conditions may be neglected and the compressors' performances are in the close vicinity of each other, controlling the mass air flow through each compressor would be equivalent to turbocharger speed control.

Control Problem Formulation

In the following the design of a MAF balancing controller capable of eliminating a possible steady state MAF difference between the engine banks will be outlined.

Eliminating a possible MAF error will minimize the danger of one turbocharger pushing the other turbocharger into surge operation. However, the control problem is difficult due to a possible presence of a sign reversal point in the θ_{vgt}–MAF characteristic. This control problem is further made worse by the fact that the existence and location of the point of sign reversal is very difficult to forecast. However, with the sign reversal estimation methodology explained earlier in section 4.1 and provided the VGT actuators have a reasonably small dead-band, it will be shown that the sign reversal point may be estimated and used to toggle the controller output sign. Although it would be possible to eliminate an eventual MAF error by only discriminating the base VGT signal from the boost pressure control strategy on one of the VGTs, such a control strategy would pose problems. When a fully opened or fully closed VGT position is reached, system controllability would be lost. Instead, the VGT base position from the ECU, $\theta_{vgt,0}$, will be offset on both VGTs, thereby

providing a broader window of system controllability. A schematic block diagram of the VGT position offset controller is shown in figure 4.5.

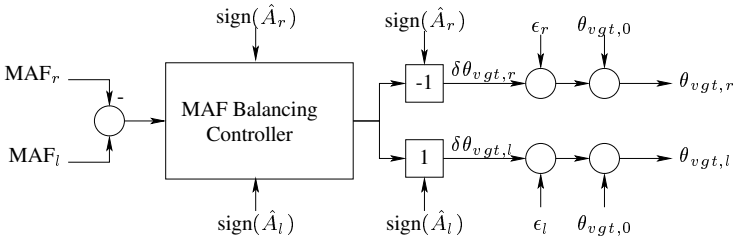

Figure 4.5: Block diagram of the VGT balancing controller setup.

A–ϕ Estimation

In order to determine the direction of control the sign of the θ_{vgt}–MAF DC amplification must be estimated. Initially different ARX (Auto Regressive eXogenous) adaptive model structures (up to fourth order) together with an imposed square wave ($\pm 0.05\theta_{vgt,span}$) on the VGT reference position were investigated as a means to determine the control direction i.e.

$$\text{sign}(\hat{A}) = \text{sign}\left(\left. \frac{\hat{b}_0 + \hat{b}_1 z^{-1} + \hat{b}_2 z^{-2} \ldots}{1 + \hat{a}_1 z^{-1} + \hat{a}_2 z^{-2} + \ldots} \right|_{z=1} \right) \tag{4.15}$$

However, the individual coefficient estimates were found to vary significantly despite quasi-steady state engine operation and therefore were not suited for DC gain estimation. Hence, further investigation of linear adaptive estimation strategies was not carried out. Instead, the nonlinear sign reversal estimator is used for control direction estimation.

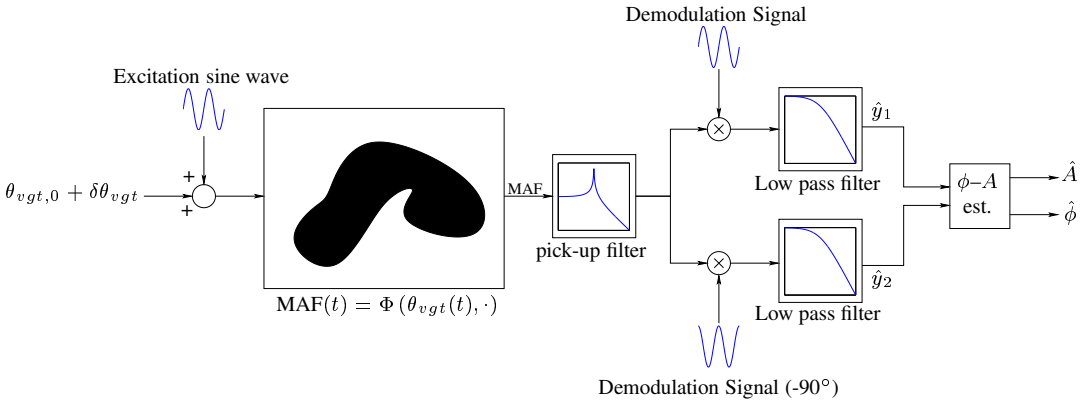

Figure 4.6: Illustration of the VGT-MAF sign reversal detection scheme for the small signal amplitude and phase.

Figure 4.6 illustrates the implementation of the estimator used for each engine bank. The control signal for the individual VGT has an excitation sine wave of frequency ω_c added to it. This excitation signal is later, after travelling through the system, isolated by a pick-up filter tuned to the frequency ω_c, followed by individual multiplications with sine and cosine waves, and sent to the A-ϕ estimation algorithm. The amplification sign is finally computed as

$$\text{sign}\left(\hat{A}\right) = \text{sign}\left(\hat{\phi} + \pi\right) \tag{4.16}$$

Due to a relative large intake manifold volume it was decided to locate the carrier frequency, ω_c, at the same frequency of 2 Hz for both banks, such that the estimation algorithms' response times are the same. Cross talk problems between the algorithms was anticipated but not encountered during simulation.

Base Control Design

The basic MAF balancing controller is a simple PI (Proportional–Integral) controller. The block diagram of the controller is shown in figure 4.7. The controller is seen to consist of two integrators and one proportional gain. The two integrators may be enabled and disabled using the $h \in \{0, 1\}$ switch and provide a method to avoid integrator wind-up.

When a control direction sign reversal is detected the individual integrator is reset through the r switch. During reset, special care must be taken when re-initializing the individual integrator to insure a bumpless transfer from one operation mode to the other i.e.

$$\begin{aligned} \delta\theta_{vgt,k} &= \delta\theta_{vgt,k-1} \\ \Downarrow & \\ I_{0,k} &= -\left(K_p\left(e_k + e_{k-1}\right) + I_{k-1}\right) \end{aligned} \tag{4.17}$$

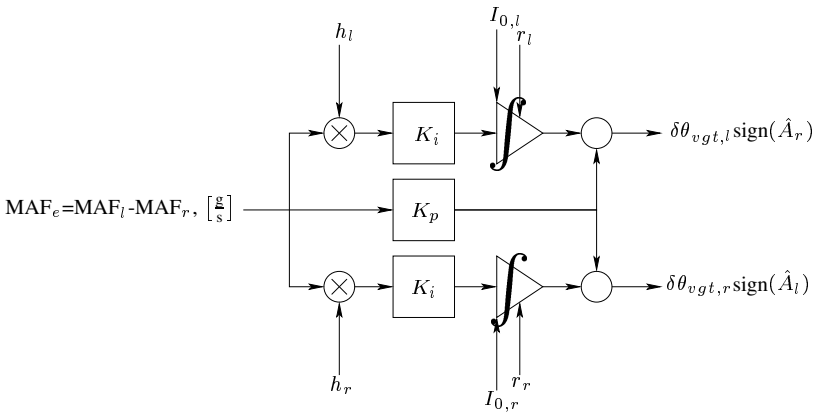

Figure 4.7: MAF balancing controller.

Carrier frequency, ω_c	2 Hz
Damping ratio, ζ	0.05
Modulation depth, A_e	0.05
Low pass filter type	Butterworth
Low pass filter order	4
Low pass filter break freq.	1 Hz
Proportional gain, K_p	1
Integration gain, K_i	5

Table 4.1: Setting of SR estimation parameters.

Logic implementation

The level of logic needed to control the integrators is limited, and basically only consists of two block, reset logic and freeze (hold) integrator logic.

The reset logic simply compares the estimated amplitude sign between neighboring samples i.e.

$$r = \left(\text{sign}(\hat{A})_k \neq \text{sign}(\hat{A})_{k-1}\right) \tag{4.18}$$

Hence, every time the sign changes the individual integrator is reset and re-initialized with the value $I_{0,k}$

Furthermore, the range of control signal, $\theta_{vgt,0} + \delta\theta_{vgt}$, has been reduced by a half of the amplitude of the excitation sine wave in each end of the control signal window. This is mandatory for the excitation sine wave to prevail independently of the control signal.

Since the offset sign of the individual VGT discrimination signal is already known, the enable/disable logic algorithm will be same for each integrator. The algorithm is listed in equation 4.19.

$$\begin{aligned} c_{low} &= (\theta_{vgt} \leq A_e)\ \&\ \left(\text{sign}(\hat{A}) < 0\right)\ \&\ (\text{MAF}_e \leq 0) \\ c_{high} &= (\theta_{vgt} \geq \theta_{vgt,max} - A_e)\ \&\ \left(\text{sign}(\hat{A}) > 0\right)\ \&\ (\text{MAF}_e \geq 0) \\ h &= \text{NOT}\,(c_{low} + c_{high}) \end{aligned} \tag{4.19}$$

The first condition checks if the minimum θ_{vgt} has been reached and the $\delta\theta_{vgt}$ control direction. If the control algorithm requests an opening of the VGT this will be allowed, however, further closure of the VGT will be prohibited. The opposite rules are valid when θ_{vgt} has reached the upper VGT position limit.

Simulation study

In order to verify the functionality of the sign reversal estimator together with the MAF balancing control strategy, several simulations with engine model presented in the beginning of section 4.1.1.1 are made in SIMULINK®. The value of some of the simulation parameters are given in table 4.1: The 2Hz carrier frequency is initially selected since it is assumed the frequency is well below the bandwidth of

the system. The MAF sensors (see e.g [6]) and VGT position actuator's dynamics are approximated by first order low-pass filters with a response time of 15ms and 100ms, respectively.

As a test sequence 430 seconds of the EUDC was chosen. However, due to the oversized turbochargers the velocity reference input to the engine speed controller is raised by 30% to insure a reasonable excitation of the turbochargers.

The base VGT control signal is acquired from a experimental mapping of a 2.0 liter Puma engine running a EUDC. The EUDC mapping has been discussed earlier in section 2.11. This base trajectory will naturally not be the same as the signal computed by the final calibrated V6 ECU, however it provides a realistic base signal input to the VGTs and spans the complete control input range of the VGTs. Furthermore, the simulations are performed without EGR to avoid cross talk between the EGR system and the turbocharger system.

The control problem is created by reducing the right engine bank's volumetric efficiency by 10%, thereby lowering the thermodynamic power available to the right bank VGT. This problem is selected since it both affects the exhaust temperature and the mass flow through the turbine. This is equivalent to control scenarios in which large temperature gradients between the exhaust manifolds exist, or when a significant difference in the bank breathing behavior is present

Figure 4.8 shows the simulation results obtained with the MAF balancing control strategy and the SR estimation algorithm enabled. The red and blue curves illustrate the right and left bank simulation results, respectively. The engine speed is seen to vary between approximately 1000rpm and 3000rpm. Below the engine speed trace the intake manifold pressure is seen. The curve clearly shows the effect of the oversized turbochargers resulting in a rather low boost pressure. The problems with the regression equation based turbocharger model are also evident, since the pressure is too large close to idle speed. Hence, the compressor model clearly overestimates the compressor mass flow here. Furthermore, the compressor efficiency is rather underestimated in the vicinity of such engine operating points and expresses itself as a too high intake temperature. It should here be note that no intercooler model is used in the simulation, and the intake temperature is thus generally high. Just below the intake manifold temperature the port mass flow for the individual bank is plotted, clearly showing the effect of the 10% volumetric efficiency difference between the engine banks.

The estimated amplitude and phase shift of the VGT–MAF system is graphically illustrated in the lower left corner of figure 4.8. The estimated amplitude, $\hat{A}$, is for both banks generally low during low load–low speed engine operation. This is as expected since the thermodynamic exhaust power is low during such operations, and the MAF sensitivity to VGT movements is thus small. During the first 60 seconds of the simulation the engine experiences a series of relatively fast tip-ins and tip-outs. The effect of this on the SR estimation is especially clear in the phase shift detection. Here, the phase shifts in a rather oscillatory manner. Between 250 and 370 seconds the engine speed is raised by a factor of two, and together with some rapid VGT tip-ins, this leads to a higher boost pressure. Due to the larger

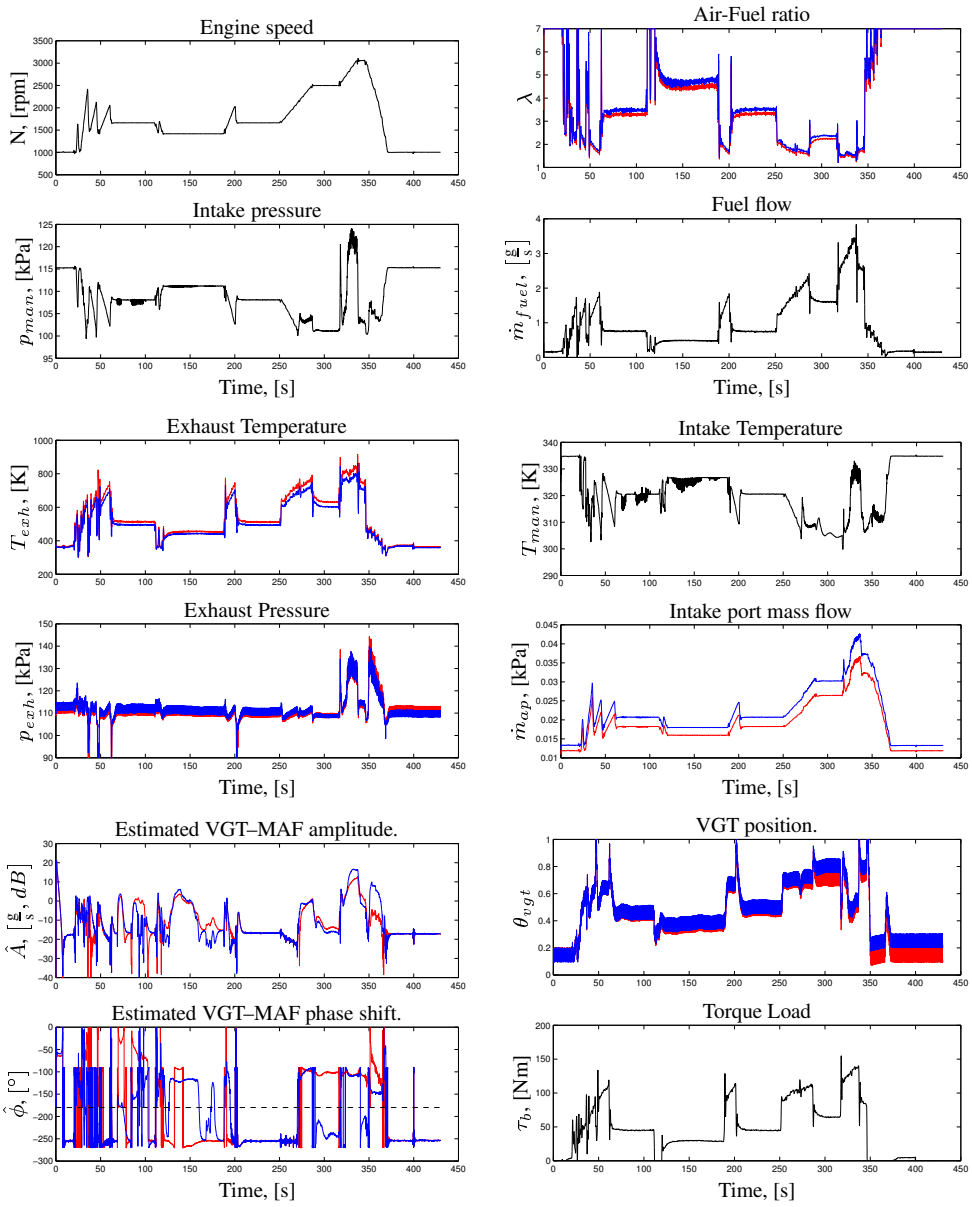

Figure 4.8: Simulation results obtained with the MAF balancing strategy and the SR estimation strategy enabled. The red and blue curves depict the right and left engine bank results, respectively. The actual sign control is depicted in the lowest left plot in the figure. Every time one of phase estimates crosses the -180° limit (dashed line) the corresponding sign is toggled.

thermodynamical power available to the turbine the VGT excitation signal propagation becomes pronounced. This is especially seen on the estimated amplitudes, $\hat{A}$, which are raised by almost 30dB. However, the amplitude $\hat{A}$ is much lower than expected and the phase change is the opposite of the expected. Hence, the carrier frequency of 2 Hz is apparently above the system bandwidth. However, assuming the structure of the system's amplitude and phase shift characteristics are maintained, this does not influence the sign reversal detection algorithm. Instead, the threshold is changed to

$$\text{sign}\left(\hat{A}\right) = -\text{sign}\left(\hat{\phi} + \pi\right) \tag{4.20}$$

and the SR algorithm thus still provides a correct estimate of the control direction. Of course the carrier frequency ω_c could be lowered, but this would effect the estimation speed negatively.

The discrimination between the individual VGT positions is clear on θ_{vgt} traces also shown in figure 4.8, and as expected the right bank VGT needs to be closed more due to the lower exhaust mass flow.

Figure 4.9 shows the simulation results obtained with no balancing control, MAF balancing control and excitation but the sign reversal algorithm disabled, and MAF balancing control, excitation and SR detection. The plots where no balancing control is implemented clearly show a difference between the MAFs during moderate boost pressures. However, during the engine idling or low load scenarios the error is negligible as expected due to the low exhaust energy available. Thus, the turbochargers are more or less inactive.

The mid section of figure 4.9 depicts the results obtain with the PI balancing controller implemented but with the SR algorithm disabled. The figures clearly show how the system becomes unstable in the regions where the control direction is the opposite of the expected. Between 300 and 430 seconds the control direction returns to normal and the MAF error between the banks is minimized.

In the last part of figure 4.9 the SR algorithm provides an estimate of the control direction. Using this estimate to toggle the control direction of the MAF balancing controller clearly improves the control performance. The scatter in the MAF error between 70 and 170 seconds on the MAF error trace is not due to the detection algorithm. This is seen by comparing the estimated phase shift in figure 4.8 with the MAF error trace, since the chatter frequency is much higher than both the sign shift and excitation frequency. Instead, the chattering is believed caused by internal discontinuities in the turbocharger model.

Figure 4.9 clearly proves the sign reversal estimators ability to correctly assess the control direction.

Implementation Issues

Implementation of the MAF balancing strategy may cause certain problems summarized below.

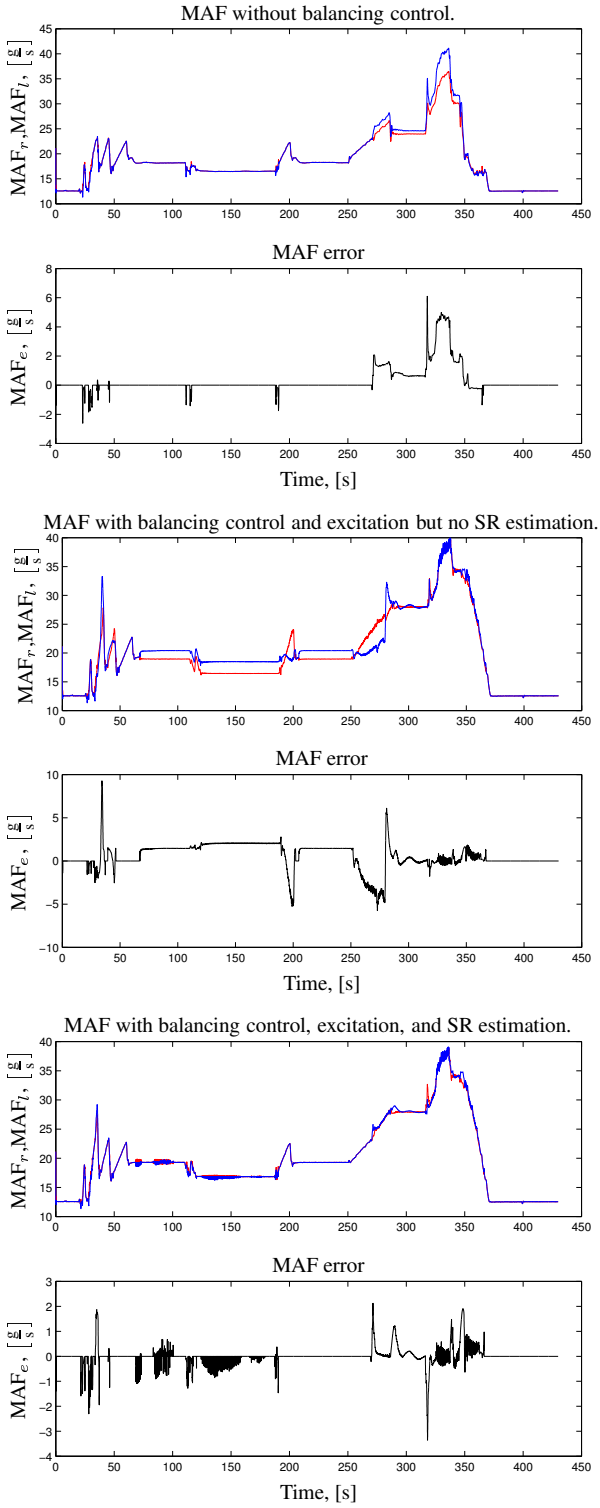

Figure 4.9: MAF balancing scenarios with no control, control and excitation but no SR detection, and control, excitation and SR detection enabled. The red and blue curves represent the right and left compressor mass flow, respectively.

MAF error: MAF sensors based on hot wire or hot film technology are known to drift with age. In [94] relative errors in the range of -25% are reported. Furthermore the relative error is found to increase with flow rate. Hence, implementation of the MAF balancing strategy might unwillingly lead to MAF imbalance and force one of the turbochargers into surge operation.

Excitation: The excitation signal imposed on the VGT position might degrade drivability.

Dead band: The pneumatic actuators normally used to control the VGT positions have a relatively large actuation dead band, which may render suitable excitation impossible. Hence, implementation of the SR algorithm may call for electrical actuation of the individual VGT position, and thus add to production cost. However, electrical drives are normally faster compared to their pneumatic equivalents and have a build-in position sensor. Therefore both OBD and the control task may benefit from this added bandwidth and feedback information.

The probably biggest hinderance for a successful implementation of MAF balancing strategy is the possible presence of a large MAF measurement error. Furthermore, the MAF measurement is together with an adaptive loop normally used to update the volumetric efficiency table when EGR is disabled. This renders it impossible to use the speed density strategy in a sensor fusion strategy to reduce the influence of MAF measurement errors.

A successful implementation of a MAF balancing strategy will require high precision MAF measurements.

4.1.2 Summary

In this section a new and simple methodology to detect sign reversal points in the input-output characteristic of a given dynamic system is presented. The method is based on system excitation by sine waves of known frequencies to assess the gain and phase shift of the system. The method is successfully applied on a bi-turbo equipped V6 engine model to balance the intake mass flow air between the two compressors. Despite local curvature in the turbocharger's characteristics resulting in derivative sign changes the sign reversal algorithm is able to detect points of sign reversal. This is later used to toggle the sign of the implemented MAF balancing controller's output thereby maintaining the desired control direction.

Chapter 5

Conclusions and recommendations

The conclusions drawn from this work will in this section be presented along with future horizons of work.

5.1 Conclusions

The dissertations opens with a presentation of two papers both about the same control problem: *Air/Fuel Ratio Control of Spark Ignition Engines*. In the article entitled "*Towards Robust $\mathcal{H}_\infty$ Control of an SI Engine's Air/Fuel Ratio*" the AFR control problem is addressed by developing a dynamic description of the AFR path through the engine to the AFR measurement point in the exhaust pipe. The fuel-film dynamics is lumped into this model. The existing transport time delay between fuel injection and λ measurement is approximated by a Padé filter. Since it was decided to implement the AFR time based the time delay varies with engine speed. The effects of this time delay variation are included in the model using physical considerations. Using a $\mathcal{H}_\infty$ framework the controller is made robust with respect to time delay and volumetric engine efficiency variations, respectively. Hence, the controller does not need the presence of a fuel-film compensator and a volumetric efficiency look-up table to function. The $\mathcal{H}_\infty$ was tested on an engine dynamometer at DTU, and found capable of keeping the experimental SI engine's AFR in the close vicinity of the desired AFR level despite fast throttle actuation.

The second article is based on a dynamic model of the intake manifold pressure and temperature augmented with models of the intake air thermocouple dynamics, engine pumping fluctuations (empirical), and a limited "integrator" state to account for possible errors in the algebraic throttle mass flow model, $\dot{m}_{at}$. This model is used in a estimator-predictor setup, where the predictor is initialized by the estimator to each sampling time. The estimator itself is a basic EKF. The noise intensities required for the observer gain calculation are prior to the filter design computed utilizing Lyapunov formula inversion. By delaying the throttle command a fixed number of engine samples, the prediction scheme makes it possible to counteract

the injection delay. Since the base controller runs open loop, steady state AFR errors are unavoidable. These errors are eliminated by a simple PI control law around the exhaust pipe λ sensor. The controller was successfully tested on an engine dynamometer setup at DTU. Despite severe throttle actuation scenarios the predictive controller was able to maintain the AFR close around the stoichiometric level. However, some tuning of the implemented fuel-film compensator was needed to reach acceptable AFR control performance, and may have masked some of the problems with the predictive control strategy.

Both controllers briefly presented above utilize an underlying observer to describe the dynamic behavior of the signal path of interest, and both observers are derived utilizing the MVEM framework. However, the control philosophies utilized in the two papers are completely different although the control target is the same. This diversity provides a basic validation of the MVEM framework since it shows that the MVEM framework makes possible a generic dynamic description of a NA SI engine's intake manifold. Hence, future research in the possibilities of this framework is of clear interest to the engine control community. However, due to new technologies this modelling framework must be extended with new engine sub-models. This is one of the main thrusts of this dissertation.

Controlling the internal combustion engine has become a challenging task and with the equipment and components being introduced to boost engine performance and lower emissions, the control burden is likely increase in the future. One way to increase performance and improve mileage is by engine-downsizing necessitating intake air compression, and with the advances made in turbocharger technology in the recent years, a big fraction of the next decade's engines are most likely to be turbocharged. Hence, the dissertation has put a large emphasis on turbocharger modelling intended for control- and simulation purposes leading to the development of a new VGT turbocharger model. The new model provides a comprehensive picture of the link between the turbine nozzle position, the mass flow through the compressor and turbine, and of the enthalpy loss distribution between the individual stages. Furthermore, since the models are based on physical considerations alone they scale very well with different turbochargers and offer good extrapolation properties.

Next, the dynamic behavior of the EGR system has been investigated especially with the goal to estimate the EGR outlet temperature using a newly developed simplified model of the EGR system. The immediate importance of a good knowledge the EGR outlet temperature is clear for an accurate dynamic description of the intake manifold temperature. Unfortunately, due to a possible unfortunate mixing processes between the EGR system's and the intake manifold's gaseous matter, correct assessment of the EGR system's outlet temperature in a MVEM framework is troublesome. This simulation finding is later confirmed by measurements obtained from a 2.0 liter turbocharged DI Diesel engine equipped with a water-mantel EGR cooler. The EGR mass flow cannot be computed from the measurement information provided by the MAF sensor and the thermocouples located upstream of EGR inlet point, in the EGR pipe connection, and intake manifold information alone,

when the pressure ratio across the EGR systems oscillates around one.

The introduction of EGR introduces additional control challenges than the temperature measurement problem mentioned above. After having set up the dynamic and algebraic equations necessary for an inspection of the burnt mass fraction in the intake manifold, it is found that the EGR rate or burnt mass fraction F_{man} may only be controlled in open loop even given exhaust gas composition information from a λ or O_2 sensor. Therefore, robust control of the EGR system is impossible.

A new method of phenomenological combustion modelling based on Locally Weighted Least Square (LWLS) estimation is introduced and evaluated on combustion data from a 2.0 liter Diesel engine. The method seems to be a good tool to capture fast and efficiently the behavior of the engine efficiency, η_i, engine mean effective friction pressure, FMEP, and the exhaust gas energy fraction, ζ_{exh}.

Most of the modelling framework presented is at the present time implemented in stand alone engine simulation models providing valuable dynamic input to extern engine emission models and power-train models. A more detailed discussion of such model applications is not included in this dissertation for confidentiality reasons.

A new family of anti-aliasing filters intended for use with event based control strategies is presented which offers optimum bandwidth without violating Shanon's sampling law. Hence, the filters will allow for a boost of event based strategies' control performance in the medium to high speed engine operating range.

The dissertation closes with a presentation of a new control methodology, the sign reversal controller. The controller is developed and discussed in this work. The estimation of the point of input–output characteristic sign reversal is computed by Amplitude Modulation methods. The sign reversal estimation is later used to toggle the output signal sign on a MAF balancing controller developed for bi-turbo V-engine designs. The estimator-controller combination is subsequently verified on a high order V6 engine simulation model. The estimator was able to maintain system stability without use of any underlying model-based observer structure.

5.2 Recommendations

One thought comes in to mind when remembering the experiences during the author's time in the automotive industry: model-controller interaction. Quite often the design of the engine's air path is changed frequently in a number of fundamental ways from the time the engine is still just a name on the paper until the first one leaves the production plant. The experience is: the design often changes faster than a proper accompanying analysis of control and estimation properties like plant observability and controllability can be made. Hence, future emphasis should be put on developing and enhancing simple object oriented engine models enabling a fast estimation and control plant analysis.

Although this work has emphasized heavily the modelling aspect, a large task

is still pending: after-treatment system modelling for control and zero-dimensional engine simulation studies. Such models would provide vital information when designing control systems as operating the engine in the most fuel efficient way is not necessarily equivalent to minimizing the emissions. A few examples are:

Catalyst light-off: Modern diesel engines with their extraordinary fuel efficiency pose a serious problem with oxidation catalysts – their low exhaust temperature when idling. Although a good oxidation catalyst lights off between 150 and 200°C this limit might not be low enough to keep the catalyst active during all driving scenarios. An idle speed exhaust temperature as low as 100° is not unlikely, and the catalyst may thus go inactive. Hence, this may lead to excessive exhaust emissions when a long period of engine idling is followed by an engine acceleration.

DPF control: DPFs pose a number of control problems of which two will be mentioned here. First, as the filter become more and more contaminated with particles the pressure drop across the filter increases (up to 70kPa at maximum rated engine speed). This will naturally offset the EGR and VGT control maps. Hence, future VGT and EGR control strategies must be designed to be robust with respect to DPF influences. Secondly, the filter must be regenerated (the particulate matter is oxidized) within regular intervals. Hence the exhaust/filter temperature needs to be controlled, especially when no fuel additives are used.

TWC control: The emission storage capacity or regeneration of the TWC requires modelling so that more realistic AFR control studies of SI engines may be initiated.

The MVEM modelling concept for AFR control itself may in the coming years need augmentation with new sub-models or restructuring. Modern throttle-less natural aspirated engines, like the BMW VVL equipped SI engine, do not share the same dynamic intake manifold behavior as their throttled equivalents, i.e. there is no filling–emptying of the intake manifold during accelerator pedal tip-ins and tip-outs. Furthermore, direct application of the speed-density equation as a means to estimate the engine port mass flow is made difficult by the extra degrees of freedom offered by the VVL and VVT technologies.

Appendix A

Reduction of $W_{1,\theta,r}$

In [84] the tangential velocity component of the fluid relative to the compressor impeller is derived to be

$$W_{1,\theta,r} = \frac{1}{\cos\beta_1}\left(\sqrt{U_1^2 + C_1^2} + \frac{\cos\left(\beta_1 - \beta_{opt}\right)}{\sin\beta_{opt}} C_1\right) \tag{A.1}$$

This expression may however be reduced considerably. First the expression is rewritten into

$$\begin{aligned} W_{1,\theta,r} &= \frac{1}{\cos\beta_1}\left(\sqrt{U_1^2 + C_1^2} + \frac{\cos\left(\beta_1 - \beta_{opt}\right)}{\sin\beta_{opt}} C_1\right) \\ &= \frac{C_1}{\cos\beta_1}\left(\sqrt{\frac{U_1^2 + C_1^2}{C_1^2}} + \frac{\cos\beta_1\cos\beta_{opt} + \sin\beta_1\sin\beta_{opt}}{\sin\beta_{opt}}\right) \\ &= \frac{1}{\cos\beta_1}\sqrt{U_1^2 + C_1^2} + C_1\left(\frac{\cos\beta_{opt}}{\sin\beta_{opt}} + \frac{\sin\beta_1}{\cos\beta_1}\right) \\ &= \frac{1}{\cos\beta_1}\sqrt{U_1^2 + C_1^2} + C_1\left(\cot\beta_{opt} + \tan\beta_1\right) \end{aligned} \tag{A.2}$$

β_1 is defined by velocities as

$$\beta_1 = \arctan\left(\frac{-C_1}{U_1}\right) \tag{A.3}$$

Inserting equation A.3 in A.2 yields

$$W_{1,\theta,r} = -\frac{C_1^2}{U_1} + C_1\cot\beta_{opt} + \frac{1}{\cos\beta_1}\sqrt{U_1^2 + C_1^2} \tag{A.4}$$

Utilizing Euler's laws allows $\arctan(y)$ to be rewritten as

$$\begin{aligned} y = \tan x &= \frac{e^{\jmath x} - e^{-\jmath x}}{\jmath\left(e^{\jmath x} + e^{-\jmath x}\right)} = \jmath\frac{1 - e^{2\jmath x}}{1 + e^{2\jmath x}} \\ \Updownarrow & \\ x = \arctan y &= \frac{1}{2}\jmath\ln\left(\frac{\jmath + y}{\jmath - y}\right) \end{aligned} \tag{A.5}$$

and $\cos(x)$ as

$$\cos x = \frac{e^{jx} + e^{-jx}}{2} \tag{A.6}$$

Using the two above equations the following may be derived

$$\cos(x) = \cos(\arctan y) = \frac{1}{\sqrt{y^2+1}} \tag{A.7}$$

Now by substituting $\frac{-C_1}{U_1}$ for y equation A.4 may be rewritten as

$$W_{1,\theta,r} = -\frac{C_1^2}{U_1} + C_1 \cot \beta_{opt} + \sqrt{1 + \frac{C_1^2}{U_1^2}}\sqrt{U_1^2 + C_1^2} \tag{A.8}$$

and after reduction the relative inlet gaseous velocity tangential to the compressor impeller blades is found to be

$$\boxed{W_{1,\theta,r} = U_1 + C_1 \cot \beta_{opt}} \tag{A.9}$$

q.e.d.

Appendix B

Impeller incidence loss

The enthalpy loss due to the collision between the fluid and the compressor impeller during compressor entry may be derived as,

$$\Delta h_{loss,inc} = \frac{1}{R_{i,s}^2 - R_{i,h}^2} \left(\frac{\pi^2 N_c^2 \left(R_{i,s}^4 - R_{i,h}^4 \right)}{60^2} + \frac{\pi N_c C_1 \cot \beta_{1,opt} \left(R_{i,s}^3 - R_{i,h}^3 \right)}{45} + \frac{C_1^2 \cot^2 \beta_{1,opt} \left(R_{i,s}^2 - R_{i,h}^2 \right)}{2} \right) \tag{B.1}$$

Furthermore, the following geometrical constraints are given

$$R_{i,s} > R_{i,h} \qquad R_{i,s}, R_{i,h} > 0 \tag{B.2}$$

along with the parameter and variable constraints

$$N_c, C_1 \geq 0 \qquad -90^\circ \leq \beta_{1,opt} \leq 0^\circ \tag{B.3}$$

Now, $\forall \left(N_c, C_1 \right)$ is there an inlet angle, β_1, such that $h_{loss,inc} = 0$? Hence, $\cot \beta_{1,opt}$ must fulfil the following

$$\begin{aligned} \cot \beta_{1,opt} &= \frac{\frac{-\pi N_c C_1 \left(R_{i,s}^3 - R_{i,h}^3 \right)}{45} \pm \sqrt{\frac{\pi^2 N_c C_1^2 \left(R_{i,s}^3 - R_{i,h}^3 \right)^2}{45^2} - 2\frac{\pi^2 N_c^2 \left(R_{i,s}^4 - R_{i,h}^4 \right)\left(R_{i,s}^2 - R_{i,h}^2 \right) C_1^2}{60^2}}}{2C_1^2 \left(R_{i,s}^2 - R_{i,h}^2 \right)} \\ &= \frac{\pi N_c}{2C_1 \left(R_{i,s}^2 - R_{i,h}^2 \right)} \left(\frac{-\left(R_{i,s}^3 - R_{i,h}^3 \right)}{45} \pm \sqrt{\frac{\left(R_{i,s}^3 - R_{i,h}^3 \right)^2}{45^2} - 2\frac{\left(R_{i,s}^4 - R_{i,h}^4 \right)\left(R_{i,s}^2 - R_{i,h}^2 \right)}{60^2}} \right) \end{aligned} \tag{B.4}$$

Thus, for real solutions to exist the following must be true,

$$\frac{8}{9}\left(R_{i,s}^3 - R_{i,h}^3\right)^2 \geq \left(R_{i,s}^4 - R_{i,h}^4\right)\left(R_{i,s}^2 - R_{i,h}^2\right) \tag{B.5}$$

Now introducing the variable $\delta = \frac{R_{i,h}}{R_{i,s}}$ for which $0 \leq \delta \leq 1$, the inequality above may be rewritten as

$$\begin{aligned} &(\delta-1)^4\left(\delta^2+4\delta+1\right) = \\ &(\delta-1)^4\left(\delta+2-\sqrt{3}\right)\left(\delta+2+\sqrt{3}\right) \leq 0 \\ \Downarrow \\ &\left(\delta+2-\sqrt{3}\right)\left(\delta+2+\sqrt{3}\right) \leq 0 \end{aligned} \tag{B.6}$$

This inequality is of course only fulfilled in the interval $\delta \in \left[-2-\sqrt{3}; -2+\sqrt{3}\right]$. Hence

$$\boxed{\{N_c > 0, C_1 > 0, R_{i,s} > 0, R_{i,h} > 0 \,|\Delta h_{loss,inc} = 0 \wedge R_{i,s} > R_{i,h}\} = \emptyset} \tag{B.7}$$

q.e.d.

Appendix C

Burnt mass fraction dynamics

The burnt mass fraction, F, in a given volume, V, is defined by

$$F = \frac{m_b}{m} \tag{C.1}$$

where m_b and m is the burnt gaseous mass and mass, respectively, in the volume. The definition assumes furthermore that the distribution of the burnt mass in the system is constant i.e.

$$\nabla_{x,y,z} F \equiv 0 \tag{C.2}$$

so that the burnt mass and fresh mass leaving the system can be compute by

$$\begin{aligned} \dot{m}_{b,out} &= F\dot{m}_{out} \\ \dot{m}_{f,out} &= (1-F)\dot{m}_{out} \end{aligned} \tag{C.3}$$

where the subscripts b and f indicate burnt mass and fresh mass respectively. The variable $\dot{m}_{out}$ is the total mass flow out the control volume V. Differentiating F with respect to the time t the following expression is obtained.

$$\dot{F} = \frac{\dot{m}_b}{m} - \frac{\dot{m}m_b}{m^2} \tag{C.4}$$

The gaseous mass, burnt as well as fresh, is assumed to be well described by the ideal gas law, hence

$$m = \frac{pV}{RT} \qquad m_b = \frac{pV}{RT}F \tag{C.5}$$

where p and T are the pressure and the temperature in the control volume V. The expression above assumes additionally that the differences in the gas properties between the burnt gas and fresh gas are negligible. The principle of mass conservation gives

$$\begin{aligned} \dot{m} &= \sum_{i=1}^{N} \dot{m}_i \\ \dot{m}_b &= \sum_{i=1}^{N} \left((\dot{m}_i > 0)F_i\dot{m}_i + (\dot{m}_i \leq 0)F\dot{m}_i\right) \end{aligned} \tag{C.6}$$

where positive mass flows, $\dot{m}_i$, are defined as mass flows going into the control volume V. The variable, F_i, is the burnt mass concentration of the corresponding positive inlet mass flow, and N is the total number of flows in and out of the control volume V.

The expressions in equation C.5 and equation C.6 are now inserted in equation C.4 to obtain

$$\boxed{\dot{F} = \frac{RT}{pV}\left(\sum_{i=1}^{N}(\dot{m}_i > 0)\,(F_i - F)\,\dot{m}_i\right)} \tag{C.7}$$

Hence, the burnt mass fraction F is only affected by positive inlet flows and their corresponding level of burnt mass content.

Appendix D

TDMVEM pressure and temperature ODEs

The generic layout intake of a turbocharged Diesel engine is schematically presented in figure D.1

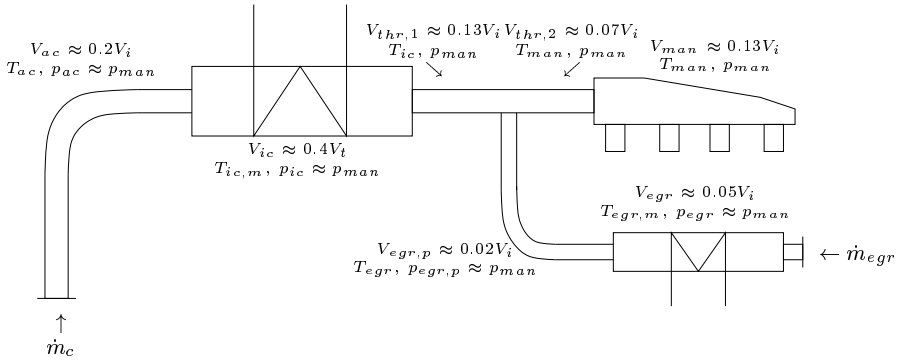

Figure D.1: Illustration of a typical intake system for a modern turbocharged Diesel engine. The figure also depicts the approximate volume fraction and the states for the individual intake system sections. The constant V_i is the total volume of the intake system.

The total mass contained in this system is

$$m_i = \frac{p_{ac}V_{ac}}{RT_{ac}} + \frac{p_{ic}V_{ic}}{RT_{ic,m}} + \frac{p_{man}V_{thr,1}}{RT_{ic}} + \frac{p_{man}(V_{thr,2}+V_{man})}{RT_{man}} + \frac{p_{egr}V_{egr}}{RT_{egr,m}} + \frac{p_{egr,p}V_{egr,p}}{RT_{egr}} \tag{D.1}$$

Neglecting the small influence of the EGR cooler and the EGR pipe connection and assuming that the overall pressure loss in the intake system is small, this equation is rewritten as

$$m_i = \frac{p_i V_{ac}}{RT_{ac}} + \frac{p_i V_{ic}}{RT_{ic,m}} + \frac{p_i V_{thr,1}}{RT_{ic}} + \frac{p_i \tilde{V}_{man}}{RT_{man}} \tag{D.2}$$

where p_i is the overall pressure level in the intake system and $\tilde{V}_{man}$ is the volume downstream of the EGR inlet point. Differentiating this equation with respect to time yields the following equation.

$$\begin{aligned}\dot{m}_i =& \frac{\dot{p}_i}{R}\left(\frac{V_{ac}}{T_{ac}} + \frac{V_{ic}}{T_{ic,m}} + \frac{V_{thr,1}}{T_{ic}} + \frac{\tilde{V}_{man}}{T_{man}}\right) \\ & - \frac{p_i}{R}\left(\frac{\tilde{V}_{ac}\cancelto{(\equiv 0)}{\dot{T}_{ac}}}{T_{ac}^2} + \frac{\tilde{V}_{ic}\cancelto{(\equiv 0)}{\dot{T}_{ic,m}}}{T_{ic,m}^2} + \frac{\tilde{V}_{thr,1}\cancelto{(\equiv 0)}{\dot{T}_{ic}}}{T_{ic}^2} + \frac{\tilde{V}_{man}\dot{T}_{man}}{T_{man}^2}\right)\end{aligned} \tag{D.3}$$

The assumptions $\dot{T}_{ac}, \dot{T}_{ic} \equiv 0$ are valid since the overall bandwidth of the inputs excitations (turbocharger and EGR valve) is small due to the throttle-less intake design. Furthermore, the temperatures T_{ac} and T_{ic} may adequately be described by the compressor outlet temperature and the intercooler models, respectively. Utilizing the law of mass conservation the equation below is obtained.

$$\begin{aligned}\dot{m}_{egr} + \dot{m}_c - \dot{m}_{ap} =& \frac{\dot{p}_i}{R}\left(\frac{V_{ac}}{T_{ac}} + \frac{V_{ic}}{T_{ic,m}} + \frac{V_{thr,1}}{T_{ic}} + \frac{\tilde{V}_{man}}{T_{man}}\right) \\ & - \frac{p_i}{R}\frac{\tilde{V}_{man}\dot{T}_{man}}{T_{man}^2} \\ \Updownarrow & \\ \dot{p}_i =& R\left(\dot{m}_{egr} + \dot{m}_c - \dot{m}_{ap} + \frac{p_i\tilde{V}_{man}\dot{T}_{man}}{RT_{man}^2}\right) \\ & \cdot \left(\frac{V_{ac}}{T_{ac}} + \frac{V_{ic}}{T_{ic,m}} + \frac{V_{thr,1}}{T_{ic}} + \frac{\tilde{V}_{man}}{T_{man}}\right)^{-1}\end{aligned} \tag{D.4}$$

The intake temperature derivative can readily be obtain from the AMVEM as

$$\dot{T}_{man} = \frac{RT_{man}}{p_i\tilde{V}_{man}}\left((\gamma T_{egr} - T_{man})\dot{m}_{egr} + (\gamma T_{ic} - T_{man})\cancelto{(\approx \dot{m}_c)}{\dot{m}_{thr,1}} - (\gamma - 1)T_{man}\dot{m}_{ap}\right) \tag{D.5}$$

Inserting this temperature description in the pressure state equation presented above yields the following TDMVEM pressure ODE.

$$\begin{aligned}\dot{p}_i &= k_p\left(T_{egr}\dot{m}_{egr} + T_{ic}\dot{m}_c - \tilde{T}_{man}\dot{m}_{ap}\right) \\ k_p &= \frac{R\gamma T_c T_{ic,m} T_{ic}}{V_{ac}T_{ic}T_{ic,m}\tilde{T}_{man} + V_{ic}T_cT_{ic}\tilde{T}_{man} + V_{thr,1}T_cT_{ic,m}\tilde{T}_{man} + \tilde{V}_{man}T_cT_{ic,m}T_{ic}}\end{aligned} \tag{D.6}$$

It is seen that the TDMVEM pressure state equation is a temperature and volume averaged version of the AMVEM pressure state equation.

Glossary

Acronyms

A/R	Area/Radius Ratio
AFR	Air/Fuel Ratio
AM	Amplitude Modulation
AMVEM	Adiabatic Mean Value Engine Model
ARX	Auto Regressive eXogenous
CDF	Cumulative Distribution Function
CFI	Central Fuel Injection.
CI	Compression Ignition
CO	Carbon Oxide
CO_2	Carbon Dioxide
DBW	Drive By Wire
DI	Direct Injection
DPF	Diesel Particle Filter
DTU	Technical University of Denmark
ECDS	Engine Control Development System
ECG	Engine Control Group
ECM	Engine Control and Monitoring
ECU	Engine Control Unit
EDF	Empirical Distribution Function
EGO	Exhaust Gas Oxygen
EGR	Exhaust Gas Recirculation
EKF	Extended Kalman Filter
EUDC	EUropean Drive Cycle
FE	Filling and Emptying
FFA	Ford Forschungszentrum, Aachen
FFT	Fast Fourier Transform
FMEP	Friction Mean Effective Pressure
GDI	Gasoline Direct Injection
HC	Hydrocarbon

HSDI ..... High Speed Direct Injection

IC ..... Internal Combustion

IMVEM ..... Isothermal Mean Value Engine Model

KKK ..... Kühnle, Kopp & Kausch

LQG ..... Linear Quadratic Gaussian

LS ..... Least Square

LWLS ..... Locally Weighted Least Square

MAF ..... Mass Air Flow

MEP ..... Mean Effective Pressure

MPI ..... Multi Point Injection

MVEM ..... Mean Value Engine Model

NA ..... Natural Aspirated

NN ..... Nearest Neighbor

NO_X ..... Oxides of Nitrogen

O_2 ..... Oxygen

OBD ..... Onboard Diagnostics

ODE ..... Ordinary Differential Equation

PDE ..... Partially Differential Equation

PI ..... Proportional–Integral

PM ..... Particulate Matter

RPM ..... Revolutions per minute

SAE ..... Society of Automotive Engineers

SI ..... Spark Ignition

SR ..... Sign Reversal

TDC ..... Top Dead Center

TDI ..... Turbo Direct Injection

TDMVEM ..... Turbo Diesel Mean Value Engine Model

TWC ..... Three Way Catalyst

U/C ..... Turbocharger wheel velocity/maximum fluid velocity Ratio

VES ..... Virtual Engine Simulation C library for SIMULINK®

VGT ..... Variable Geometry Turbine

VNT ..... Variable Nozzle Turbine

VVL ..... Variable Valve Lift

VVT ..... Variable Valve Train

WOT ..... Wide Open Throttle

Variables

A_{eq} ..... Equivalent area $\triangleq C_D A_{noz} \frac{p_{01,ref}}{\sqrt{RT_{01,ref}}}$.

α ..... Heat exchanger variable.

α_1 ..... VGT nozzle inlet flow angle.

α_2 ..... VGT nozzle outlet flow angle.

α_n ..... VGT nozzle blade angle.

A_{noz} ..... Minimum sectional nozzle area.

A_s ..... Inlet area of the VGT scroll.

β ..... Distribution between premixed and diffusion combustion.

β_2 ..... Slip angle.

$\beta_{2,b}$ ..... Impeller blade angle.

C_D ..... Discharge Coefficient.

χ ..... VGT pressure ratio distribution variable.

$C_{2,r}$ ..... Radial exit velocity of the compressor fluid.

C_s ..... Gas velocity following isentropic expansion *or* absolute VGT scroll flow velocity.

$C_{1,\theta}$ ..... Tangential velocity component of C_1 at entry diameter D_1.

$C_{2,\theta}$ ..... Tangential velocity component of C_2 (impeller tip).

$C_{2,\theta b}$ ..... Ideal fluid exit velocity (no slip).

$C_{3,\theta}$ ..... Tangential velocity component of C_3 at rotor inlet.

$C_{4,\theta}$ ..... Tangential velocity component of C_4 at rotor outlet radius R_4.

D_1 ..... Averaged inducer diameter.

$\delta\alpha_n$ ..... VGT nozzle ring flow angle change.

δ_n ..... Minimum distance between neighboring VGT blades.

$\delta\theta_{comb}$ ..... Nominal combustion duration.

Δh_{01} ..... Total enthalpy rise at station 1.

Δh_{02} ..... Total enthalpy rise at station 2.

Δh_{03} ..... Total enthalpy rise at station 3.

Δh_{04} ..... Total enthalpy rise at station 4.

Δh_{0c} ..... Total enthalpy rise across compressor stage.

$\Delta h_{0,i}$ ..... Isentropic enthalpy rise across compressor stage.

$\Delta h_{0,t}$ ..... Effective enthalpy drop across turbine stage.

$\Delta h_{0t,i}$ ..... Isentropic enthalpy drop across turbine stage.

Δh_1 ..... Static enthalpy rise at station 1.

Δh_2 ..... Static enthalpy rise at station 2.

Δh_3 ..... Static enthalpy rise at station 3.

Δh_4 ..... Static enthalpy rise at station 4.

Δh_{loss} ..... Total enthalpy loss.

$\Delta h_{loss,fric}$ ..... Enthalpy loss due to friction.

$\Delta h_{loss,inc}$ ..... Enthalpy loss due to collision.

$\dot{m}_{ap}$ ..... Intake port mass flow.

$\dot{m}_{ap,f}$ ..... Fresh intake port mass flow.

$\dot{m}_c$ ..... Compressor mass flow.

$\dot{m}_{c,c}$ ..... Compressor mass flow, corrected.

$\dot{m}_{egr}$ ..... EGR mass flow.

$\dot{m}_{noz}$ ..... Isentropic nozzle mass flow *or* mass flow through the VGT nozzle ring.

$\dot{m}_{rot}$ ..... Mass flow through the rotor.

$\dot{m}_t$ ..... Turbine mass flow.

$\dot{m}_t$ ..... Turbine mass flow, corrected.

E_k ..... Kinetic energy.

ϵ ..... Slip factor parameter or model–measurement error *or* noise *or* heat exchanger effectiveness.

ϵ_{ic} ..... EGR cooler effectiveness.

ϵ_{ic} ..... Intercooler effectiveness.

$\overline{\epsilon}_{ic}$ ..... Descriptive intercooler effectiveness.

$\eta_{c,TT}$ ..... Isentropic compressor efficiency, total to total.

η_i ..... Engine fuel efficiency.

$\eta_{t,TT}$ ..... Isentropic turbine efficiency, total to total.

I ..... Pulsation level index.

J_{min} ..... Minimum cost function value.

Λ ..... Coefficient vector to the polynomial P.

m_{ac} ..... Mass between compressor and intercooler.

M_d ..... Normalized diffusion combustion function.

m_{egr} ..... EGR cooler gas mass.

$m_{egr,p}$ ..... Gaseous mass in the EGR pipe connection.

m_f ..... Total entrapped fuel mass in the individual cylinder.

$m_{f,b}$ ..... Total entrapped fuel mass burnt in the individual cylinder.

m_{ic} ..... Contained mass in the intercooler.

m_{man} ..... Intake plenum gas mass.

M_p ..... Normalized premixed combustion function.

$m_{thr,1}$ ..... Mass between intercooler and EGR inlet point.

$m_{thr,2}$ ..... Mass between EGR inlet point and plenum.

N ..... Engine speed.

N_c ..... Compressor revolutions.

N_p ..... No. of EGR cooler pipes.

N_t ..... Turbine revolutions.

Nu ..... Nusselt number.

Ω ..... LWLS weight matrix.

P ..... LWLS polynomial *or* power.

p_{01} ..... Stagnated pressure at station 1.

p_{02} ..... Stagnated pressure at station 2.

p_{03} ..... Stagnated pressure at station 3.

p_{04} ..... Stagnated pressure at station 4.

p_1 ..... Static pressure at station 1.

p_2 ..... Static pressure at station 2.

p_3 ..... Static pressure at station 3.

p_4 ..... Static pressure at station 4.

P_c ..... Compressor power consumption.

p_{cyl} ..... Cylinder pressure.

$P_{fric,pump}$ ..... Power loss to engine pumping.

ϕ ..... Ratio between $C_{r,2}$ and U_2 *or* LWLS regressor vector *or* fuel/air ratio.

p_i ..... Overall pressure level in the intake system.

p_{ic} ..... Intercooler pressure.

p_r ..... Pressure ratio across compressor or turbine ($\frac{p_c}{p_{01}}$ or $\frac{p_{01}}{p_4}$).

p_r ..... Effective pressure ratio the VGT ($\triangleq p_{r,noz}p_{r,rot}$).

$p_{r,min}$ ..... Minimum turbine pressure ratio needed to overcome the centrifugal pressure gradient around the rotor.

p_r ..... Effective pressure ratio across the VGT nozzle ring.

p_r ..... Effective pressure ratio across the rotor.

p_r ..... Pressure ratio across turbine, total to total.

P_t ..... Turbine power production.

Q ..... Heat transfer.

Q_{comb} ..... Combustion heat release rate.

r ..... Radius

Re ..... Reynolds number.

r_g ..... Kernel bandwidth.

ρ_1 ..... Static fluid density at impeller eye.

ρ_2 ..... Static fluid density at impeller tip.

ρ_c ..... Static compressor outlet density.

$R_{i,h}$ ..... Inducer radius, hub side.

$R_{i,s}$ ..... Inducer radius, shroud side.

R_r ..... Rotor radius.

σ ..... Compressor slip factor, or variance.

T_{04} ..... Stagnation temperature at station 4.

$T_{0,x}$ ..... Stagnation temperature at station x.

T_2 ..... Static impeller fluid exit temperature.

T_{ac} ..... Temperature in the compressor-intercooler pipe connection.

T_{amb} ..... Ambient temperature.

τ ..... Torque *or* time constant.

τ_2 ..... Torque exerted on the fluid by the impeller (impeller tip conditions).

T_c ..... Static compressor outlet temperature.

T_{egr} ..... EGR temperature.

$T_{egr,m}$ ..... Mean EGR cooler temperature.

T_{ep} ..... Exhaust port temperature.

T_{exh} ..... Exhaust gas temperature.

$T_{he,in}$ ..... Heat exchanger cooling element inlet temperature.

$T_{he,out}$ ..... Heat exchanger cooling element outlet temperature.

θ ..... Input variable vector.

θ_0 ..... Input variable vector origin.

$\theta_{0,g}$ ..... LWLS grid point.

θ_e ..... Crankshaft position.

θ_{ign} ..... Crank position where the combustion initiated.

θ_{vgt} ..... VGT position.

$T_{he,x}$ ..... Heat exchanger temperature at position x.

$T_{ic,m}$ ..... Mean intercooler temperature.

$T_{ic,out}$ ..... Intercooler exit temperature.

T_{man} ..... Intake manifold temperature.

T_{out} ..... Heat exchanger outlet temperature.

T_{wall} ..... Heat exchanger wall temperature.

U ..... Internal energy *or* turbocharger related velocities.

u ..... Specific internal energy.

U_1 ..... Inducer blade velocity at diameter D_1.

U_2 ..... Impeller tip velocity.

U_3 ..... Rotor tip velocity (station 3).

U_4 ..... Exducer velocity at radius R_4 (station 4).

V ..... Volume.

ς ..... U/C ratio at which $p_r = p_{r,min}$.

$\overline{v}_p$ ..... Average laminar pipe fluid velocity.

W ..... Relative fluid velocity.

W_1 ..... Relative fluid inlet velocity (inducer).

W_1 ..... Relative fluid inlet velocity (inducer).

$W_{1,\theta,r}$ ..... Tangential component of W_1 at radius r.

W_n ..... Vectorial velocity difference between C_1 and C_2 (VGT model).

$W_{n,\theta}$ ..... Tangential velocity component of W_n.

$\tilde{W}_{n,\theta}$ ..... Approximated tangential velocity component of W_n .

ζ_{cool} ..... Coolant energy fraction.

ζ_{exh} ..... Exhaust energy fraction.

ζ_n ..... Spherical distance between VGT blade tips.

Z ..... LWLS data kernel.

Constants

a ..... Δh_{0c} model parameter.

α_1 ..... Impeller friction parameter.

α_2 ..... Impeller friction parameter.

α_3 ..... Impeller friction parameter.

α_{ρ_2} ..... ρ_2 model parameter.

b ..... Impeller outlet width or Δh_{0c} model parameter.

β_1 ..... Inducer blade angle.

$\beta_{1,opt}$ ..... Optimal fluid entry angle (inducer).

b_r ..... Rotor inlet width.

c_1 ..... Müller friction model coefficient.

c_2 ..... Müller friction model coefficient.

C_{d1} ..... Diffusion combustion parameter.

C_{d2} ..... Diffusion combustion parameter.

c_p ..... Specific heat capacity at fixed pressure.

C_{p1} ..... Premixed combustion parameter.

C_{p2} ..... Premixed combustion parameter.

c_v ..... Specific heat capacity at fixed volume.

D_I ..... Impeller outlet diameter.

$D_{i,h}$ ..... Inducer diameter, hub side.

$D_{i,s}$ ..... Inducer diameter, shroud side.

$\dot{m}_{t,c,max}$ ..... Maximum corrected turbine mass flow.

D_p ..... Diamter of the individual heat exchanger pipe.

D_r ..... Rotor diameter.

$D_{r,a}$ ..... Nozzle ring diameter (blade axel centroid).

$D_{r,i}$ ..... Inner nozzle ring diameter.

$D_{r,o}$ ..... Outer nozzle ring diameter.

E_{HV} ..... Fuel heating value.

γ ..... $\frac{c_p}{c_v}$ ratio

J_{eng} ..... Moment of inertia of the engine.

k ..... Heat transfer coefficient.

l_n ..... VGT nozzle blade length.

$l_{n,tip}$ ..... VGT nozzle blade length from axel to tip.

L_p ..... Length of the individual heat exchanger pipes.

L_{stroke} ..... Engine stroke length.

N_{noz} ..... No. of VGT nozzle blades.

τ_{ign} ..... Ignition delay.

Θ ..... Parameter vector.

V_{ac} ..... Volume between compressor and intercooler.

V_d ..... Engine displacement volume.

V_{egr} ..... EGR cooler volume.

$V_{egr,p}$ ..... EGR pipe connection volume.

V_i ..... Total intake system volume.

V_{ic} ..... Intercooler volume.

V_{man} ..... Intake plenum volume.

$V_{thr,1}$ ..... Volume between intercooler and EGR inlet point.

$V_{thr,2}$ ..... Volume between EGR inlet point and plenum.

ξ_{ρ_2} ..... ρ_2 model parameter.

Z ..... Impeller/Rotor blade number.

Bibliography

[1] United States Patent No. 4,939,658, July 3, 1990. Assignee: Hitachi Ltd., Tokyo, Japan.

[2] Private communication with Dr. Ing. Arnd Sommerhoff, technical specialist at Ford Fordschungszentrum Aachen GmbH.

[3] Private communication with Dipl. Ing. Daniel Röttger, research engineer at Ford Fordschungszentrum Aachen GmbH.

[4] The specially prepared 7 port head for the 1275cc British Leyland engines was provided by Georg Mikkelsen, ÅKM Racing, Lerpyttevaj 31, 7700 Thisted, Denmark, Phone: (+45) 97920182.

[5] E-mail communication between Christian Laurent, PSA, and the author on the 5th of June, 2000.

[6] BOSCH sensor program 98/99, Bosch No. 1 987-720-535/804.

[7] A. A. Amsden, *KIVA-3: A KIVA Program with Block-Structured Mesh for Complex Geometries*, Los Alamos National Laboratory, 1993, Report No: LA-12503-MS.

[8] A. A. Amsden, P. J. O'Rourke, and T. D. Butler, *KIVA-II: A Computer Program for Chemically Reactive Flows with Sprays*, Los Alamos National Laboratory, 1989, Report No: LA-11560-MS.

[9] A. Gelb (ed.), *Applied optimal estimation*, The M.I.T. Press, 12th printing, 1992.

[10] A. M. R. Chevalier, *Wide Bandwidth Control of the Air/Fuel Ratio of Spark Ignition Engines*, Ph.D. dissertation, Technical University of Denmark, Institute for Automation, 2000.

[11] ECM (Engine Control and Monitoring), 101 Street, Suite 365, Los Altos, CA 94022,USA.

[12] C. F. Aquino, *Transient A/F Control Characteristics of the 5 Liter Central Fuel Injection Engine*, SAE Technical Paper (1981), no. 810494.

[13] B. Ault, V. K. Jones, J. D. Powell, and G. F. Franklin, *Adaptive Air-Fuel Ratio Control of a Spark Ignition Engine*, SAE Technical Paper (1994), no. 940373.

[14] B. Horner, *Garrett Turbocharger Specifications and Calculations*, Allied Signals, 1980, Garrett is now part of Allied Signals.

[15] B. Qvale and V. Bothmann, *Notes in turbomachinery*, Laboratory for Energetics, Technical University of Denmark, 1994, Part 1–3.

[16] C. Hong and N. Watson, *Turbocharged S.'I. Engine Simulation under Steady and Transient Conditions*, SAE Technical Paper (1988), no. 880122.

[17] C. W. Vigild, A. Chevalier, and E. Hendricks, *Avoiding Signal Aliasing in Event-Based Engine Control*, SAE Technical Paper (2000), no. 2000-01-0268.

[18] Carl-Anders Hergart, *Modeling Combustion and Soot Emissions in a Small-Bore Direct-Injection Diesel Engine*, Ph.D. dissertation, Rheinisch-Westälische Technische Hochschule Aachen, 2001.

[19] C.-F. Chang, N.P. Fekete, and J. D. Powell, *Engine Air-Fuel Ratio Control Using an Event-Based Observer*, SAE Technical Paper (1993), no. 930766.

[20] G. Chen, M. T. Vincent, and T. R. Gutermuth, *The Behavior of Multiphase Fuel-Flow in the Intake Port*, SAE Technical Paper (1994), no. 940445.

[21] A. Chevalier and M. Müller, *On the Validity of Mean Value Engine Models During Transient Operation*, SAE Technical Paper (2000), no. 2000-01-1261.

[22] A. Chevalier and C. W. Vigild, *Predicting the Port Air Mass Flow of SI Engines in A/F Ratio Control Applications*, SAE Technical Paper (2000), no. 2000-01-0260.

[23] S.B. Choi, M. Won, and J.K. Hedrick, *Fuel Injection Control of SI Engines*, Proceedings of the 33rd IEEE Conference on Des. and Control (CDC) (1994), Lake Buena Vista, Florida.

[24] Urs Christen, *Engineering Aspects of $\mathcal{H}_\infty$ Control*, Ph.D. dissertation, Swiss Federal Institute of Technology, 1996, Diss. ETH No. 11433.

[25] D. A. Kouremenos, C. D. Rakopoulos, and E. Karvounis, *Thermodynamic Analysis of Direct Injection Diesel Engines by Multi-zone Modeling*, ASME WA-Meeting, Boston, MA, USA **3.3** (1987), 67–77.

[26] DieselNet, *Exhaust Gas Recirculation*, URL: `http://www.dieselnet.com`.

[27] D.N. Assanis and J.B. Heywood, *Development and Use of a Computer Simulation of the Turbocompounded Diesel System for Engine Performance and Component Heat Transfer Studies*, SAE Technical Paper (1986), no. 860329.

[28] Donald J. Dobner, *A Mathematical Engine Model for Development of Dynamic Engine Control*, SAE Technical Paper (1980), no. 800054.

[29] E. Trostmann, *Pneumatical Control - Notes to Course 8204*, Technical University of Denmark, 1987, in danish.

[30] Inc Electromotive, *TEC-I,TEC-II and HPV-3B, Total Engine Control, Engine Management Systems by Electromotive, Inc, Installation and User's Manual*, Electromotive, Inc, 14004 - J Willard Road, Chantilly, Virgina 22021.

[31] D. Engler, *Manifold Fuel Film, Modelling and Prevention*, Master's thesis, Technical University of Denmark, Institute of Automation, 2001.

[32] David Eppstein, *Delunay triangulation – part of geometry in action, a collection of applications of computational geometry.*, Theory Group, ICS, UC Irvine., URL: `http://www.ics.uci.edu/~eppstein/gina/delaunay.html`.

[33] Evangelos Karvounis, *Development and use of a multi-purspose simulation framework for internal combustion engine design*, Master's thesis, University of Illinois at Urbana-Champaign, 1991.

[34] F. S. Bhinder, *Investigation of flow in a nozzleless spiral casing of a radial–inward flow gas turbine*, Proc. Inst. Mech. Engers. **184** (1969/70), Pt 3G(II).

[35] N.P. Fekete, J.D. Powell, U. Nester, and I. Gruden, *Model Based Air-Fuel Ratio Control of a Lean Multi-Cylinder Engine*, SAE Technical Paper (1995), no. 950846.

[36] C.R. Ferguson, *The Centrifugal Compressor Stage*, Butterworth, 1963, London.

[37] M. Føns, *Indførelse af Recirkulering af Udstødningsgas (EGR) i SI-Motorer*, Master's thesis, The Technical University of Denmark, Department of Energy and Institute of Automation, DTU, 1997, In danish.

[38] G. F. Hiett and I. H. Johnston, *Experiments concerning the aerodynamic performance of inward radial turbines*, Proc. Inst. Mech. Engers. **178** (1963/64), Pt 31(II).

[39] G. L. Gissinger, P. M. Frank, and J. Wunnennberg, *Model-Based Electronic Engine and Turbocharger Control*, SAE Technical Paper (1990), no. 900595.

[40] J. T. Gravdahl, *Modeling and Control of Surge and Rotating Stall in Compressors*, Ph.D. dissertation, Norwegian University of Science and Technology, Trondheim, Norway, 1998, Report 98-6-W.

[41] H. Kwakernaak and R. Sivan, *Linear optimal control systems*, first ed., Wiley-Interscience, 1972.

[42] E. Hendricks, *A Compact, Comprehensive Model of Large Turbocharged, Two-Stroke Diesel Engines*, SAE Technical Paper (1986), no. 861190.

[43] _____, *The Analysis of Mean Value Engine Models*, SAE Technical Paper (1989), no. 890563.

[44] _____, *Errors in Hot Wire MAF Measurement Systems*, Revised Interim Report, Technical University of Denmark, 1992.

[45] E. Hendricks and A. Chevalier, *Emerging Engine Control Technologies*, 29th ISATA Conference on Automotive Electronics (1996), no. 96AE029, Florence, Italy.

[46] E. Hendricks, A. Chevalier, and M. Jensen, *Event Based Engine Control: Practical Problems and Solutions*, SAE Technical Paper (1995), no. 950008.

[47] E. Hendricks, M. Jensen, A. Chevalier, S. C. Sorenson, D. Trumphy, and J. Asik, *Modelling of the Intake Manifold Filling Dynamics*, SAE Technical Paper (1996), no. 960037.

[48] E. Hendricks, M. Jensen, A. Chevalier, and T. Vesterholm, *Conventional Event Based Engine Control*, SAE Technical Paper (1994), no. 940377.

[49] E. Hendricks and S. C. Sorenson, *Mean Value Modeling of Spark Ignition Engines*, SAE Technical Paper (1990), no. 900616.

[50] _____, *SI Engine Controls and Mean Value Engine Modeling*, SAE Technical Paper (1991), no. 910258.

[51] E. Hendricks and T. Vesterholm, *The Analysis of Mean Value SI Engine Models*, SAE Technical Paper (1992), no. 920682.

[52] E. Hendricks, T. Vesterholm, P. Kaidantzis, P. Rasmussen, and M. C. Jensen, *Nonlinear Transient Fuel Film Compensation*, SAE Technical Paper (1993), no. 930767.

[53] E. Hendricks, T. Vesterholm, and S. C. Sorenson, *Nonlinear, Closed Loop, SI Engine Control Observers*, SAE Technical Paper (1992), no. 920237.

[54] J. B. Heywood, *Internal Combustion Engine Fundamentals*, McGraw-Hill, Inc., 1988.

[55] J. B. Heywood, J. M. Higgins, P. A. Watts, and R. J. Tabaczynski, *Development and Use of a Cycle Simulation to Predict SI Engine Efficiency and NO_x Emissions*, SAE Technical Paper (1979), no. 790291.

[56] J. Gerhardt, N. Benninger, and W. Hess, *Torque-Based System Structure of an Electronic Engine Management System as a New Base for Drive Train Systems (Bosch ME7 System)*, 6. Aachener Kolloqium, Fahrzeug- und Motortechnik (Aachen, Germany), 20.-22. October 1997, in german.

[57] J. H. Horlock and D. E. Winterbone, *The Thermodynamics and Gas Dynamics of Internal-Combustion Engines*, vol. 2, Oxford University Press, 1986.

[58] J. Lillelund, *Design of an Engine Control Development System*, Master's thesis, The Technical University of Denmark, Institute of Automation, 1991.

[59] J. M. Luján, F. Payri, F. Vera, and C. Guardiola, *Modelling, Effect and Behaviour of the EGR Venturi in a Heavy-Duty Diesel Engine*, SAE Technical Paper (2001), no. 2001-01-3227.

[60] J. M. Luján, J. Galindo, and J. R. Serrano, *Efficiency Characterization of Centripetal Turbines under Pulsating Flow Conditions*, SAE Technical Paper (2001), no. 2001-01-0272.

[61] J.-P Jensen and A. F. Kristensen, *Development of Dynamic Diesel Engine Models, Modelling Principle for Turbocharged Diesel Engine*, Master's thesis, The Technical University of Denmark, Department of Energy, DTU, 1990, In danish.

[62] J.-P. Jensen, Kristensen, A.F., S.C Sorenson, N. Houbak, and E. Hendricks, *Transient simulation of a small turbocharged diesel engine*, Proc. I Mech E Sem. on Engine Transient Perm. (1990).

[63] ———, *Mean value modeling of a small turbocharged diesel engine*, SAE Technical Paper (1991), no. 910070.

[64] J. P. Mello and A. M. Mellor, *NO_X Emmisions from Direct Injection Diesel Engines with Water/Steam Dilution*, SAE Technical Paper (1999), no. 1999-01-0836.

[65] J. W. Daily and R. E. Nece, *Chamber dimension effects on induced flow and frictional resistance of enclosed rotating discs*, Trans. ASME J. Basic Engng **82** (1960).

[66] P.B. Jensen, M.B. Olsen, J. Poulsen, E. Hendricks, M. Føns, and C. Jepsen, *A New Family of Nonlinear Observers for SI-Engine Air-Fuel Ratio Controls*, SAE Technical Paper (1997), no. 970615.

[67] Jun-Lon Chen, Mark Eubank, and Robert Wattleworth, *Improving Valve Retainer Life for Fuel Pressure Regulators*, SAE Technical Paper (1999), no. 1999-01-0794.

[68] K. J. Åström and B. Wittenmark, *Computer-Controlled Systems: Theory and Design*, 2nd ed., Prentice-Hall International, Inc., 1990.

[69] P. Kaidantzis, P. Rasmussen, M. Jensen, T. Vesterholm, and E. Hendricks, *Robust Self-Calibrating Lambda Feedback for SI Engines*, SAE Technical Paper (1993), no. 930860.

[70] R. E. Kalman and R. S. Bucy, *New Results in Linear Filtering and Prediction Theory*, Journal of Basic Engineering, Trans. ASME **83D** (1961), 95–108.

[71] Kemin Zhou and John C. Doyle, *Essentials of robust control*, Prentice-Hall International, Inc., 1998.

[72] Lennart Ljung, *System Identification: Theory for the User*, second ed., Prentice Hall, Inc, 1999.

[73] J. Lillelund and E. Hendricks, *A PC Engine Control Development System*, SAE Technical Paper (1991), no. 910259.

[74] B. M. Lyko, *Application Manual for the Linear Exhaust Gas Reciculation Valve*, Delphi Energy and Engine Management Systems, 1995.

[75] M. Føns, M. Müller, A. Chevalier, C. W. Vigild, S. C. Sorenson, and E. Hendricks, *Mean Value Engine Modeling of an SI engine with EGR*, SAE Technical Paper (1999), no. 1999-01-0909.

[76] M. Nyberg and L. Nielsen, *Model-based diagnosis for the air intake system of the SI engine*, SAE Technical Paper (1997), no. 970209.

[77] P.J. Maloney, *An Event-Based Transient Fuel Compensator with Physically Based Parameters*, SAE Technical Paper (1999), no. 1999-01-0553.

[78] P.J. Maloney and P.M. Olin, *Pneumatic and Thermal State Estimations for Production Engine Control and Diagnostics*, SAE Technical Paper (1998), no. 980517.

[79] J. J. G. Martins and I. C. Finlay, *Fuel Preparation in Port-Injected Engines*, SAE Technical Paper (1992), no. 920518.

[80] Mathworks, *Matlab function reference*, release 11 revision ed.

[81] H. Melgaard, E. Hendricks, and H. Madsen, *Continuous Identification of a Four-Stroke SI Engine*, American Control Conference (ACC) (1990), no. TP10, 5:30, San Diego, CA.

[82] M. Morari and E. Zafiriou, *Robust Process Control*, Prentice-Hall, Inc., 1989, Englewood Cliffs, N.J.

[83] M. Müller, *Mean Value Modelling of Turbocharged Spark Ignition Engines*, Master's thesis, The Technical University of Denmark, Institute of Automation and Department of Energy, 1997.

[84] M. Müller, E. Hendricks, and S. C. Sorenson, *Mean Value Modeling of Turbocharged Spark Ignition Engines*, SAE Technical Paper (1998), no. 980784.

[85] Müller, Martin, Olin, Peter M., and Schreurs, Bart, *Dynamic EGR estimation for production engine control*, SAE Technical Paper (2001), no. 2001-01-0553.

[86] N. Watson, A. D. Pilley, and M. Marzouk, *A Combustion Correlation for Diesel Engine Simulation*, SAE Technical Paper (1980), no. 800029.

[87] N. Watson and M. S. Janota, *Turbocharging the internal combustion engine*, first ed., MACMILLIAN EDUCATION LTD, 1982.

[88] NIST/SEMATECH, *Engineering statistical handbook*, NIST/SEMATECH, URL: `http://www.itl.nist.gov/div898/handbook/index.htm`.

[89] T. Nogi, Y. Ohyama, T. Yamauchi, and H. Kuroiwa, *Mixture Formation of Fuel Injection Systems in Gasoline Engines*, SAE Technical Paper (1988), no. 880558.

[90] P. Azzoni, G. Minelli, D. Moro, and G. Serra, *A Model for EGR Flow Rate Estimation*, SAE Technical Paper (1997), no. 970030.

[91] P. E. Moraal and I. V. Kolmanovsky, *Turbocharger Modeling for Automotive Control Applications*, SAE Technical Paper (1999), no. 1999-01-0908.

[92] R. C. Pampreen, *Small turbomachinery compressor and fan aerodynamics*, Journal of engineering for power (1973), no. 95, 251–256.

[93] Randall P. Izydorek and G. Clarke Oberheide, *Improved Pulsation Damper for the Fuel Injector Rail*, SAE Technical Paper (1997), no. 971071.

[94] Reuter, Wolfgang, Loesing, Karl-Heinrich, and Golden, John E, *An improved anti-pulsation mass airflow sensor*, SAE Technical Paper (2001), no. 2001-01-0985.

[95] Rober W. Weeks and John. J. Moskwa, *Automotive Engine Modeling for Real-Time Control Using MATLAB/SIMULINK*, SAE Technical Paper (1995), no. 950417.

[96] Robert A. Granger, *Fluid mechanics*, first ed., Dover, 1985.

[97] Robert. W. Fox and Alan T. McDonald, *Introduction to Fluid Mechanics*, fourth ed., John Wiley & Sons, Inc, 1994, SI version.

[98] S. M. Futral and C. A. Wasserbauer, *Off-design performance prediction with experimental verification for a radial inflow turbine*, National Advisory Committee for Aeronautics (now NASA), 1965, NACA TN D-2621.

[99] S. Skogestad and I. Postlethwaith, *Multivariable Feedback Control, Analysis and Design*, John Wiley & Sons, 1996.

[100] P.J. Shayler and M.S. Goodman, *Mixture Control with Air-Flow Anticipation Using Neural Networks*, 29th ISATA Conference on Automotive Electronics (1996), no. 96AE025, Florence, Italy.

[101] M. A. Stephens, *EDF Statistics for Goodness of Fit and Some Comparisons*, Journal of the American Statistical Association **69** (1974), 730–737.

[102] D. L. Stivender, *Engine Air Control - Basis of a Vehicular Systems Control Hierarchy*, SAE Technical Paper (1978), no. 780346.

[103] M. Struwe and C. W. Vigild, *Robust $\mathcal{H}_\infty$ Control of an SI Engine's Air/Fuel Ratio*, Master's thesis, Technical University of Denmark, Institute of Automation, 1997, In danish.

[104] Thomas Morel, Rifat Keribar, and Paul N. Blumberg, *A New Approach to Integrating Engine Performance and Component Design Analysis Through Simulation*, SAE Technical Paper (1988), no. 880131.

[105] L. Trajkovski, *Computer Controlled Engine Management System*, Master's thesis, Technical University of Denmark, Institute of Automation, 1997, In danish.

[106] Turbodyne, URL: `http://www.turbodyne.com`.

[107] R. C. Turin and H. P. Geering, *Model-Based Adaptive Fuel Control in an SI Engine*, SAE Technical Paper (1994), no. 940374.

[108] U. Christen, P.E. Moraal, and K.J. Vantine, *Model identification and implementation in* MATLAB/SIMULINK *for the 90 PS PUMA 2.4 liter DI Diesel engine*, Technical Report SRR 1998-0136, Ford Motor Company, Ford Forschungszentrum, Aachen, Süsterfeldstrasse 200, D-52072 Aachen, Germany, 1998.

[109] U. Kiencke and L. Nielsen, *Automotive Control Systems*, Springer Verlag, 2000.

[110] Tamon Ueda, *Temperature- and flow-measurement by ultrasonics* , Revised Interim Report, Technical University of Denmark, in danish, 1999.

[111] Urs Christen, Katie J. Vantine, and Nick Collings, *Event-Based Mean-Value Modeling of DI Diesel Engines for Controller Design*, SAE Technical Paper (2001), no. 2001-01-1242.

[112] C. W. Vigild, K. P. H. Andersen, E. Hendricks, and M. Struwe, *Towards Robust H-infinity Control of an SI Engine's Air/Fuel Ratio*, SAE Technical Paper (1999), no. 1999-01-0854.

[113] Michael Wahle, *Dynamic (Kinematik und Kinetik)*, Wissenschaftsverlag Mainz in Aachen, 1998, in German.

[114] M. H. Westbrook and J. D. Turner, *Automotive Sensors*, Institute of Physics Publishing, Bristol and Philadelphia, 1994.

[115] A. Whitfield, *Slip factor of a centrifugal compressor and its variation flow rate*, Proc. Inst. Mech, Engrs, 188 (1974), no. 32/74.

[116] H.-M. Wiedenmann, G. Hötzel, H. Neumann, J. Riegel, and H. Weyl, *Exhaust Gas Sensors*, Automotive Electronics Handbook (R. K. Jurgen, ed.), McGraw-Hill, Inc., 1995.

[117] F. J. Wiesner, *A review of slip factors for centrifugal impellers*, ASME Publication 66-WA-FE-18 (1966).

[118] Xiao Hu and Patrick B. Lawless, *Prediction of On-Engine Efficiency for the Radial Turbine of a Pulse Turbocharged Engine*, SAE Technical Paper (2001), no. 2001-01-1238.